

**CHARACTERIZATION OF SPIN TRANSFER
TORQUE AND MAGNETIZATION
MANIPULATION IN MAGNETIC
NANOSTRUCTURES**

A Dissertation

Presented to the Faculty of the Graduate School

of Cornell University

in Partial Fulfillment of the Requirements for the Degree of

Doctor of Philosophy

by

Chen Wang

August 2012

© 2012 Chen Wang

ALL RIGHTS RESERVED

CHARACTERIZATION OF SPIN TRANSFER TORQUE AND
MAGNETIZATION MANIPULATION IN MAGNETIC NANOSTRUCTURES

Chen Wang, Ph.D.

Cornell University 2012

This dissertation describes a number of research projects with the common theme of manipulating the magnetization of a nanoscale magnet through electrical means, and the major part is devoted to exploring the effect of spin angular momentum transfer from a spin-polarized current to a nanomagnet, which we call spin transfer torque.

Spin transfer torque is a promising new mechanism to “write” magnetic storage elements in magnetic random access memory (MRAM) devices with magnesium oxide (MgO)-based magnetic tunnel junction (MTJ) architecture. The first part of our work aims at a quantitative measurement of the spin transfer torque exerted on one of the ferromagnetic electrodes in exactly this type of tunneling structures used for MRAM applications. We use a technique called spin-transfer-driven ferromagnetic resonance (ST-FMR), where we apply a microwave-frequency oscillating current to resonantly excite magnetic precession, and we describe two complementary methods to detect this precession. We resolve previous controversies over the bias dependence of spin transfer torque, and present the first quantitative measurement of spin transfer torque in MgO-based MTJs in full bias range. We also analyze and test the potential to use the ST-FMR technique for microwave detection and microwave amplification.

In the second part of the our work, we fabricate ferromagnetic nanoparticles made of CoFeB or Co embedded in the MgO tunnel barrier of a typical magnetic

tunnel junction device, and study the spin transfer torque exerted on these nanoparticles 2-3 nm in size. We present the first evidence of spin transfer torque in magnetic nanoparticles insulated from electrodes by mapping out the switching phase diagram of a single nanoparticle. We also study ferromagnetic resonance of a small number of nanoparticles induced by spin transfer torque, with the goal of approaching single electron tunneling regime.

The last part of our work explores a dramatically different way to manipulate magnetization electrically. We couple a ferromagnet to a multiferroic material, bismuth ferrite (BiFeO_3), by exchange bias interaction, and try to manipulate the ferromagnet by ferroelectric switching of the BiFeO_3 .

BIOGRAPHICAL SKETCH

Chen Wang was born on February 24th, 1984 in Shanghai, China, and enjoyed his beautiful childhood in Ma'anshan, a mid-sized city¹ about 200 miles to the west of Shanghai, where both his parents teach college lab courses in analytical chemistry for their lifetime. His father played a key role in inspiring his curiosity in understanding nature since very young age, while his mother told him early that a chemistry major does not translate well on the job market². As the combined effect turns out many years later, he is now pursuing a research career in physics.

In his early school years, he loved modifying or remaking board games mostly related to fighter jets or rocket missiles. His initial dream was to build spacecrafts for his country when he grew up, but this ambition took a hit after his frustration with a middle school engineering competition in building “robots”. He found his occasional brilliance in independent ideas and tricks would never match somebody with better knowledge of available commercial packages on the market. Physics is arguably better suited for his way of thinking, which earned him firstly admission to the special science class in Attached High School of Fudan University in Shanghai, and then School of Physics at Peking university in Beijing. He enjoyed his dorm life immensely in his high school, where he got unprecedented college-like freedom to study and play with a bunch of smart, nerdy and crazy classmates day and night, which even made his later college experience comparatively boring. Nevertheless, he executed his plan for a career in physics and did not look back, tasting research life following his sophomore year and working with Prof. Qi Ouyang

¹He has been calling it a “small town” for 20 years until he came to upstate New York and had a feeling of what a “small town” is by US standard. Ma'anshan has an urban population roughly equal to District of Columbia – capital of the United States.

²Apparently she forgot to mention at that time physics is not any better

on simulation and modeling of non-linear wave propagation and instability. Confirmed that he could survive both lab and snow, he applied to the Ph.D program in physics at Cornell University and flew across the Pacific to the wonderland of Ithaca, New York in the summer of 2006. This adventure turned out a blessing to him where he met the girl of his life one month later. They have happily lived together ever since, married with a daughter.

He had the luck to join Prof. Dan Ralph's nanomagnetics group at Cornell and studied interaction between nanometer-sized magnets and itinerant electron spins. His next stop will be Prof. Schoelkopf's superconducting qubit group at Yale.

To my parents and my wife, for their love and support.

ACKNOWLEDGEMENTS

The researches described in this dissertation would not be possible without the enormous amount of help from many people. I would like to take this opportunity to thank my colleagues, friends and families for making the past six years at Cornell such a special experience.

I'm extremely grateful to have Prof. Dan Ralph as my advisor for my Ph.D. With his knowledge, experience, patience and rigorous attitude on research, Dan is the ideal role-model as a scientist to me. He has built up such a great lab that I can take shelter of, provided so much heritages and resources to make my research life much easier, guided me from project directions to presentation styles, paid me for more than five years of my graduate studies, landed postdoc offers for me with his unreserved support and incredible academic reputation. On top of all these he is an extremely nice person, working so hard and demanding so little from others, almost too nice of a boss and nearly spoiled me.

I would like to thank Prof. Robert Buhrman for his insights and knowledge in physics, material sciences, and scientific career in general. With a busy schedule serving multiple duties, Bob always made himself available for a discussion with me, as if I am a student in his own group. Bob and Dan fostered the close collaborative relationships between the two groups, which is a key factor to the works described in this dissertation. I would like to thank Prof. James Sethna for serving on my special committee, for his generous support on my postdoc search, and for our interesting discussions on folding a piece of paper. I would also like to thank other Cornell professors that have helped me during my early graduate school years, including Erich Mueller, Don Hartill, Julia Thom, Piet Brower, Paul McEuen and Chris Henley. I also thank Greg

Fuchs, for coming back to Cornell as a professor so that I have a second chance to learn from him and get his advices on career directions.

I had the privilege to work with many talented colleagues in Ralph Group. Jack Sankey paved the way leading up to my first research project. Even without much chance to work together, he provided tremendous help throughout my graduate research through his huge package of Labwindows and Python codes for both data acquisition and analysis. Dr. Zhipan Li guided me through my first round of device fabrication in CNF for a good month, and his instructions written down on my notes are essentially my textbook for fabrication. Kiran Thadani was my officemate for more than two years before she graduated, and taught me many little things from fabrication to measurements when I joined the group. It was fun listening to her complaining about life in Ithaca in various ways. Dr. Takahiro Moriyama joined our group as a postdoc and had been my best consultant on magnetic materials during his three years with us. Yongtao Cui and Sufei Shi are one year senior to me, and I'm lucky to have both of them as good friends, mentors, and advanced Google engines¹ on just about everything I encountered inside and outside lab. Yongtao has been my closest co-worker in experiments, and has been instrumental in many of my research projects. I admire his intelligence and extraordinary learning capability. Sufei has been my closest officemate sitting next to my desk for nearly four years, and had numerous discussions between us. His encyclopedic knowledge of research trends, science community and every useful piece of news have benefited me significantly. Thanks to Lin Xue who has been such a diligent worker, directly contributing to many of my spin-transfer publications as well as many of my pictures (as the photography professional). I would like to thank Alex Mellnik and Jennifer Grab for their assistance on bringing the vector magnetic cryostat

¹Nowadays I have to use the ordinary Google more often since they left.

back to life, Colin Heikes for his expertise in complex oxides and cryogenic techniques and Greg Stiehl for his help on fabrication and wiring bonding. Thanks to Joshua Parks, Eugenia Tam and Wan Li for the lasting funs they brought to the group over the many years. Those group lunches with everybody together have been a really good memory. I would also like to thank other previous and current group members: Dr. Saikat Ghosh, Ferdinand Kummeth, Jacob Grose, Ted Gudmundsen, David MacNeill and Colin Jermain.

Many colleagues in Buhrman group have been very helpful to my graduate school career as well. I thank Hsinwei Tseng for his guidance on fabrication of nanopillar MTJ devices. Luqiao Liu and Yun Li are my college alumni in the same class and I feel grateful that we ended up as semi-labmates in this small world. A powerhouse experimentalist covered by extremely humbled personality, Luqiao is one of my best friends and I thank him for all his help and company over the years. I would like to thank Chi-Feng Pai, Vlad Pribiag, Praveen Gowtham, Oakjae Lee, Junbo Park and of course, Luqiao, for keeping the sputtering and ion beam systems in good order. Special thanks to Praveen for bringing such a hilarious and pleasant atmosphere to the lab that is really enjoyable.

I am thankful to Cornell University and its vibrant physical science complex for providing such an abundance of hardware resources, outstanding management and collaborative environment. I thank Eric Smith for his low-temperature expertise, Nathan Ellis for his teaching and hands-on assistance in machine shop, Jonathan Shu and Steve Kriske for their technical support and maintenance of the shared facilities in CCMR (Cornell Center of Material Research). I would like to thank the staff members of CNF (Cornell NanoScale Science and Technology Facility), who run the facility to the best in the country.

Also at Cornell, I would like to thank Ye Zhu, Pinshane Huang and Qingyun Mao in Prof. David Muller's group, who directly contributed to my work with their transmission electron microscopy imaging. I thank Jon Petrie and Huanan Duan in Prof. Bruce Van Dover's group for maintaining the vibration sample magnetometer and making it available. I also thank Carolina Adamo in Prof. Darrell Schlom's group for supplying BiFeO₃ samples.

John Heron and Morgan Trassin in Prof. Ramamoorthy Ramesh's group at UC-Berkeley have been my collaborators for more than two years on the multiferroic project. I thank Morgan for his years of hard work on sample growth and his tolerance on my endless requests for more samples. I thank John for our numerous conversations, answering my questions, organizing data and keeping me updated on new progresses. I thank Prof. Ramesh's encouragement and his invitation for my visit, and thank Dr. Martin Gajek for teaching me about BiFeO₃ and multiferroicity. I have always felt indebted that I could not push our grand mission forward as we had hoped for, and I am grateful to everyone's kindness in this memorable collaboration.

I would like to thank Jordan Katine at HGST of Western Digital Corp., one of the creators of the field of spin transfer, for providing the low-RA MTJ devices to us. Without him, many of my researches would not be possible. I thank Jonathan Sun for the high quality MTJ devices from IBM T. J. Watson research center, and for his valuable insights and helpful discussions. I also thank Mark Stiles at NIST for his support in theories and calculations.

I am grateful to my advisor Prof. Qi Ouyang during my undergraduate studies at Peking University. He took me to the world of scientific research with impressive vision, prepared me for graduate school, and always lent me his strongest support. I thank many of my college friends and high school friends

spreading around US, for our mutual support and exciting visits to each other in this new country to our lives.

Now I would like to take this opportunity to express my deepest gratitude to my family. I would not be where I am and what I am without my parents who raised me with their whole-hearted love and completely selfless support. I would not have the opportunity to pursue an academic career and would not have the luxury to focus on my research without the moral support and direct help from my parents and my parents-in-law. I am extremely lucky and deeply indebted that they have all flown to the US multiple times to help taking care of my little daughter, Ella. I also thank Ella for bringing priceless joys and excitements to my life, and for being reasonably well-behaved in not deleting or editing my thesis at her will. At the end of the day, I cannot be grateful enough to my beloved wife, Jia. She is the beautiful angel coming to my life, filling the years with joys and caring, standing by my side to support my demanding career path with her selfless love, clinching a job in this improbable area with her extraordinary capability, showing our daughter around the beauty of the world, and empowering me through all the difficult times. Thank you and I love you!

TABLE OF CONTENTS

Biographical Sketch	iii
Dedication	v
Acknowledgements	vi
Table of Contents	xi
List of Tables	xiv
List of Figures	xv
1 Introduction	1
1.1 Spin Transport and Magnetism	1
1.1.1 Giant Magnetoresistance	2
1.1.2 Spin Transfer Torque	6
1.1.3 Magnetic Dynamics Induced by Spin Transfer Torque	9
1.2 Magnetic Tunnel Junctions	13
1.2.1 Spin-Polarized Tunneling and Tunneling Magnetoresistance	14
1.2.2 MgO-Based Magnetic Tunnel junctions	18
1.2.3 Spin Transfer Torque in Magnetic Tunnel Junctions	22
1.2.4 Spin Transfer Torque Approaching Single Electron Tunneling Regime	26
1.3 Electrical Manipulation of Magnetism: Other Research Directions	29
1.3.1 Manipulation of Magnetic Moments by Pure Spin Current	30
1.3.2 Manipulation of Magnetic Moments by Electric Field	32
2 DC Mixing Voltage Detection of Spin-Transfer-Driven Ferromagnetic Resonance	35
2.1 Spin-Transfer-Driven Ferromagnetic Resonance (ST-FMR)	36
2.1.1 DC Detection of Spin-Transfer-Driven Ferromagnetic Resonance	37
2.1.2 Early Measurements of Spin Transfer Torque by ST-FMR and Discrepancies	38
2.2 Device Structures and Measurement Procedures	43
2.2.1 Device Structures	43
2.2.2 Measurement Circuit and Methods	45
2.2.3 ST-FMR Spectra and Uncorrected Spin Transfer Torkance	50
2.3 Quantitative Modeling of DC-detected ST-FMR within the Macrospin Approximation	57
2.4 Bias and Angular Dependence of the Spin Transfer Torque	63
2.4.1 Discussion of the Artifact Terms	63
2.4.2 Corrected Spin Transfer Torkance	65
2.4.3 Discussions and Comparisons to Theories and Other Experiments	68
2.4.4 Bias Dependence of Effective Damping and Frequency	73
2.5 Summary	78

3 Time-Resolved Detection of Spin-Transfer-Driven Ferromagnetic Resonance	79
3.1 Measurement Scheme and Data Processing for Time Domain ST-FMR	80
3.1.1 Measurement Circuit Details	81
3.1.2 Device Structures	85
3.1.3 Data Acquisition and Background Subtraction Procedure	87
3.1.4 Fitting to a Damped Driven Harmonic Oscillator	90
3.2 Quantitative Modeling of Time Domain Detection of ST-FMR	93
3.3 Calibration Procedures	100
3.3.1 Calibrations of Device Resistance and Actual Voltage at High Bias	100
3.3.2 Estimate of the Effect of Device Capacitance	104
3.4 Full-Range Bias Dependence of the Spin Transfer Torque	108
3.4.1 Combination of DC Detected and Time-Domain Detected ST-FMR	109
3.4.2 Bias Dependence of Effective Damping	112
3.4.3 Comparison with Other Methods of Spin Torque Measurements – Role of Heating and Spatial Non-Uniformity	115
3.4.4 Discussions and Implications	118
3.5 Applicability on other MTJ devices and Potential Improvements	120
3.6 Other Studies Enabled by Time-domain ST-FMR	126
3.6.1 Selective Excitation of Different Magnetic Normal Modes	127
3.6.2 Fine Dependence of the Precession Mode and Effective Damping on Excitation Frequency	132
3.7 Appendices	134
3.7.1 Effect of Parasitic Capacitance	134
3.7.2 Effect of Finite Fall Time of the RF pulse	138
4 Potential Applications of Spin-Transfer-Driven Ferromagnetic Resonance	143
4.1 Microwave Detector	144
4.1.1 Analytical Prediction for the Sensitivity of Spin-Torque Diodes for Microwave Detection	145
4.1.2 Experimental Testing of the Sensitivity of Spin-Torque Diodes	148
4.1.3 Strategies for Optimization	154
4.1.4 Summary	157
4.2 Microwave Amplifier	157
4.2.1 Conditions of Microwave Amplification by ST-FMR	158
4.2.2 Mathematical Analysis of Amplification and the Feedback Effect	161
4.2.3 Summary	166

5 Spin Dependent Tunneling and Spin Transfer Torque in Ferromagnetic Nanoparticles	167
5.1 Device Fabrication	168
5.2 Device and Film Characterization for CoFeB nanoparticles	174
5.2.1 Magnetometry Characterization of CoFeB Nanoparticle Assembles	174
5.2.2 STEM images of the Embedded Nanoparticles	179
5.2.3 Full Wafer Electrical Characterization	181
5.3 Measurement Apparatus–PPMS and Vector Magnet Cryostat	184
5.4 Electrical Measurements on CoFeB/ MgO/ CoFeB (Nanoparticles)/ MgO/ Ru Devices	188
5.4.1 Temperature Dependence of the Tunneling Magnetoresistance	189
5.4.2 Pulsed Switching Measurements	198
5.4.3 Spin-Transfer-Driven Ferromagnetic Resonance	209
5.5 Summary and Outlook	215
5.6 Appendices	219
5.6.1 Electrical Measurements on CoFeB/ MgO/ CoFeB (Nanoparticles)/ MgO/ CoFeB Devices	219
5.6.2 CoFeB/ MgO/ Co (Nanoparticles)/ MgO/ Ru Devices	222
5.6.3 Effects of Annealing on Nanoparticle MTJ devices	227
6 Making Spin Valve Devices with Multiferroic Heterostructures	229
6.1 Introduction to BiFeO ₃	230
6.1.1 Multiferroicity and Magnetoelectric Coupling in BiFeO ₃ .	230
6.1.2 Early Experiments on Exchange Bias at the BiFeO ₃ /Ferromagnet Interface	233
6.2 Statistical Study of Exchange Bias at the BiFeO ₃ /Permalloy Interface	237
6.3 Spin Valve Devices Exchange-Biased by BiFeO ₃	244
6.3.1 Device Structure and Fabrication	244
6.3.2 Electrical Measurements of GMR and Exchange Bias	248
6.3.3 Effect of Electric Field Pulses on Exchange bias	250
6.4 Study of Nanoscale Variations of Exchange Bias at the BiFeO ₃ /Permalloy Interface	255
6.4.1 Fabrication	257
6.4.2 Nanoscale Variations of Exchange Bias Illustrated by GMR Measurements	261
6.4.3 Piezoresponse Force Microscopy Imaging and Correlation with Exchange bias	267
6.5 Summary	270

LIST OF TABLES

4.1	Sample parameters for microwave detector characterization . . .	150
4.2	Results of the detector diode sensitivity measurements, with a comparison to the sensitivity predicted by Eq. (4.7), calculated using the measured values of σ , R , R_P , and R_{AP}	153
5.1	Layer structures and growth parameters for magnetic nanoparticle tunnel junctions	170
5.2	The resistances (in $k\Omega$) of $500 \text{ nm} \times 500 \text{ nm}$ magnetic nanoparticles tunnel junction devices across 13×13 dies at different locations of a 4-inch wafer	182
5.3	The resistances (in $k\Omega$) of $500 \text{ nm} \times 500 \text{ nm}$ magnetic nanoparticles tunnel junction devices across 13×13 dies on a 4-inch wafer after annealing at 350°C	227

LIST OF FIGURES

1.1	Band structure of cobalt	3
1.2	Schematic of the giant magnetoresistance (GMR) effect.	4
1.3	A simplified illustration of spin transfer torque.	7
1.4	Schematic structure of a nanopillar device for spin torque studies	10
1.5	Magnetization dynamics in the presence of spin transfer torque.	12
1.6	Spin-polarized tunneling	15
1.7	Jullière's model of tunneling magnetoresistance	17
1.8	Calculated distribution of tunneling density of states for a Fe/MgO/Fe MTJ by atomic layers	20
1.9	Schematic of the in-plane torque and the perpendicular torque in a magnetic tunnel junction	23
1.10	Schematics of three-terminal devices that utilize spin transfer torque generated by pure spin current	31
2.1	Illustration of spin-transfer-driven ferromagnetic resonance . . .	37
2.2	Illustration of the relation between the ST-FMR line-shape and the direction of spin transfer torque	40
2.3	A comparison of the spin transfer torkance $d\vec{\tau}/dV$ as a function of bias voltage V in MgO-based MTJs measured in two initial ST-FMR experiments.	42
2.4	Schematics of MTJ devices used for ST-FMR measurements and definition of coordinate system	44
2.5	Schematic circuit for DC-detected ST-FMR measurements.	45
2.6	Adjustment factors for mixing voltage measurement	49
2.7	Measured ST-FMR spectra from MgO-based MTJ devices	52
2.8	Bias dependence of the uncorrected in-plane and out-of-plane torkances	55
2.9	Illustration of the origin and magnitude of the artifact terms in ST-FMR signal	64
2.10	Bias dependence of the corrected in-plane and out-of-plane torkances	66
2.11	The in-plane and perpendicular torkances for an $RA \approx 14.5 \Omega\mu\text{m}^2$ Fe/MgO/Fe tunnel junction by ab initio calculation	70
2.12	Bias dependence of (a) the effective damping and (b) the resonance frequency in ST-FMR measurements for a $RA = 12 \Omega\mu\text{m}^2$ MTJ sample at various initial offset angles	75
2.13	Bias dependence of (a) the effective damping and (b) the resonance frequency in ST-FMR measurements for a $RA = 1.5 \Omega\mu\text{m}^2$ MTJ sample at various initial offset angles	77
3.1	Schematic of the measurement circuit for time domain ST-FMR .	82
3.2	Schematic geometry and resistance characterization of the MTJ device	86

3.3	Illustration of the background subtraction and resulting signal of magnetic precession in ST-FMR	89
3.4	Dynamic response of the magnetization to oscillating spin transfer torque as a function of driving frequency	91
3.5	Calibration of the resistance of MTJ from the amplitude of the reflected RF pulse	102
3.6	Illustration of the various origins of capacitance for a MTJ device	106
3.7	Measured bias dependence of the spin-transfer torque vector	111
3.8	Bias dependence of the effective damping α_{eff} determined from a combination of the DC and time-domain detected ST-FMR	113
3.9	Bias dependence of the spin-transfer torque vector measured by time-domain ST-FMR for a $RA = 1 \Omega\mu\text{m}^2$ MTJ device	121
3.10	Schematic of an alternative measurement circuit for time domain ST-FMR experiment	123
3.11	An unresolved puzzle for microwave reflection off a MTJ device in the presence of an additional transmission line	125
3.12	Time-domain ST-FMR measurement of two different precession modes.	130
3.13	The fine dependence of precession mode and effective damping on RF driving frequency	133
4.1	Bias dependence of the diode-detector sensitivity	146
4.2	Selected ST-FMR resonance spectra measured at different initial offset angles	151
4.3	Measured gain factor for microwave reflection from a MTJ device	160
4.4	Calculated microwave gain factor of a MTJ device in the phase space of offset angle and bias current	161
4.5	Schematic illustration of microwave amplification with (a) a conventional 2-terminal MTJ and (b) a proposed 3-terminal MTJ device.	166
5.1	Schematic geometry of a nanopillar MTJ device with embedded magnetic nanoparticles.	168
5.2	SQUID magnetometry of CoFeB nanoparticles	176
5.3	STEM images of a MgO-based ferromagnetic nanoparticle tunnel junction	180
5.4	Bias and temperature dependence of the resistance of magnetic nanoparticle tunnel junction devices	183
5.5	Magnetoresistance measurement of CoFeB nanoparticle MTJs	190
5.6	Tunneling magnetoresistance of CoFeB nanoparticle MTJs at various temperatures and bias voltages	194
5.7	Hysteretic magnetoresistance of a single nanoparticle	199
5.8	Temperature dependence of the nanoparticle hysteresis	201
5.9	Switching phase diagram (H vs. V) of a CoFeB nanoparticle	204

5.10	ST-FMR spectra associated with CoFeB ferromagnetic nanoparticles	211
5.11	ST-FMR spectra associated with CoFeB ferromagnetic nanoparticles and its dependence on history	213
5.12	A naive picture of a ferromagnetic quantum dot for considering spin transfer torque in the single-electron tunneling regime.	218
5.13	Magnetoresistance measurement of magnetic nanoparticle tunneling devices with double magnetic electrodes	221
5.14	Electrical measurements on Co nanoparticle MTJ devices	225
6.1	Schematic diagram of the (001)-oriented BiFeO ₃ crystal structure and the ferroelectric polarization and antiferromagnetic plane	231
6.2	Schematic of an approach for electrical control of ferromagnetism based on exchange bias	234
6.3	The exchange bias between CoFe and BiFeO ₃ of mosaic or striped domain patterns	235
6.4	Magnetometry measurements of BiFeO ₃ /Py samples for characterization of exchange bias	239
6.5	Brief statistics of the exchange bias observed for various BFO samples with Py	241
6.6	STEM images of the BFO/Py interfaces for two samples with and without exchange bias respectively.	243
6.7	EELS spectra of different atomic layers in a BFO/Py/Cu/Py spin valve film stack.	243
6.8	Magnetometry measurement (M-H) for a spin valve layer stack of BFO/Py/Cu/Py/Pt.	245
6.9	Schematic of our GMR device based on BFO and Py.	247
6.10	Giant magnetoresistance of a Py/Cu/Py spin valve device pinned by BiFeO ₃	249
6.11	Images of spin valve devices under electric-field induced ferroelectric switching	252
6.12	Electric-field induced changes (or no changes) to the exchange bias of BFO/Py in spin valve devices	253
6.13	PFM image of nano-wire spin valve devices for study of local exchange bias at the BFO/Py interface	259
6.14	Large variations of exchange bias for nano-wire devices patterned parallel to the domain stripes of BFO	262
6.15	Relatively small variations of exchange bias for nano-wire devices patterned orthogonal to the domain stripes of BFO	264
6.16	Nanoscale variations and enhancements of exchange bias for a BFO sample with back-sputtering treatment	266
6.17	Correlation of exchange bias with location of nano-wire spin valve devices	268

CHAPTER 1

INTRODUCTION

1.1 Spin Transport and Magnetism

For thousands of years people have known ferromagnetism as an attractive or repulsive property related to certain materials, but only after the discovery of electron spins in the 1920's did the microscopic origin of ferromagnetism start to unravel. It is a striking fact that electrons that are widely recognized and used as electric charge carrier happen to be little magnets by themselves at the same time. Now as we know, each electron not only carries an elementary unit of charge $-e$, but also carries an elementary unit of angular momentum, or spin, $\frac{\hbar}{2}$, which is directly related to a somewhat elementary magnetic moment approximately one μ_B . Whenever we produce an electrical current by inducing motions of electrons, it could indeed be viewed as a collection of little magnets that are moving around. In other words, any electron charge transport is simultaneously accompanied by a transport of spin, or magnetic moment carried by these electrons.

Utilization of electron flow is arguably the most important corner stone of our modern technology. However, the spin transport associated with electron flows went essentially unnoticed until the recent decades. This happened for a number of reasons. Firstly most materials in the world, especially those found their way into electronic applications have randomly oriented or alternating spins so that the total spin or magnetic moment of the electron ensemble is close to zero. Secondly spin flow is not constrained by continuity requirement because electron spins can easily flip directions during the transport typically

on the length scale of nanometers, so one cannot source spin flow over long distance for detection or application. Thirdly it was difficult to detect flow or accumulation of either angular momentum or magnetic moment in small magnitude.

With the recent development of nanotechnology, people eventually are able to access the length scale shorter than the spins can flip, and the discovery of giant-magnetoresistance (GMR) by Fert *et al.* and Grünberg *et al.* in 1988 [1, 2] became the monumental moment that spin transport came into mainstream focus in researches and received the 2007 Nobel Prize in physics. The wide-reaching prospects of using the electrons' spin degree of freedom in modern electronics have lead to the vibrant field dubbed "spintronics".

1.1.1 Giant Magnetoresistance

In studying and utilizing spin transport, ferromagnetic materials such as some 3d transition metals (Fe, Co, Ni) naturally play a significant role. These materials have an intrinsic property that some of the electrons tend to align their spins with each other. If we choose this collectively preferable direction of spins S as the quantization axis \hat{z} in a quantum mechanical representation, the electrons with $S_z = \frac{1}{2}$ ("spin-up") have a larger population than the electrons with $S_z = -\frac{1}{2}$ ("spin-down"). This not only explains the macroscopic intrinsic magnetic moment for the ferromagnet, but also leads to a highly intuitive picture that electron flows in ferromagnetic metals should carry a non-zero flow of spin due to the lack of spin symmetry. In other words, the electric current in ferromagnetic materials is intrinsically "spin-polarized". This was

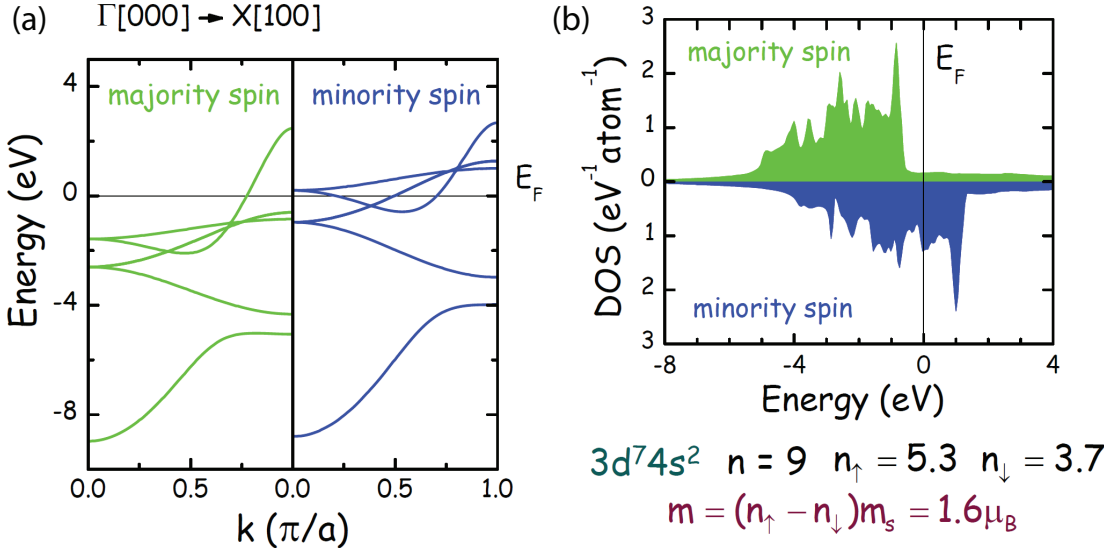


Figure 1.1: (a) Band structure of cobalt along one high symmetry axis. (b) Density of states of cobalt. Adapted from ref. [7].

first discussed by Mott [3] in 1936 in explaining some features of the resistivity of ferromagnetic metals at the Curie temperature, but had to wait till the early 1970's to find experimental evidences [4–6].

In a slightly more rigorous picture, the conductance of a metal is controlled by the property of the electronic states close to the Fermi surface. For non-magnetic metals (if we ignore spin-orbit coupling), all the electronic states are spin degenerate, so the scattering probability for a particular electronic state should not depend on its spin state. In ferromagnetic metals, there is an energy difference, ϵ (called exchange splitting), between the spin-up state and spin-down state for the same electronic wavefunction, which leads to a relative shift between the spin-up band and the spin-down band [Fig.1.1(a)]. In this case spin-up states around the Fermi energy are very different from spin-down states not only in the total number of states [density of the states, as shown in Fig.1.1(b)] but also in their detailed wavefunction structures. Therefore electrons at different spin states should experience a different scattering environment in

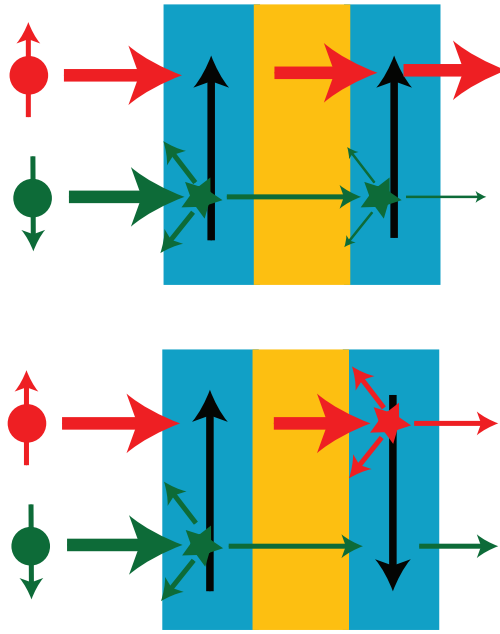


Figure 1.2: Schematic of the giant magnetoresistance effect (GMR) effect. Parallel alignment corresponds to low resistance (top panel) and anti-parallel alignment corresponds to high resistance (bottom panel).

transport, and a ferromagnetic metal would appear to be more resistive to one type of spin state and more conductive to the other.

A more interesting effect arises when one considers electrons flowing out of a ferromagnetic metal into a non-magnetic material. The electron flow can maintain its spin imbalance for a characteristic time (spin relaxation time), or diffuse by a characteristic length (spin diffusion length) into the non-magnetic material to induce a local spin accumulation. This explicit use of a ferromagnetic metal as a “spin filter” was first reported by Johnson and Silsbee [8] in 1985, and the accumulated spin was electrically detected a few microns away by a second ferromagnetic electrode.

Giant magnetoresistance, discovered in 1988 [1, 2], describes the total resistance of a FM/NM/FM multi-layer thin film structure (where FM stands

for ferromagnet and NM stands for non-magnetic “normal” metal). When electrons flow sequentially through two ferromagnetic layers, both layers act as spin filters. A simplified model of the total resistance can be illustrated by Fig.1.2, which separates the total conduction of the multilayer into a spin-up channel and a spin-down channel in parallel. When the magnetizations of the two layers are anti-parallel to each other, both spin-up and spin-down electrons are blocked by one of the ferromagnets, resulting in high total resistance. On the other hand when the magnetizations are parallel to each other, electrons with one of the spin states can pass through both layers smoothly, resulting in low total resistance. When the magnetizations are not collinear with each other, *i.e.* at an intermediate relative angle θ between 0 and 180 degree, the total resistance roughly follows the form of $\cos \theta$:

$$R = \frac{R_{AP} + R_P}{2} - \frac{R_{AP} - R_P}{2} \cos \theta \quad (1.1)$$

The magnitude of GMR, or how much the relative magnetization orientation changes the resistance, is generally characterized by the GMR ratio defined as $(R_{AP} - R_P)/R_P$. The GMR ratio can be as large as several tens of percent (85% in the initial report by Baibich *et al.* [1]), much larger than any other magnetoresistance reported before, which earned its name “giant” magnetoresistance.

The spin dependent scattering inside a ferromagnet is actually only part of the origin of GMR. Arguably of more importance is the scattering process at the FM/NM interface due to the band structure mismatch between the two materials. Since the ferromagnet has different spin-up and spin-down bands, this interface scattering is also spin-dependent and generally add to the magnitude of the GMR effect. A more rigorous analysis should also take account of spin mixing, which describes the cross talk between two spin channels due to spin-flip scattering processes inside a ferromagnet.

In early experiments of GMR, the antiparallel configuration between the two magnetizations was realized at small magnetic field, taking advantage of the inter-layer coupling including both the exchange interaction and the dipole interaction. The parallel configuration was realized by applying high magnetic field. Later on a type of structure called “spin valve” has become the standard architecture to study and utilize the GMR. In a spin valve one ferromagnetic layer acquires a unidirectional anisotropy through an exchange bias interaction with an adjacent antiferromagnetic layer, which essentially pins the ferromagnetic layer into a predefined direction as long as the external field does not exceed the pinning strength, and this ferromagnet is called a “fixed layer”. The other ferromagnetic layer is composed of a soft magnetic material and can sensitively respond to an external magnetic field, which is called a “free layer”. [See Fig.1.3(b) for a simple schematic picture.] By measuring the total resistance of the spin valve for perpendicular current flow, the spin valve can be used as a sensitive nanoscale magnetic field sensor. This type of GMR field sensor has been integrated into the read-head of magnetic hard disk drives since 1997, and revolutionized the data storage industry by helping to increase the storage density by nearly three orders of magnitude over a decade.

1.1.2 Spin Transfer Torque

In the spin valve structure, when the two ferromagnetic layers are not collinear, electrons moving from left to right are spin-polarized sequentially along two different axes and therefore lose a transverse angular momentum to the right-hand ferromagnet [Fig.1.3(a)]. From conservation of angular momentum, the right-hand magnet absorbs this transverse angular momentum and therefore

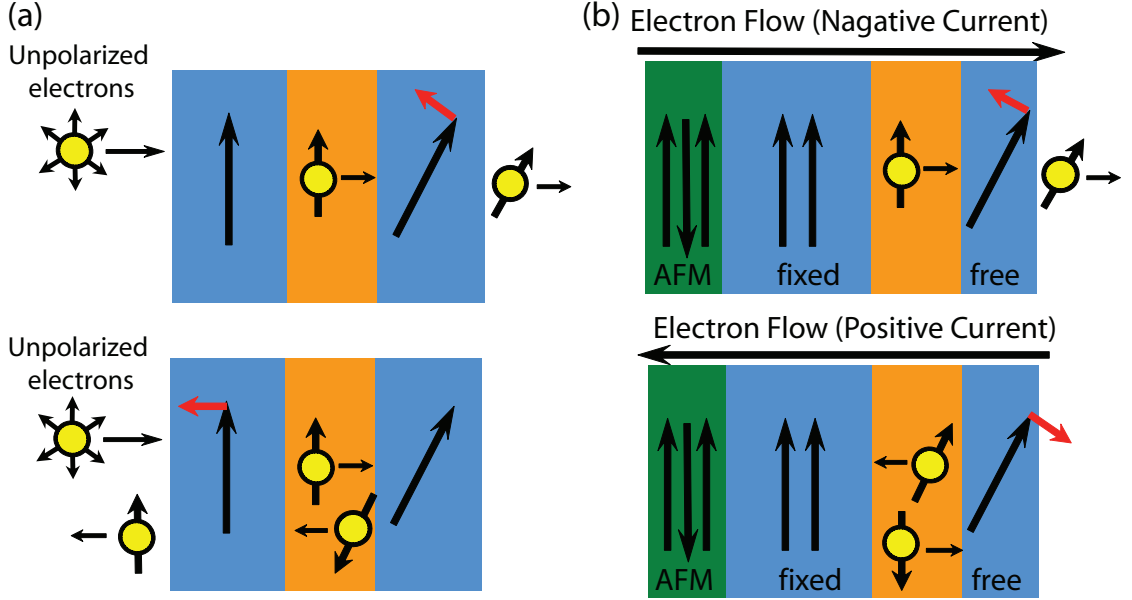


Figure 1.3: A simplified illustration of spin transfer torque. (a) Origin of spin torque experienced by both magnetic layers. (b) The direction of the spin torque for both current polarities for a typical metallic spin valve structure.

receives a torque. At the same time, the electrons reflected from the right-hand magnet are spin-polarized again by the left-hand magnet, which also receives a torque. Note that the magnetic moment \vec{M} and angular momentum \vec{L} are intrinsically coupled to each other via the electron g factor ($g \approx 2$) for both the itinerant electrons and the local magnet, we often equivalently view the local magnet moment \vec{M} as receiving a transverse "kick" in the form of $d\vec{M}/dt$ from the itinerant electrons, which we call spin transfer torque. This effect was proposed by Slonczewski [9] in 1996 and also appeared in a paper from Berger [10]. It was subsequently first observed in metallic point-contact devices at around 1999 [11, 12], and then reported in the more prototypical spin valve structure etched into 100 nm-sized pillars [13] (Fig. 1.4). (For an overview of spin transfer torque from both theoretical and experimental perspective, see ref. [14] and references therein.)

The discovery of spin transfer torque has drawn tremendous interest from both academia and industry because it presents a very promising way to electrically and locally manipulate a nanoscale magnet. For a typical spin valve with one layer pinned by exchange bias, we can focus on the spin transfer torque experienced by the free layer [Fig.1.3(b)]. The direction of the spin transfer torque depends on the polarity of the current flow. Positive current (electrons flowing from free layer to fixed layer) promotes anti-parallel alignment between the two ferromagnetic layers, while negative current (electrons flowing from fixed layer to free layer) promotes parallel alignment.

Since each electron carries angular momentum of $\hbar/2$, the transverse angular momentum that can be absorbed by a ferromagnetic layer is $\hbar \sin \theta/2$, where θ is the relative angle between the magnetization of the two ferromagnetic layers. The spin transfer effect on the local magnetic moment should be $\mu_B \sin \theta$ per spin-polarized electron. If we use a spin polarization factor P to roughly describe the efficiency of the first ferromagnetic layer to spin-polarize the conduction electrons coming to the second magnet (which is typically tens of percent for 3d transition metal ferromagnets), the simplest prediction of the magnitude of spin transfer torque therefore reads:

$$\frac{d\hat{\mathbf{M}}}{dt} = P \frac{I \mu_B}{e M_s V_{free}} \hat{\mathbf{M}} \times (\hat{\mathbf{M}} \times \hat{\mathbf{M}}_{fix}) \quad (1.2)$$

where $\hat{\mathbf{M}}$ and $\hat{\mathbf{M}}_{fix}$ are unit vectors for the magnetization of the two ferromagnetic layers, μ_B is the Bohr magneton, I is the current, e is the electron charge, M_s is the saturation magnetization of the free layer, V_{free} is the volume of the free layer. This simplified expression includes two approximations. Firstly, it assumes the transverse angular momentum of incoming electrons is completely absorbed by a ferromagnet, which is approximately correct for metallic transport in spin valves. Secondly it parametrizes the asymmetric

spin population in transport into a material parameter P of the ferromagnetic polarizer. This is hardly justified since the real spin distribution comes from a dynamic balance of transmission and reflection at both FM/NM interfaces and depends on all three materials. One should also take into account the interface electronic structure as well as both ballistic and diffusive transport contributions. Moreover, the spin polarization P for a given ferromagnetic material is by itself a relative concept because different electronic states have to be weighted differently in transport since they have different mobility, which in turn depends on the full layer structure. (This becomes strikingly evident in spin dependent tunneling studies as we will discuss in Section 1.2.) A more general form of spin transfer torque can be written by replacing the spin polarization factor P by $g(\theta)$, which is the dimensionless spin transfer efficiency and has the form [15]:

$$g(\theta) = \frac{A}{1 + B \cos(\theta)} \quad (1.3)$$

in FM/NM/FM spin valves. A and B depend on details of the layer structure.

1.1.3 Magnetic Dynamics Induced by Spin Transfer Torque

Most of the spin transfer torque studies have been carried out on the spin valve or magnetic tunnel junction (see Section 1.2) structures patterned into nanopillars (Fig.1.4), where the magnetic free layer is a circular or elliptical disc with thickness of 2-5 nm and lateral dimensions of 50-300 nm. The simplest way to describe the magnetic dynamics of the free layer is to treat it as a spatially uniform magnet with a fixed total magnetic moment $M_s V_{free}$, where M_s is the saturation magnetization of the material, and V_{free} is the volume of the free layer. This so-called “macrospin approximation” allows one to use just one

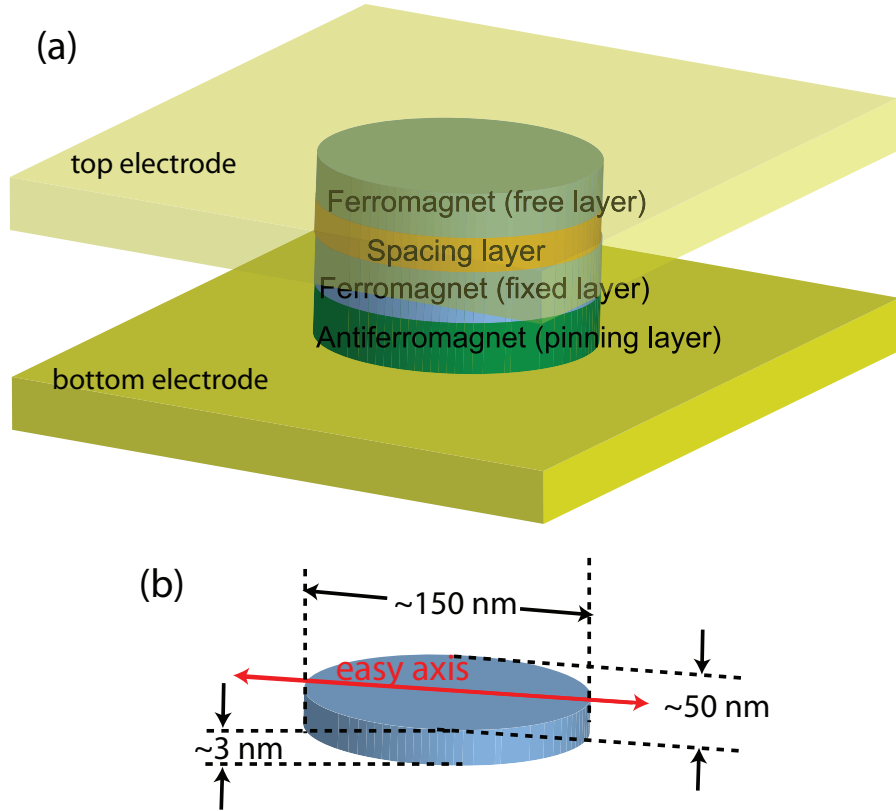


Figure 1.4: (a) Schematic layer structure of a nanopillar device for spin torque studies. (b) Typical dimension of the free layer ferromagnet.

unit vector $\hat{\mathbf{m}}$ to represent the magnetic state of the free layer. Macrospin turns out to be a pretty useful approximation in many experiments especially with smaller nanopillars (≤ 100 nm in lateral size). This is justifiable since the size of nanopillars are comparable or smaller than the scale of magnetic domains for typical ferromagnetic metals (such as alloys of Ni/Fe or Co/Fe) determined by the competition between the exchange interaction and dipole interaction.

The dynamics of the free layer magnetization (unit vector $\hat{\mathbf{m}}$) in the presence of spin transfer can be described by the classical Landau-Lifshitz-Gilbert (LLG) equation including an additional “Slonczewski” term for the spin torque:

$$\frac{d\hat{\mathbf{m}}}{dt} = -\gamma \hat{\mathbf{m}} \times \vec{H}_{eff} + \alpha \hat{\mathbf{m}} \times (\hat{\mathbf{m}} \times \vec{H}_{eff}) + g(\theta) \frac{\mu_B I}{e M_s V_{free}} \hat{\mathbf{m}} \times (\hat{\mathbf{m}} \times \hat{\mathbf{M}}) \quad (1.4)$$

where \vec{H}_{eff} is the total effective field including the applied field \vec{H}_{app} and any anisotropy field \vec{H}_{anis} arising from shape, surface and crystalline effect, and α is the Gilbert damping constant. In the absence of the spin torque, the stationary solution of the equation requires $\hat{\mathbf{m}} \times \vec{H}_{eff} = 0$, or that the magnetization rest along the direction of the total effective field, which is typically close to the external field direction under high field or close to the in-plane easy axis of the elliptical disc under zero field. When the magnetization experience a small perturbation away from equilibrium, the first term provides a field torque (τ_H) which makes the magnetization precess around the effective field direction, as illustrated in Fig. 1.5(a). The second term is the damping torque ($\tau_{damping}$) that accounts for energy dissipation and gradually relaxes the magnetization towards equilibrium. The third term describes the effect of the spin transfer torque (τ_{ST}). For simplicity we consider a case where the effective field is collinear with the fixed layer magnetic moment. (See Section 2.3 for a more general treatment.) The spin transfer torque described by $\hat{\mathbf{m}} \times (\hat{\mathbf{m}} \times \hat{\mathbf{M}})$ is collinear with the damping torque, and therefore either enhances or reduces the damping depending on the sign of the electric current I . It should be noted that, in general, the relative strength and even relative sign between the damping torque and the spin transfer torque also depend on the instantaneous state of the free layer magnetization (due to the dependence of \vec{H}_{eff} and $g(\theta)$ on $\hat{\mathbf{m}}$). However, if we are limited to a stability analysis of a stationary state, the spin torque effect can be further simplified to a modification to the Gilbert damping constant α . For the configuration shown in Fig. 1.5(a), negative current effectively increases α while positive current effectively reduces α .

Most interesting effects happen when the spin torque is large enough so that the effective damping constant becomes negative, which means that the

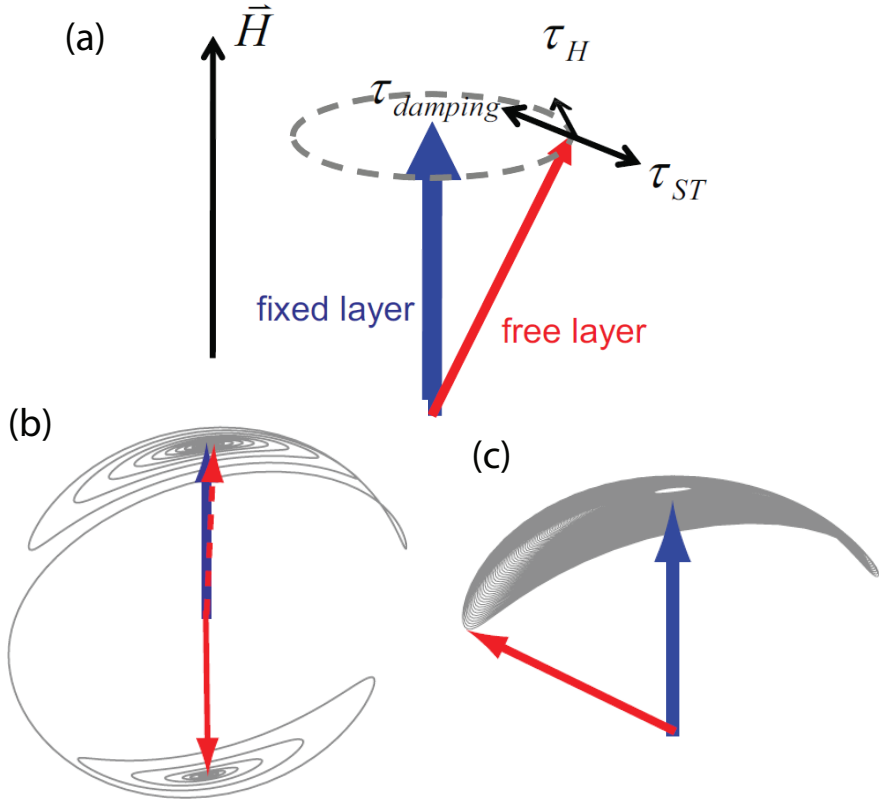


Figure 1.5: Magnetization dynamics in the presence of spin transfer torque. (a) Directions of the field torque τ_H , the damping torque $\tau_{damping}$, and the spin transfer torque τ_{ST} . (b) Simulated magnetization trajectory of the spin-transfer-driven magnetic switching process. (c) Simulated magnetization trajectory of persistent precession driven by spin transfer torque. Adapted from ref. [16].

stationary state becomes unstable. When such an instability occurs, as a nonlinear dynamic system, there are typically two different scenarios. The free layer magnetization either eventually finds another stationary state that is stable (with a positive effective damping) or finds a limit cycle. The first scenario usually occurs for a nanomagnet with uniaxial anisotropy (*i.e.* from elliptical shape) higher than external magnetic field, where spin transfer torque makes one magnetic easy direction unstable so that its magnetization flips (or “switches”) to the opposite easy direction [12, 13]. Figure 1.5(b) illustrates a simulated magnetization trajectory during such a magnetic switching process under spin

transfer torque. This type of spin-torque-driven switching presents a very promising writing mechanism for magnetic random access memory (MRAM) applications, and many research efforts are focused on realizing such a switching process with higher speed, lower energy consumption and more robustness. The second scenario usually occurs under relatively high external magnetic field so that there is no second magnetic energy minimum. Figure 1.5(c) illustrates a simulated magnetization trajectory in this case. The magnetization undergoes persistent precession, resulting in a gigahertz oscillation of the resistance of the device that can be detected from both microwave power emission spectrum and from time domain measurements [17, 18]. This persistent precession provides a mechanism that can convert energy from external DC current into GHz microwave emission, and leads to potential application of spin valves (or magnetic tunnel junctions) as nanoscale microwave-frequency oscillators. A slightly more detailed overview of magnetization dynamics driven by spin transfer torque can be found in the introductory chapter of Y.-T. Cui's thesis [16] and references therein.

1.2 Magnetic Tunnel Junctions

Giant magnetoresistance describes metallic transport in a FM/NM/FM tri-layer structure (where FM stands for ferromagnet and NM stands for normal metal), and originates from the spin dependent scattering processes inside a ferromagnet and at the FM/NM interface. In this section we describe a very similar but yet physically different phenomenon: tunneling magnetoresistance. If the normal metal spacing layer in a standard spin valve structure is replaced by a thin insulator, the resulting FM/I/FM structure (where I stands for

insulator) is a magnetic tunnel junction. Electrons can quantum mechanically tunnel through the insulating barrier from one ferromagnetic electrode to the other, and the tunneling probability (or tunneling conductance) depends on the relative orientation of the two ferromagnets. The evolution of the field of spin dependent tunneling has historically followed its own route separated from the studies of spin dependent metallic transport. However, after the inspiration of GMR applications, the two fields are increasingly merging together, with the parallel advancement of spin transfer torque study in both systems as a prime example.

1.2.1 Spin-Polarized Tunneling and Tunneling Magnetoresistance

Electron tunneling experiments date back to 1960 when Giaever [19] published his classic measurements of the tunneling current between a superconductor and a normal metal through a thin oxide barrier (Fig. 1.6(a)). His demonstration of measuring differential conductance and observation of the superconducting gap paved the way for the Nobel prize discovery of Josephson effect and the development of electron tunneling spectroscopy, and more relevantly to the topic of this dissertation, inspired the first demonstration of spin-polarized tunneling by Tedrow and Meservey in 1971 [20]. In this spin-polarized tunneling experiment, the non-magnetic normal metal electrode in the SC/I/NM tunnel junction of Ref. [19] is replaced by a ferromagnetic electrode to form a SC/I/FM tunnel junction [Fig. 1.6(a)]. The tunneling conductance is dominated by the electron density of states (DOS) at the two electrodes. In particular, the

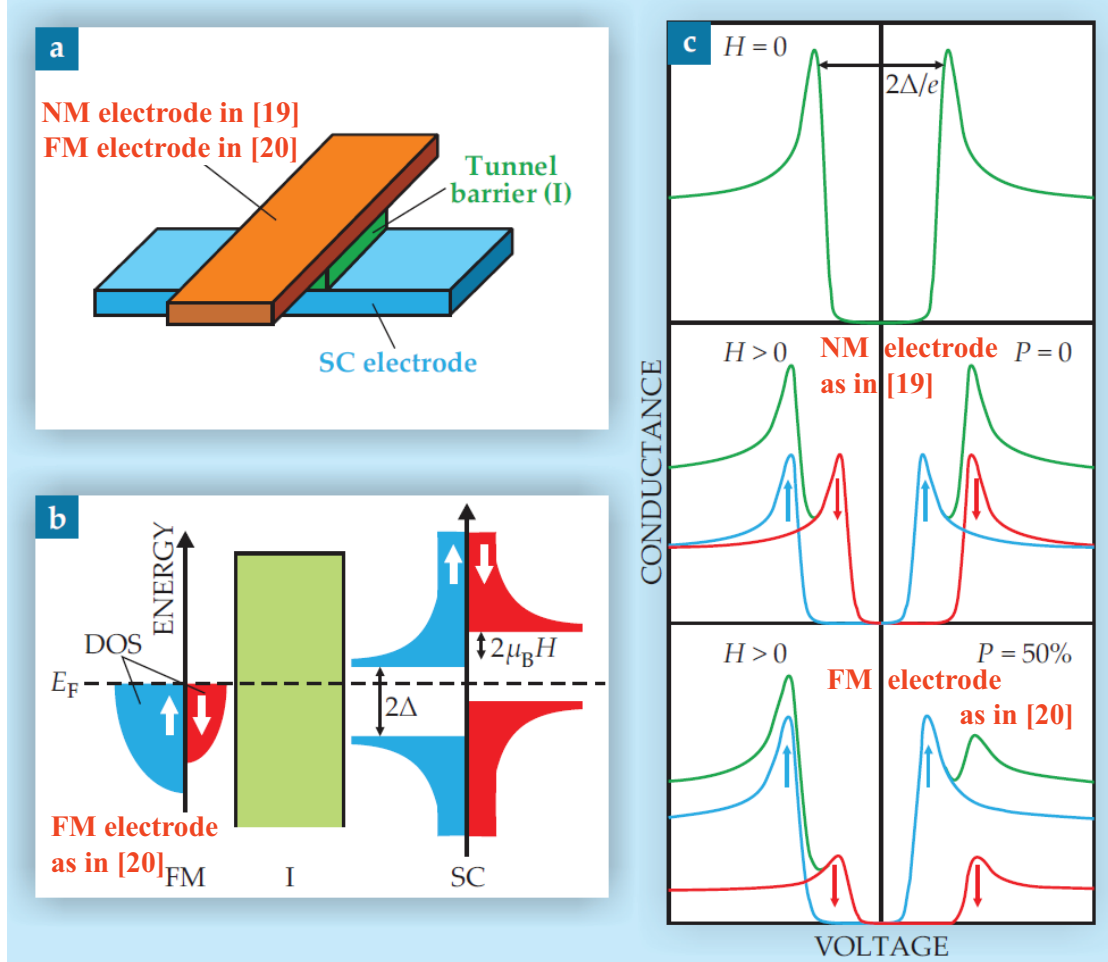


Figure 1.6: Spin-polarized tunneling. (a) A tunnel junction with one superconducting electrode and one normal metal or ferromagnetic electrode (b) An energy diagram illustrating the density of state profile of a ferromagnet and a superconductor (c) Typical tunneling conductance as a function of bias voltage without magnetic field (top panel), for a SC/I/NM junction as in Ref. [19] with magnetic field (middle panel) and for a SC/I/FM junction as in Ref. [20] with magnetic field (bottom panel). Adapted from ref. [21].

DOS of the superconductor is very sensitive to energy close to Fermi level, showing a strong peak at a few millivolts and dropping to zero inside the superconducting gap [Fig. 1.6(b)]. On the other hand, the DOS of a ferromagnet or non-magnetic normal metal is only weakly dependent on energy at the scale of a few millivolts. When a potential difference across the tunnel barrier (which we will call bias voltage) is applied in the absence of external magnetic field, the differential conductance dV/dI illustrates such a DOS profile for the superconductor in both Ref. [19] and Ref. [20] [top panel of Fig. 1.6(c)]. When an external magnetic field H is applied, the DOS profile for the superconductor shows a Zeeman splitting of $2\mu_B H$. In the case of a NM electrode [19], tunneling electrons have equal spin populations and the two Zeeman branches have equal contribution to the tunneling conductance [middle panel of Fig. 1.6(c)], but in the case of a FM electrode [20], tunneling electrons are spin polarized and the two Zeeman branches contribute unequally and make the tunneling conductance asymmetric [bottom panel of Fig. 1.6(c)].

The pioneering work on spin-polarized tunneling provided the first hint that electrons maintain their spin during the tunneling process, and that the tunneling current is, in general, proportional to the interfacial density of states of the two electrodes. These two properties of electron tunneling, coupled with the unequal density of states for majority and minority spins in ferromagnets, led to the hypothesis that the tunneling conductance between two ferromagnetic electrodes should depend on their relative orientation of magnetizations, which is known today as the Jullière's model of tunneling magnetoresistance: [22]

$$G_P \propto \rho_{L\uparrow}\rho_{R\uparrow} + \rho_{L\downarrow}\rho_{R\downarrow} \quad (1.5)$$

$$G_{AP} \propto \rho_{L\uparrow}\rho_{R\downarrow} + \rho_{L\downarrow}\rho_{R\uparrow} \quad (1.6)$$

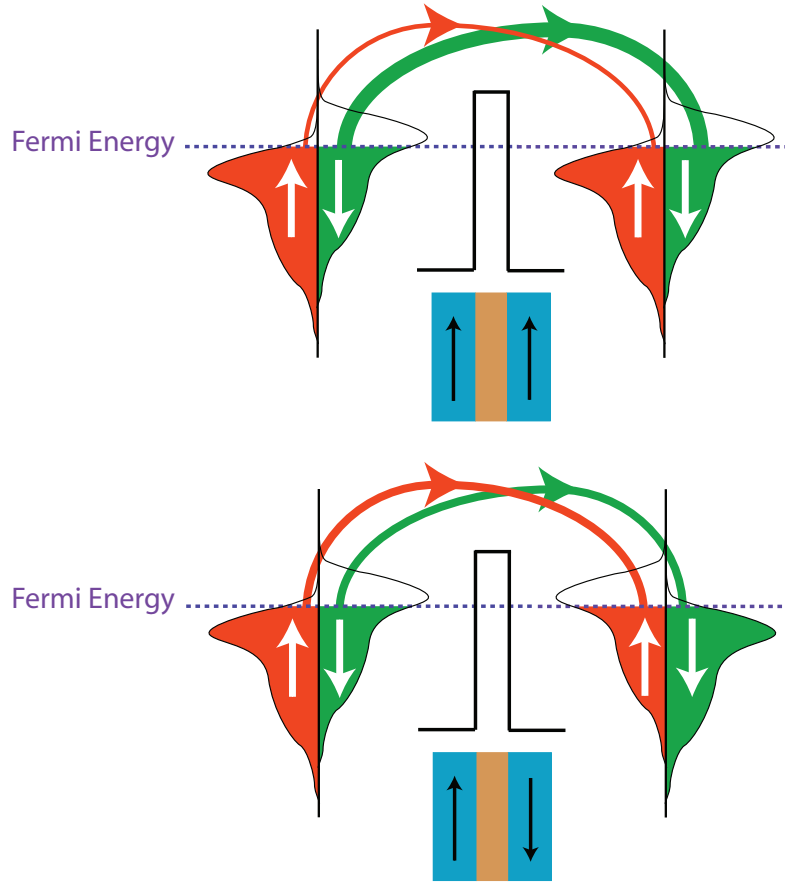


Figure 1.7: Jullière's model of tunneling magnetoresistance. The parallel configuration of the two ferromagnetic electrodes corresponds to high conductance (top panel) and the anti-parallel configuration corresponds to low conductance (bottom panel).

where G_P (G_{AP}) is the tunneling conductance at parallel (anti-parallel) state, $\rho_{L\uparrow}$ and $\rho_{L\downarrow}$ ($\rho_{R\uparrow}$ and $\rho_{R\downarrow}$) are the densities of states for majority and minority spins of the left (right) ferromagnet. If we define spin polarization P as the percentage of net spin for all electronic states at the Fermi surface:

$$P = \frac{\rho_{\uparrow} - \rho_{\downarrow}}{\rho_{\uparrow} + \rho_{\downarrow}} \quad (1.7)$$

the tunneling magnetoresistance ratio or TMR, can be defined and calculated as:

$$TMR \equiv \frac{R_{AP} - R_P}{R_P} = \frac{G_P - G_{AP}}{G_{AP}} = \frac{2P_L P_R}{1 - P_L P_R} \quad (1.8)$$

The first measurement of tunneling magnetoresistance, 14% for a Fe/GeO/Co magnetic tunnel junctions (MTJ) at 4.2 K, was reported by Jullière in 1975 [22], a dozen years earlier than the discovery of the GMR effect. However, his early experiment on MTJs, together with another report from Maekawa and Gäfvert [23], went essentially unnoticed or was hardly reproducible for a long time since it was so challenging to create a suitable tunneling barrier on top of a ferromagnetic film while still maintaining a clean interface at that time [21]. Inspired by the immediate technological impact of GMR, the breakthrough reports on TMR at room temperature [24, 25] using aluminum oxide as tunnel barrier eventually revived interest in this field. With later advancement in both thin film deposition techniques and understanding in spin dependent tunneling mechanism, tunneling magnetoresistance ratios have been shooting dramatically higher, and magnetic tunnel junctions are now taking a center stage in the research of spintronics.

1.2.2 MgO-Based Magnetic Tunnel junctions

The tunneling magnetoresistance ratio predicted by the conclusion of Jullière's model [Eq. (1.8)] is generally pretty consistent with experimental values as long as one uses the tunneling spin polarization P extracted from a Tedrow & Meservey type SC/I/FM tunneling measurement using the same ferromagnet and tunnel barrier. However, the tunneling spin polarization measured in this way almost never agrees with the prediction [Eq. (1.7)] from total density of states at the Fermi energy. For example, cobalt and nickel are expected to have strong negative spin polarization at the Fermi energy (with much higher density of states for minority spin than for majority spin) based on band structure

calculations (as is evident in Fig. 1.1 for Co), which was also confirmed by spin-resolved photoemission measurements [26]. On the contrary, superconductor tunneling experiments through Al₂O₃ measure positive spin polarizations for both Co and Ni. It turns out that one must account for the different mobilities (or transmission probabilities) of the hybridized sp- and d-orbital electrons during tunneling, and the more itinerant electrons dominating the tunneling are positively polarized in Co and Ni even though the whole electron population has a negative spin polarization at the Fermi Surface [27].

The fact that tunneling process is highly selective on the wavefunction of electronic states becomes strikingly significant with the emergence of magnesium oxide (MgO) as the tunnel barrier of choice. While the improvement of the TMR ratio achieved in Al₂O₃-based MTJs has stagnated at 70-80%, it was predicted in 2001 [28, 29] that a highly crystalline tunnel junction with MgO tunnel barrier should yield far higher TMR values, which was later confirmed experimentally by a dramatic jump in room temperature TMR record to 180% [30] and 220% [31] in 2004.

In these MgO-based epitaxial tunnel junctions, proper orientation of the crystals leads to well matched electron wavefunctions across the interface for selective bands at particular wave-vectors, which provide the dominant contribution to the tunneling current, an effect known as symmetry-filtered tunneling. In the case of Fe[001]/MgO[001]/Fe[001], a spd-hybridized band with Δ_1 symmetry at Γ point (or $k_{||} = 0$) has the slowest decay rate across the tunnel barrier, which happens to have only majority states but not minority states (Fig. 1.8). Therefore when the magnetizations of the two Fe electrodes are in parallel state, the MTJ has high conductance through majority-majority

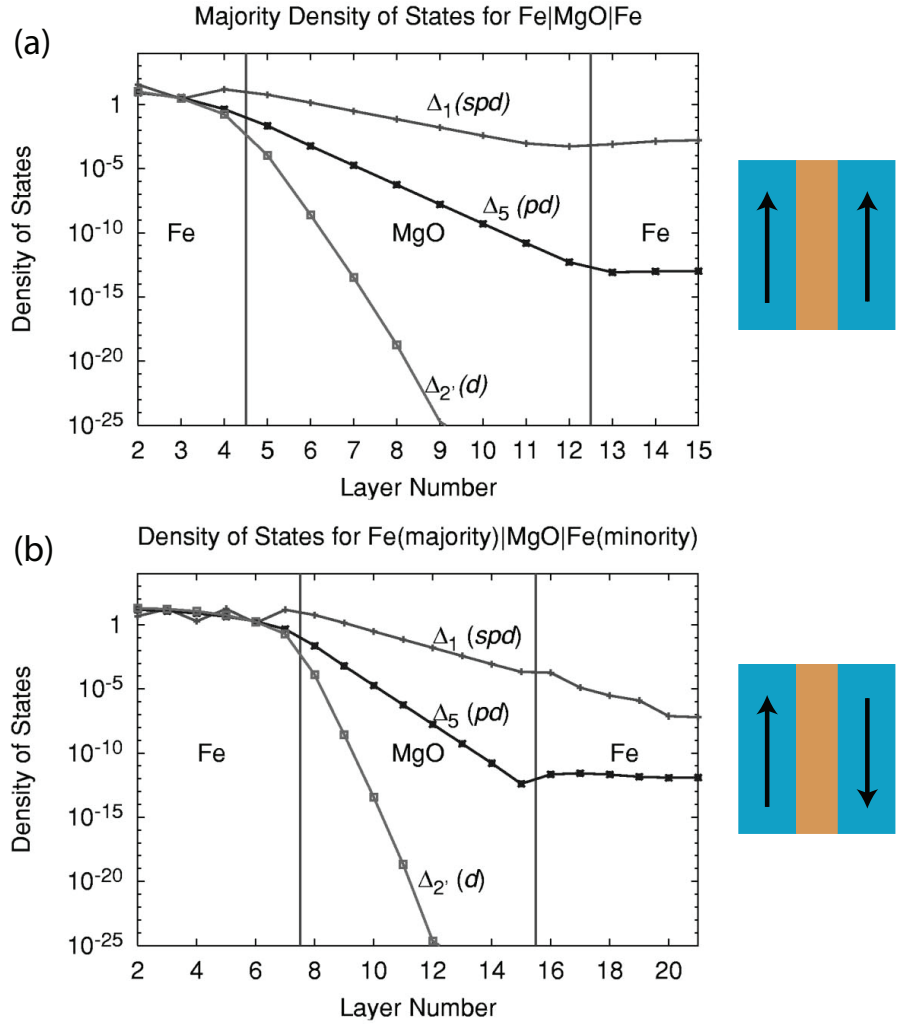


Figure 1.8: Layer-by-layer distribution of tunneling density of states for $k_{||} = 0$ in a Fe/MgO (8 atomic layer)/ Fe MTJ. (a) Δ_1 states have the slowest decay rate inside MgO tunnel barrier and dominate the tunneling current in the parallel (P) configuration. (b) In the antiparallel (AP) configuration, Δ_1 states are absent for minority spins and continue decay exponentially in the right electrode. Adapted from ref. [28].

tunneling via the Δ_1 band. On the other hand, in the antiparallel state the majority-minority tunneling has to rely on Δ_5 states which decay a lot faster in MgO, resulting in theoretically at least an order of magnitude lower conductance. Indeed TMR above 1000% in MgO-based MTJs has been reported under low temperature and the room temperature TMR record so far has exceeded 600%. From a more technical perspective the MgO-based MTJs have also shown amazing robustness on the chemical and material choices. Replacing Fe with Co or many Co/Fe based alloys provides similar symmetry filtering effect [32]. TMR in the range of 100-200% are readily achievable even with significant amount of interdiffusion of different atomic layers in the tunnel junction [33]. By virtue of the gigantic TMR ratio, nowadays MgO-based MTJs have seen huge success in commercial markets, replacing traditional GMR sensors in magnetic hard disc drives and also leading to the application of magnetic random access memories (MRAM). At this stage further improvement of TMR ratio is no longer limited by fundamental properties such as spin polarization of the ferromagnet but more of an engeneering issue in controlling the material complexity during the annealing process. The large TMR ratios so far achieved, though unprecedeted, still far trail theoretical predictions of thousands of percent calculated for an ideal system, possibly affected by interface oxidation [34], resonant tunneling through defect states [35], etc. In addition to the TMR applications, MgO has also become the ideal tunneling system for a broad scope of spin injection experiments and applications.

1.2.3 Spin Transfer Torque in Magnetic Tunnel Junctions

When spin-polarized electrons tunnel through the insulating barrier of a MTJ, the magnetic electrodes experience spin transfer torque from absorption of transverse angular momentum in a similar way to the case of a metallic spin valve. Even though tunneling current in a MTJ is generally weaker than one can apply to a metallic spin valve, recent improvements in making ultra-thin MgO tunnel barrier have enabled MTJs with sufficiently low resistance-area (RA) product to realize spin transfer driven magnetization switching. Owing to the gigantic TMR ratios in MgO-based tunnel junctions as opposed to the GMR in metallic spin valves, and better impedance matching to the prevailing semiconductors in electronics industry, most applications of spin transfer torque are expected to use MgO-based MTJs, including the spin-transfer-torque MRAM (STT-MRAM) that is pretty close to commercialization.

Due to the filtering effect of the MgO tunnel barrier, the spin transfer torque in a MgO-based MTJ is carried predominantly by certain electronic states within a small area of the Fermi surface, *i.e.* Δ_1 band around Γ point for majority to majority tunneling. One of the consequences of sharply defined tunneling states, as it turns out, is some subtle relative phase between the two spin components acquired at the interfaces that acts macroscopically to turn the direction of the spin transfer torque out of the common plane of the two magnetizations. One can think of this effect coming from some electrons reflected by the second ferromagnetic electrode after some “precession” during the process (Fig. 1.9). These electrons carry transverse angular momentum away from being absorbed and this “lost” angular momentum has both an in-plane component and an out-of-plane component. Therefore in MgO-based

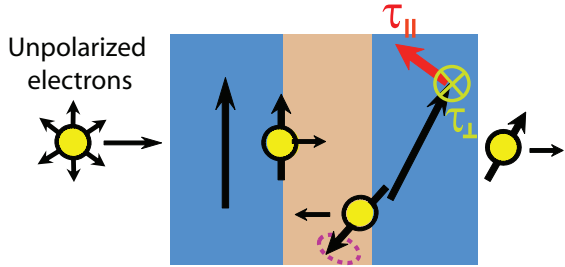


Figure 1.9: Schematic of the in-plane Slonczewski torque (marked by $\tau_{||}$) and the perpendicular field-like torque (marked by τ_{\perp}) in a magnetic tunnel junction. One can intuitively consider the reflected electrons taking away transverse angular momentum after precession.

tunnel junctions, spin transfer torque generally has two components: one in-plane component (or “Slonczewski torque”) that lies within the plane defined by the magnetizations of free layer and fixed layer, and one perpendicular component (or “field-like torque”) that is perpendicular to the common plane of the two magnetizations (Fig. 1.9). This effect reflects the details of the particular electronic state that carries tunneling current in the MTJ, which would otherwise be canceled out if a large number of states all contribute to transport as in the case of a metallic spin valve device.

Another interesting aspect of the spin transfer torque that arises in tunnel junctions is its dependence on the applied voltage across the tunnel barrier. With a finite bias V present, the range of electronic states participating in tunneling is significantly widened from very close to the Fermi energy (E_F) to those within $E_F \pm eV/2$. The energy dependence of the density of states, the combined effect of elastic tunneling and inelastic tunneling, and hot electron effects could come into play to significantly change the amplitude and direction of spin transfer torque. This is a trivial problem for metallic spin valve devices since practically one cannot apply any meaningful voltage on the scale of electronic band structures across several nanometers of metal. However

in MTJs, it is always at high bias voltage (hundreds of millivolts) that the spin transfer torque becomes strong enough to be relevant to applications like magnetic switching. Therefore the bias dependence of spin transfer torque in MgO-based MTJs is an important question from both a physics point of view and also from an application perspective.

There have been several experimental methods used to measure the spin transfer torque in MTJs. One method is by analyzing the magnetic switching induced by spin transfer torque. This sounds very straightforward since the critical torque, τ_c , needed to cancel Gilbert damping and induce dynamic instability can be easily calculated from basic device parameters, and if one can find the critical current I_c (or voltage V_c) for such an instability, one essentially measures $\tau(I_c) = \tau_c$. However, experimentally switching occurs at biases far lower than I_c (or V_c) due to thermal fluctuation. According to a thermally assisted switching model [36], below critical threshold spin transfer torque effectively heats up one magnetic state (through reduction of damping) and cools down the other magnetic state (through enhancement of damping), making switching from the former state to the later state thermally preferable. Only under zero temperature can the critical current I_c be directly measured, but Joule heating is very significant at high bias approaching I_c making any cryogenic environment not very helpful. To overcome this difficulty, what is routinely done is to apply electric pulses $V < V_c$ to induce magnetic switching with the help of thermal fluctuation, measure the switching threshold V as a function of the duration of the electric pulses [37–40], and fit to the thermally assisted switching model [36] to extract V_c . Alternatively, one can also measure the switching threshold V as a function of magnetic field H and fit to the same model [41].

Another method is called thermally excited ferromagnetic resonance (TE-FMR). Even without spin transfer torque, the magnetization of a nanomagnet receives random thermal excitations. In other words, a white noise is constantly pumping the nanomagnet out of equilibrium, while the damping dissipates these excited state energies as required by fluctuation-dissipation theorem. While the thermal excitation itself is frequency-independent (white), the magnetization response of the nanomagnet is frequency-dependent. At a particular frequency that matches the frequency of a magnetic normal mode of the nanomagnet (*e.g.* small-angle uniform precession), it shows resonant response with maximum fluctuation in its magnetization orientation. From the TMR effect, one can read out the thermal fluctuations of the magnetization orientation by measuring the microwave emission from the MTJ device. Therefore, the microwave emission spectrum, or TE-FMR spectrum, shows a resonant peak (as a function of frequency) correspondingly. It can be shown that in-plane component of spin transfer torque alters the linewidth of the TE-FMR peak, while perpendicular component of spin transfer torque shifts its frequency [42]. By measuring the linewidth and frequency at different biases spin torque can be calculated.

A third method is spin-transfer-driven ferromagnetic resonance (ST-FMR), which is a big part of this dissertation and will be discussed later. This method has some similarities with TE-FMR in its ferromagnetic resonance nature, but is excited by spin transfer torque from a radio-frequency oscillating current. As of the state of 2007, the reported experimental results by all three categories of methods were significantly conflicting to each other. In Chapter 2 and Chapter 3 of the dissertation, I describe our subsequent experiments to measure the spin transfer torque in MgO-based MTJs using two detection techniques of ST-

FMR and present a detailed breakdown of the ST-FMR method. Eventually we achieved the first quantitative measurement of spin torque in MTJs as a function of bias voltage and offset angle between the magnetic moments of the two layers across the full bias range, and explained the controversies around the various experiments with different methods.

1.2.4 Spin Transfer Torque Approaching Single Electron Tunneling Regime

So far as of the writing of this dissertation, nearly all previous experiments on spin transfer torque were performed using lithographically patterned free layer magnets with typically \sim 100 nm size as was shown in Fig. 1.4(b). This size of nanomagnet is composed of millions of ferromagnetic atoms and millions of net electron spins, which is essentially a semi-classical object in the following sense. Firstly, the huge number of electron spins makes the addition or subtraction of an extra spin via tunneling insignificant and also makes the quantization of the collective spin states insignificant, so this free layer is essentially treated as a classical vector with fixed amplitude in the LLGS equation [Eq. (1.4)]. Secondly, the huge number of atoms makes its electronic states equivalent to the continuous band structure of the bulk metal so that any energy quantization from nanoscale size confinement is absent. These conditions are expected to change dramatically if the volume of the “free layer” is reduced to $3\text{-}10 \text{ nm}^3$ corresponding to less than one thousand atoms and less than one thousand net electron spins. This type of tiny magnetic objects can be obtained by the self assembly mechanism during deposition of very thin magnetic films

or granular materials, which leads to formation of small islands known as magnetic nanoparticles.

These nanoparticles have discrete electronic energy levels with level spacing of 1-10 meV and also have large single-electron Coulomb charging energy on the order of tens of meV, so under low temperature electrons can tunnel through a nanoparticle only one by one via one or very few individual electron levels. Unlike in bulk (100 nm nanopillar) electrodes where spin transfer torque is effectively averaged over many electronic states, the spin transfer torque in nanoparticles should be carried by very small number of electronic states, and may show large fluctuations in magnitude and even the direction of the torque. In this single electron tunneling regime, spin transfer torque may display strong discreteness as a function of bias related to the quantized electronic states. A large enhancement of the torque is predicted when the bias is resonant with discrete levels on the nanoparticle [43, 44]. Furthermore, detailed studies of the spin transfer torque carried through individual energy levels, if possible, should reflect the property of these electronic states and may help unravel the electron interaction inside magnetic nanoparticles.

The nature of magnetic damping might also be altered dramatically in magnetic nanoparticles. The Gilbert damping constant α for a bulk ferromagnet such as CoFe or NiFe is typically around 0.01, corresponding to relaxation of non-equilibrium magnetic excitation on the time scale of 1 nanosecond. There is evidence [45, 46] that the corresponding relaxation scale may be much longer for magnetic nanoparticles, because the discrete spectrum may block the production of electron-hole excitation when the magnetic moment precesses so that the normal source of magnetic damping in ferromagnetic metals [47, 48]

becomes inoperative. Since the critical current needed to induce magnetic dynamics is directly proportional to the damping of the magnet, there have been predictions for magnetization reversal at very low current densities in magnetic nanoparticles [49–51].

In spite of all the interesting predictions on spin transfer torque approaching single electron tunneling regime, such experiments have been extremely challenging. There have been a few delicate fabrication techniques in achieving tunneling contact to a single ferromagnetic nanoparticle for transport study, including deposition into sub-10 nm holes on a silicon nitride membrane [45, 52] and multi-angle shadow-mask deposition of nanoparticles [53]. The technique of insertion of chemically synthesized nanoparticles into break junctions produced by electro-migration [54] is also potentially applicable to magnetic nanoparticles. In addition, there have been a lot of researches on electrical transport in granular films (*e.g.* Al-Co-O), which contain a large ensemble of magnetic nanoparticles embedded in an insulating material. Due to statistical variation of the layer thickness and nanoparticle distribution etc., single-electron tunneling effects have also been observed [46] even though there are a huge amount of relevant nanoparticles present in principle. However, all of these experiments feature very high single particle resistances (close to $G\Omega$ range), so none of those devices have (effectively) thin enough tunnel barrier to conduct significant tunneling current to produce any measurable effect from spin transfer torque. For magnetic nanoparticles in metallic contact with its environment, spin transfer torque has been studied in a few experiments [55–57], but these particles do not have a size-confined electronic structure, and therefore most of the interesting predictions related to spin torque in single-electron tunneling regime is not applicable.

Recent technical improvements in making ultra-thin MgO tunnel barrier have allowed fabrication of standard magnetic tunnel junctions of resistance-area product (RA) as low as $1 \Omega\mu\text{m}^2$, corresponding to $1 \text{ M}\Omega$ resistance (or 80 times resistance quantum $\hbar/2e^2$) through a 1 nm^2 tunneling area of a nanoparticle, if one can prepare this type of tunnel barrier on both sides of a nanoparticle. In chapter 5 of this dissertation, I report our first effort towards probing spin transfer torque in magnetic nanoparticles using nanoparticles embedded in MgO tunnel barriers. By patterning a tunnel junction multilayer into nanopillars smaller than $50 \text{ nm} \times 50 \text{ nm}$ by electron-beam lithography, we are able to make low-RA tunnel junction devices containing only 50-100 nanoparticles, resolve the magnetoresistance from individual particles, and provide the first experimental evidence of spin transfer torque in magnetic nanoparticles in an insulating tunnel barrier.

1.3 Electrical Manipulation of Magnetism: Other Research Directions

As described in previous sections, spin transfer torque from spin-polarized tunneling current in MTJs is one of the most promising approaches for electrical manipulation of magnetic moments, and is already at advanced development stage for industrial applications such as STT-MRAM. On the other hand, there are a number of research fields that use different approaches to realize electric manipulation of magnetism for potential magnetic memory applications.

1.3.1 Manipulation of Magnetic Moments by Pure Spin Current

An approach closely related to the content of preceding sections is to use spin transfer torque induced by a pure spin current. Although most spin torque experiments involve a charge current passing through the manipulated magnet (free layer) that is spin-polarized by a second magnet (fixed layer), the spin transfer torque is a consequence of the inflow/outflow of spin and should not depend on the existence of charge current. There are ways that a spin current can be generated without net charge transport in certain areas of a nanostructure, such as the initial spin injection experiment demonstrated by Johnson and Silsbee [8]. Pure spin current can be injected into a ferromagnet and exert a spin transfer torque in much the same way as a spin-polarized charge current does [58, 59], with the potential advantage of lower energy consumption. One realization of this idea is a three-terminal magnetic device [60, 61] [Fig.1.10(a)] that integrates a MgO-based MTJ [F2 and F3 in Fig.1.10(a)] with a non-local metallic spin valve [F1 and F2 in Fig.1.10(a)]. In this structure, current is sourced from T1 to T2, and pure spin current is injected into the ferromagnet F2 to allow manipulation even though F2 is not in the current path. The MTJ is used to read out the magnetization of F2 with a small detection current. This design completely avoids the large voltage required for switching in a MTJ by tunneling current, and therefore greatly improves the durability of MTJs as potential magnetic storage elements. It should be noted that the spin transfer efficiency can be similar in this type of non-local geometry compared with in more traditional two-terminal devices [61].

Another very promising approach to generate pure spin current is by the

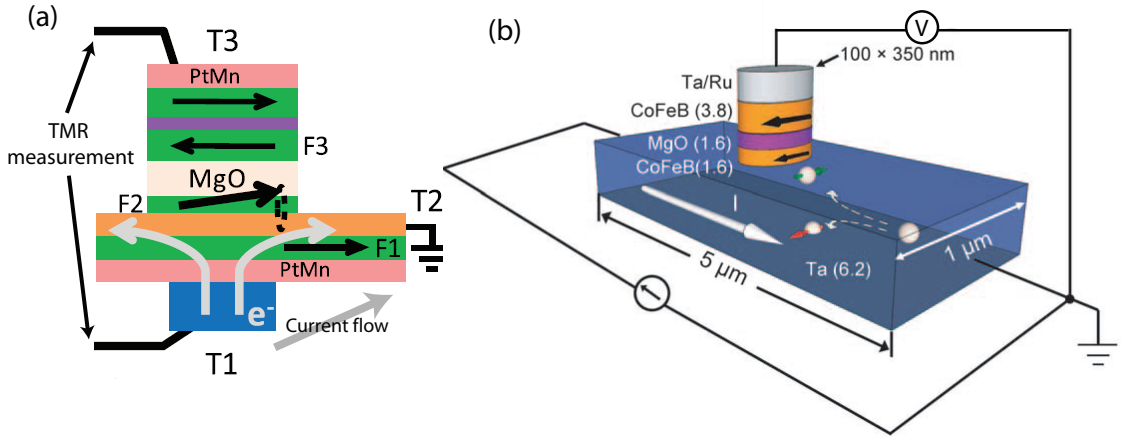


Figure 1.10: Schematics of three-terminal devices that utilize spin transfer torque generated by pure spin current. (a) A three-terminal device with an MTJ integrated to a non-local spin valve. Adapted from ref. [61]. (b) A three-terminal device using the spin Hall effect for magnetization manipulation. Adapted from ref. [62].

spin Hall effect. The spin Hall effect describes the conversion of a longitudinal charge current density J_C into a transverse spin current density $J_S(\hbar/2e)$ inside certain non-magnetic metals or semiconductors. It originates from spin-orbit scattering, whereby conduction electrons with opposite spin orientations are deflected in opposite directions. It is still under debate whether this effect is mostly intrinsic to band structures of these materials from spin-orbit mixing or extrinsic due to impurities. Since the first electric measurement of the spin Hall effect in 2006 in aluminum [63], studies of the spin Hall effect in metals with strong spin-orbit coupling have gained a lot of interest. Soon after the development of a reliable experimental technique to quantify the magnitude of the spin Hall effect in a given material [64], larger and larger spin Hall effect has been discovered in platinum (Pt), tantalum (Ta) and then tungsten (W). For instance, it is measured that in Ta, for every electric charge $-e$ flowing in the longitudinal direction, there is a spin flow of about $0.13 \hbar/2$ [62] in the transverse

direction. When a ferromagnetic material is placed adjacent to the spin Hall material, this spin current can be injected into the ferromagnet to generate spin transfer torque. Very recently three terminal devices have been built to use the spin Hall effect to manipulate the adjacent ferromagnet and read out its magnetization by a magnetic tunnel junction [62] [Fig. 1.10(b)].

1.3.2 Manipulation of Magnetic Moments by Electric Field

Spin transfer torque is a transport effect generally associated with applying external current, which generates Joule heat in all the demonstrated experiments. On the other hand, the ultimate limit on low energy consumption for magnetic storage devices resides in the possibility of eliminating electric current. There are a number of magnetoelectric effects that one can employ to modify magnetic properties of devices by applying an electric field (or voltage) alone. Several areas of investigation have been suggested, including voltage control of magnetic anisotropy [65], voltage control of ferromagnetism in ferromagnetic semiconductors [66], magnetoelectric switching of exchange bias and anisotropy [67] with multiferroic materials, and magnetostriction in a hybrid system with piezoelectric materials [68].

Recently a notable breakthrough came from voltage control of magnetic anisotropy. In 2007 it was discovered that the magneto-crystalline anisotropy (MCA) of thin film magnets FePt(Pd) at room temperature can be changed by a few percent by electric field applied in electrolyte, which opened new possibilities in engineering interface MCA that is controllable by electric field. This type of field effect has been attributed to a change of occupation of

3d orbitals of interface magnetic atoms under electric field, which alters the magnetism of the thin film. In 2009 successful electric-field control of interface MCA was reported in the core element of spintronics research and applications – MgO-based MTJs, accompanied with significant improvement in magnitude – 40% change of anisotropy by electric field less than 100 mV/nm [69]. It has been demonstrated very recently this voltage control of interface MCA can been utilized to switch the magnetization of an MTJ electrode [70, 71], which represents a promising route towards low-power writing of magnetic storage devices.

Another field under intensive investigation is to build hybrid structures taking advantage of magnetoelectric coupling intrinsic to multiferroic materials. “Multiferroicity” stands for a (relatively rare) property of certain materials exhibiting more than one primary ferroic order parameter simultaneously (*i.e.* in a single phase), including ferromagnetism, ferroelectricity, ferroelasticity and (perhaps) ferrotoroidicity. To realize applicable electric-field control of ferromagnetism, a multiferroic material with both substantial ferromagnetism and ferroelectricity at room temperature would be ideal, but such a material has yet to be discovered. With a slightly relaxed standard, antiferromagnetism is often counted towards multiferroicity as well. BiFeO₃ has come into focus in recent years [72, 73] as the only material known at room temperature exhibiting strong ferroelectricity and antiferromagnetism. Since the ferroelectricity and antiferromagnetism in BiFeO₃ are intrinsically coupled to each other through the crystal lattice, one can quite robustly control the antiferromagnetic axis with an electric field [74]. Just as many widely used antiferromagnets (such as IrMn, FeMn, etc.), BiFeO₃ also reportedly shows an exchange coupling at its interface with an adjacent ferromagnetic metal. Since this exchange coupling originates

from the antiferromagnetic order, a natural question to ask is whether one can control this exchange coupling acting on a ferromagnet by controlling the antiferromagnetic order of BiFeO_3 electrically. In Chapter 6 of this dissertation, I report our experimental efforts to make giant magnetoresistance (GMR) devices exchange biased by multiferroic BiFeO_3 , and investigate the possibility to operate the GMR device by electric fields. We also use these GMR devices as a readout scheme to study the spatial variation of exchange bias locally at sub-100 nm length scale, comparable to the domain size of BiFeO_3 .

CHAPTER 2

DC MIXING VOLTAGE DETECTION OF SPIN-TRANSFER-DRIVEN FERROMAGNETIC RESONANCE

As discussed in Chapter 1, determining the magnitude and direction of the spin-torque vector, τ , in MgO-based magnetic tunnel junctions, especially its dependence on voltage bias, is fundamental to understanding spin dependent transport and also for making practical devices. Several experiments methods have been applied to measure the spin transfer torque but have produced qualitatively conflicting results, and theoretical predictions differ significantly as well. In this chapter, I present our measurement of spin-transfer torque vector in MgO-based MTJs as a function of the offset angle, θ , between the magnetic moments of the electrodes and as a function of bias, V , using DC-detected spin-transfer-driven ferromagnetic resonance (ST-FMR).

In this experiment, we build upon a previous experiment carried out by J. C. Sankey *et al.* [75, 76] in Ralph Group at Cornell with the ST-FMR technique [77, 78], and investigate the conflicting conclusions drawn from Sankey *et al.*'s experiment [76] and a similar experiment carried out by a different group [79]. We resolve the contradiction by accounting for additional terms that contribute to the ST-FMR signal at large V arising from a change of average resistance of the MTJ with and without precession. Numerically accounting for the additional terms gives us improved precision in the determination of $\tau(V)$, allowing us to distinguish among competing predictions. We determine that the in-plane component of $d\tau/dV$ has a moderate dependence on bias, varying by 30%–35% over the bias range where the measurements are accurate, and that the perpendicular component can be large enough to be technologically

significant. We also make comparisons to other experimental techniques that have been used to try to measure $\tau(V)$. The contents of this chapter are mostly adapted from work originally published as *Phys. Rev. B* **79**, 224416 (2009) [80].

2.1 Spin-Transfer-Driven Ferromagnetic Resonance (ST-FMR)

In Chapter 1, a couple of scenarios of magnetization dynamics induced by spin transfer torque from a direction current (DC) have been discussed. These types of dynamics require application of a large current exceeding a critical threshold to completely suppress the Gilbert damping of the nanomagnet so that instability occurs. When the applied DC current is below the threshold, the spin transfer torque is not strong enough to excite definitive magnetization dynamics¹, and the nanomagnet will stay at the stationary state taking only minor effects from the spin transfer torque. However, if a small oscillating current is applied, the alternating spin transfer torque can drive the nanomagnet into resonant precession when the frequency of the current matches the intrinsic precession frequency of the nanomagnet (which depends on applied magnetic field). Since the resonance is typical at high radio-frequency range of 1-15 GHz, I will refer to this driving current as RF (radio-frequency) current as opposed to DC current or AC current at kHz range. This is a linear response effect (at least at small RF current) – precession always occurs no matter how small the RF current is, and its amplitude scales linearly with the RF current. Compared with the well-known ferromagnetic resonance technique where a RF magnetic field is applied to drive precession of a ferromagnet thin film, this is a similar type of ferromagnetic resonance on an individual nanomagnet driven locally by

¹At non-zero temperature, sub-critical spin torque does alter the thermally-excited magnetization dynamics

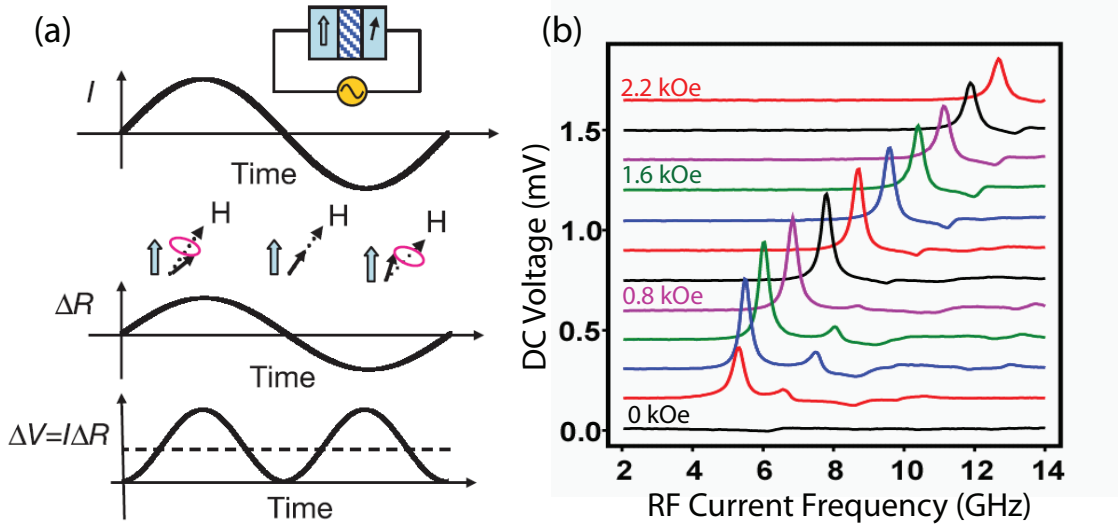


Figure 2.1: Illustration of spin-transfer-driven ferromagnetic resonance. (a) A cartoon of the origin of the DC mixing voltage. Adapted from ref. [77]. (b) Typical ST-FMR spectrum – the DC mixing voltage as a function of frequency at selected external magnetic field. Adapted from ref. [76].

spin transfer torque at RF frequency. Therefore this resonance effect is dubbed “spin-transfer-driven ferromagnetic resonance”.

2.1.1 DC Detection of Spin-Transfer-Driven Ferromagnetic Resonance

Spin-transfer-driven ferromagnetic resonance, or ST-FMR, was first reported by Tulapurkar *et al.* [77] from National Institute of Advanced Industrial Science and Technology (AIST) of Japan and was also independently demonstrated by Sankey *et al.* [78] at Cornell. In both experiments and the majority of experiments thereafter, ST-FMR is detected from an additional DC voltage arising from the resonant precession, which can be illustrated in Fig. 2.1(a). When magnetization of the MTJ’s free layer precesses, the resistance of the

MTJ oscillates at the same frequency, f , as the RF current. Consequently the voltage across the MTJ, which is a product of resistance and current, receives a DC contribution together with a $2f$ oscillation due to the inter-mixing of resistance oscillation and current oscillation. One can use a lock-in technique to chop the RF current on and off at 100's of Hz or kHz frequency and measure this "DC" mixing voltage at the lock-in frequency relatively easily. This mixing voltage can be analyzed either as a function of RF driving frequency at a fixed magnetic field, or as a function of magnetic field at a fixed frequency. The first method is more widely used in the context of this dissertation. In this case, maximum signal is expected when the frequency is swept through the resonance frequency, while very small signal is expected at frequencies far off resonance. In Fig. 2.1(b), a typical series of primary resonance peaks at different applied magnetic fields are shown, with the resonance frequency shifting to higher frequencies at higher magnetic field as expected.

2.1.2 Early Measurements of Spin Transfer Torque by ST-FMR and Discrepancies

In a ST-FMR measurement, in addition to the RF current, one can also apply a DC bias current (or bias voltage) so that the total current across the MTJ is time-dependent as:

$$I(t) = I + \delta I(t) = I + I_{RF} \text{Re}(e^{i\omega t}) \quad (2.1)$$

where we set the phase of the RF current to zero at $t = 0$. When the DC current is lower than the critical threshold of instability, the DC current does not induce any significant effect on the free layer magnetization. Its stationary direction

does shift by a small amount under the DC current bias so that the field torque balances with the DC spin transfer torque to reach a new equilibrium. In a typical ST-FMR measurement, an external magnetic field is applied such that the offset-angle between the free layer and the fixed layer is between 45° to 135° , where the spin transfer torque is much stronger than close to the parallel (P) or the antiparallel(AP) states, giving better resonance signal. The critical current for instability in this geometry is much higher than close to P or AP state, and diverges at about 90° , usually not reached in ST-FMR experiments. Therefore one can generally consider the DC current as a stationary biasing condition, and the RF current produces an additional small alternating spin transfer torque. ST-FMR is a small-angle linear response, leading to a resistance oscillation of

$$R(t) = R + \delta R(t) = R + (\delta R)\text{Re}(e^{i\omega t+\phi}) \quad (2.2)$$

where the amplitude of the resistance oscillation δR is proportional to I_{RF} , and the ratio of proportionality reflects the incremental strength of the spin torque at that particular current (or voltage) bias. By determining the magnitude of this linear response at various biases, ST-FMR allows one to measure the spin transfer torque in a differential way, $d\vec{\tau}/dV$ as a function of V , so as the map out the bias dependence of spin transfer torque. Moreover, the phase factor ϕ in Eq. (2.2) directly relates the shape of the resonance peaks in the DC mixing voltage spectrum to the direction of spin transfer torque as illustrated in Fig. 2.2.

The voltage arising from current-resistance mixing is proportional to $\cos \phi$,

$$\begin{aligned} \langle V(t) \rangle &= \langle I(t)R(t) \rangle = IR + \langle I_{RF}\text{Re}(e^{i\omega t})(\delta R)\text{Re}(e^{i\omega t+\phi}) \rangle \\ &= IR + \frac{1}{2}I_{RF}(\delta R)\cos \phi \end{aligned} \quad (2.3)$$

where $\langle \rangle$ stands for time averaging. As an externally-driven harmonic oscillator, the relative phase ϕ between the dynamic response and its external drive drops

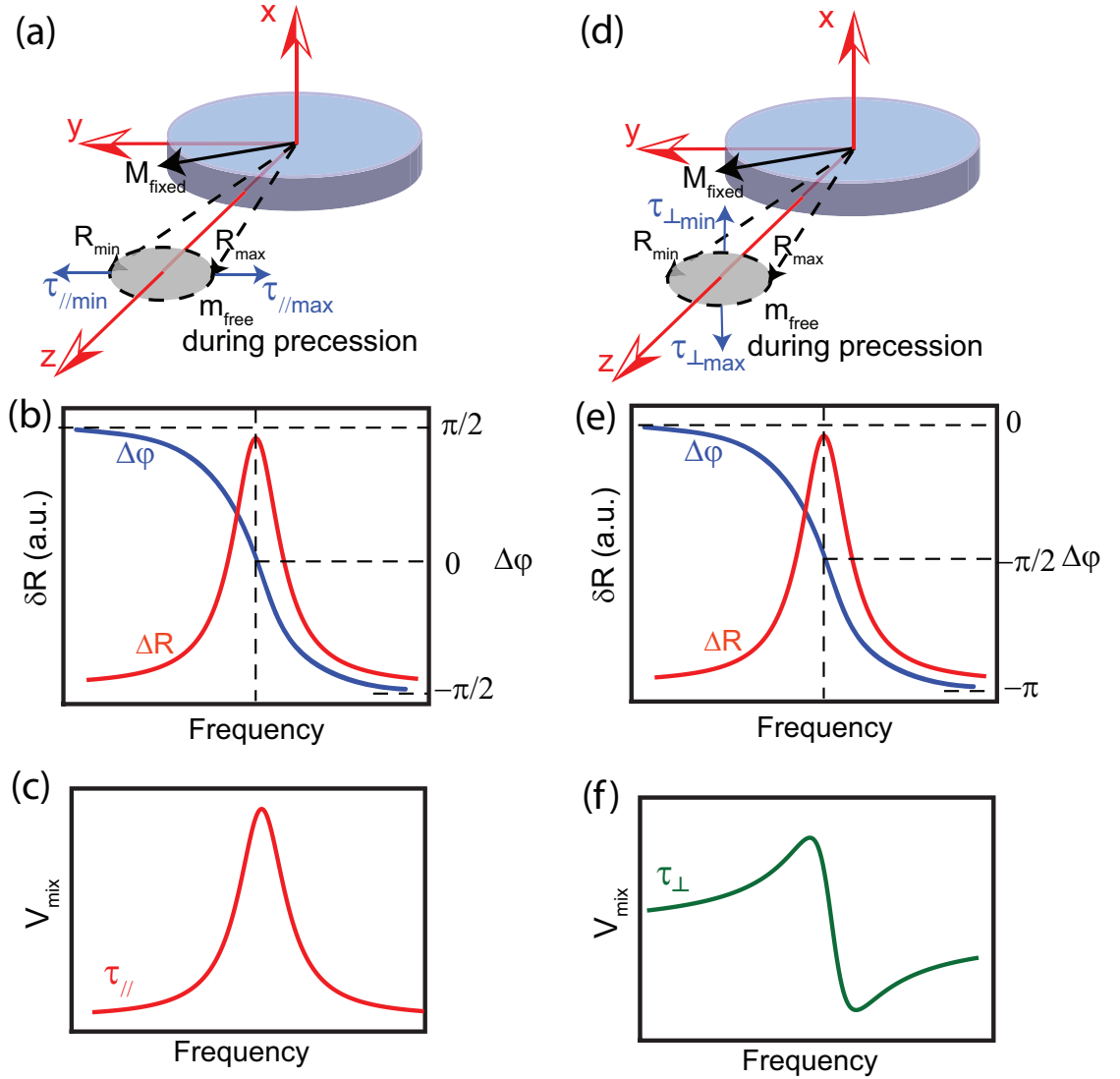


Figure 2.2: Illustration of the relation between the ST-FMR line-shape and the direction of spin transfer torque. For in-plane spin torque (a), the resistance oscillation is in-phase with the driving current at the resonance point (b), and the ST-FMR line-shape is a symmetric Lorentzian (c). For perpendicular spin torque (d), the resistance oscillation is 90° out-of-phase with driving current at the resonance point (e), and the ST-FMR line-shape is an anti-symmetric Lorentzian (f).

smoothly by π when the driving frequency is gradually tuned through the resonance. If the spin transfer torque is purely within the plane defined by the free layer and fixed layer (Slonczewski torque) [Fig. 2.2(a)], at the resonance point, the in-plane projection of the magnetization precession of free layer is in-phase with the RF drive. Since the resistance of the MTJ, determined by TMR, is sensitive to the in-plane projection of the precession, the resistance oscillation should also be in-phase. Therefore tuning through resonance ϕ changes from $\pi/2$ to $-\pi/2$ [Fig. 2.2(b)]. From the $\cos\phi$ factor in Eq. (2.3) it results in a symmetric Lorentzian line-shape for the ST-FMR spectrum [Fig. 2.2(c)]. On the other hand, if the spin transfer torque is purely perpendicular (field-like torque) [Fig. 2.2(d)], at the resonance point, the out-of-plane projection of the magnetization precession becomes in-phase, so the resistance oscillation should be 90° out-of-phase. This implies a change from 0 to $-\pi$ for ϕ tuning through resonance [Fig. 2.2(e)], leading to an anti-symmetric Lorentzian line-shape for the ST-FMR spectrum [Fig. 2.2(f)]. By fitting experimental ST-FMR data to a sum of a symmetric Lorentzian and an anti-symmetric Lorentzian one can determine the magnitude of both in-plane and perpendicular components of spin transfer torque.

This method for quantitative measurement of the spin transfer torque was first reported by Sankey *et al.* at Cornell [76] and Kubota et al. [79] at AIST in Japan. Their main results are shown on Fig. 2.3 for the magnitude of the in-plane component and perpendicular component of the differential spin transfer torque, $d\vec{\tau}/dV$, as a function of bias voltage. $d\vec{\tau}/dV$ has a name “torkance” coined by J. C. Slonczewski, which I will use for the rest of this dissertation. Both measurements confirm the existence of a perpendicular component, or field-like torque, which grows approximately quadratically with bias voltage

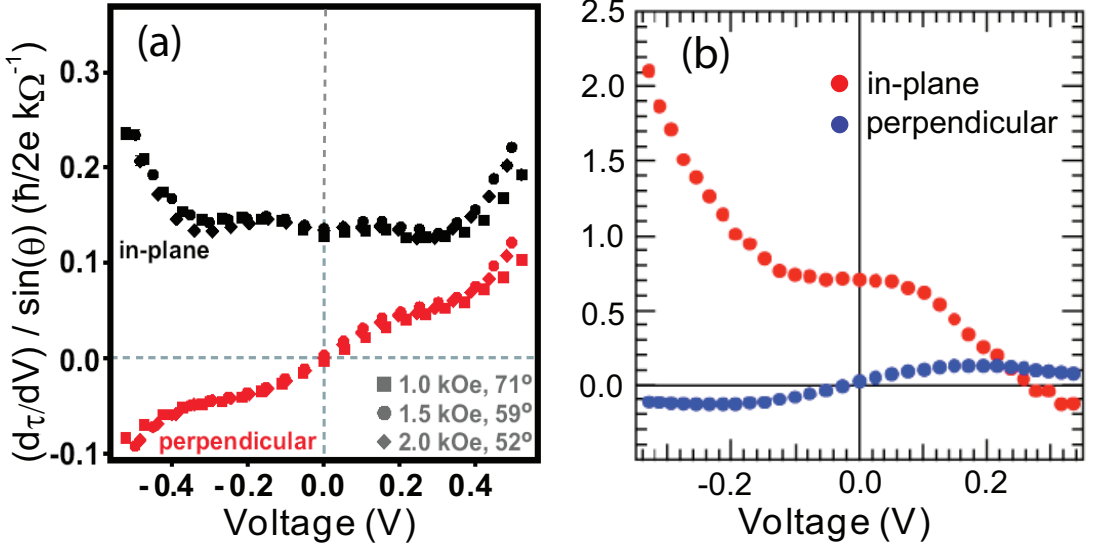


Figure 2.3: A comparison of the spin transfer torkance $d\vec{\tau}/dV$ as a function of bias voltage V in MgO-based MTJs measured in (a) ref. [76] and (b) ref. [79].

(shown as a linear dependence on torkance). However, the discrepancy on the in-plane component of spin transfer torque is significant. The Cornell group [76] reported an approximately constant bias dependence for in-plane torkance, while the Japan group measured the in-plane torkance to be strongly asymmetric, increasing sharply on one sign of bias and decreasing to change sign on the other.

Since the techniques used by the two groups are essentially the same, the outstanding question was, whether the spin transfer torque behaves very differently in different devices, or there are actually minor differences in experimental setups that have artificially resulted in different conclusions on the in-plane torkance. If we take a closer look at the experimental details, there are differences on both the device parameters and the experimental conditions between the two reports. Here at Cornell, the first approach we took towards resolving this disagreement was to explore various experimental parameters and see how one can reproduce the results in both experiments.

2.2 Device Structures and Measurement Procedures

2.2.1 Device Structures

We have investigated devices from two different sets of magnetic tunnel junctions. We measured seven MTJs from the same batch of devices studied in ref. [76], which was fabricated by J. Z. Sun and colleagues at IBM T. J. Watson Research Center. They have nominal $RA = 12 \Omega\mu\text{m}^2$ and the following layers (in nm) deposited onto an oxidized silicon wafer: bottom electrode [Ta(5)/Cu(20)/Ta(3)/Cu(20)], synthetic antiferromagnet (SAF) layer pinned to PtMn [PtMn(15)/Co₇₀Fe₃₀(2.5)/Ru(0.85)/Co₆₀Fe₂₀B₂₀(3)], tunnel barrier [MgO(1.25)], magnetic free layer [Co₆₀Fe₂₀B₂₀(2.5)], and capping layer [Ta(5)/Ru(7)]. The top (free) magnetic layer of these samples is etched to be a rounded rectangle, with dimensions either $50 \times 100 \text{ nm}^2$ or $50 \times 150 \text{ nm}^2$. The bottom SAF layers are left extended, with an exchange bias parallel to the magnetic easy axis of the top layer [Fig. 2.4(c)]. The insulator surrounding the sides of these devices is silicon oxide, and the top electrode is made using layers of Ta, Cu, and Pt.

We also measured about five different samples from a second batch of devices fabricated by J. A. Katine and colleagues at Hitachi Global Storages. These devices have nominal $RA = 1.5 \Omega\mu\text{m}^2$ and the layer structure (in nm): bottom electrode [Ta(3)/CuN(41.8)/Ta(3)/CuN(41.8)/Ta(3)/Ru(3.1)], SAF layer pinned to IrMn [IrMn(6.1)/CoFe(1.8)/Ru/CoFeB(2.0)], tunnel barrier [MgO_x], free layer [CoFe(0.5)/CoFeB(3.4)], capping layer [Ru(6)/Ta(3)/Ru(4)]. In these samples, both the top magnetic free layer [the CoFe(0.5)/CoFeB(3.4) composite layer] and the bottom magnetic “pinned” layers [the CoFe(1.8)/Ru/CoFeB(2)

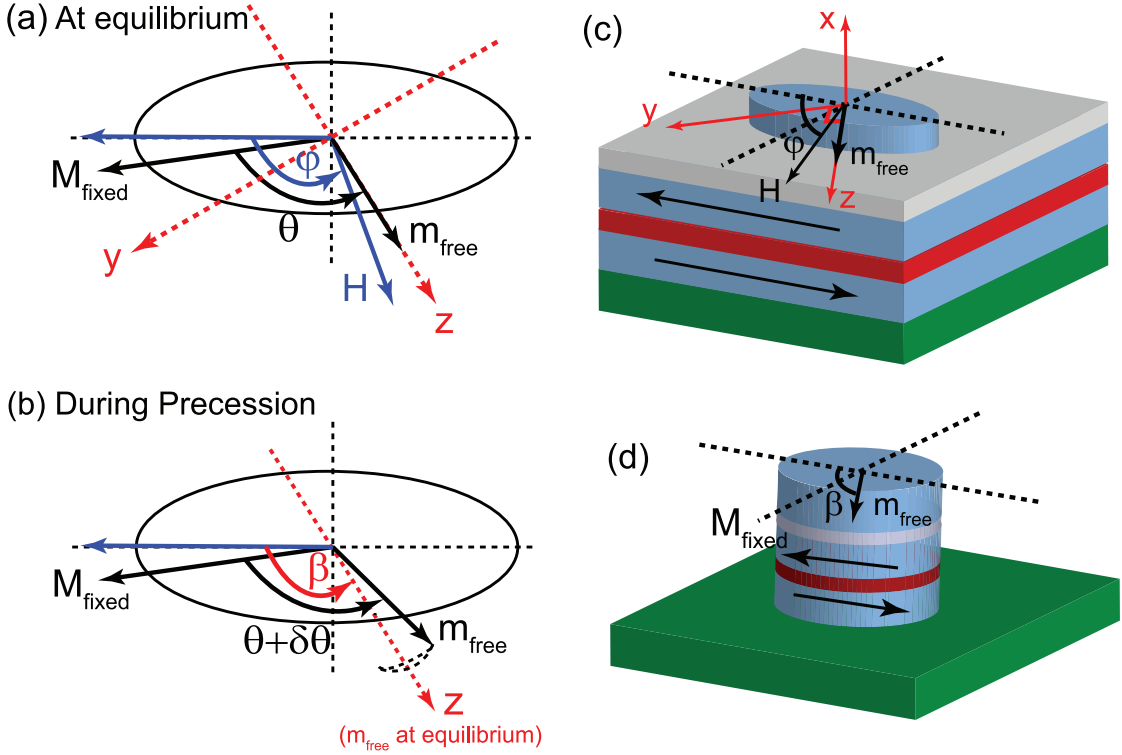


Figure 2.4: (a) Definition of the coordinate system. The z axis is defined as the equilibrium direction of the precessing layer moment m_{free} . (b) Schematic of the free-layer precession. The precession axis may be slightly misaligned from the z axis when the terms Eq. (2.19d)–(2.19g) in Eq. (2.19) are considered. (c) Schematic geometry for our samples with $RA = 12 \Omega\mu\text{m}^2$. The free layer is etched into a rounded rectangle while the bottom pinned layers are left extended. (d) Schematic geometry for our samples with $RA = 1.5 \Omega\mu\text{m}^2$. The synthetic antiferromagnetic pinned layers are etched, as well as the top free layer.

SAF structure] are etched into a circular shape with diameter nominally 90 nm [Fig. 2.4(d)]. These samples are similar to the devices studied by Kubota *et al.* [79] both in the value of RA ($12 \Omega\mu\text{m}^2$) and in that the pinned SAF electrode is etched. The insulator to the side of these devices is aluminum oxide, and top contact is made with Au.

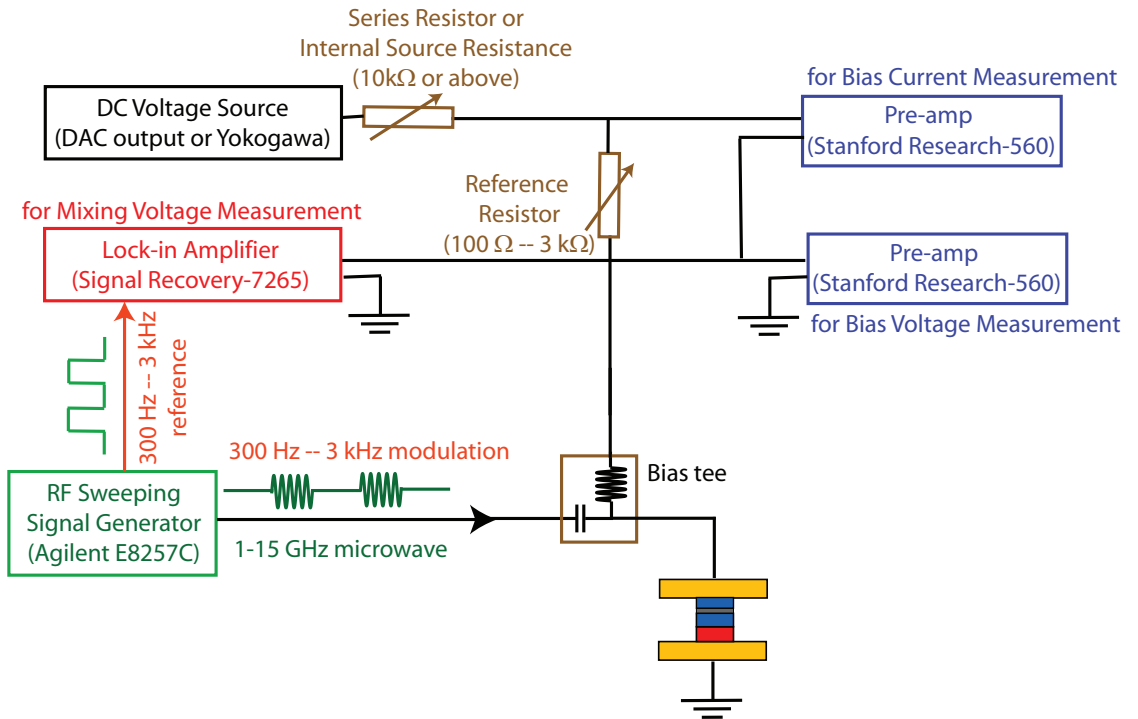


Figure 2.5: Schematic circuit for DC-detected ST-FMR measurements.

2.2.2 Measurement Circuit and Methods

A schematic circuit for our ST-FMR measurement is shown in Fig. 2.5. We use an Agilent E8257C sweeping signal generator (“sweeper”) as the RF current source in the frequency range of 1 GHz to 15 GHz. This RF output is chopped (switched on and off) at a selected modulation frequency between 300 Hz and 3 kHz. A DC bias current/voltage is provided by either a Yukogawa 7651 DC power supply or one of the voltage output channels from the computer DAQ. The RF and DC currents are combined through a Picosecond Pulse Labs 5541A bias-tee and applied to the MTJ device. A lock-in amplifier measures the mixing voltage from the device at the (300 Hz – 3 kHz) modulation frequency. Two preamps are used to monitor the DC voltages on the MTJ device and a calibrated reference resistor respectively, with the later converted to the DC current of the

device.

In order to study the differential spin transfer torque at various offset angles, θ (between fixed layer and free layer), we perform our measurement on the projected field magnet probe station in D-10 Clark Hall and apply an external magnetic field \vec{H} within the plane of the magnetic layers along various directions, φ , defined relative to the exchange-bias direction. It should be noted that the sample has to be placed at the calibrated center position of the probe station (within 1 or 2 mm) to receive pure in-plane field. To measure the ST-FMR spectrum, we keep the applied magnetic field and the bias voltage constant, and measure the mixing voltage, V_{mix} , while sweeping the frequency, f , of the RF current with the sweeping mode of the Agilent E8257C signal generator. The instant frequency during the sweep is read from a “sweep out” voltage output channel on the sweeper. One could also probe ST-FMR by sweeping magnetic field while fixing the frequency, but the offset angle and device impedance will change during the sweep, which will make the data analysis a lot more complex and obscure. Therefore we adopt the first method for our measurements.

RF Flatness Procedure

Since the mixing voltage is proportional to the RF current squared (I_{RF}^2 , see Eq. (2.19) in the next section), the measured ST-FMR spectrum (V_{mix} vs f) needs to be normalized by I_{RF}^2 to account for any variation of I_{RF} during the frequency sweep. Generally speaking, the magnitude of RF current always varies during the frequency sweep due to 1) the frequency-dependent transmission loss in the microwave cables that leads to a decay of microwave power at higher frequencies and 2) the existence of impedance discontinuities in the microwave

circuit that produce standing waves that lead to oscillation of I_{RF} as a function of f with period of a few 10's of MHz. One can simply account for this effect in data analysis by dividing a measured spectrum by a separately measured baseline. However, a better solution is to eliminate this variation in measurements in the first place. This can be done by “flatness correction” using the internal “flatness” function of the sweeper. J. C. Sankey briefly described the calibration of RF current and the use of flatness correction in the supplementary material of ref. [76] and his thesis [75]. To measure I_{RF} , we apply an external magnetic field \vec{H} high enough so that all ST-FMR resonances have frequencies higher than the range of interest, and then measure the ST-FMR spectrum at a fixed DC bias, which shows a non-resonant background rectification signal from the I-V nonlinearity of the device:

$$\langle V_{background} \rangle = \frac{1}{4} \frac{\partial^2 V}{\partial I^2} I_{RF}^2 \quad (2.4)$$

We calculate a correction factor as a function of f from this background, and feed it to the sweeper numerically, and the sweeper will adjust its output power to “flatten” the real RF current applied to the device. There are a few tricks related to this flatness process. Firstly, one-time correction is usually not enough, and one needs to do multiple iterations to achieve good flatness. Moreover, the sweeper tends to “under-correct” using the exact numbers from the previous run, especially at higher output powers, so when calculating the numerical arrays for flatness correction, one can deliberately somewhat “over-correct” by a factor of 1.2-1.5. Secondly, if correction for the standing wave oscillations is desired, one needs to sweep slowly (99 s or 200 s per cycle as the maximum allowed by the slightly different models of our available Agilent sweepers), and take flatness correction points as dense as 5 or 10 MHz per point. Thirdly, there is a small delay between the instant rectification voltage and the

lock-in reading related to the time constant setting on the lock-in. For signal stability we typically use about 50 ms for time constant, which is comparable or even longer than the data acquisition time for each flatness correction point. Therefore, one has to take account of this delay by universally shifting the numerical correction array by certain amount on frequency, otherwise the flatness may get divergently worse after iterations.

Mixing Voltage Adjustment

One would naively assume the voltage displayed on the lock-in amplifier (in Fig. 2.5) can be immediately used as the DC mixing voltage, V_{mix} , arising from the applied RF current, I_{RF} . However, there are two adjustment to be considered. The first adjustment is a constant pre-factor that is relatively straightforward: one has to take into account the mechanism of lock-in integration versus the chopping of RF current. As shown Fig. 2.6(a), the chopping of RF current produces a square-shaped step voltage (red), and the magnitude of this step voltage is the mixing voltage produced by the RF current. On the other hand, what the lock-in measures is the Fourier component of the signal at the lock-in frequency, which is the RMS amplitude of an equivalent sinusoidal AC voltage (blue). The peak-peak value of this equivalent AC voltage is equal to $\frac{\pi}{2}V_{mix}$, and the measured lock-in voltage is therefore $\frac{\pi}{4\sqrt{2}}V_{mix}$.

The second adjustment can be illustrated by the effective circuit shown by Fig. 2.6(b). As far as the mixing voltage is concerned, the MTJ device is essentially a battery providing a voltage at the lock-in frequency in the circuit. There are three relevant impedance elements in the circuit: 1) the internal resistance of the “battery” (resistance of the MTJ device), 2) a resistive “load”

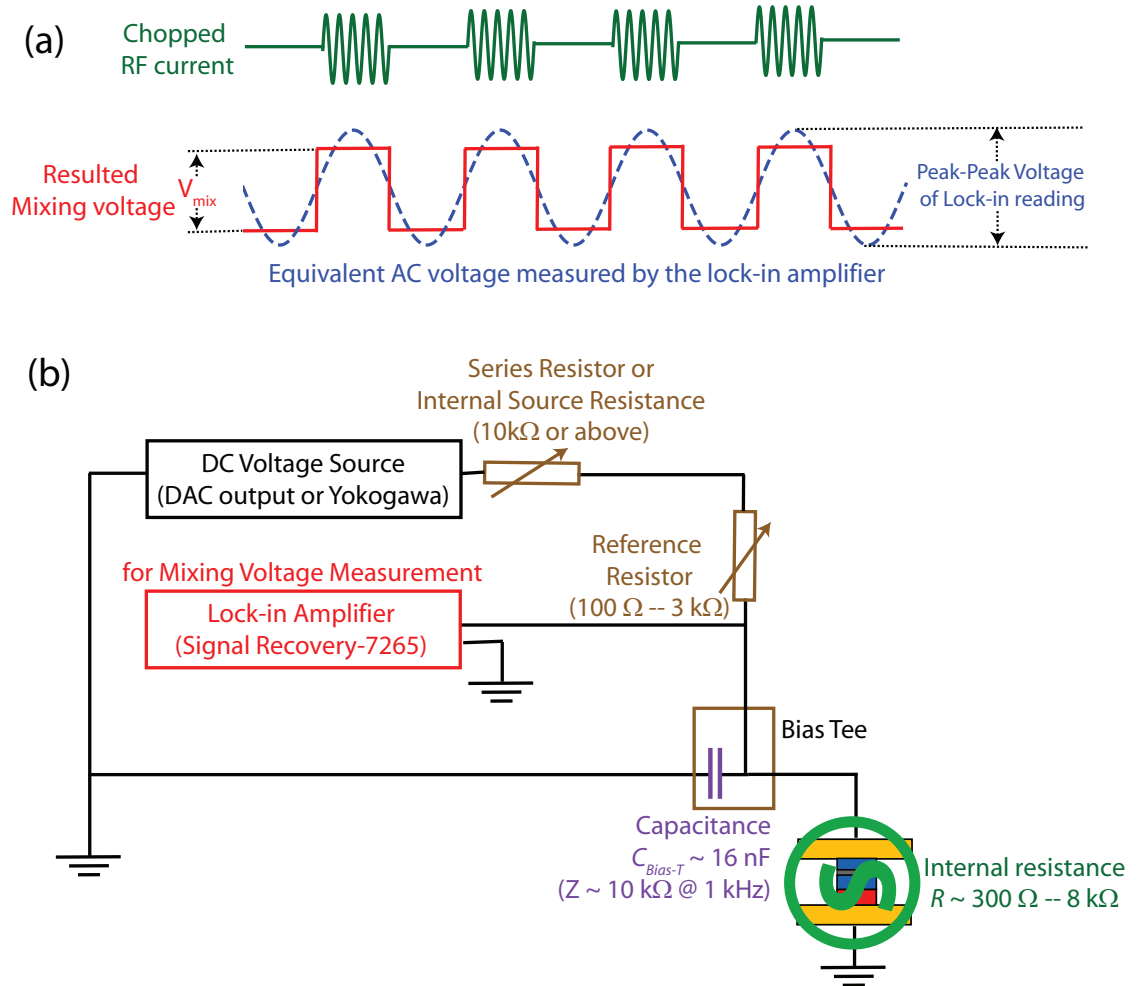


Figure 2.6: Illustrations of two adjustment factors for mixing voltage measurement. (a) Conversion from measured RMS lock-in voltage to the step voltage. (b) Adjustment for voltage drop absorbed by the device itself.

composed of our reference resistor, any other resistors connected in series and the internal resistance of our DC power supply at lock-in frequency, 3) a “leakage” capacitance from the bias tee. Only when the combined resistive and capacitive load is much larger (essentially an open circuit) compared with the resistance of the device does the lock-in accurately measure the full mixing voltage produced by the devices. This condition approximately holds for low resistance devices ($R \ll 1 \text{ k}\Omega$), but for high resistance devices, especially the first type of MTJ samples ($\text{RA}=12\Omega\mu\text{m}^2$ from IBM), the mixing voltage lost to the

internal resistance of the device has to be taken into account. By using a near-ideal constant current source for DC biasing one can achieve effectively infinite resistive load on the low frequency line. However, the capacitance of the bias tee is hard to eliminate. The Picosecond Pulse Lab 5541A bias tee has a capacitance around 16 nF, corresponding to an impedance of about $10\text{ k}\Omega$ at 1 kHz, and the bias tees from Mini-circuit are worse. One can reduce the lock-in frequency to mitigate this effect, but empirically below 500 Hz one starts to get higher noise. The approach I took is simply adjusting numerically in data analysis based on the internal loss ratio calculated from the circuit parameters. The effect does not depend on the RF frequency and therefore does not change the shape of the ST-FMR spectrum, but one has to keep in mind that this adjustment ratio depends on the resistance of the MTJ, which is bias and angular dependent.

2.2.3 ST-FMR Spectra and Uncorrected Spin Transfer Torkance

I will report data from a single $50 \times 100\text{nm}^2$ sample (sample #1) of the first type on MTJs with $\text{RA} = 12\text{ }\Omega\mu\text{m}^2$ and another sample (sample #2) of the second type with $\text{RA} = 1.5\text{ }\Omega\mu\text{m}^2$, but the results from all of the devices within each type were similar. Sample #1 had a zero-bias resistance of $3.9\text{ k}\Omega$ in the parallel state and a tunneling magnetoresistance ratio of 160%. (This resistance is greater than for the sample in ref. [76], $3.19\text{ k}\Omega$, with the consequence that the torkances we report for sample #1 are smaller than in ref. [76] by a factor of approximately $3.19/3.9 = 0.8$.) Sample #2 had a zero-bias resistance of $279\text{ }\Omega$ in the parallel state and a tunneling magnetoresistance ratio of 92%. In our ST-FMR measurements, we always keep the magnitude of the RF current relatively low ($< 10\mu\text{A}$ for sample #1 and $< 100\mu\text{A}$ for sample #2), resulting in an average precession angle

$< 1^\circ$. All the measurements were done at room temperature.

ST-FMR spectra

Figure Fig. 2.7(a) shows measured ST-FMR resonance peaks at selected values of θ for sample #1. In each spectrum we observe only a single large resonance. Each resonance can be fit accurately by a sum of symmetric and antisymmetric Lorentzians with a frequency-independent background. For sample #2, in contrast to sample #1, we always observe two closely-spaced peaks in the ST-FMR spectra [Fig. 2.7(b)]. We attribute this difference to the fact that the pinned electrode in sample #2 is etched, while the pinned magnetic electrode in sample #1 is left as an un-etched extended film. This etching leaves the upper CoFeB layer within the CoFe/Ru/CoFeB SAF in sample #2 free to precess in response to a spin torque (in addition to the free layer), giving a second resonant mode. Coupling between the two modes has the potential to alter the magnitudes and the line-shapes of ST-FMR resonances in ways that are not included in our model. In an attempt to minimize such coupling effects, when analyzing the data from sample #2 we have selected values of magnetic field (both magnitude and angle) to maximize the frequency difference between the two resonances. However, we do not claim that coupling effects are entirely absent.

As discussed in ref. [76] and in our previous section, the FMR line-shape at a given bias voltage reflects the direction of the spin transfer torkance. It is clear from Fig. 2.7(a) that the spin transfer torkance is purely in-plane at zero bias ($V = 0$), as predicted for a symmetric MTJ [81], and acquires a perpendicular component at non-zero biases. Moreover the sign of the asymmetry for the antisymmetric Lorentzian component changes with the sign of bias, reflecting

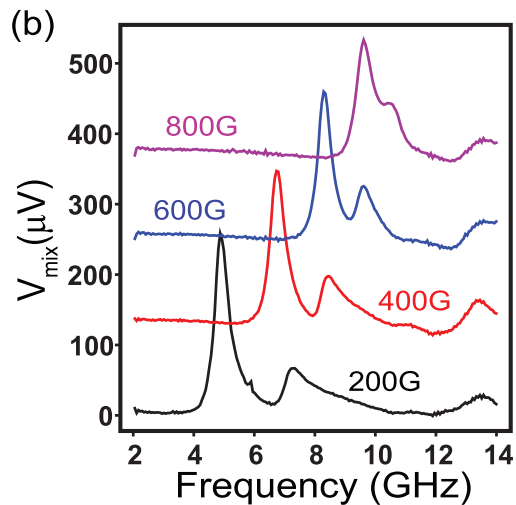
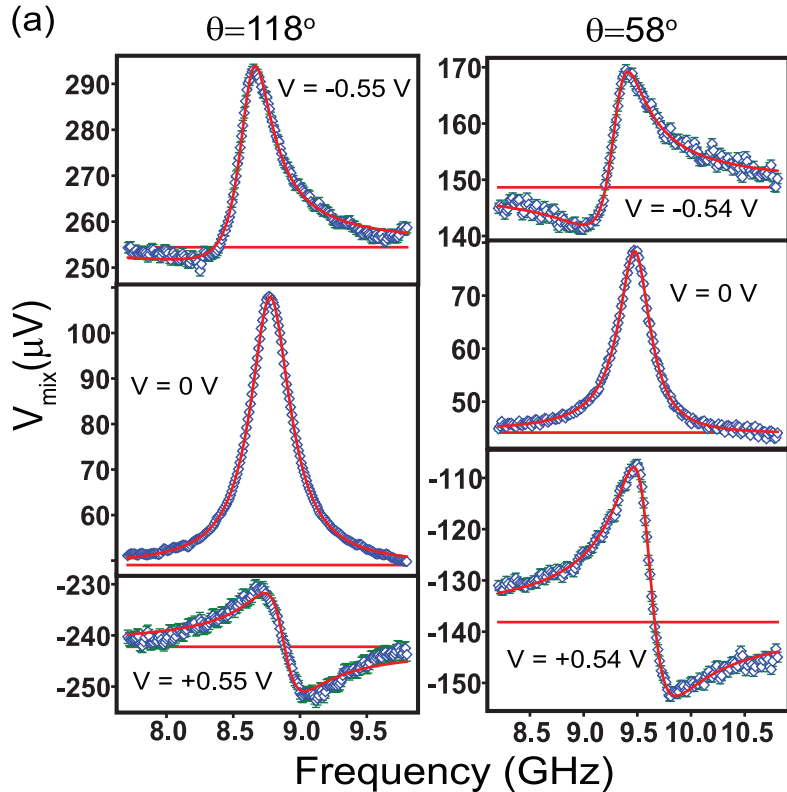


Figure 2.7: (a) Measured ST-FMR spectra from sample #1 at negative, zero, and positive biases for offset angles of $\theta = 115^\circ$ and 58° , with fits to sums of symmetric and antisymmetric Lorentzians. (b) Measured ST-FMR spectra from sample #2 at zero bias with magnetic fields of various magnitudes applied in the $\varphi = 130^\circ$ direction. The spectra for sample #2 show two closely spaced peaks, suggesting the existence of precessional dynamics in both the free magnetic layer and the etched synthetic antiferromagnet pinned layer.

different sign for the perpendicular torkance for different polarities of current. We use the sign convention that positive current is defined such that electrons flow from the top (free) layer to the pinned layer.

More quantitatively, the measured DC mixing voltage across the MTJ can be related to the spin transfer torkance base on the formalism from ref. [76]

$$V_{mix} = \frac{1}{4} \frac{\partial^2 V}{\partial I^2} I_{RF}^2 + \frac{\partial^2 V}{\partial I \partial \theta} \frac{\hbar \gamma \sin \theta}{4eM_s V_{free} \sigma} I_{RF}^2 [\xi_{||} S(\omega) - \xi_{\perp} \Omega_{\perp} A(\omega)] \quad (2.5)$$

Here $\xi_{||} = [(2e/\hbar)/\sin \theta]d\tau_{||}/dI$ and $\xi_{\perp} = [(2e/\hbar)/\sin \theta]d\tau_{\perp}/dI$ represent the differential torque in dimensionless units, $S(\omega) = 1/[1 + (\omega - \omega_m)^2/\sigma^2]$ and $A(\omega) = [(\omega - \omega_m)/\sigma]S(\omega)$ are symmetric and anti-symmetric Lorentzians, σ is the linewidth of the ST-FMR spectrum, ω_m is the resonant precession frequency, and $\Omega_{\perp} = \gamma(4\pi M_{eff} + H)/\omega_m$ is a dimensionless factor ($\approx 3 - 8$) describing the ellipticalness of the precession trajectory in our experiments.

Calibration procedures

In order to calculate the spin transfer torkance based on Eq. (2.5), we need to calibrate the various derivative quantities $\partial^2 V / \partial I^2$, $\partial^2 V / \partial I \partial \theta$, etc. This is done by measuring $\partial V / \partial I$ over a range of biases and angles using a lock-in amplifier, integrating to determine V vs I , determining θ by assuming that the angular dependence of the zero-bias conductance is proportional to $\cos \theta$ and that θ does not change with bias, and then calculating the necessary terms numerically. (Within the voltage range we investigated, for $H \geq 250$ Oe, the DC spin torque due to the DC bias should change θ by less than 1° for sample #1 and less than 3° for sample #2.)

As in ref. [76], we use $M_s V_{free} = 1.06 \times 10^{14}$ emu ($\pm 15\%$), $M_s = 1100$

emu/cm³, and $4\pi M_{eff} = 11 \pm 1$ kOe for sample #1. For sample #2 we use $M_s V_{free} = 1.8 \times 10^{14}$ ($\pm 15\%$) based on the measured value for the magnetization per unit area ($\langle M_s \rangle = 3.2 \times 10^{-4}$ emu/cm²) and our estimate of the sample area from scanning electron microscopy. The true area of the free layers in both types of devices is less than the nominal lithography dimensions because the sidewalls of the device are not vertical. We estimate $4\pi M_{eff} = 13 \pm 1$ kOe for sample #2 by comparing our measured FMR frequency at zero bias to the textbook Kittel frequency.

Uncorrected Torkance

Following Eq. (2.5) (as was done in ref. [76] and ref. [79]), the in-plane and perpendicular torkances $d\tau_{||}/dV$ and $d\tau_{\perp}/dV$ can be determined separately from the frequency-symmetric and antisymmetric components of each resonance (Fig. 2.8). For sample #1, as the offset angle between the electrode magnetizations is varied from 58° to 131°, the in-plane component of this uncorrected torkance changes continuously from the form reported previously at Cornell [76] (approximately independent of bias for $|V| < 0.3$ V and increasing at higher bias for both signs of V) to a form that is strongly asymmetric in bias (increases sharply at negative bias), similar to the results of ref. [79]. The torkances for sample #2, with the much lower value of RA, show a very similar evolution as a function of θ . We therefore conclude that the dramatic difference between the two previous experimental results (refs. [76] and [79]) is a consequence of the use of different initial offset angles (50°-90° in the Cornell report [76], 137° in the AIST Japan's report [79]).

This dramatically different bias dependence for different angles was ob-

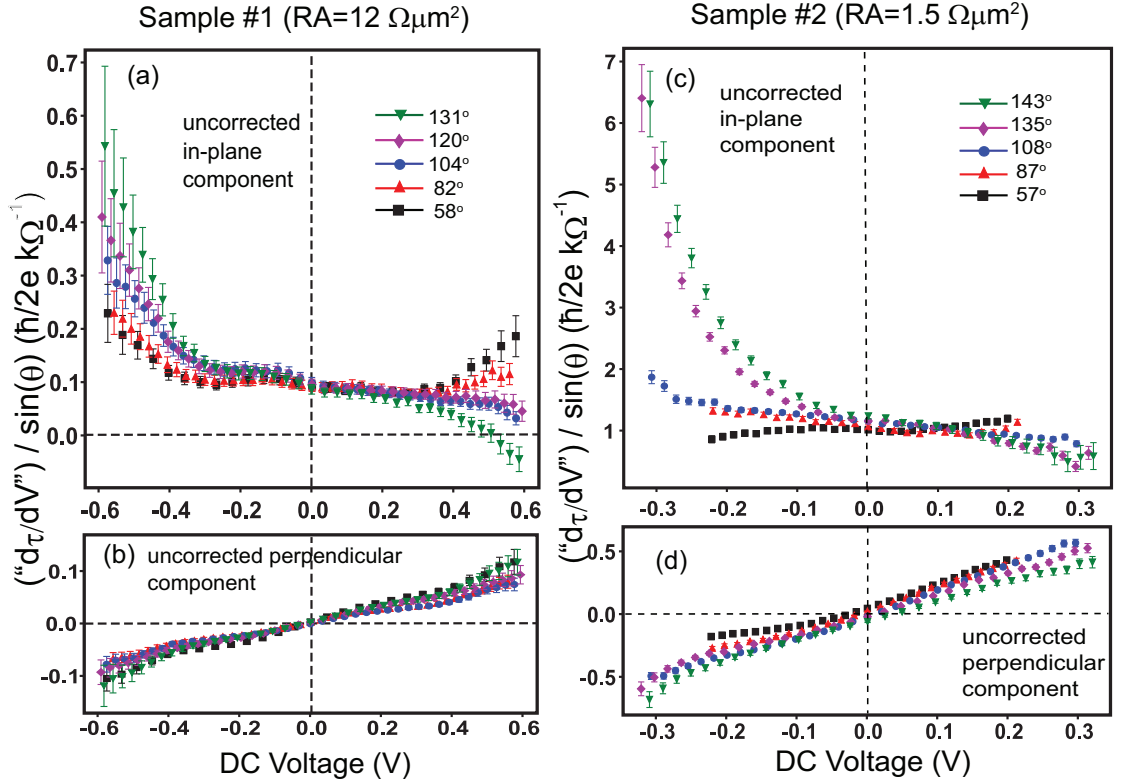


Figure 2.8: Bias dependence of the uncorrected (a) in-plane and (b) perpendicular torkances for sample #1 and uncorrected (c) in-plane and (d) perpendicular torkances for sample #2 at several different offset angles, θ , respectively. The different offset angles are achieved by different combinations of applied field magnitude and direction. For sample #1, for $\theta = 131^\circ$, $H = 0.38$ kOe with $\varphi = 120^\circ$, giving $\beta = 142^\circ$; for $\theta = 120^\circ$, $H = 0.40$ kOe with $\varphi = 110^\circ$, giving $\beta = 133^\circ$; for $\theta = 104^\circ$, $H = 0.75$ kOe with $\varphi = 130^\circ$, giving $\beta = 142^\circ$; for $\theta = 82^\circ$, $H = 1.00$ kOe with $\varphi = 120^\circ$, giving $\beta = 129^\circ$; for $\theta = 58^\circ$, $H = 1.00$ kOe with $\varphi = 90^\circ$, giving $\beta = 96^\circ$. For sample #2, for $\theta = 143^\circ$, $H = 0.25$ kOe with $\varphi = 150^\circ$; for $\theta = 135^\circ$, $H = 0.25$ kOe with $\varphi = 140^\circ$; for $\theta = 108^\circ$, $H = 0.30$ kOe with $\varphi = 125^\circ$; for $\theta = 87^\circ$, $H = 0.20$ kOe with $\varphi = 85^\circ$; for $\theta = 57^\circ$, $H = 0.30$ kOe with $\varphi = 55^\circ$. The value of β is not needed in the calculations for sample #2 because its cross section is circular.

served in every sample and had puzzled us for quite a few months. All the existing theories predict that the spin transfer torque in magnetic tunnel junctions has an angular dependence of $\sin \theta$. This is a quite general conclusion as long as there is no spin-orbit mixing in the tunneling matrix, *i.e.* the tunneling probability between an electronic state in one electrode and another electronic state in the other can be separately evaluated by their orbital overlap and spin state overlap. We had to decide whether there exists an unexpected tunneling mechanism or the ST-FMR did not produce reliable results for the spin transfer torque. There are reasons for me to have more faith in $\sin \theta$ than the torkances measured so far (Fig. 2.8). Firstly, if there is indeed a tunneling mechanism that mixes up the orbit states and the spin states, the tunneling magnetoconductance should no longer follow $\cos \theta$. However, even at the biases where Fig. 2.8 suggests a complete breakdown of $d\tau/dV \propto \sin \theta$, we did not see clear violation of $dI/dV = A + B \cos \theta$. Secondly, the largest torkance at high negative bias displayed on Fig. 2.8 far exceeds $\hbar/2$ per electron, which is highly unlikely. This does not immediately violate conservation of angular momentum, because the electrons can draw extra angular momentum from one electrode to supply the other, which seems to be confirmed by the negative torkances on high positive bias, but the numbers don't add up quantitatively. Later we found out and we will argue below that the apparent variation as a function of offset angle shown in Fig. 2.8 does not reflect the true, correct values of the spin-transfer torkances, but that it is an artifact of neglecting additional contributions to the measured mixing voltage arising from a change of average resistance of the device due to precession.

2.3 Quantitative Modeling of DC-detected ST-FMR within the Macrospin Approximation

In this section, we reexamine the various contributions to the measured mixing voltage V_{mix} in our experiment. We provide a more general model of the mixing voltage signal compared with the Supplementary material of the early Cornell work [76]. This section is mostly adapted from the Appendix of our published work [80], but has corrected a couple of typos and taken into account that the directions of the in-plane and out-of-plane components of the spin torque vector will rotate slightly relative to the sample axes as the free layer undergoes small-angle precession. We were able to correctly include this effect in a later publication [82].

In our macrospin (single-domain) model, we consider the pinned layer completely fixed, and only consider the precession of the free layer in response to the time dependent current described by Eq. (2.1), $I(t) = I + \delta I(t) = I + I_{RF} \text{Re}(e^{i\omega t})$. The precession can be described as a time series of the relative angle, $\theta(t)$, between the free layer and fixed layer

$$\theta(t) = \theta + \delta\theta(t) \quad (2.6)$$

Taking a Taylor expansion on the voltage, $V(t)$, across MTJ as a function of current $I(t)$, and relative angle $\theta(t)$, the leading order contributions to the DC mixing voltage are

$$V_{mix} = \frac{1}{2} \frac{\partial^2 V}{\partial I^2} \langle (\delta I(t))^2 \rangle + \frac{\partial^2 V}{\partial I \partial \theta} \langle (\delta I(t))(\delta\theta(t)) \rangle + \frac{1}{2} \frac{\partial^2 V}{\partial \theta^2} \langle (\delta\theta(t))^2 \rangle + \frac{\partial V}{\partial \theta} \langle \delta\theta(t) \rangle \quad (2.7)$$

The $I - V$ characterization and the TMR properties of the tunnel junction are included implicitly by various partial derivatives of voltage in Eq. (2.7), all of

which need to be measured for each device, in general. Treating resistance R explicitly in equations would not help simplify expressions, since the resistance is just a secondary concept V/I or $\partial V/\partial I$ and has an equally undetermined dependence $R(I, \theta)$ on both current I and angle θ that needs to be calibrated.

We assume that the magnetic moment of the free layer has a constant magnitude $M_S V_{free}$ and we denote its instantaneous direction by the unit vector $\hat{\mathbf{m}}(t)$. As shown in Fig. 2.4(a) and (b), we define \hat{z} as the equilibrium direction of the free layer (and assume that it is within the plane of the thin-film sample to a good approximation even at non-zero bias V), \hat{x} as the direction perpendicular to the film plane, and \hat{y} is the in-plane direction satisfying $\hat{z} = \hat{x} \times \hat{y}$. At the equilibrium position, the free layer direction is $\hat{\mathbf{m}} = (0, 0, 1)$. We assume that the reference magnetic layer remains fixed in the in-plane direction $\hat{\mathbf{M}} = (0, \sin \theta, \cos \theta)$. Small-angle precession of the free layer in response to a DC + oscillatory current $I(t) = I + \delta I(t) = I + \delta I \text{Re}(e^{i\omega t})$ can be expressed in the form $\hat{\mathbf{m}} = (m_x(t), m_y(t), \sqrt{1 - (m_x(t))^2 - (m_y(t))^2})$, where

$$\begin{aligned} m_x(t) &= m_{x0} + \text{Re}(m_{x1} e^{i\omega t}) + \text{Re}(m_{x2} e^{2i\omega t}) + \dots \\ m_y(t) &= m_{y0} + \text{Re}(m_{y1} e^{i\omega t}) + \text{Re}(m_{y2} e^{2i\omega t}) + \dots \end{aligned} \quad (2.8)$$

Here m_{x0} and m_{y0} are real numbers, and $m_{x1}, m_{y1}, m_{x2}, m_{y2}$ are complex. We expect the oscillation to be harmonic to the first order in δI , so all of the coefficients except m_{x1} and m_{y1} should be at least second order in δI .

Because of the large magnetic anisotropy of the thin film sample, the precession amplitude is much larger in the in-plane direction than the out-of-plane direction, *i.e.*, $|m_x| \ll |m_y|$. Therefore the time-dependent offset angle $\theta(t)$ during the precession is approximately determined by m_y , or $\delta\theta \approx -m_y$.

Therefore the measured mixing voltage signal expressed by Eq. (2.7) becomes:

$$V_{mix} = \frac{1}{4} \frac{\partial^2 V}{\partial I^2} I_{RF}^2 - \frac{1}{2} \frac{\partial^2 V}{\partial I \partial \theta} I_{RF} \operatorname{Re}(m_{y1}) + \frac{1}{2} \frac{\partial^2 V}{\partial \theta^2} |m_{y1}|^2 - \frac{\partial V}{\partial \theta} m_{y0} \quad (2.9)$$

Within the macrospin approximation, the dynamics of the free layer moment is governed by the Landau-Lifshitz-Gilbert-Slonczewski (LLGS) equation [Eq. (1.4)]. If we include the perpendicular (field-like) component of the spin torque in MTJs, $\tau_\perp(V, \theta)$, together with the in-plane (Slonczewski) component of the spin torque, $\tau_\parallel(V, \theta)$, as a function of voltage and offset angle between the two layers, the LLGS equation reads

$$\frac{d\hat{\mathbf{m}}}{dt} = -\gamma \hat{\mathbf{m}} \times \vec{H}_{eff} + \alpha \hat{\mathbf{m}} \times \frac{d\hat{\mathbf{m}}}{dt} + \gamma \frac{\tau_\parallel(V, \theta)}{M_s V_{free}} \hat{\mathbf{m}} \times \frac{\hat{\mathbf{m}} \times \hat{\mathbf{M}}}{|\hat{\mathbf{m}} \times \hat{\mathbf{M}}|} + \gamma \frac{\tau_\perp(V, \theta)}{M_s V_{free}} \frac{\hat{\mathbf{m}} \times \hat{\mathbf{M}}}{|\hat{\mathbf{m}} \times \hat{\mathbf{M}}|} \quad (2.10)$$

where $\gamma = 2\mu_B/\hbar$ is the absolute value of the gyromagnetic ratio, and α is the Gilbert damping coefficient, $\vec{H}_{eff} = \vec{H}_{demag} + \vec{H}_{dip} + \vec{H}_{app}$ is the total effective field acting on the free layer, including the demagnetizing field \vec{H}_{demag} , the dipole field \vec{H}_{dip} from the pinned layer, and the external applied field \vec{H}_{app} . We assume that the dipole field and the external field both have orientations within the sample plane as appropriate in our measurement. We use H_y and H_z to denote the y and z components of the sum of these two fields, *i.e.* $\vec{H}_{dip} + \vec{H}_{app} = H_y \hat{y} + H_z \hat{z}$. The demagnetizing field consists of a large perpendicular-to-the-plane component $-m_x 4\pi M_{eff} \hat{x}$ favoring an easy-plane anisotropy plus a smaller component $-m_{hard} H_{anis} \hat{d}_{hard}$ favoring the easy axis within the sample plane. Here $m_{hard} = -m_y \cos \beta + m_z \sin \beta$ is the component of $\hat{\mathbf{m}}$ along the hard in-plane magnetic direction $\hat{d}_{hard} = -\hat{y} \cos \beta + \hat{z} \sin \beta$, where β is the angle between \hat{z} axis and the magnetic easy axis [Fig. 2.4(a)]. The total demagnetizing field depending on the instantaneous direction of the precessing

moment therefore has the form

$$\begin{aligned}\vec{H}_{demag} = & -m_x 4\pi M_{eff} \hat{x} - (m_y \cos \beta - m_z \sin \beta) (\cos \beta) H_{anis} \hat{y} \\ & + (m_y \cos \beta - m_z \sin \beta) (\sin \beta) H_{anis} \hat{z}\end{aligned}\quad (2.11)$$

At equilibrium the total effective field must be along z axis, giving the constraint
 $H_y + H_{anis} \sin \beta \cos \beta = 0$.

For small RF excitation voltages, the magnitude of the spin-torque components can be Taylor-expanded,

$$\begin{aligned}\tau_{||}(I + \delta I(t), \theta + \delta \theta(t)) = & \tau_{||}(I, \theta) + \frac{\partial \tau_{||}}{\partial I} \delta I(t) + \frac{\partial \tau_{||}}{\partial \theta} \delta \theta(t) \\ & + \frac{1}{2} \frac{\partial^2 \tau_{||}}{\partial I^2} \delta I^2(t) + \frac{\partial^2 \tau_{||}}{\partial I \partial \theta} \delta I(t) \delta \theta(t) + \frac{1}{2} \frac{\partial^2 \tau_{||}}{\partial \theta^2} \delta \theta^2(t) \\ \tau_{\perp}(I + \delta I(t), \theta + \delta \theta(t)) = & \tau_{\perp}(I, \theta) + \frac{\partial \tau_{\perp}}{\partial I} \delta I(t) + \frac{\partial \tau_{\perp}}{\partial \theta} \delta \theta(t) \\ & + \frac{1}{2} \frac{\partial^2 \tau_{\perp}}{\partial I^2} \delta I^2(t) + \frac{\partial^2 \tau_{\perp}}{\partial I \partial \theta} \delta I(t) \delta \theta(t) + \frac{1}{2} \frac{\partial^2 \tau_{\perp}}{\partial \theta^2} \delta \theta^2(t)\end{aligned}\quad (2.12)$$

The directions of the torque components also change slightly during precession,

$$\begin{aligned}\hat{\mathbf{m}} \times \frac{\hat{\mathbf{m}} \times \hat{\mathbf{M}}}{|\hat{\mathbf{m}} \times \hat{\mathbf{M}}|} = & -\hat{y} + [m_x \cot \theta + m_x m_y (1 + \cot^2 \theta)] \hat{x} + (m_y - m_x^2 \cot \theta) \hat{z} \\ \frac{\hat{\mathbf{m}} \times \hat{\mathbf{M}}}{|\hat{\mathbf{m}} \times \hat{\mathbf{M}}|} = & -\hat{x} - (m_x \cot \theta + m_x m_y \cot^2 \theta) \hat{y} + (m_x + m_x m_y \cot \theta) \hat{z}\end{aligned}\quad (2.13)$$

to second order in m_x and m_y . After substituting Eq. (2.12) and Eq. (2.13) into

Eq. (2.10), the time-dependent part is, to first order,

$$\begin{aligned}
\frac{dm_x(t)}{dt} = & -\gamma m_y(t) N_y M_{eff} - \alpha \frac{dm_y(t)}{dt} \\
& + \frac{\gamma}{M_s V_{free}} \left[\tau_{||} m_x(t) \cot \theta - \frac{\partial \tau_{\perp}}{\partial I} \delta I(t) - \frac{\partial \tau_{\perp}}{\partial \theta} m_y(t) \right] \\
& - \frac{3}{2} m_y^2(t) \gamma H_{anis} \sin \beta \cos \beta + \frac{\gamma}{M_s V_{free}} \left[\tau_{||} m_x(t) m_y(t) (1 + \cot^2 \theta) \right] \\
& - \frac{\gamma}{M_s V_{free}} \left[\frac{1}{2} \frac{\partial^2 \tau_{\perp}}{\partial I^2} \delta I^2(t) - \frac{\partial^2 \tau_{\perp}}{\partial I \partial \theta} \delta I(t) m_y(t) + \frac{1}{2} \frac{\partial^2 \tau_{\perp}}{\partial \theta^2} m_y^2(t) \right] \\
\frac{dm_y(t)}{dt} = & \gamma m_x(t) N_y M_{eff} + \alpha \frac{dm_x(t)}{dt} \\
& - \frac{\gamma}{M_s V_{free}} \left[\frac{\partial \tau_{||}}{\partial I} \delta I(t) - \frac{\partial \tau_{||}}{\partial \theta} m_y(t) + \tau_{\perp} m_x(t) \cot \theta \right] \\
& - m_x(t) m_y(t) \gamma H_{anis} \sin \beta \cos \beta - \frac{\gamma}{M_s V_{free}} \left[\tau_{\perp} m_x(t) m_y(t) \cot^2 \theta \right] \\
& - \frac{\gamma}{M_s V_{free}} \left[\frac{1}{2} \frac{\partial^2 \tau_{||}}{\partial I^2} \delta I^2(t) - \frac{\partial^2 \tau_{||}}{\partial I \partial \theta} \delta I(t) m_y(t) + \frac{1}{2} \frac{\partial^2 \tau_{||}}{\partial \theta^2} m_y^2(t) \right]
\end{aligned} \tag{2.14}$$

where $N_x = 4\pi + (H_z - H_{anis} \sin^2 \beta)/M_{eff}$ and $N_y = (H_z + H_{anis} \cos 2\beta)/M_{eff}$ for our sample geometry. Then, substituting Eq. (2.8) into Eq. (2.14), collecting the terms for different frequency components, and solving these equations for m_{y1} and m_{y0} , we have

$$m_{y1} = \frac{\gamma I_{RF}}{2M_s V_{free}} \frac{1}{(\omega - \omega_m - i\sigma)} \left[i \frac{\partial \tau_{||}}{\partial I} + \frac{\gamma N_x M_{eff}}{\omega_m} \frac{\partial \tau_{\perp}}{\partial I} \right] \tag{2.15}$$

$$\begin{aligned}
m_{y0} = & -\frac{1}{N_y M_{eff}} \frac{1}{M_s V_{free}} \left(\frac{1}{4} \frac{\partial^2 \tau_{\perp}}{\partial I^2} I_{RF}^2 - \frac{1}{2} \frac{\partial^2 \tau_{\perp}}{\partial I \partial \theta} \text{Re}(m_{y1}) I_{RF} + \frac{1}{4} \frac{\partial^2 \tau_{\perp}}{\partial \theta^2} |m_{y1}|^2 \right) \\
& - \frac{1}{N_y M_{eff}} \frac{3}{4} H_{anis} \sin \beta \cos \beta |m_{y1}|^2
\end{aligned} \tag{2.16}$$

Here, the resonance precession frequency is

$$\omega_m \approx \gamma M_{eff} \sqrt{N_x \left(N_y - \frac{1}{M_{eff} M_s V_{free}} \frac{\partial \tau_{\perp}}{\partial \theta} \right)} \tag{2.17}$$

and the linewidth is

$$\sigma \approx \frac{\alpha \gamma M_{eff} (N_x + N_y)}{2} - \frac{\gamma}{2M_s V_{free}} \left[\frac{\partial \tau_{||}}{\partial \theta} + \tau_{||} \cot \theta \right] \tag{2.18}$$

Substituting Eq. (2.16) and Eq. (2.15) into Eq. (2.9), we arrive at the full expression for the DC mixing voltage up to second order in I_{RF} in ST-FMR measurement:

$$V_{mix} = \frac{1}{4} \frac{\partial^2 V}{\partial I^2} I_{RF}^2 \quad (2.19a)$$

$$+ \frac{\partial^2 V}{\partial I \partial \theta} \left(\frac{\hbar \gamma \sin \theta}{4eM_s V_{free} \sigma} \right) I_{RF}^2 [\xi_{||} S(\omega) - \xi_{\perp} \Omega_{\perp} A(\omega)] \quad (2.19b)$$

$$+ \frac{\partial^2 V}{\partial \theta^2} \left(\frac{\hbar \gamma \sin \theta}{4eM_s V_{free} \sigma} \right)^2 I_{RF}^2 [\xi_{||}^2 + \xi_{\perp}^2 \Omega_{\perp}^2 S(\omega)] \quad (2.19c)$$

$$+ \frac{3}{8} \frac{\partial V}{\partial \theta} \frac{H_{anis} \sin 2\beta}{H_z + H_{anis} \cos 2\beta} \left(\frac{\hbar \gamma \sin \theta}{4eM_s V_{free} \sigma} \right)^2 I_{RF}^2 [\xi_{||}^2 + \xi_{\perp}^2 \Omega_{\perp}^2 S(\omega)] \quad (2.19d)$$

$$+ \frac{\partial V}{\partial \theta} \frac{1}{M_s V_{free} (H_z + H_{anis} \cos 2\beta)} \left\{ \frac{1}{4} \frac{\partial^2 \tau_{\perp}}{\partial I^2} I_{RF}^2 \right. \quad (2.19e)$$

$$\left. + \frac{1}{2} \frac{\partial^2 \tau_{\perp}}{\partial I \partial \theta} \left(\frac{\hbar \gamma \sin \theta}{4eM_s V_{free} \sigma} \right) I_{RF}^2 [\xi_{||} S(\omega) - \xi_{\perp} \Omega_{\perp} A(\omega)] \right\} \quad (2.19f)$$

$$+ \frac{1}{4} \frac{\partial^2 \tau_{\perp}}{\partial \theta^2} \left(\frac{\hbar \gamma \sin \theta}{4eM_s V_{free} \sigma} \right)^2 I_{RF}^2 [\xi_{||}^2 + \xi_{\perp}^2 \Omega_{\perp}^2 S(\omega)] \quad (2.19g)$$

where $\xi_{||} = (2e/\hbar \sin \theta)(dV/dI)d\tau_{||}/dV$ and $\xi_{\perp} = (2e/\hbar \sin \theta)(dV/dI)d\tau_{\perp}/dV$ represent the in-plane and out-of-plane torkances in dimensionless units, $S(\omega) = [1 + (\omega - \omega_m)^2/\sigma^2]^{-1}$ and $A(\omega) = [\omega - \omega_m/\sigma]S(\omega)$ are the symmetric and anti-symmetric components of the line-shape, with ω_m the resonance frequency as shown in Eq. (2.17), σ the linewidth shown in Eq. (2.18), and $\Omega_{\perp} = \gamma N_x M_{eff}/\omega_m$ is the same dimensionless factor as in Eq. (2.5), describing the ellipticalness of the precession trajectory ($\approx 3 - 8$) in our experiments.

2.4 Bias and Angular Dependence of the Spin Transfer Torque

2.4.1 Discussion of the Artifact Terms

Equation (2.19) includes seven terms in total. Eq. (2.19a) is a frequency-independent background voltage from the rectification effect due to the $I - V$ nonlinearity, which we use to calibrate the RF current as discussed in the last section. Eq. (2.19b) is the major mixing voltage term that we used to calculate the spin transfer torque shown in Fig. 2.8. Only these two terms are shown in Eq. (2.5) and included in the analysis in ref. [76] and ref. [79]. Eq. (2.19c) arises at non-zero bias caused by a change of average resistance of the device due to precession. This is because the $R \sim \theta$ relation is generally nonlinear ($R(\theta + \delta\theta) + R(\theta - \delta\theta) \neq 2R(\theta)$), so there is a rectification effect when the free layer precesses, which translates into a voltage at non-zero bias [Fig. 2.9(a)]. Eq. (2.19d) describes another effect causing a change of average resistance during precession, which comes from asymmetric precession around the equilibrium axis due to the shape anisotropy [Fig. 2.9(b)]. In other words, the precession axis is not exactly the equilibrium axis, \hat{z} . Instead it is slightly shifted towards the magnetic easy axis. The other three corrections Eq. (2.19e)–(2.19g) in Eq. (2.19) describes another in-plane shift of precession axis to counter-balance a change of average perpendicular torque during the precession.

In Fig. 2.9(c) and (d) we plot estimates of the contributions to the ST-FMR signal from the terms Eq. (2.19c) and Eq. (2.19d) for sample #1, normalized by the part of the direct mixing contribution (the term Eq. (2.19b)) proportional to $S(\omega)$. The terms Eq. (2.19c) and Eq. (2.19d) are negligible for $|V| < 0.10$ V for sample #1, give 10-20% corrections for $0.10 \text{ V} < |V| < 0.30$ V, and can grow to

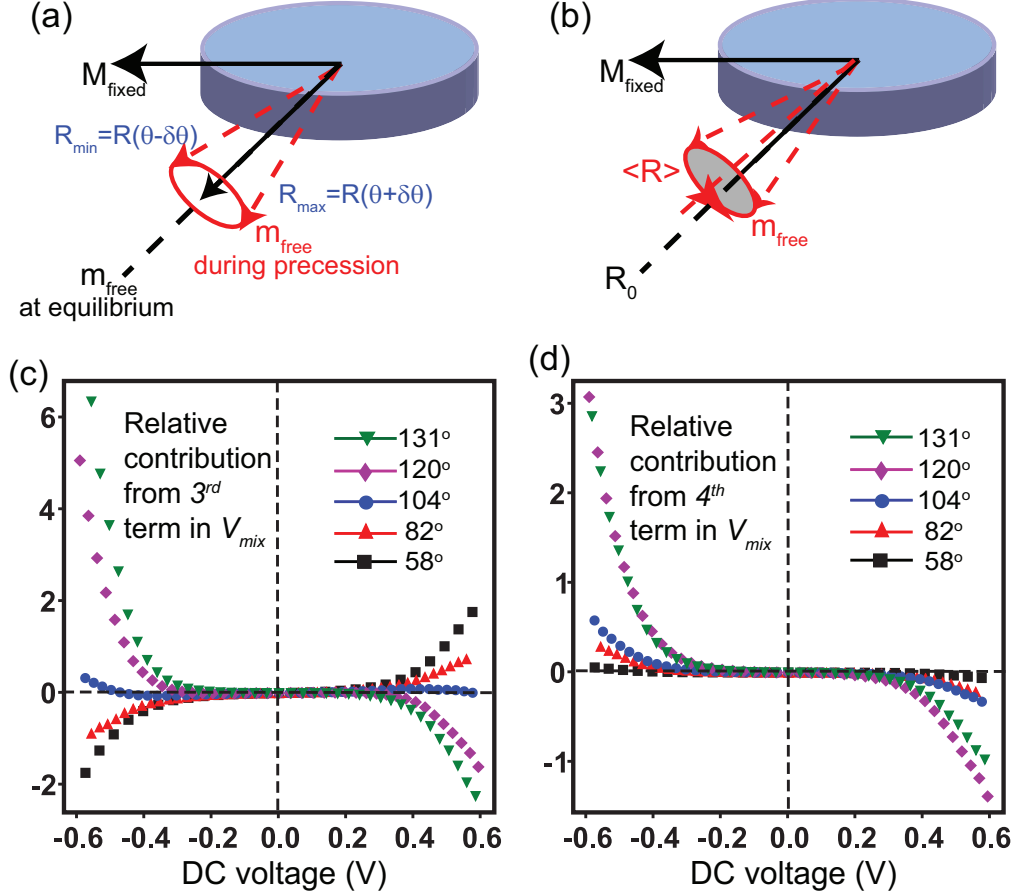


Figure 2.9: (a, b) Illustration of the term Eq. (2.19c) (a) and term Eq. (2.19d) (b) that contribute to the measured ST-FMR mixing voltage signal. (c, d) Estimated magnitudes of (c) the term Eq. (2.19c) and (d) the term Eq. (2.19d), relative to the frequency-symmetric part of the direct mixing signal [term Eq. (2.19b)]. The angles in the legends are the initial offset angles, θ . In both (c) and (d), we assume for simplicity that the in-plane torkance is a constant $d\tau_{||}/dV = 0.10(\hbar/2e)\text{k}\Omega^{-1}$ and the perpendicular torkance has a constant slope $d^2\tau_{\perp}/dV^2 = 0.16(\hbar/2e)\text{k}\Omega^{-1}\text{V}^{-1}$.

be larger than the direct mixing contribution for $|V| > 0.4$ V. Both terms also depend strongly on the offset angle, with particularly large corrections for large θ , near antiparallel alignment. The other three terms are generally negligible when $H \geq 1$ kOe, but they may be as large as 20% of V_{mix} under very weak fields and high bias. We find that the terms Eq. (2.19c) and Eq. (2.19d) have the correct bias dependence (both terms are asymmetric in bias) and sufficient

magnitude to fully explain the strongly-asymmetric bias dependence seen for larger θ in Fig. 2.8(a). For the circular sample #2, the term Eq. (2.19d) is zero since H_{anis} is negligible, but the term Eq. (2.19c) has a significant amplitude relative to the direct mixing contribution for $|V| > 0.1$ V, and can explain the large asymmetric dependence seen for large θ in Fig. 2.8(b).

2.4.2 Corrected Spin Transfer Torkance

An improved measurement of $d\vec{\tau}/dV$ as a function of bias can be obtained by including all of the terms in Eq. (2.19) in the analysis. After doing so, our revised measurements of the spin-transfer torkances are plotted in Fig. 2.10(a,b) for sample #1 and Fig. 2.10(c,d) for sample #2. Theory predicts that both $d\tau_{||}/dV$ and $d\tau_{\perp}/dV$ should be proportional to $\sin \theta$, so when these quantities are normalized by $\sin \theta$ as in Fig. 2.10, they should collapse onto single curves for each sample [81]. We find that including all of the terms from Eq. (2.19) does improve the quality of the collapse for $(d\tau_{||}/dV)/\sin \theta$ for a significant range of $|V|$. For sample #1 in the range $|V| < 0.35$ V the spread in values becomes less than 15%, comparable to the estimated uncertainty [see the inset in Fig. 2.10(a)]. In Fig. 2.10(e) we show in more detail the degree to which the extracted values of $(d\tau_{||}/dV)/\sin \theta$ in the range $|V| < 0.3$ V are modified for sample #1 when the contributions of the correction terms are accounted for. For sample #2, the quality of the data collapse is likewise significantly improved in the range $|V| < 0.15$ V.

For higher biases, for $|V| > 0.3$ V for sample #1 or for $|V| > 0.15$ V for sample #2, the corrected values of $(d\tau_{||}/dV)/\sin \theta$ differ strongly from Fig. 2.8, but the

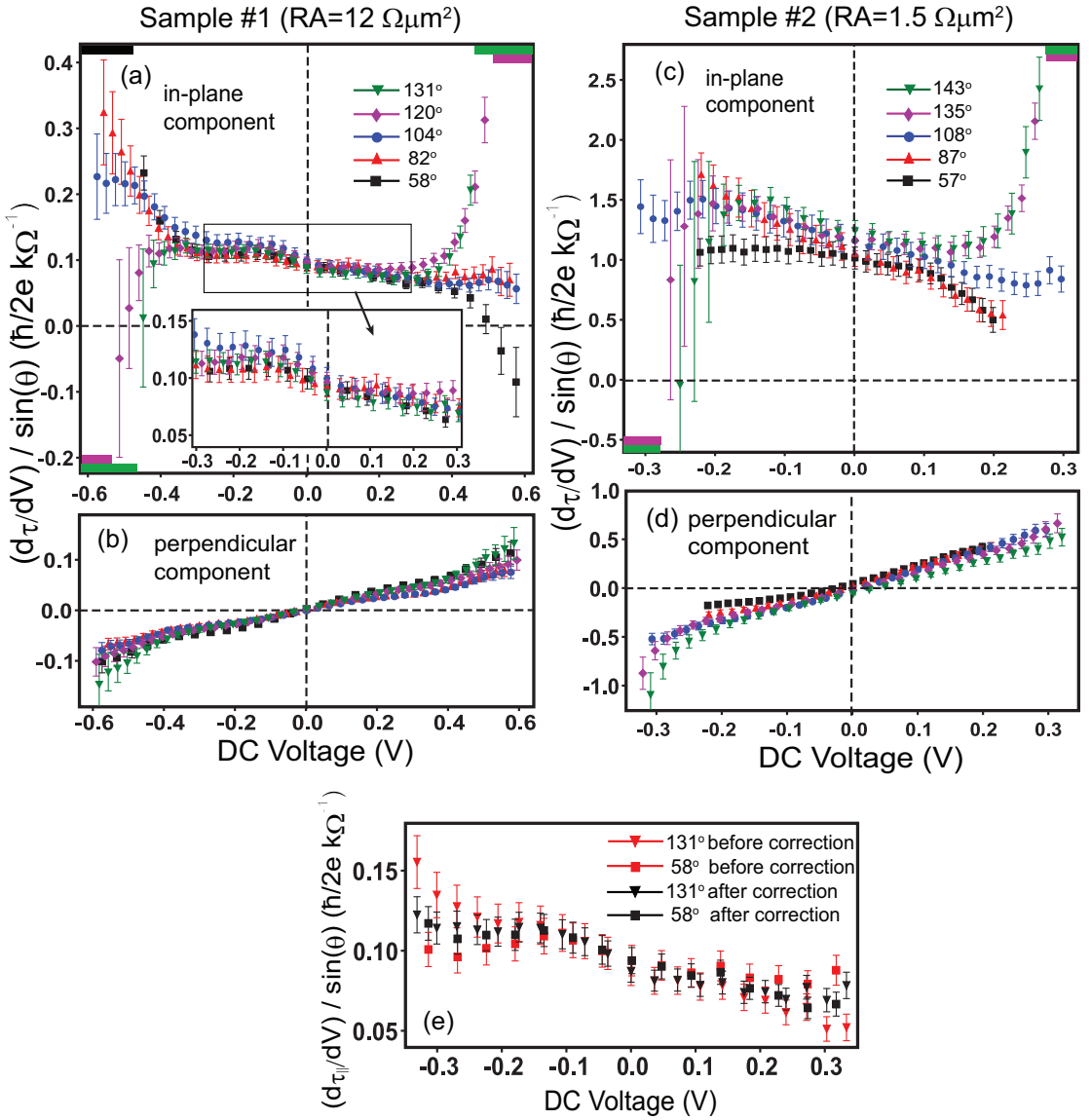


Figure 2.10: Bias dependence of the (a) in-plane and (b) perpendicular torkances for sample #1 and (c) in-plane and (d) perpendicular torkances for sample #2 from an analysis that includes all of the contributions to the ST-FMR signal in Eq. (2.19) at several different offset angles, θ , as listed on the legend. The corresponding values of H , φ and β are listed in the caption of Fig. 2.8. At the largest values of $|V|$ for some angles there is no real-valued solution for $d\tau_{||}/dV$ based on Eq. (2.19) and our ST-FMR data, and we have marked these regimes with bars along the top or bottom axes in (a) and (c). (e) Uncorrected and corrected determinations of the in-plane component of the torkance for sample #1 for two values of the initial offset angle between the electrode magnetizations, $\theta = 58^\circ$ and 131° . Note that there is better consistency between the measurements for the two angles after the correction.

results for different values of θ are not consistent. Moreover, at high bias for some values of θ there is no real-valued solution for $(d\tau_{||}/dV)/\sin \theta$ based on Eq. (2.19). We conclude from these results that the ST-FMR technique does not give reliable values of the torkances at very large biases. As can be seen in Fig. 2.9, at large $|V|$ the artifacts that result from the changing DC resistance [the terms Eq. (2.19c) and Eq. (2.19d)] grow rapidly to become larger than the mixing term [Eq. (2.19b)] from which the torkances are extracted. Therefore at high bias even small uncertainties in the calibrations of $\partial^2 V/\partial\theta^2$ (10-20%) and $\partial^2 V/\partial I\partial\theta$ (5-20%) can prevent an accurate subtraction of the artifacts, and the desired mixing signal cannot be isolated. Effects of heating and inelastic scattering, which are not included in Eq. (2.19), might also affect the measurements for large $|V|$.

The primary discrepancy between the results of the previous ST-FMR experiments concerned the bias dependence of the in-plane torkance, $d\tau_{||}/dV$. After our correction, we observe a moderate bias dependence consistent for all angles in the bias ranges where our calibrations are accurate, with $(d\tau_{||}/dV)/\sin \theta$ decreasing by 35 ± 10 % from $V = -0.3$ V to $V = 0.3$ V for sample #1, and with the same quantity decreasing by 30 ± 15 % from $V = -0.15$ V to $V = 0.15$ V for sample #2. This is a much weaker variation than for the "uncorrected" torkances at large values of θ [Figs. 2.8(a) and (c)], although it is stronger than originally reported in ref. [76].

In contrast to the in-plane component of the spin-transfer torkance, the bias dependence that we measure for the perpendicular component, $d\tau_{\perp}/dV$, displays only a small correction after including the additional terms in Eq. (2.19). In agreement with the previous ST-FMR experiments [76, 79] we find that to a

good approximation $d\tau_{\perp}/dV \propto V$, so that after integrating we have $\tau_{\perp}(V) \approx A_0 + A_1 V^2$, with A_0 and A_1 constants (differing for different samples). The bias-dependent part of this torque in our experiments is in the $+\hat{m} \times \hat{M}_{fixed}$ direction for both signs of bias, meaning that the “effective field” on the precessing moment due to the spin-transfer torque is oriented antiparallel to \hat{M}_{fixed} . The magnitude of $d\tau_{\perp}/dV$ can become comparable to $d\tau_{||}/dV$ at high bias, so that this in-plane torque may certainly be significant for technological applications.

2.4.3 Discussions and Comparisons to Theories and Other Experiments

Our measured spin transfer torque in magnetic tunnel junctions can be compared to several theoretical models. Theodosis and collaborators [81] have calculated the bias dependence of the spin transfer torques in MTJs within a tight-binding model of the electron bands, and Xiao, Bauer, and Brataas [83] have calculated the torques within the Stoner model by scattering theory. In comparing to the experiments, these groups have focused to a significant extent on explaining the strongly asymmetric-in-bias dependence of the type present in the “uncorrected” curves for large θ in Fig. 2.8(a, c) and reported by Kubota et al [79]. As we have explained above, we argue that these strong asymmetries in the torkance are an artifact of neglecting significant terms in the analysis for the ST-FMR signal at high bias, and that the true values of the in-plane torkances are only moderately bias dependent in both types of MTJs that we have measured throughout the bias range in which the measurements are trustworthy. We do not claim that either the tight-binding or Stoner calculations

are necessarily inaccurate, but we suggest that the parameter regimes in which they predict a strongly asymmetric bias dependence for $d\tau_{||}/dV$ are not the correct regimes for analyzing the existing experiments. Heiliger and Stiles have calculated the bias dependence of the spin transfer torkances by an *ab initio* Green's function approach for an Fe/MgO/Fe MTJ [84]. They plotted $\tau_{||}(V)$ and $\tau_{\perp}(V)$ in Fig. 4(a) of ref. [84]; we show the corresponding values of $d\tau_{||}/dV$ and $d\tau_{\perp}/dV$ in Fig. 2.11 after converting to the same units we use for our experimental data and assuming the same device area as for sample #1 (3.9×10^3 nm 2). The agreement between the form of the calculated bias dependence and the measurements is excellent, including even the existence of a small negative slope in the dependence of $d\tau_{||}/dV$ on V. In the calculation, $d\tau_{||}/dV$ decreases by $\sim 60\%$ between -0.5 V and 0.5 V, the same relative slope per unit voltage measured for our sample #1 (a decrease of $35 \pm 10\%$ between $V = 0.3$ V and 0.3 V).

In regard to the absolute magnitude of the in-plane torkance, the average value that we measure for $(d\tau_{||}/dV)/\sin \theta$ near $V = 0$ is 0.10 ± 0.02 ($\hbar/2e$)kΩ $^{-1}$ for sample #1 and 1.1 ± 0.2 for sample #2. For a symmetric magnetic tunnel junction, the zero bias value of $(d\tau_{||}/dV)/\sin \theta$ is predicted to be: [85]

$$\frac{d\tau_{||}/dV}{\sin \theta} = \frac{\hbar}{4e} \frac{2P}{1 + P^2} \left(\frac{dI}{dV} \right)_P \quad (2.20)$$

where $(dI/dV)_P$ is the conductance for parallel magnetic electrodes. Evaluating Eq. (2.20) for a spin polarization factor $P = 67\%$ and $(dI/dV)_P = 3.9$ kΩ appropriate for sample #1 gives $(d\tau_{||}/dV)/\sin \theta = 0.12$ ($\hbar/2e$)kΩ $^{-1}$. Therefore for this sample our measured torkance at $V = 0$ agrees with Eq. (2.20) within the experimental uncertainty associated with our estimate of the sample volumes. The result of Heiliger and Stiles (Fig. 2.11) is also in good accord with Eq. (2.20): given the calculated polarization ($P \sim 1$) and RA product (~ 14.5 Ωμm 2) of

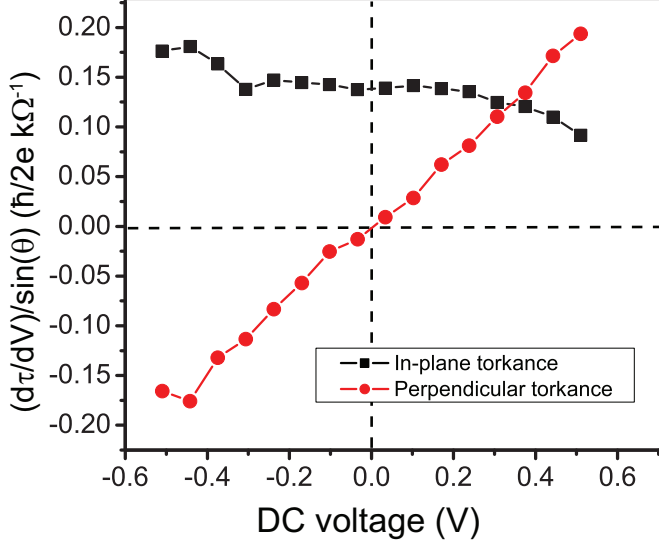


Figure 2.11: The in-plane and perpendicular torkances for an $RA \approx 14.5 \Omega\mu\text{m}^2$ Fe/MgO/Fe tunnel junction calculated in ref. [84] using an *ab initio* multiple-scattering Green’s function approach. The points are determined by numerical differentiation of the data in Fig. 4(a) of ref. [84]. We have converted to the units we use in describing the experiments assuming that the device area is the same as for sample #1 ($3.9 \times 10^3 \text{ nm}^2$).

their junction, together with the device area of sample #1, we have $(dI/dV)_P = 0.27 \text{ k}\Omega^{-1}$ so that Eq. (2.20) predicts $(d\tau_{||}/dV)/\sin \theta = 0.13 (\hbar/2e)\text{k}\Omega^{-1}$, to be compared to the value of $0.14 (\hbar/2e)\text{k}\Omega^{-1}$ from the *ab initio* calculation. However, for our sample #2, using the values $P = 56\%$ and $(dI/dV)_P = 279 \Omega$, Eq. (2.20) predicts $(d\tau_{||}/dV)/\sin \theta = 1.52 (\hbar/2e)\text{k}\Omega^{-1}$ at $V = 0$. This is approximately 40% larger than the value of the in-plane torkance extracted from the ST-FMR measurement for sample #2. While this difference could be interpreted as casting doubt on the prediction of Eq. (2.20) for the lower-RA tunnel junction devices, we suspect that the discrepancy is due to coupling between the free layer and the top CoFeB layer within the CoFe/Ru/CoFeB SAF “pinned layer” in sample #2. If we assume that the larger, lower-frequency resonance peaks in Fig. 2.7(b) that we use in analyzing the torkance correspond to the acoustic mode in which these two layers precess with the same phase,

coupled motion of these layers would reduce the mixing voltage because the relative excitation angle would be reduced, thereby decreasing the size of the resistance oscillation. Coupling between the precessing layers may also be the reason that the measurements of $(d\tau_{||}/dV)$ at different values of θ for sample #2 in Fig. 2.10(c) show more of a spread than the corresponding data for sample #1 in Fig. 2.10(a). The degree of coupling via the magnetic dipole interaction should vary as a function of θ .

Our measured quadratic dependence on bias voltage for the perpendicular torque in our approximately symmetric tunnel junction can be qualitatively explained by a symmetry consideration. Without spin-flip scattering, conservation of angular momentum requires that, at any bias voltage, the perpendicular torque acting on the free layer $\tau_{m\perp}$ and the fixed layer $\tau_{M\perp}$ should be of the same magnitude and opposition sign,

$$\tau_{m\perp}(V) = -\tau_{M\perp}(V) \quad (2.21)$$

On the other hand, in a symmetric tunnel junction, the spin torque should operate on free layer at $-V$ in exactly the same way as it operates on the fixed layer at $+V$. Therefore,

$$\tau_{m\perp}(-V) = -\tau_{M\perp}(+V) \quad (2.22)$$

where the negative sign comes from the fact that $\vec{m} \times \vec{M} = -\vec{M} \times \vec{m}$. Combine the two equations, we get:

$$\tau_{m\perp}(V) = \tau_{m\perp}(-V) \quad (2.23)$$

Therefore the perpendicular component of spin torque is an even function of bias in symmetric MTJs, and a quadratic form is the lowest order Taylor expansion of such a bias dependence. It should be noted that Eq. (2.23)

can be violated when spin-flip scattering is considered, which allows angular momentum of electrons to be absorbed by lattices. While we do not claim such an effect is completely absent, there is little indication of significant spin-flip scattering (or spin relaxation) at ferromagnet/insulator interface in the existing literature, argued by Slonczewski [15]. Spin-flip scattering occurs in the bulk of the ferromagnets on the length scale of at least several nanometers (50 nm for Co and 5.5 nm for NiFe at low temperature [86]). This is much longer than the length scale relevant to spin transfer torque in magnetic tunnel junctions, which is only a few atomic layers near the tunnel barrier.

A different bias dependence for the perpendicular torkance has been suggested by Li *et al.*, based on the switching statistics of MTJs at high bias [40]. They argue that $d\tau_{\perp}/dV \propto |V|$, meaning that the bias-dependent part of $\tau_{\perp}(V)$ would change sign upon reversing the bias. However, this contradicts with the symmetry property of perpendicular torque in symmetric junctions discussed above [Eq. (2.23)] unless there is strong spin-flip scattering present. Li *et al.* also noted that their data could in principle be explained by an alternative mechanism – by a bias-dependent reduction of the within-plane magnetic anisotropy strength (H_K in ref. [40]) much stronger than one would expect from simple Ohmic heating. Li *et al.* argued that this scenario was unlikely, but more recent measurements by Sun *et al.* [87] suggest that indeed the within-plane magnetic anisotropy in MTJs can be much more strongly bias dependent than is expected from Ohmic heating. Therefore, in our opinion, the experiments of Li *et al.* are more likely to be explained by very strong variations in magnetic anisotropy rather than by a spin-transfer torkance of the form $d\tau_{\perp}/dV \propto |V|$.

In asymmetric MTJs where the two ferromagnetic electrodes are made

of different materials, the symmetry of the perpendicular spin torque can deviate substantially from Eq. (2.23). More recently Oh *et al.* [41] studied the perpendicular component of spin transfer torque in specially designed MTJs with the two ferromagnetic electrodes with different materials. They showed that the perpendicular spin torque has a linear component whose sign depends on the material asymmetry of the electrodes.

2.4.4 Bias Dependence of Effective Damping and Frequency

Up to this point of our analysis, we have focused on the magnitudes and the line-shapes of the ST-FMR resonances. The linewidths and center frequencies can also provide valuable information. The linewidth, σ , can be related to the magnetic damping via Eq. (2.18). In Fig. 2.12(a) we present for sample #1 the bias dependence of the effective damping defined as $\alpha_{eff} = 2\sigma / [\gamma M_{eff}(N_x + N_y)]$. From Eq. (2.18), and taking into account that $\tau_{||}(V, \theta) = \tau_{||,max}(V) \sin \theta$, where $\tau_{||,max}$ is the maximum torque at a given bias, V , (reached at $\theta = \pi/2$), our macrospin model predicts (a more rigorous version will be discussed in the next two chapters)

$$\alpha_{eff} \approx \alpha - \frac{2}{M_{eff}(N_x + N_y) M_s V_{free}} \tau_{||,max} \cos \theta \quad (2.24)$$

which reduces to the Gilbert damping α at $V = 0$ since the spin-torque is zero. We find a value for the Gilbert damping $\alpha = 0.010 \pm 0.002$ for sample #1, consistent for all angles, a value in agreement with previous studies [88, 89]. Theory predicts that $\tau_{||}(\theta, V) \propto \text{const}(V) \sin \theta$, so that the bias dependence of the effective damping should be small near $\theta = \pi/2$, negative for smaller angles, and positive for larger angles. The bias dependence predicted by Eq. (2.24) is

shown in Fig. 2.12(a) by the shaded regions, which depict the $\pm 15\%$ uncertainty associated with our determination of the sample volume. These center lines of these regions correspond to the average values $d\tau_{||}/dV$ determined above for sample #1 in the region $-0.3 \text{ V} < V < 0.3 \text{ V}$, and we have assumed a simple linear extrapolation to higher values of $|V|$. We find the slope of α_{eff} vs. V does indeed increase as a function of θ , qualitatively as expected, and passes through zero near $\theta = \pi/2$.

The bias dependent changes of the center frequency of the ST-FMR resonances for sample #1 is shown in Fig. 2.12(b) for the different offset angles, along with the values predicted by Eq. (2.17). In computing the predicted values, we have assumed that $d\tau_{\perp}/dV$ is linear in V over the entire bias range and that $d\tau_{\perp}/dV \propto \sin \theta$, we have used the average value of the slope determined above for sample #1, and then we integrated to determine $d\tau_{\perp}/d\theta$. We find that the measured frequency variation is in most cases much stronger than the variation expected to result from the measured value of the perpendicular torkance by itself, and is of a different functional form [Eq. (2.17) predicts a symmetric bias dependence]. Our interpretation of this result is that the influence of the perpendicular torkance on the precession frequency is so small that other bias-dependent effects are dominant. For example, Petit *et al.* have shown that heating effects can produce significant bias-dependent shifts in the precession frequency for aluminum-oxide-based MTJs [42]. We suspect that a combination of Ohmic and Peltier heating might explain the bias dependence of the frequency seen in Fig. 2.12(b). Spin-transfer associated with lateral spin diffusion, which can increase the degree of spatial nonuniformity of the precessional mode for one sign of bias and decrease the spatial nonuniformity for the other sign could also provide an asymmetric contribution to the bias

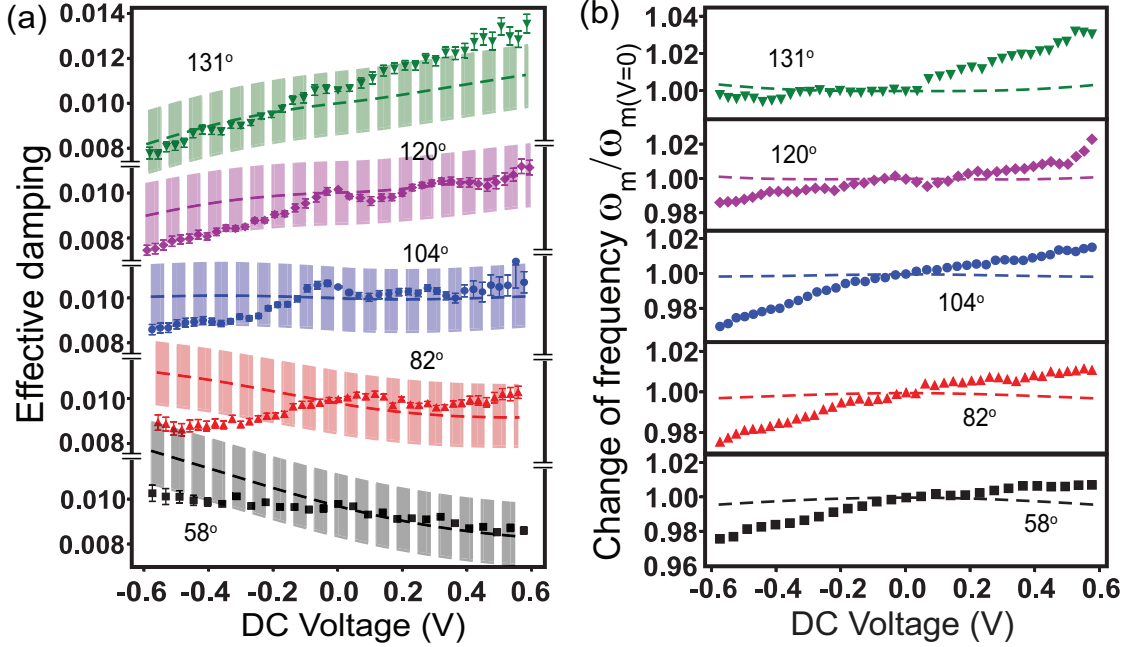


Figure 2.12: Bias dependence of (a) the effective damping and (b) the resonance frequency in ST-FMR measurements for sample #1 at various initial offset angles. The corresponding values of H , φ and β are listed in the caption of Fig. 2.8. The dashed lines represent the effective damping predicted by Eq. (2.24), with the Gilbert damping constant $\alpha = 0.010$ and a fit to the measured in-plane spin-transfer torkance. The shaded regions reflect a $\pm 15\%$ uncertainty in the value of $M_s V_{free}$. (b) The bias dependent change of the resonance frequency ω_m for various initial offset angles θ for sample #1. The lines show the bias-dependent changes predicted by Eq. (2.17), using the measured value of the perpendicular component of the spin-transfer torkance. The measured bias dependence is much greater than the small variation expected from Eq. (2.17), suggesting that other effects (e.g., heating) may dominate the bias dependence of ω_m , rather than spin torque being the only significant effect. The measured resonance frequencies at zero bias are: 9.47 GHz for $\theta = 58^\circ$, 9.68 GHz for $\theta = 82^\circ$, 8.93 GHz for $\theta = 104^\circ$, 5.81 GHz for $\theta = 120^\circ$, and 5.91 GHz for $\theta = 131^\circ$.

dependence to the precession frequency [90, 91]. Voltage-induced changes to magnetic anisotropy [69, 87] is another possible mechanism that can result in a bias dependence of resonance frequency. If we are correct that these other effects produce larger changes in the precession frequency than the perpendicular spin-transfer torkance, this would explain why previous experiments which attempted to determine the perpendicular spin-torque by measuring the bias

dependence of the frequency have reached conclusions that conflict with the ST-FMR measurements [42, 92].

Readers may be concerned that heating or these other effects might also affect the ST-FMR magnitude or line-shape significantly, thereby making our analysis [Eq. (2.19)] inaccurate and invalidating our determination of the torkances. However, we have calculated that at low bias simple heating should produce a much weaker relative effect on the ST-FMR magnitude and line-shape than on the frequency, and that any heating-induced ST-FMR signal should produce a different bias dependence than is observed at low $|V|$ (see the Supplementary Material in ref. [76]). At higher biases, where Eq. (2.19) ceases to describe the experiments accurately, heating effects may well influence the ST-FMR magnitudes and line-shapes.

For completeness, Fig. 2.13(a) and (b) show the bias dependence of the effective damping and the center frequency for sample #2. We see that the bias dependence of the the effective damping is well explained by the effect from the in-plane spin transfer torque. The original figures we published on Phys. Rev. B [Fig. 7(a) and 8(a) in ref. [80]] had an underestimate in the prediction of bias dependence of effective damping by a factor of 2 as we had pointed in last section. This has been corrected in this dissertation and improved the agreement between the measured effective damping and the prediction based on Eq. (2.24). The effective damping near zero bias is $\alpha = 0.014 \pm 0.002$, on the high end of the typical Gilbert damping 0.006-0.013 measured in CoFeB films [88, 89]. We suggest that this results from the same cause that we invoked to explain why the measured in-plane torkance for sample #2 is less than the value predicted by Eq. (2.20): coupling between the free layer and the top layer of the SAF.

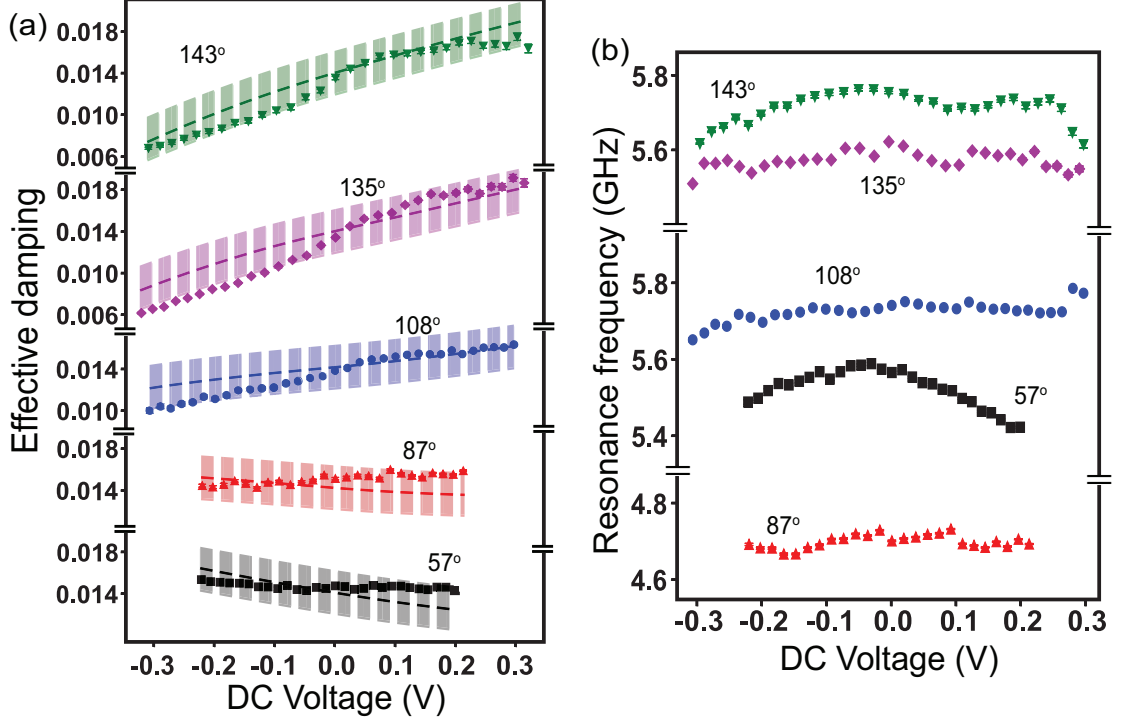


Figure 2.13: Bias dependence of (a) the effective damping and (b) the resonance frequency in ST-FMR measurements for sample #2 at various initial offset angles. The dashed lines represent the effective damping predicted by Eq. (2.24), with the Gilbert damping constant $\alpha = 0.014$ and a fit to the measured in-plane spin-transfer torkance. The shaded regions reflect a $\pm 15\%$ uncertainty in the value of $M_s V_{free}$. (b) The bias dependence of the resonance frequency ω_m for various initial offset angles θ for sample #2.

The increased effective volume of the two coupled layers may contribute to an overall increased damping. As for the bias dependence of the precession frequency [Fig. 2.13(b)], just as for sample #1 [Fig 2.12(b)], the measured bias dependence is stronger than the changes expected due to the perpendicular component of the spin torque by itself.

2.5 Summary

We have achieved improved measurements of the spin-transfer torkance, $d\vec{\tau}/dV$, in MgO-based MTJs by ST-FMR studies as a function of the offset angle θ and by accounting for all contributions to the ST-FMR signal of order I_{RF}^2 . We show that discrepancies between two previous measurements resulted from using different θ and neglecting angle-dependent contributions to the ST-FMR signal caused by changes in the DC resistance in response to I_{RF} . We believe that a very strongly asymmetric bias dependence for $d\tau_{||}/dV$ reported in ref. [79], which was claimed to support the predictions of tight-binding calculations [81], is an artifact of neglecting these contributions. After correcting for the additional terms, we find that the bias dependence of $d\tau_{||}/dV$ for both sets of MTJs that we have measured is weaker but still strong enough to be technologically relevant, varying by 30-35% in the range $|V| < 0.3$ V for samples with $RA = 12 \Omega\mu\text{m}^2$ and $|V| < 0.15$ V for samples with $RA = 1.5 \Omega\mu\text{m}^2$. These results appear to be in good accord with the ab initio calculations of ref. [84]. For larger values of $|V|$, the artifacts in the ST-FMR signal become so dominant that the extraction of torkance values by this technique becomes unreliable, which motivated us to find a new method to study ST-FMR and measure the spin transfer torque at high bias (see the next chapter). The perpendicular component $d\tau_{\perp}/dV$ is less affected by the correction terms than $d\tau_{||}/dV$. At high bias $d\tau_{\perp}/dV$ can become comparable to $d\tau_{||}/dV$, so that both components should be taken into account when modeling spin-torque dynamics in magnetic tunnel junctions.

CHAPTER 3

TIME-RESOLVED DETECTION OF SPIN-TRANSFER-DRIVEN FERROMAGNETIC RESONANCE

In the previous chapter we described the spin-transfer-driven ferromagnetic resonance (ST-FMR) technique based on DC mixing voltage detection, which allowed us to measure the spin transfer torque up to a moderate bias voltage. With careful modeling and analysis we were able to identify the cause of previous conflicting results [76, 79] regarding the bias dependence of spin transfer torque. However, as we concluded in Chapter 2, we were not able to quantitatively determine the spin transfer torkance vector for the high bias regime because the artifact voltage from the change of average resistance during precession becomes dominant at high bias [80]. On the other hand, it is the high bias regime that may provide a sensitive probe into the fundamental spin physics of hot electrons and is critical for applications. In this chapter, I present our experiment on time-resolved detection of spin-transfer-driven ferromagnetic resonance (ST-FMR), which for the first time allows us to quantitatively probe the spin torque in MgO-based MTJs in the high bias regime.

In this experiment, we detect the resistance oscillation due to the resonant magnetic precession in response to an oscillating spin torque in the time domain, which represents so far the most direct observation of ST-FMR. We directly determine the amplitude and phase of the resonant precession as a function of RF driving frequency, which we use to extract the spin transfer torque at various offset angles and bias voltages up to the breakdown voltage of the tunnel junctions. This technique has the benefit to detect directly small-angle linear-response magnetic dynamics caused by spin torque, and as a

result is relatively immune to artifacts affecting competing techniques. (Other methods to measure the spin torque [40–42, 92–96] suffer from various effects such as heating induced change of anisotropy, bias dependent non-uniform magnetic dynamics, etc.) At high bias we find that the spin-torque vector differs markedly from the simple lowest-order Taylor series approximations commonly assumed. The contents of this chapter are mostly adapted from work originally published as *Nature Phys.* 7, 496–501 (2011) [82].

3.1 Measurement Scheme and Data Processing for Time Domain ST-FMR

The concept of our technique is to apply a microwave current through the MTJ to exert an oscillating spin-transfer torque near the magnetic resonance frequency of one magnetic electrode, and to measure the resulting magnetic precession via oscillations of the MTJ resistance. Our measurement circuit is illustrated in Fig. 3.1. To accomplish the measurement, we apply two electrical pulses simultaneously to the MTJ via a 50Ω transmission line: a microwave (RF) pulse $V_{in}(t)$ with duration 5 - 10 ns, long enough to reach steady-state resonant magnetic precession via the spin-torque effect, together with a longer square-wave pulse (~ 25 ns duration) that starts a few nanoseconds earlier and ends several nanoseconds later than the RF pulse so that it provides the equivalent of a DC bias during the resonance measurement. We record the signal reflected from the sample using a 12.5 GHz bandwidth sampling oscilloscope. The time-dependent part of the reflected voltage (prior to amplification) is:

$$V_{ref}(t) = \frac{(50\Omega)}{R_0 + (50\Omega)} I \Delta R(t) + \frac{R_0 - (50\Omega)}{R_0 + (50\Omega)} V_{in}(t) \quad (3.1)$$

The first term on the right is the signal from the resistance oscillation that we aim to measure, with I the effective DC current through the device provided by the square pulse and $\Delta R(t)$ the time dependent part of the MTJ resistance. The second term arises from the reflection of $V_{in}(t)$ from the impedance discontinuity between the 50Ω cable and the sample with differential resistance R_0 [97]. One might consider trying to determine $\Delta R(t)$ by simply measuring the reflected signal during the time when $V_{in}(t)$ is nonzero, but the term due to the impedance discontinuity is generally 1-2 orders of magnitude larger than the term involving $\Delta R(t)$, and it is difficult to subtract this large background. Instead, we achieve a better signal-to-noise ratio by recording the reflected signal shortly (100 ps - 2 ns) after the falling edge of the RF pulse. In this time span, the resistance oscillation excited by the RF pulse (ST-FMR) is still present (although gradually decaying) while the strong background due to $V_{in}(t)$ is diminished. After subtracting the much-weakened background, we are able to clearly resolve the resistance oscillation of the MTJ.

3.1.1 Measurement Circuit Details

The microwave (RF) pulse in our measurement is generated by using a mixer (Miteq Model DM0208LW2 with a bandwidth of 2-8 GHz) and a short gating pulse to modulate a continuous-wave source. The short gating pulse is generated by a Picosecond Pulse Labs 10070A pulse generator (“pulser”) with pulse rise time of 65 ps and maximum pulse length of 10 ns. The continuous-wave is generated by an Agilent E8257C sweeping signal generator (“sweeper”) operated in continuous wave (CW) mode. The RF pulse length is 5-10 ns, set by the length of the gating pulse. 5 ns is roughly required to reach a stable

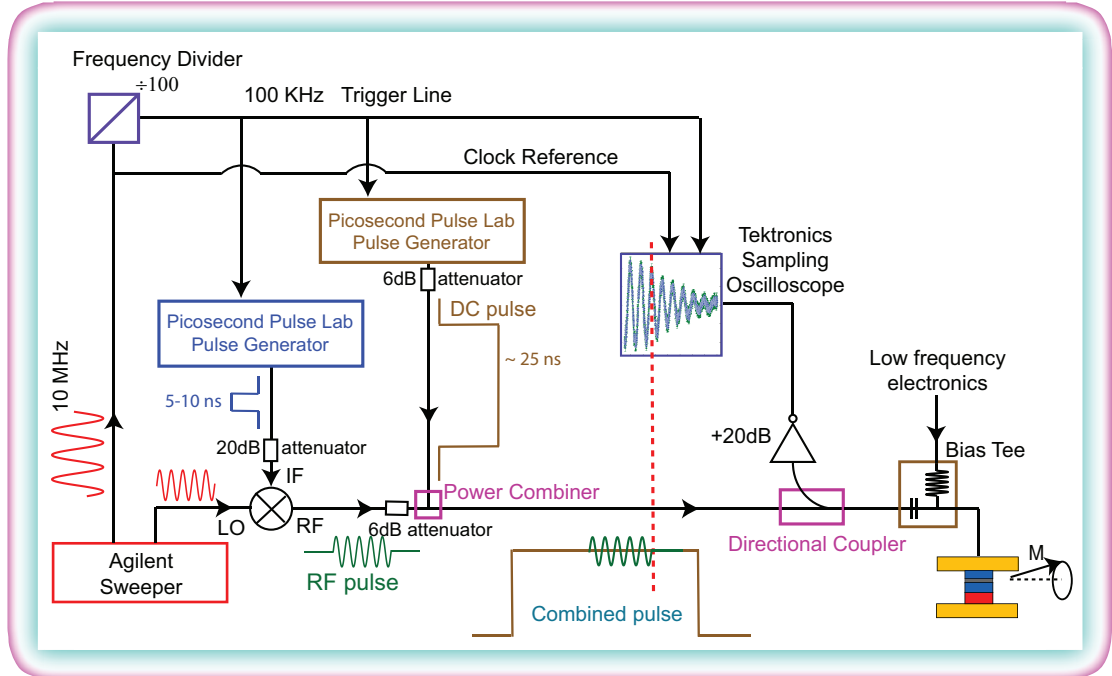


Figure 3.1: Schematic of the measurement circuit for time domain ST-FMR

a stable resonant precession state, estimated from the decay time of magnetic precession of 0.5-1 ns. The RF pulse generated using the mixer has rise and fall times of 100 ps and 180 ps respectively, not surprisingly, slightly longer than the corresponding times of the gating pulse itself. The small non-zero fall time has negligible effect on determining the amplitude and phase of the damped precession after the pulse because (by defining the center of the fall time as time zero) the extra torque after time zero and the reduced torque before time zero cancel to first order. There is some ringing following the RF pulse, but its amplitude is about a factor of 25 smaller than the main excitation signal and our calculations indicate that spin torque from the ringing also has negligible effect on our final results. The magnitude of the RF pulse can be adjusted by the amplitude of either the gating pulse or the CW source. The effects of adjusting these two amplitudes are similar, but it appears that using a combination of higher gating pulse and lower CW source produces better on/off ratio for the

RF pulse, compared with a combination of lower gating pulse and higher CW source (which is understandable). We typically set the sweeper to around 0 dBm (subject to flatness correction) and set the gating pulser to about 20 dBm, which results in a RF peak-to-peak voltage acting on the device of 20-40 mV after attenuation.

The longer square pulse (25 ns) is generated by another Pulse generator of a different model (Picosecond Pulse Labs 10300A). This square pulse acts as an equivalent DC bias, which we will refer as “DC pulse”. Using a DC pulse instead of an actual DC voltage to bias the MTJ significantly reduces the probability of electrical breakdown at high voltages and allows us to access higher biases than in DC-detected ST-FMR or TE-FMR experiments. The DC pulse and the RF pulse are combined by a power combiner/divider (Picosecond Pulse Labs 5331) and then applied to the MTJ device via a directional coupler (Krytar Model 102050010) and a bias-tee (Picosecond Pulse Labs 5541A). The bias-tee is used to integrate low-frequency electronics to facilitate device characterization and mixing voltage detection of ST-FMR. The directional coupler is essential for reading out the magnetic precession signal from the reflected microwave from the device. One can also try to just use a power divider for this purpose, but using a directional coupler has the advantage of avoiding picking up the incoming microwave on the oscilloscope, which would otherwise produce another large background. A circulator could potentially work, but they typically have narrower bandwidth that is insufficient for our measurement.

The use of multiple attenuators and cables of proper lengths is a key part in building a well-performing circuit. For some reason the Picosecond Pulse Lab pulsers have internal impedance different from 50Ω , therefore it is important

to have attenuators attached to each of the pulsers to mitigate the reflected microwave back from the pulsers. We used just a 6 dB attenuator on the pulser for the DC pulse, compromising for the large power we need from the pulser to reach large DC bias. The gating pulser for RF pulse could make use of a 20 dB attenuator¹ since it is relevant to the on/off ratio of the generated RF pulse. Another attenuator could be used on the RF pulse line before the power combiner to suppress the reflected waves associated with the power combiner. In general, one needs to monitor carefully possible reflections from all of the circuit elements and connection joints and consider the use of attenuators as long as the power requirement can be met. While multiple reflections within the left side of the directional coupler in Fig. 3.1 affect the RF pulse shape and on/off ratio, multiple reflections involving the device itself are more critical in that they produce magnetic dynamics in multiple traces and they can potentially overlap and interfere with our measurement. A good solution to this problem is to use a relatively long transmission cable to connect the device so that the higher order reflection pulse is well spaced out by more than the duration of the RF pulse. Using a 5 foot cable (resulting in more than 10 ns in a microwave round-trip) together with a 6 ns RF pulse can easily reach such a goal.

The reflected signal from the device is collected by a Tektronix TDS8000B sampling oscilloscope via the directional coupler and a Picosecond Pulse Labs 5840A 20-dB amplifier with a bandwidth of 80 kHz – 9.3 GHz. A sinusoidal 10 MHz clock output from the sweeper is used to synchronize the clock of the oscilloscope. We also use a (Pulse Research Lab) PRL-260ANT variable frequency divider (set at 1/100) to convert the same 10 MHz clock output into a 100 kHz sinusoidal signal which triggers both pulse generators and the

¹I could not remember exactly whether I used a 6 dB or 20 dB attenuator for the published data though.

oscilloscope. These synchronization measures fix the phase of the RF pulse and allow for signal averaging. This 100 kHz repetition rate is limited by the maximum firing rate of the pulser generators. We typically average for 25 seconds by the “average” function of the oscilloscope itself before we store the waveform to the computer. 25 sec corresponds to about 1250 repetitions for 2000 sampling points across 1 ns of time span that we measure the magnetic dynamics.

3.1.2 Device Structures

Most of the devices we measure are from the same batch of low RA MgO-based magnetic tunnel junctions we described in Chapter 2, fabricated by J. A. Katine and colleagues at Hitachi Global Storages. The layer structures are: bottom electrode [Ta(3)/CuN(41.8)/Ta(3)/CuN(41.8)/Ta(3)/Ru(3.1)], synthetic antiferromagnet (SAF) layer pinned to IrMn [IrMn(6.1)/CoFe(1.8)/Ru/CoFeB(2.0)], tunnel barrier [MgO_x], free layer [CoFe(0.5)/CoFeB(3.4)] and capping layer [Ru(6)/Ta(3)/Ru(4)]. Both the free layer and the SAF pinned layer are etched into a circular shape with diameter nominally either 80 nm or 90 nm. The devices have a nominal resistance-area (RA) product of $1.5 \Omega\mu\text{m}^2$ and measured TMR ratios 85-100%. We monitor the resistance and TMR throughout the experiment to ensure that the MTJs are not degraded at high bias [98]. During the measurements, we apply an in-plane magnetic field H (200-450 Oe) at an angle, φ ($45^\circ - 135^\circ$), relative to the exchange bias of the SAF in order to produce a nonzero offset angle θ between the free layer and the reference layer of the SAF [Fig. 3.2(a)]. We use the convention that positive bias corresponds to electron flow from the free layer to the SAF. We have measured ten of these samples,

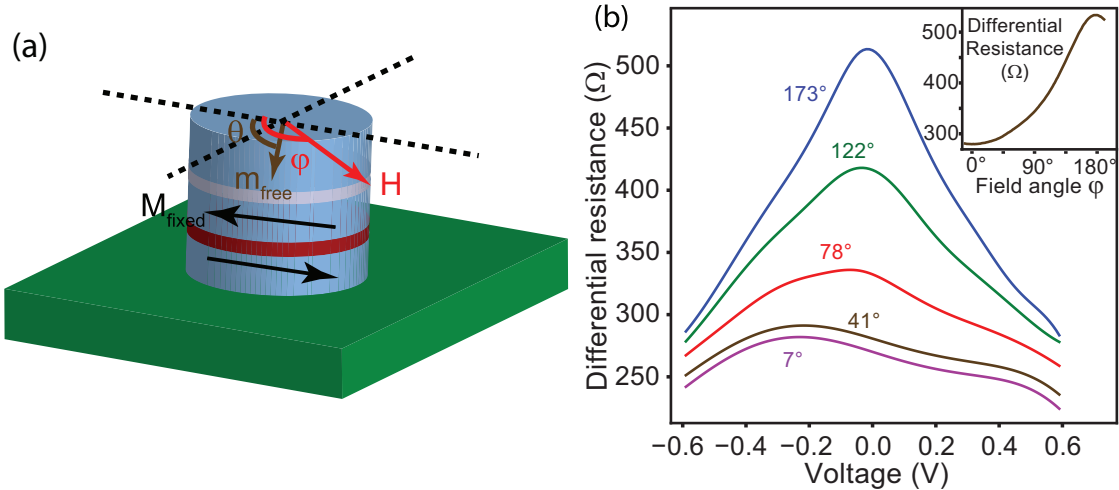


Figure 3.2: (a) Schematic geometry of the MTJ devices used for time-domain ST-FMR measurements. (b) (Main panel) Bias dependence of the differential resistance for sample 1 at selected offset angles θ as labeled, (inset) zero-bias resistance as a function of field angle φ for $H = 600$ Oe.

all with similar results, and we will report data from two of them. Sample 1 (nominally $90 \times 90 \text{ nm}^2$) has a parallel-state resistance of 272Ω and TMR of 91% [Fig. 3.2(b)], and sample 2 (nominally $80 \times 80 \text{ nm}^2$) has a parallel-state resistance of 381Ω and TMR of 97%. The total magnetic moment of the free layer $M_s V_{free}$ is estimated to be 1.8×10^{-14} emu for sample 1 and 1.6×10^{-14} for sample 2 based on vibrating sample magnetometer measurements of test films, and the easy plane anisotropy strength of the free layer film is $4\pi M_{eff} = 13 \pm 1$ kOe, estimated by comparing our measured ST-FMR resonance frequency to a our derived formula [Eq. (3.15)]. We have also measured two samples from a different batch of devices with nominal RA of $1.0 \Omega \mu\text{m}^2$ with similar layer structures and geometries, also fabricated by Katine and colleagues. We will very briefly show our result from one of these samples as well.

3.1.3 Data Acquisition and Background Subtraction Procedure

Even with our pulsing technique to shut off the large voltage background [the first term on the right in Eq. (3.1)] from applied RF drive, our RF pulse shape is not perfect, with some remnant voltage oscillation present after the falling edge of the pulse. An on/off ratio of about 25 for our pulses still leaves this background with similar or larger magnitude than the real magnetic precession signal. Therefore it is critical to separate the magnetic precession signal from this residual background.

In order to perform this background subtraction, for any given state of the device (for magnetic field magnitude H , field direction φ and bias voltage V), we identify a non-resonance reference state of the same device with equal impedance to measure the background. With the same impedance, the reflected signal of the same RF pulse should be the same for both states, so that the difference between the two waveforms represents the net signal produced by the magnetic precession. To find a reference state for the (H, φ, V) state, we first determine the differential resistance R_0 of the device at the $(H, \varphi, 0)$ state with a low-frequency (about 1 kHz) lock-in measurement, then we increase the external magnetic field to H' (typically by 500 Oe) to shift the resonance peak completely out of the frequency range of our measurement, and finally we fine-tune the field direction to φ' (typically by a few degrees) so that the lock-in measurement of the resistance $R_0(H', \varphi', 0)$ is equal to $R_0(H, \varphi, 0)$. Throughout the measurement under the same field set (H, φ) at arbitrary biases V , we use the (H', φ', V) state as the reference state for the (H, φ, V) state. Because the resistance is strongly dependent on bias voltage in MTJs, $R_0(H, \varphi, V)$ is very different from $R_0(H, \varphi, 0)$. However, if we assume that an applied bias voltage

does not change the direction of the magnetization dramatically (we estimate the effect of the static spin torque can result in a change of θ by at most 3° for all our field conditions), to a good approximation $R_0(H', \varphi', V) = R_0(H, \varphi, V)$ should still hold because the two states have the same offset angle and bias voltage. We verified this by comparing the reflected waveform of an off-resonance RF pulse (typically with a frequency lower than the resonance of either state) at the two states, and found that the difference between the two was negligible compared to our measured signal after subtraction.

To make a time-domain measurement of the resistance oscillation at the state (H, φ, V) under a given RF driving pulse, we first record the waveform at the state of interest (H, φ, V) after averaging for 25 seconds (about 1250 repetitions for 2000 sampling points) [the red curve in Fig. 3.3(a) and (b)]. We then keep the applied RF driving pulse on to maintain the same phase and amplitude, switch quickly to the reference state (H', φ', V) , and record the background waveform, again averaging for 25 seconds [the black curve in Fig. 3.3(a) and (b)]. Afterwards we switch back to the original state (H, φ, V) and repeat the measurement [the blue curve in Fig. 3.3(a) and (b) which is hardly visible since it overlaps with the red curve]. It is important to record the the signal trace both before and after recording the background trace because either the falling edge of the RF pulse or the phase of the RF pulse can drift with respect to the time base of the oscilloscope by a few picoseconds over several minutes of measurements. We discard any data taken when this drift is significant (*i.e.* more than one picosecond) during the overall measurement time of about 1.5 minutes. Finally we average the signal traces and subtract the background, and get the resulting waveform that is proportional to the resistance oscillation of the MTJ.

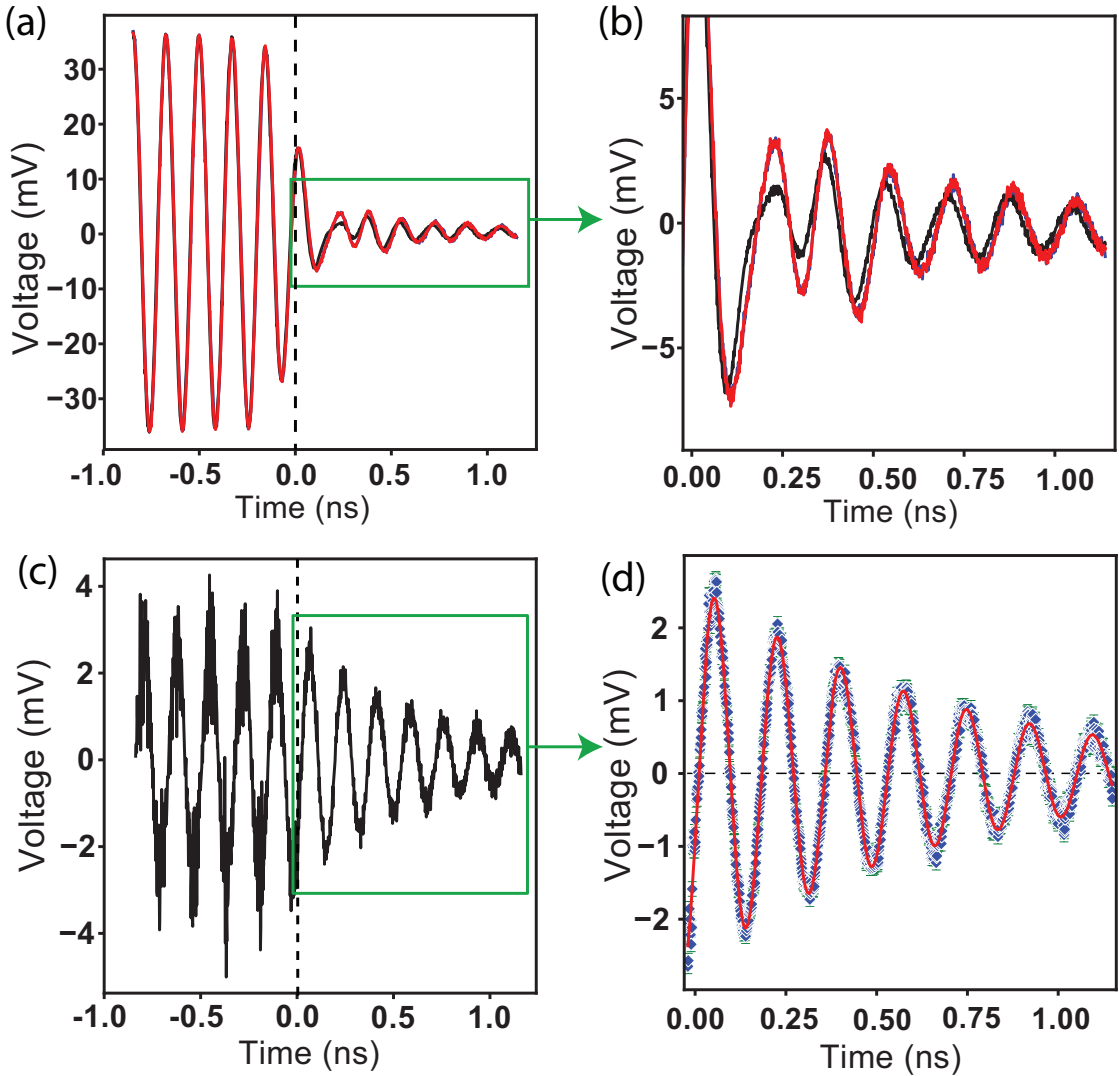


Figure 3.3: Illustration of the background subtraction and resulting signal of magnetic precession in ST-FMR. (a) The raw signal (red and blue, overlapping with each other) and background (black) waveform traces used to yield the resistance oscillation signal in ST-FMR. The raw signal traces are the reflected voltage waveforms measured by the sampling oscilloscope for a 5.8 GHz RF driving pulse, taken from sample 1 under the following bias parameters: magnetic field $H = 200$ Oe, field direction $\varphi = 90^\circ$, offset angle $\theta = 85^\circ$, $V = 0.38$ V. The background trace is the reflected voltage waveform measured for the same driving pulse but for a different magnetic field $H = 600$ Oe, $\varphi = 94^\circ$, so as to provide a non-resonant background measurement. (b) Zoom-in of the green box area in (a). (c) Time-resolved resistance oscillation of the MTJ during and after an RF drive, resulting from a subtraction of waveforms in (a). (d) Zoom-in of the green box area in (c) and a fit to a decaying sinusoid (red curve).

Figures 3.3(c) and (d) show such a subtracted precession signal for the case of $H = 200$ Oe, field direction $\varphi = 90$, offset angle $\theta = 85^\circ$, $V = 0.38$ V for sample 1. Following the falling edge of the RF pulse, the measurement shows a resistance oscillation that decays gradually in time. The magnitude of oscillation corresponds to a maximum precession angle of about 1.5° , well within the linear-response regime. The decay rate for the oscillations agrees quantitatively with the magnetic damping rate measured by DC-detected ST-FMR in the same samples as we will discuss later, indicating that the decay is due to a true decrease in precession amplitude, and is not dominated by dephasing between different repetitions of the measurement. Ideally our background subtraction should work not only after the RF pulse but also during the pulse, and we have indeed resolved the steady-state persistent resistance oscillation during the pulse as well (for time < 0 in Fig. 3.3(c)). This persistent oscillation confirms that the RF pulse is long enough to saturate the MTJ to steady-state dynamics. However, the oscillations measured during the pulse are noisy because of the large background that is subtracted, so we do not use them for quantitative analysis.

3.1.4 Fitting to a Damped Driven Harmonic Oscillator

The damped resistance oscillation following the falling edge of the RF pulse [Fig. 3.3(d)] can be accurately fit into an exponentially decaying sinusoid $A_1 e^{-\Gamma t} \cos(\omega t + \Phi_1)$ with four parameters: amplitude A_1 , phase Φ_1 , frequency ω and decay rate Γ , defining the centre of the falling edge of the pulse as time zero ($t = 0$). The fitting uncertainty for the phase is less than 0.04 radian, which corresponds to a time precision of ~ 1 ps. Using the same $t = 0$ point, we also

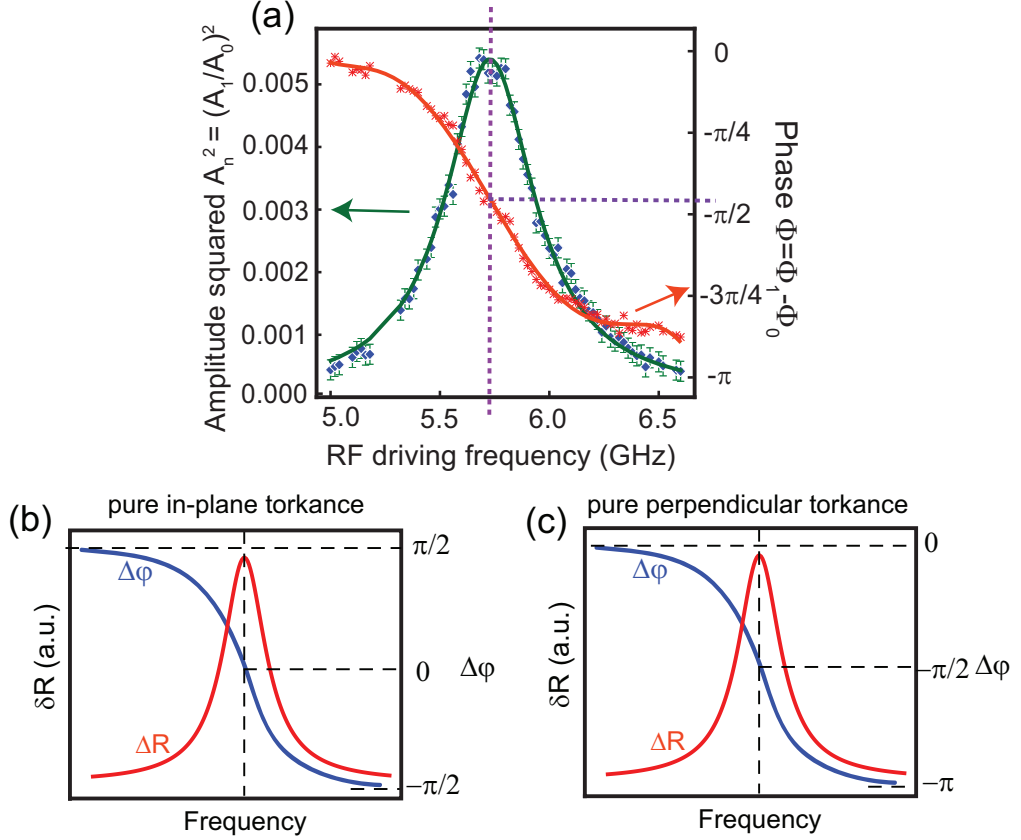


Figure 3.4: (a) Dependence on the frequency of the RF drive pulse for the normalized oscillation amplitude squared $A_n^2 = (A_1/A_0)^2$ (diamonds) and the oscillation phase relative to the drive pulse, $\Phi - \Phi_1 - \Phi_0$ (asterisks). The green curve is a symmetric Lorentzian fit to the amplitude data, and the red curve is a smooth polynomial fit of the phase. This can be compared with the intuitively expected frequency dependence of the resistance oscillation amplitude and phase driven by (b) pure in-plane and (c) pure perpendicular spin transfer torkance as appeared in Fig. 2.2.

fit the RF driving signal [the black curve in Fig. 3.3(a)] prior to the falling edge of the pulse to a simple sinusoid $A_0 \cos(\omega_0 t + \Phi_0)$ with fitting parameters A_0 and Φ_0 . The phase of the magnetic response relative to the externally applied RF driving voltage is then $\Phi = \Phi_1 - \Phi_0$.

Performing this procedure for various RF driving frequencies under the same biasing conditions, the dynamic response of the magnetization to oscillating spin transfer torque can be determined as a function of driving frequency. In

Fig. 3.4(a) we plot the normalized oscillation amplitude squared, $A_n^2 = (A_1/A_0)^2$, and relative phase Φ as a function of the RF pulse frequency for the same biasing conditions as for Fig. 3.3. The measured A_n^2 vs. f relation and Φ vs. f relation perfectly demonstrates the property of an externally driven classic harmonic oscillator, and directly match our schematic diagram in Fig. 2.2(b) and (e), which we show again here as Fig. 3.4(b) and (c). The resonant amplitude squared A_n^2 is accurately fit by a symmetric Lorentzian line shape and the phase changes by π as the frequency is tuned through the resonance. We determine the natural frequency of the oscillator ω_m and the maximum normalized oscillation amplitude $A_{n,max}$ from the fit to the amplitude response, and then determine the phase Φ_m of the magnetization precession at resonance by interpolating to the value at ω_m on a smooth polynomial fit of Φ vs. driving frequency.

Intuitively the magnitude of the resonant response $A_{n,max}$ is related to the amplitude of the spin transfer torque. A comparison of the phases in Fig. 3.4(a) with the schematic model Fig. 3.4(b) and (c) also provides intuitive insights into the direction of the spin transfer torque. The Φ_m in Fig. 3.4(a) is at a value between 0 for pure in-plane torkance [Fig. 3.4(b)] and $-\pi$ for pure perpendicular torkance [Fig. 3.4(c)], confirming the coexistence of both torkance components. Moreover, Φ_m in Fig. 3.4(a) is much closer to the $-\pi$ than to 0, indicating that at this bias voltage ($V = 0.38$ V) it is the perpendicular spin transfer torkance that is more significant in driving ferromagnetic resonance.

3.2 Quantitative Modeling of Time Domain Detection of ST-FMR

From the values of $A_{n,max}$, Φ_m , and Γ , we can make a quantitative determination of the spin-torque vector. In Section 2.3, we have derived the equations describing the precession dynamics under RF drive [Eq. (2.14)], and further solved the complex precession amplitude m_{y1} [Eq. (2.15)] as a function of RF driving frequency. Based on a very similar procedure, together with the microwave transmission/reflection relations, we will derive the exact form of the resistance oscillation signal that directly corresponds to our time-domain reflection measurement described in section 3.1. This section is partially adapted from the Supplementary Note 3 of our published work [82].

In deriving the analytical form of our measured signal in time-domain ST-FMR, keep in mind that we are measuring a signal that is first order to the RF driving current I_{RF} . This is different from the case in DC-detected ST-FMR, where the mixing voltage $V_{mix} \propto \langle \delta I \delta R \rangle$ is second order to I_{RF} . Therefore here we can limit our calculations to just the first order terms, as opposed to keeping all the second order terms as in Section 2.3. This allows tremendous simplification in the algebra, and the dynamic equations of $m_x(t)$ and $m_y(t)$ [Eq. (2.14)] now becomes,

$$\begin{aligned} \frac{dm_x(t)}{dt} &= -\gamma m_y(t) N_y M_{eff} - \alpha \frac{dm_y(t)}{dt} \\ &\quad + \frac{\gamma}{M_s V_{free}} \left[\tau_{||} m_x(t) \cot \theta - \frac{\partial \tau_{\perp}}{\partial I} \delta I(t) - \frac{\partial \tau_{\perp}}{\partial \theta} m_y(t) \right] \\ \frac{dm_y(t)}{dt} &= \gamma m_x(t) N_y M_{eff} + \alpha \frac{dm_x(t)}{dt} \\ &\quad - \frac{\gamma}{M_s V_{free}} \left[\frac{\partial \tau_{||}}{\partial I} \delta I(t) - \frac{\partial \tau_{||}}{\partial \theta} m_y(t) + \tau_{\perp} m_x(t) \cot \theta \right] \end{aligned} \quad (3.2)$$

where $N_x = 4\pi + H_z/M_{eff}$ and $N_y = H_z/M_{eff}$ for our circular shaped samples that allow us to drop the in-plane anisotropy field H_{anis} included in Section 2.3. Noting that the first order response of magnetic dynamics is purely at frequency f , we can also use a much simpler form of Eq. (2.8) by cutting off other frequency terms ($m_{x0}, m_{y0}, m_{x2}, m_{y2}$, etc...) so that

$$\begin{aligned} m_x(t) &= \text{Re}(m_{x1}e^{i\omega t}) \\ m_y(t) &= \text{Re}(m_{y1}e^{i\omega t}) \end{aligned} \quad (3.3)$$

Substituting Eq. (3.3) into Eq. (3.2), and also considering $\delta I(t) = \text{Re}(I_{RFE}e^{i\omega t})$,

$$\begin{aligned} i\omega m_{x1} &= -m_{y1}(\gamma N_y M_{eff} + i\alpha\omega) + \frac{\gamma}{M_s V_{free}} \left[\tau_{||} m_{x1} \cot\theta - \frac{\partial\tau_{\perp}}{\partial I} I_{RF} - \frac{\partial\tau_{\perp}}{\partial\theta} \Big|_I m_{y1} \right] \\ i\omega m_{y1} &= +m_{x1}(\gamma N_y M_{eff} + i\alpha\omega) - \frac{\gamma}{M_s V_{free}} \left[\tau_{\perp} m_{x1} \cot\theta + \frac{\partial\tau_{||}}{\partial I} I_{RF} - \frac{\partial\tau_{||}}{\partial\theta} \Big|_I m_{y1} \right] \end{aligned} \quad (3.4)$$

In our experiments, we apply an external RF voltage $V_{in}(t) = V_{in}\text{Re}(e^{i\omega t})$ to the MTJ device, which is related to the resulting voltage V_{RF} and current I_{RF} at the device by the following microwave circuit equations,

$$\begin{aligned} V(t) &= V + \text{Re}(V_{RFE}e^{i\omega t}) = V + V_{in}\text{Re}(e^{i\omega t}) + \text{Re}(V_{ref}e^{i\omega t}) \\ I(t) &= I + \text{Re}(I_{RFE}e^{i\omega t}) = I + V_{in}\text{Re}(e^{i\omega t})/(50\Omega) - \text{Re}(V_{ref}e^{i\omega t})/(50\Omega) \end{aligned} \quad (3.5)$$

where V_{ref} represents the complex amplitude of the reflected (backwards propagating) microwave voltage. We note that the resistance of the MTJ imposes a restriction,

$$V(t) = V + \frac{\partial V}{\partial I} \Big|_{\theta} \delta I(t) + \frac{\partial V}{\partial\theta} \Big|_I \delta\theta(t) \quad (3.6)$$

From Eq. (3.5) and Eq. (3.6), together with the relation $\delta\theta(t) = \text{Re}(-m_{y1}e^{i\omega t})$,

$$V_{in} + V_{ref} = R_0 \frac{V_{in} - V_{ref}}{(50\Omega)} - \frac{\partial V}{\partial\theta} \Big|_I m_{y1} \quad (3.7)$$

where $R_0 = (\partial V / \partial I)|_\theta$ is the differential resistance of the MTJ. Therefore the reflected microwave is

$$V_{ref} = \frac{R_0 - (50\Omega)}{R_0 + (50\Omega)} V_{in} - \frac{(50\Omega)}{R_0 + (50\Omega)} \frac{\partial V}{\partial \theta} \Big|_I m_{y1} \quad (3.8)$$

The actual RF voltage and current and current across the MTJ are

$$V_{RF} = V_{in} + V_{ref} = \frac{2R_0}{R_0 + (50\Omega)} V_{in} - \frac{(50\Omega)}{R_0 + (50\Omega)} \frac{\partial V}{\partial \theta} \Big|_I m_{y1} \quad (3.9)$$

$$I_{RF} = \frac{V_{in} - V_{ref}}{(50\Omega)} = \frac{2V_{in}}{R_0 + (50\Omega)} + \frac{1}{R_0 + (50\Omega)} \frac{\partial V}{\partial \theta} \Big|_I m_{y1} \quad (3.10)$$

Equations (3.9) and (3.10) have deep implications for ST-FMR type of experiments. When we first started to model ST-FMR in the context of mixing voltage detection, we considered a RF current I_{RF} that is applied to the MTJ. Our underlying assumption is that this predetermined RF current I_{RF} is rigorously imposed onto the MTJ without any knowledge of the magnetic dynamics. As was done in ref. [76, 80] we assumed in the solution to m_{y1} [Eq. (2.15) and rewritten here as Eq. (3.11)] that I_{RF} (after flatness correction) is a constant:

$$m_{y1} = \frac{\gamma I_{RF}}{2M_s V_{free}} \frac{1}{(\omega - \omega_m - i\sigma)} \left[i \frac{\partial \tau_{||}}{\partial I} + \frac{\gamma N_x M_{eff}}{\omega_m} \frac{\partial \tau_{\perp}}{\partial I} \right] \quad (3.11)$$

However, Eq. (3.10) shows that I_{RF} is not a constant but depends on m_{y1} . In other words, an RF current I_{RF} drives magnetic precession m_{y1} as described by Eq. (3.11), which in turn produces an extra RF current [the last term in Eq. (3.10)]. The same feedback effect happens as well in the language of voltage driven magnetic dynamics if we Taylor expand the spin transfer torque as a function of voltage (as we published in the Supplementary Note 3 of ref. [82]). In Section 4.2, we will discuss this feedback effect in more detail and in the context of a potential application in microwave amplifier.

In order to take this feedback effect into account and solve the equations self-consistently, we express the magnetic dynamics equations in terms of the

applied RF drive V_{in} (which does not change due to feedback when the free layer rotates) rather than the actual oscillating current I_{RF} or voltage V_{RF} across the tunnel junction (which does change due to feedback). Substituting Eq. (3.10) into Eq. (3.4) and noting that $(\partial \vec{\tau}/\partial \theta)|_I = (\partial \vec{\tau}/\partial \theta)|_V + (\partial \vec{\tau}/\partial V)|_\theta (\partial V/\partial \theta)|_I$, we get:

$$\begin{aligned} i\omega m_{x1} &= -m_{y1}(\gamma N_y M_{eff} + i\alpha\omega) - \frac{\gamma}{M_s V_{free}} \left[\frac{2R_0}{R_0 + (50\Omega)} \frac{\partial \tau_\perp}{\partial V} V_{in} \right. \\ &\quad \left. - \left(\frac{\partial \tau_\perp}{\partial \theta} \Big|_V + \frac{(50\Omega)}{R_0 + (50\Omega)} \frac{\partial V}{\partial \theta} \Big|_I \frac{\partial \tau_\perp}{\partial V} \Big|_\theta \right) m_{y1} - \tau_{||} m_{x1} \cot \theta \right] \\ i\omega m_{y1} &= -m_{x1}(\gamma N_x M_{eff} + i\alpha\omega) - \frac{\gamma}{M_s V_{free}} \left[\frac{2R_0}{R_0 + (50\Omega)} \frac{\partial \tau_{||}}{\partial V} V_{in} \right. \\ &\quad \left. - \left(\frac{\partial \tau_{||}}{\partial \theta} \Big|_V + \frac{(50\Omega)}{R_0 + (50\Omega)} \frac{\partial V}{\partial \theta} \Big|_I \frac{\partial \tau_{||}}{\partial V} \Big|_\theta \right) m_{y1} - \tau_\perp m_{x1} \cot \theta \right] \end{aligned} \quad (3.12)$$

Solving Eq. (3.12) for m_{y1} yields

$$m_{y1} = \frac{R_0}{R_0 + (50\Omega)} \frac{\gamma V_{in}}{M_s V_{free}} \frac{2\omega}{(\omega^2 - \omega_m^2 - 2i\omega\sigma)} \left[i \frac{\partial \tau_{||}}{\partial V} + \frac{\gamma N_x M_{eff}}{\omega} \frac{\partial \tau_\perp}{\partial V} \right] \quad (3.13)$$

which close to resonance $\omega \approx \omega_m$ becomes

$$m_{y1} = \frac{R_0}{R_0 + (50\Omega)} \frac{\gamma V_{in}}{M_s V_{free}} \frac{1}{(\omega - \omega_m - i\sigma)} \left[i \frac{\partial \tau_{||}}{\partial V} + \frac{\gamma N_x M_{eff}}{\omega_m} \frac{\partial \tau_\perp}{\partial V} \right] \quad (3.14)$$

where

$$\omega_m \approx \gamma M_{eff} \sqrt{N_x \left[N_y - \frac{1}{M_{eff} M_s V_{free}} \left(\frac{\partial \tau_\perp}{\partial \theta} \Big|_V + \frac{(50\Omega)}{R_0 + (50\Omega)} \frac{\partial V}{\partial \theta} \Big|_I \frac{\partial \tau_\perp}{\partial V} \right) \right]} \quad (3.15)$$

is the resonance frequency, and σ is the half linewidth of the resonance,

$$\sigma \approx \frac{\alpha \gamma M_{eff} (N_x + N_y)}{2} - \frac{\gamma}{2 M_s V_{free}} \left[\frac{\partial \tau_{||}}{\partial \theta} \Big|_V + \tau_{||} \cot \theta + \frac{(50\Omega)}{R_0 + (50\Omega)} \frac{\partial V}{\partial \theta} \Big|_I \frac{\partial \tau_{||}}{\partial V} \right] \quad (3.16)$$

Substituting Eq. (3.14) in Eq. (3.8), we relate the measured reflected signal

with the spin transfer torkance,

$$V_{ref} = \frac{R_0 - (50\Omega)}{R_0 + (50\Omega)} V_{in} - \frac{R_0(50\Omega)}{[R_0 + (50\Omega)]^2} \frac{\partial V}{\partial \theta} \Big|_I \frac{\gamma}{M_s V_{free}} \frac{1}{(\omega - \omega_m - i\sigma)} \left[i \frac{\partial \tau_{||}}{\partial V} + \frac{\gamma N_x M_{eff}}{\omega_m} \frac{\partial \tau_{\perp}}{\partial V} \right] V_{in} \quad (3.17)$$

where the first term is the measured background V_{bg} in our experiment, and the second term is the measured signal arising from the resistance oscillation V_{sig} . Therefore the normalized complex precession amplitude $Ae^{i\Phi}$ that we analyze in our time-domain experiment takes the form

$$Ae^{i\Phi} = V_{sig}/V_{bg} = \frac{-R_0(50\Omega)(\partial V/\partial \theta)|_I}{[R_0 + (50\Omega)][R_0 - (50\Omega)]} \frac{\gamma}{M_s V_{free}} \frac{1}{(\omega - \omega_m - i\sigma)} \left[i \frac{\partial \tau_{||}}{\partial V} + \frac{\gamma N_x M_{eff}}{\omega_m} \frac{\partial \tau_{\perp}}{\partial V} \right] \quad (3.18)$$

This is a convenient quantity for analysis because amplifier gains and transmission losses cancel on account of the normalization. At the resonance frequency,

$$A_{n,max} e^{i\Phi_m} = \frac{R_0(50\Omega)}{[R_0 + (50\Omega)][R_0 - (50\Omega)]} \frac{\partial V}{\partial \theta} \Big|_I \frac{\gamma}{M_s V_{free} \sigma} \left[\frac{\partial \tau_{||}}{\partial V} - i \frac{\gamma N_x M_{eff}}{\omega_m} \frac{\partial \tau_{\perp}}{\partial V} \right] \quad (3.19)$$

Experimentally we measure $A_{n,max}$ and Φ_m , and we only need to know σ to completely determine the spin transfer torkance $d\vec{\tau}/dV$. It is possible to determine σ by a Lorentzian fit of A_n^2 vs. f in Fig. 3.4(a), but a better way is to use the decay rate Γ of the resistance oscillations in the time-domain experiment to replace σ . Fitting σ from A_n^2 vs. f involves large uncertainty because those off-resonance data points with small dynamic response (and therefore the worst signal/noise ratio) contribute critically to the value of σ . On the other hand, Γ can be extracted independently by fitting any damped resistance oscillation

excited by any RF driving frequency. It not only can be determined at resonance or close to resonance (with good signal/noise ratio) but also enjoys the luxury of massive averaging over all the RF driving frequencies. Here we will show that the decay rate Γ of the damped resistance oscillations has exactly the same value as half linewidth σ in Eq. (3.19).

To prove this, we analyze the equation of motion in the case that $V_{in} = 0$, and assume exponential decay forms for both the magnetization components and the RF current associated with the precession:

$$\begin{aligned} m_x(t) &= \text{Re}(m_x e^{(-\Gamma_i \omega)t}) \\ m_y(t) &= \text{Re}(m_y e^{(-\Gamma_i \omega)t}) \\ \delta I(t) &= \text{Re}(\delta V e^{(-\Gamma_i \omega)t}) \end{aligned} \quad (3.20)$$

From Eq. (3.10), we have

$$\delta I(t) = \frac{(50\Omega)}{R_0 + (50\Omega)} \frac{\partial V}{\partial \theta} \Big|_I m_y(t) \quad (3.21)$$

Substituting Eq. (3.20) and Eq. (3.21) into Eq. (3.2), and noting that $(\partial \vec{\tau}/\partial \theta)|_I = (\partial \vec{\tau}/\partial \theta)|_V + (\partial \vec{\tau}/\partial V)|_\theta (\partial V/\partial \theta)|_I$, we have:

$$\begin{aligned} (-\Gamma + i\omega)m_x &= -m_y (\gamma N_y M_{eff} + i\alpha\omega - \alpha\Gamma) + \frac{\gamma}{M_s V_{free}} \tau_{||} m_{x1} \cot \theta \\ &\quad + \frac{\gamma}{M_s V_{free}} \left[\frac{\partial \tau_{\perp}}{\partial \theta} \Big|_V + \frac{(50\Omega)}{R_0 + (50\Omega)} \frac{\partial V}{\partial \theta} \Big|_I \frac{\partial \tau_{\perp}}{\partial \theta} \Big|_V \right] m_{y1} \\ (-\Gamma + i\omega)m_y &= -m_x (\gamma N_x M_{eff} + i\alpha\omega - \alpha\Gamma) - \frac{\gamma}{M_s V_{free}} \tau_{\perp} m_{x1} \cot \theta \\ &\quad + \frac{\gamma}{M_s V_{free}} \left[\frac{\partial \tau_{||}}{\partial \theta} \Big|_V + \frac{(50\Omega)}{R_0 + (50\Omega)} \frac{\partial V}{\partial \theta} \Big|_I \frac{\partial \tau_{||}}{\partial \theta} \Big|_V \right] m_{y1} \end{aligned} \quad (3.22)$$

These equations determine the natural frequency ω_m and the decay rate Γ of the damped resistance oscillation,

$$\omega_m \approx \gamma M_{eff} \sqrt{N_x \left[N_y - \frac{1}{M_{eff} M_s V_{free}} \left(\frac{\partial \tau_{\perp}}{\partial \theta} \Big|_V + \frac{(50\Omega)}{R_0 + (50\Omega)} \frac{\partial V}{\partial \theta} \Big|_I \frac{\partial \tau_{\perp}}{\partial \theta} \Big|_V \right) \right]} \quad (3.23)$$

$$\Gamma \approx \frac{\alpha\gamma M_{eff}(N_x + N_y)}{2} - \frac{\gamma}{2M_s V_{free}} \left[\frac{\partial \tau_{||}}{\partial \theta} \Big|_V + \tau_{||} \cot \theta + \frac{(50\Omega)}{R_0 + (50\Omega)} \frac{\partial V}{\partial \theta} \Big|_I \frac{\partial \tau_{||}}{\partial V} \right] \quad (3.24)$$

The frequency ω_m in Eq. (3.23) is identical to the resonance frequency of ST-FMR in Eq. (3.15), and the decay rate Γ is indeed equal to σ , the half linewidth of the ST-FMR resonance.

Up to this point, we have completed the formula to convert the experimental measurables $A_{m,max}$, Φ_m , Γ to the in-plane and perpendicular component of the spin transfer torkance (noting $\gamma = 2\mu_B/\hbar$):

$$\begin{aligned} \frac{\partial \tau_{||}}{\partial V} \Big|_\theta &= \frac{[R_0 + (50\Omega)][R_0 - (50\Omega)]}{R_0(50\Omega)} \frac{M_s V_{free} \hbar}{\mu_B} \left(\frac{\partial V}{\partial \theta} \Big|_I \right)^{-1} \Gamma A_{m,max} \cos \Phi_m \\ \frac{\partial \tau_{\perp}}{\partial V} \Big|_\theta &= \frac{[R_0 + (50\Omega)][R_0 - (50\Omega)]}{R_0(50\Omega)} \frac{M_s V_{free} \hbar}{\mu_B} \left(\frac{\partial V}{\partial \theta} \Big|_I \right)^{-1} \Gamma A_{m,max} \sin \Phi_m / \Omega_{\perp} \end{aligned} \quad (3.25)$$

where $\Omega_{\perp} \approx (4\pi + H)M_{eff}\gamma/\omega_m$. In the following sections, we will use Eq. (3.25) to determine the spin transfer torkance vector $d\vec{\tau}/dV$ from our experimental data taken as we discussed in the previous section (section 3.1).

On the bias dependence of the decay rate Γ (or linewidth σ), we can further use the angular dependence of spin torque for a tunnel junction $\tau_{||}(V, \theta) = \tau_{||} \sin \theta$ [99] on Eq. (3.24), and we have

$$\Gamma = \frac{\alpha\gamma M_{eff}(N_x + N_y)}{2} - \frac{\gamma}{M_s V_{free}} \left[\tau_{||,max} \cos \theta + \frac{(50\Omega)/2}{R_0 + (50\Omega)} \frac{\partial V}{\partial \theta} \Big|_I \frac{\partial \tau_{||,max}}{\partial V} \sin \theta \right] \quad (3.26)$$

where $\tau_{||,max}$ is the maximum in-plan torque at a given bias, V , (reached at $\theta = \pi/2$). If we make an approximation to neglect the last term of Eq. (3.26), then

$$\Gamma = \frac{\alpha\gamma M_{eff}(N_x + N_y)}{2} - \frac{\gamma}{M_s V_{free}} \tau_{||,max} \cos \theta \quad (3.27)$$

This equation leads to our formula for effective damping in Section 2.4.4 [Eq. (2.24)], where we did not provide a rigorous treatment on the partial

derivative $\partial\tau_{||}/\partial\theta$. $\partial\tau_{||}/\partial\theta$ is proportional to $\cos\theta$ only when this partial derivative is taken at a constant voltage, not at a constant current. We were ambiguous in Section 2.4.4 about which constant the partial derivative was taken with respect to. In fact, one can not expect a rigorous solution in Section 2.4.4 when the feedback effect is not taken into consideration. Here we see exactly that the underlying assumption of Eq. (3.27) [or equivalently Eq. (2.24)] is a justification to neglect the last term in Eq. (3.26):

$$\frac{(50\Omega)}{R_0 + (50\Omega)} \frac{\partial V}{\partial\theta} \Big|_I \frac{\partial\tau_{||}}{\partial V}$$

This term is zero when the resistance of the MTJ is much larger than 50Ω so that we reach the limit of no voltage feedback. But for low resistance tunnel junction, since $\tau_{||,max}$ and $(\partial V/\partial\theta)(\partial\tau_{||,max}/\partial V)$ is on the same order, this term can become as significant as the main bias dependent term $\tau_{||,max} \cos\theta$ at θ close to 90° .

3.3 Calibration Procedures

3.3.1 Calibrations of Device Resistance and Actual Voltage at High Bias

In order to use Eq. (3.25) for calculation of spin transfer torque, one needs to calibrate the differential resistance, R_0 of the MTJ, as well as $(\partial V/\partial\theta)|_I$ which is related to the DC resistance of the device at finite bias. These quantities need to be mapped out as a function of offset angle, θ , and bias voltage, V , just as was required in the calibration procedures for our DC mixing voltage detection of ST-FMR in Chapter 2.

Quantitative measurement of the resistance of a MTJ at high bias is a non-trivial task because traditional low-frequency lock-in measurement of resistance requires biasing the MTJ device with a constant DC voltage. This voltage, at high bias, can easily damage or destroy the tunnel barrier even if the bias is still comfortably below the breakdown voltage for nanosecond pulses. One of the key advantages our pulse-based ST-FMR technique offers is to access the high bias regime not accessible by DC-based measurements. For exactly the same reason we have to develop a pulse-based method to measure the resistance of the device at high bias. Furthermore, the actual voltage on the MTJ provided by the square pulse during time-domain ST-FMR measurement needs to be calibrated as well. The actual voltage is not only affected by circuit transmission loss, but also depends on resistance of the device. Therefore this voltage calibration is intimately related to the high bias resistance calibration, and here we describe the method we developed to perform these calibrations.

Our method is based on the fact that the amplitude of a reflected RF pulse from the MTJ depends on its differential resistance. For an incident RF pulse with small amplitude V_{in} at a frequency far away from resonance (so that it does not excite magnetic dynamics), the reflected amplitude is simply [from Eq. (3.1)]

$$V_{ref} = \frac{R_0 - (50\Omega)}{R_0 + (50\Omega)} V_{in} \quad (3.28)$$

where R_0 is the differential resistance, dependent on the offset angle and bias voltage across the MTJ. For calibration, we measure the reflected amplitude V_{ref} using the same incident RF pulse for the whole range of different resistances we can access safely with a DC bias, ranging from a maximum value corresponding to the anti-parallel state with $V = 0$ to a minimum value corresponding to the parallel state with $V = 0.35$ V in our case. At the same time, we measure the differential resistances for all these states using a lock-in amplifier. This

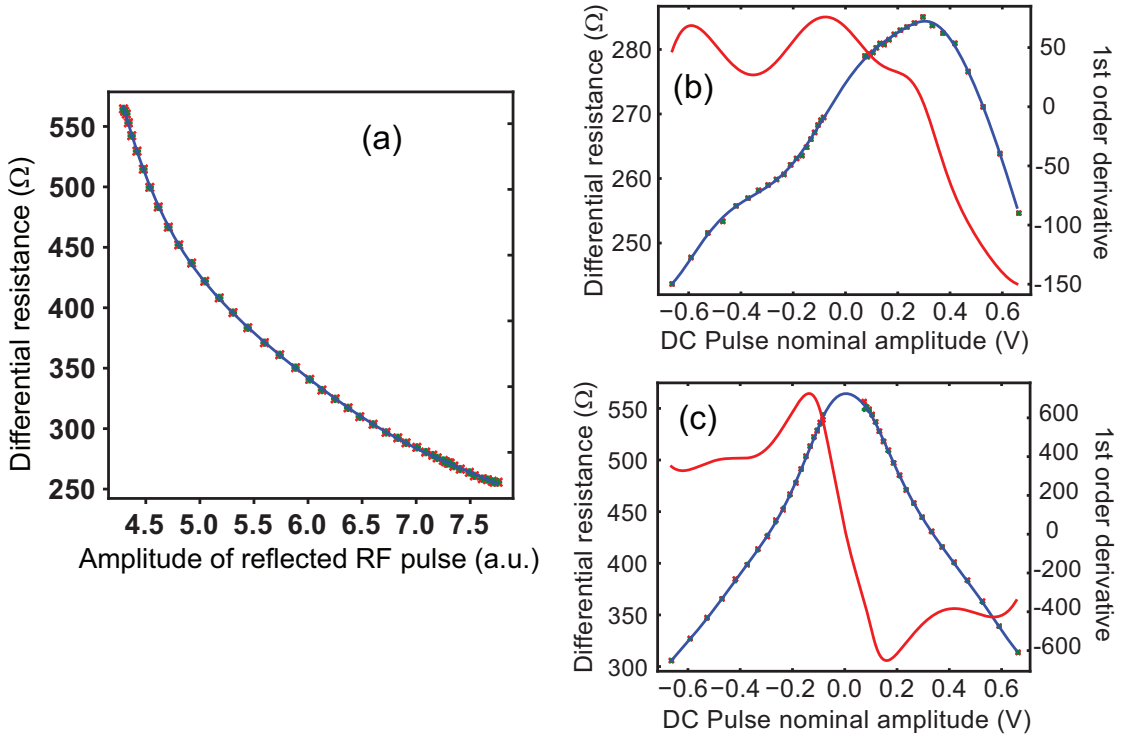


Figure 3.5: Calibration of the resistance of MTJ from the amplitude of the reflected RF pulse. (a) The conversion relation between differential resistance and reflection amplitude of RF pulse, calibrated at low bias with low-frequency lock-in measurements. (b) and (c), The measured differential resistance R_0 converted from RF reflectometry as a function of nominal DC pulse amplitude V_{sq} (defined as the pulser output voltage divided by 3, which is close to the real bias voltage) for (b) a close-to-parallel state and (c) a close-to-antiparallel state of the MTJ device. Red curves represent 1st order derivative of R_0 vs V_{sq} for fitting guidance.

procedure provides the basis to convert V_{ref} to R_0 [Fig. 3.5(a)]. We then apply square-wave pulses (“DC pulses”) of various amplitudes (which can access higher biases) instead of a constant DC voltage, and sweep the directions of the magnetic field (which changes the offset angle between the two moments), while measuring the reflected amplitude V_{ref} of the RF pulse. Using this process, we map out R_0 as a function of offset angle θ and nominal amplitude V_{sq} of the applied DC pulse (read from the set output voltage of the pulse generator), *i.e.* $R_0 = R_0(\theta, V_{sq})$ [Fig. 3.5(b) and (c)].

It should be noted that the calibration described so far has determined the differential resistance R_0 for any given square pulse (with nominal pulse amplitude V_{sq}), but the actual value of bias voltage V across the MTJ is not yet known. The equivalent bias V under a square pulse depends on the DC resistance R (defined as $R = V/I$):

$$V = \frac{2R}{R + (50\Omega)} \lambda V_{sq} \quad (3.29)$$

where λ is a constant ratio between the nominal pulse amplitude and the actual incoming pulse amplitude arriving on the device, determined by transmission and contact losses. In order to calibrate V for any given V_{sq} , we must first determine the coefficient λ . Taking advantage of the significant bias dependence of resistance of the MTJ (especially in the anti-parallel state), this can be done easily within the DC-accessible range $|V| < 0.35$ V where both R and R_0 can be directly measured by low-frequency techniques. We compare the value of R_0 as a function of V_{sq} we measure from the microwave reflection method and a separate measurement of R_0 as a function of V by low-frequency lock-in technique. This comparison provides a quantitative measurement of the bias V on the MTJ for any V_{sq} up to $|V| = 0.35$ V, which is sufficient to determine λ using Eq. (3.29). We have also further tested that Eq. (3.29) with this calibrated λ is indeed still accurate for higher bias (larger pulse height) by applying a large DC pulse together with a DC voltage in the opposite polarity so that the added bias voltage is within the DC-accessible range and therefore can be calibrated.

After we determine λ , we must still determine the DC resistance R in order to use Eq. (3.29) to determine the actual bias voltage V at high bias. Since we have measured differential resistance $R_0 = R_0(\theta, V_{sq})$ using the RF pulse reflection method as discussed above, V , I and R can all be determined by numerical integration from low bias to higher bias. Because $R=V/I$, we can

write Eq. (3.29) as $2\lambda V_{sq} = V + I(50\Omega)$, which can then be used to determine the relationship between an incremental change in incident pulse height and the resulting incremental change in voltage or current:

$$\begin{aligned} dV &= \frac{2\lambda dV_{sq}}{1 + (50\Omega/R_0)} \\ dI &= \frac{2\lambda dV_{sq}}{R_0 + (50\Omega)} \end{aligned} \quad (3.30)$$

where $R_0 = dV/dI$ is the differential resistance. Therefore,

$$\begin{aligned} V(\theta, V_{sq}) &= \int_0^{V_{sq}} \frac{2\lambda R_0(\theta, V_{dq})}{R_0(\theta, V_{dq}) + (50\Omega)} dV_{sq} \\ I(\theta, V_{sq}) &= \int_0^{V_{sq}} \frac{2\lambda}{R_0(\theta, V_{dq}) + (50\Omega)} dV_{sq} \end{aligned} \quad (3.31)$$

We can thus obtain calibrated values of V , R_0 and $dV/d\theta$ at any given θ and V_{sq} , giving us a full calibration of the resistance of the MTJ such as shown in Fig. 3.2.

3.3.2 Estimate of the Effect of Device Capacitance

Since we directly measure the resistance oscillation signal at GHz frequencies, and our determination of spin transfer torque by Eq. (3.25) is very sensitive to the relative phase Φ_m , any parasitic capacitance effect on the device side could potentially be detrimental to our measurement. Therefore we perform a brief estimate of the maximum capacitance of the device and its potential impact on our time-domain measurement and eventually our results on the spin transfer torkance vector.

We characterize the device capacitance by measuring the phase shift of a reflected microwave pulse before and after the microwave probe touches the contact pads of the device. When the microwave probe is lifted (and

disconnected from the device), the end load of the transmission line is infinity, and the microwave is completely reflected at the tip of the probe with zero phase change. When the probe is pushed down and touches the contact pads of the device, the microwave is partially reflected due to impedance mismatch. If the device is purely resistive, under far off-resonance condition (which can be met by applying a proper magnetic field), the reflected microwave is described by Eq. (3.28), acquiring no extra phase upon reflection. If there is an extra capacitance C connected in parallel with the resistance R_0 of the tunnel junction, the total impedance of the device is $Z = (\frac{1}{R_0} + i\omega C)^{-1}$, and the complex amplitude of the reflected microwave voltage V_{ref} is

$$\begin{aligned} V_{ref} &= \frac{Z - (50\Omega)}{Z + (50\Omega)} V_{in} \\ &= \frac{\frac{R_0}{(50\Omega)} - 1 - i\omega R_0 C}{\frac{R_0}{(50\Omega)} + 1 + i\omega R_0 C} V_{in} \end{aligned} \quad (3.32)$$

Therefore the additional phase angle acquired upon reflection is

$$\begin{aligned} \Phi_{ref} &= \frac{\text{Im}(V_{ref})}{\text{Re}(V_{ref})} \\ &= - (100\Omega)(\omega C) \left[1 - \left(\frac{50\Omega}{R_0} \right)^2 - ((50\Omega)\omega C)^2 \right]^{-1} \\ &\approx - \frac{2(50\Omega)}{(1/\omega C)} \end{aligned} \quad (3.33)$$

where we made an approximation based on $R_0 \gg 50 \Omega$ and $1/\omega C \gg 50 \Omega$. In our experiment we measure a phase delay of $\Phi_{ref} \approx 0.10 - 0.15 \text{ rad}$ at RF pulse frequency of $f = 5.0 \text{ GHz}$ (the typical frequency of our time-domain ST-FMR experiment), which corresponds to a capacitance of about $3 \times 10^{14} - 5 \times 10^{-14} \text{ F}$.

It should be noted that this phase delay Φ_{ref} upon connecting to the sample is not necessarily due to the capacitance effect. When a small extra length l of transmission cable is connected to the end of our RF probe, the reflected

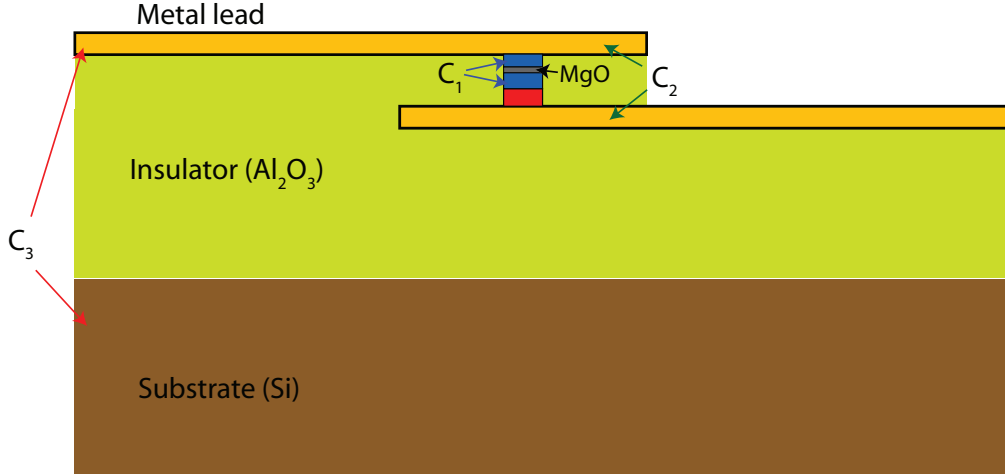


Figure 3.6: Illustration of the various origins of capacitance for a MTJ device

microwave is also expected be delayed by a certain amount of time $\Delta t \sim nl/c$, where c is the speed of light in vacuum, and n is an analogous index of refraction which is greater than 1 and typically on the order or unity, reflecting the reduced speed for surface microwave propagation. As an estimate of order of magnitude, we consider an extra length of $200 \mu\text{m}$ of metallic leads on the device connected into the circuit, taking $n = 2$, we get $\Delta t = 1.3 \text{ ps}$, which translates to a phase delay of about 0.04 rad , smaller but at the same order as we measured. Therefore our measured capacitive delay could be partly due to this effect from extra transmission distance. We did not find a good way to separate the capacitive effect from the extra distance effect. Either effect produces a constant time delay, or equivalently a phase delay proportional to RF frequency. It is probably difficult to quantify the effective extra transmission distance since it is related to the modeling of distribution of electromagnetic waves on the particular contact geometry and involves material properties as well. However, our measured phase delay should place a reliable upper bound for possible capacitance in our MTJ devices.

On a separate route, one can make a rough estimate of the capacitance of the

device based on its relevant dimensions. There are three areas on a typical MTJ device forming capacitances that one can think of (Fig. 3.6). The first capacitance C_1 comes from the MTJ device itself between the two ferromagnetic electrodes across the MgO tunnel barrier. Using an area of $S_1 \sim 90 \times 90 \text{ nm}^2$, a spacing distance of $d_1 \sim 1 \text{ nm}$, and a reported dielectric constant of $\epsilon_1 \sim 9.8$ for MgO, one can estimate that $C_1 = \epsilon_1 \epsilon_0 S_1 / d_1 \approx 7 \times 10^{-16} \text{ F}$. The second capacitance C_2 comes from the overlapping area between the top contact and the bottom contact. Such an overlapping area for our devices from Hitachi is $S_2 \sim 25 \mu\text{m}^2$, separated by 100 nm of alumina, whose dielectric constant is around 9, so $C_2 \approx 2 \times 10^{-14} \text{ F}$. The third capacitance C_3 is between the metallic lead and the substrate, separated by 7 μm of alumina. If we estimate the signal lead has an area of $100 \times 30 \mu\text{m}^2$, $C_3 \approx 3 \times 10^{-14} \text{ F}$. It should be noted that the Si substrate is a semiconductor instead of grounded metal, so that the capacitance with substrate has to be considered to be connected in series with some appreciable resistance and may not contribute a capacitive shunting as large as C_3 suggests. Therefore we think the major capacitance is probably attributable to C_2 and to some degree C_3 , the same order as we have estimated in our phase shift measurement.

Assuming we have a parasitic capacitance of $5 \times 10^{-14} \text{ F}$ at maximum connected in parallel to our device, how much does it affect our time-domain ST-FMR measurement? Our calculation shows that it produces an extra relative phase delay of $\Delta\phi = (50\Omega/R_0)2(50\Omega)\omega C$ between the magnetic response signal and the reflected drive voltage. This calculation is included as an appendix for this chapter. For typical sample parameters $R_0 = 350 \Omega$ and $\omega = 2\pi(5\text{GHz})$, this extra phase is less than 0.03 rad, slightly smaller than our fitting uncertainty (0.04 rad), but we have taken it into account in our experimental uncertainty for Φ_m .

3.4 Full-Range Bias Dependence of the Spin Transfer Torque

Now that we have a complete characterization of the device, we can calculate the in-plane and perpendicular component of the spin transfer torkance vector, $d\vec{\tau}/dV$, based on our time-domain ST-FMR measurements using our macrospin model laid out in section 3.2. For example with the data of Fig 3.4, we measure $\partial\tau_{||}/\partial V = (0.44 \pm 0.10)(\hbar/2e)k\Omega^{-1}$, $\partial\tau_{\perp}/\partial V = (0.47 \pm 0.03)(\hbar/2e)k\Omega^{-1}$ at $V = 0.38$ V. From Eq. (3.25), the in-plane torkance is proportional to $A_{n,max} \sin \phi_m$, while the perpendicular torkance is proportional to $A_{n,max} \cos \phi_m / \Omega_{\perp}$. It should be noted in particular, the elliptical factor, Ω_{\perp} (≈ 5 in our experiments), makes the perpendicular torkance about 5 times more effective in driving magnetic precession. An experimental uncertainty $\delta A_{n,max}$ in precession amplitude is passed on to both torkance components in a proportional fashion, which is at most a few percent in our measurement. On the other hand, an uncertainty of each 0.01 rad on phase $\delta\Phi_m$ produces an uncertainty in the perpendicular torkance whose absolute value is equal to 1% of in-plane torkance divided by Ω_{\perp} , and an uncertainty in the in-plane torkance whose absolute value is equal to 1% of the perpendicular torkance times Ω_{\perp} . Therefore, our measurement of the in-plane torkance has much higher uncertainty than the perpendicular torkance in terms of absolute values, and determining the phase is the dominant uncertainty in our final result of the torkances, especially for the in-plane component.

It should be noted that in response to a microwave excitation there is often more than one resonance mode in our devices at a given external field, usually one large amplitude mode and a second mode at least a factor of 3 smaller in amplitude [see Fig. 2.7(b)]. We suspect that the smaller mode

involves oscillation of the magnetizations in the SAF, and that there may be coupling to the free layer oscillations. To limit the effects of mode coupling, for the data in this paper we have selected the direction and magnitude of the external magnetic field so that any secondary resonance mode is weak and well-separated in frequency from the primary resonance. The primary resonance can be identified with oscillations of the free magnetic layer based on the sign of the resonant response in the DC-detected ST-FMR spectrum [78] and the sign of the bias dependence of the magnetic damping as described by Eq. (3.27) or Eq. (2.24).

3.4.1 Combination of DC Detected and Time-Domain Detected ST-FMR

By varying the amplitude of the square-wave pulse (and therefore DC bias), we can measure the spin transfer torkance for any value of $|V|$ above about 0.1 V for our samples. Because the bias current in our time-domain ST-FMR also functions as a detection current to convert the resistance oscillations to measurable voltage oscillations, our method is inherently superior for the high bias range, and the signal-to-noise ratio becomes worse at low bias. On the other hand, the traditional DC mixing voltage detection of ST-FMR provides accurate measurements of spin transfer torque at low-bias regime, and can be extended to a moderate bias range, $|V| < 0.2$ V in these samples, with numerical corrections for the non-mixing artifact terms (see Chapter 2). Therefore, these two different detection techniques of ST-FMR are ideally complementary to each other and allow us to achieve a full-bias characterization of spin transfer

torque vector.

Figures 3.7(a) and (b) show our measurements of $d\tau_{||}/dV$ and $d\tau_{\perp}/dV$ over a large bias range for two samples. We display data up to $|V| = 0.6$ V because the distribution of critical voltages for sample degradation or breakdown in our low-RA MTJs extends below 0.7 V. We have normalized the torkances by $\sin \theta$, because this is the angular dependence predicted for MTJs, [85, 99] and indeed we find good agreement with this dependence within our experimental uncertainty. The figures show both the results of our new time-domain measurements for $|V| > 0.1$ V (square symbols), and the results in the same samples of the older DC-detected ST-FMR technique [76, 80] for $|V| < 0.2$ V (triangles). In the range of overlap, 0.1 V $< |V| < 0.2$ V, we find excellent quantitative agreement between these two independent techniques with no adjustment of parameters. This cross-check provides added confidence that both methods are quantitatively correct. By integrating the torkances with respect to voltage, we can plot the bias dependence of the spin-torque vector $\vec{\tau}(V)$ itself [Fig. 3.7(c) and (d)].

We observe that the in-plane component of the spin transfer torkance has an appreciable negative slope in the bias range $|V| < 0.2$ V in all of our MgO-based tunnel junctions, and is a factor of 3-4 stronger at high negative bias ($V < -0.2$ V) than at high positive bias ($V > 0.2$ V). Although this is a weaker bias dependence than had been suggested (incorrectly) in the past by uncorrected DC-detected ST-FMR measurements [79, 80], the in-plane component of the spin torque after integration does show significant nonlinearity and can become stronger by approximately a factor of 2.5 at large negative bias compared to positive bias [Fig 3.7(c),(d)]. While an asymmetric bias dependence of the in-plane

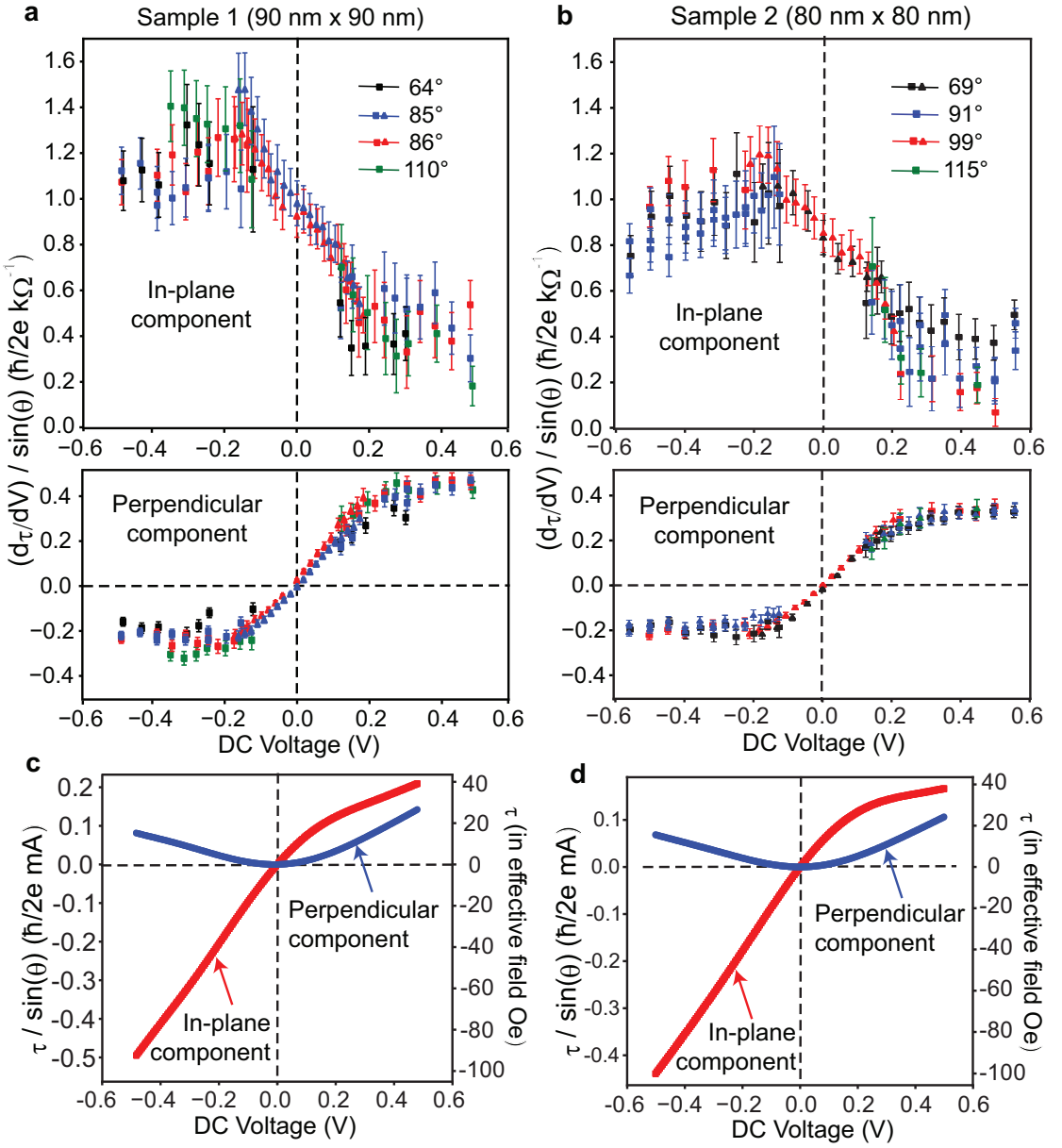


Figure 3.7: Measured bias dependence of the spin-transfer torque vector. (a) and (b), in-plane and perpendicular components of the torkance vector $d\vec{\tau}/dV$ (normalized by $\sin \theta$) as a function of bias voltage for sample 1 (a) and sample 2 (b), for different initial offset angles, θ . The square symbols correspond to our time-resolved measurements and the triangles to DC-detected ST-FMR on the same samples. (c) and (d), in-plane and perpendicular components of the spin-transfer torque $\vec{\tau}$ (normalized by $\sin \theta$) for sample 1 (c) and sample 2 (d), determined by integrating the data in (a), (b) after averaging over the different initial offset angles.

torkance is consistent with qualitative predictions [81, 83, 100, 101] and ab initio calculations at low bias [84], we suggest that a more quantitative theoretical understanding of the asymmetry at high bias should be a priority. Regarding the perpendicular component of the torkance, it had been known previously from calculations [81] and DC-detected ST-FMR measurements [76, 79] that near $V = 0$ this component of the torkance in a symmetric MTJ has a linear dependence on bias (so that the perpendicular torque $\propto V^2$). We now observe departures from this behavior at high bias, in that $d\tau_{\perp}(V)/dV$ saturates (and $\tau_{\perp}(V)$ crosses over to an approximately linear dependence). Interestingly, the saturated value of perpendicular torkance differs significantly between positive and negative bias, which is forbidden by symmetry for an exactly symmetric MTJ when spin-flip scattering is negligible [14]. We suspect that this may be the result of a slight asymmetry in the structure of our MTJs (e.g., the average Co:Fe ratio in the reference layer of the SAF is 1.5:1 while in the free layer it is 1.25:1) or in the distribution of defects in the tunnel barrier or at the interfaces between the electrodes and the barrier. The strength of the perpendicular torque at the highest biases we measure is equivalent to a 30 Oe magnetic field, strong enough to play an important role in magnetic dynamics.

3.4.2 Bias Dependence of Effective Damping

One possible caveat to the validity of our measured resistance ring-down and therefore the measured spin transfer torque vector is whether the observed decaying oscillation is due to the dephasing over time after averaging or a true decrease in amplitude of the magnetization precession. These two can be distinguished by a quantitative analysis of the decay rate in our measurement.

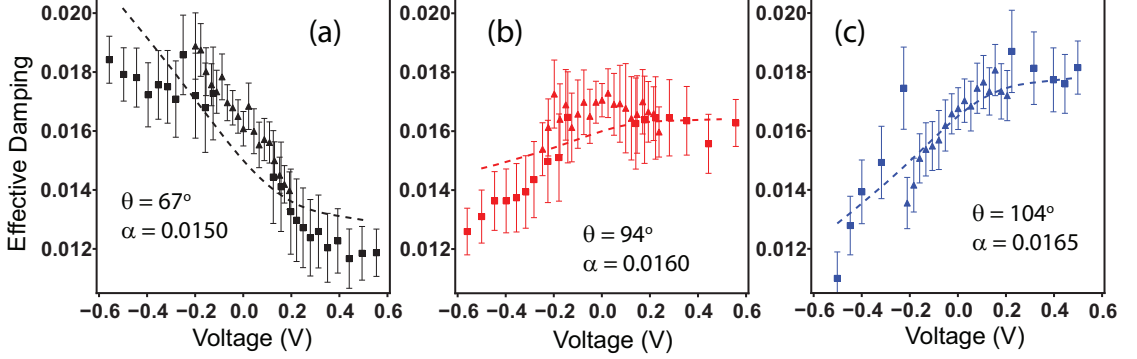


Figure 3.8: Measurement of effective damping. (squares) Bias dependence of the effective damping α_{eff} determined from the decay rate Γ of the resistance oscillation in the time-resolved measurements (averaging over RF driving frequencies close to the resonance peak). (triangles) Bias dependence of the effective damping determined from the linewidth σ of the resonance peak in DC-detected ST-FMR measurements. The different panels correspond to different initial offset angles θ for the same sample (sample 2). The dashed lines show the effective damping predicted by Eq. (3.34), using the in-plane torkances measured in the time-resolved experiment. Slightly different values of the Gilbert damping α were used for different offset angles to provide better fits of the data.

As analyzed in Section 3.2, the decay rate Γ measured from the time-domain resistance oscillations and the resonance half linewidth σ measured using DC-detected ST-FMR should be equal and can be expressed in terms of the effective damping α_{eff} of the free layer defined as $\Gamma = \sigma = \alpha_{eff}\gamma M_{eff}(N_x + N_y)/2$. Any dephasing effect would produce an extra decay and increase our decay rate to exceed the corresponding half-linewidth of the ST-FMR resonance.

Using $N_x \approx 4\pi$, $N_y \approx 0$, and $4\pi M_{eff} = 13 \pm 1$ kOe, we plot in Fig. 3.8 the bias dependence of the effective damping we determine from both Γ (using the time-resolved measurements) and σ (using DC-detected ST-FMR). We observe quantitative agreement between the two methods within our experimental uncertainties. From this we conclude that the time-domain decay rate corresponds to the true decay of amplitude for the magnetization dynamics, with negligible

contribution from dephasing between repetitions of the measurement. In the presence of significant dephasing between experimental repetitions, the time-domain oscillations would decay more quickly than the damping rate indicated by the ST-FMR linewidth.

From Eq. (3.26), the effective damping should be related to the Gilbert damping and the spin transfer torque as:

$$\alpha_{eff} \approx \alpha - \frac{1}{M_s V_{free} M_{eff} (N_x + N_y)} \left[\tau_{||,max} \cos \theta + \frac{(50\Omega)}{R_0 + (50\Omega)} \frac{\partial V}{\partial \theta} \right]_I \frac{\partial \tau_{||,max}}{\partial V} \sin \theta \quad (3.34)$$

The Gilbert damping coefficient α for the samples can be determined from the data in Fig. 3.8 near zero bias. We find $\alpha = 0.016 \pm 0.001$ for sample 2 (shown in Fig 3.8) and $\alpha = 0.014 \pm 0.001$ for sample 1 (not shown). These values are at the high end of the typical reported value of Gilbert damping of CoFeB films [89], possibly due to sidewall oxidation [102] or coupling to the SAF pinned layer. Using our measured spin torque and torkance results (Fig. 3.7 of the main paper), we can check whether the bias dependence of the damping that we measure is consistent with the prediction in Eq. (3.34) (dashed lines in Fig. 3.8). We find good agreement, to within the level of uncertainty of the damping measurements. We should also note that the bias dependence of the effective damping could also be affected by factors such as heating and/or changes in the degree of spatial uniformity for the magnetic precession that are not included in our model.

3.4.3 Comparison with Other Methods of Spin Torque Measurements – Role of Heating and Spatial Non-Uniformity

One of the advantages of our ST-FMR technique is its insensitivity to heating. ST-FMR is a definitive dynamic behavior that scales proportionally with the strength of the spin transfer torque, and does not rely on finite temperature to occur. At least for a circular sample, an oscillatory temperature should not drive magnetic precession with a definite phase relationship relative to the input RF signal. Therefore, the presence of heating should not give rise to any artifact signals in a time-domain experiment in which the measurements are made following the end of the drive pulse. For a non-circular sample and an equilibrium free-layer orientation away from symmetry direction for the magnetic anisotropy, it is possible for oscillatory heating to drive precession via modulation of the magnetic anisotropy fields, but the torques we measure show reasonable agreement with the expected angular dependence ($\propto \sin \theta$) without this effect, which indicates that it is not a significant factor. In this case the effect of heating could only come into play through the temperature dependence of the coefficient of proportionality, most notably a decrease in the average moment of the free layer in our samples at high bias, therefore increasing slightly the apparent value of the torkances for large $|V|$. However, we anticipate that this is a small effect unless the bias is high enough that the effective magnetic temperature approaches the Curie temperature (> 800 K).

One may also question the applicability of the macrospin approximation we use to extract the value of the spin-torque vector from our measurements. Our measurements are designed to minimize the likelihood of any significant spatial nonuniformities in the magnetic dynamics, so that the macrospin

model should be a good approximation. We employ small, circular samples (as small as 80 nm diameter) with an in-plane equilibrium magnetic state, take measurements in an external in-plane magnetic field of 200-400 Oe that promotes a uniform initial state, and excite only small angle precession from this state ($\sim 1^\circ$) mean deflection. However, even in the presence of small deviations from the macrospin approximation, the results of ST-FMR with time-domain detection should be largely insensitive to these deviations, particularly relative to previous techniques for determining the spin torque vector. Our measurements begin with a large equilibrium offset angle between the magnetic orientation of the reference layer and the average orientation of the free layer, so that the spin torque applied throughout the free layer is large, in the same direction, and approximately uniform. By measuring resistance, we determine, to a good approximation, the average deflection induced by the spin torque over the entire free layer. Via the time-domain measurement, we also measure directly the oscillation decay rate integrated over the whole sample. Under these circumstances, the average precession amplitudes we measure, and hence the values of the spin-torque vector that comprise our final result, should be determined by conservation of spin angular momentum integrated over the whole free layer (total spin angular momentum absorbed in each cycle equals spin angular momentum lost to damping in each cycle), even if the magnetic dynamics may contain small spatial nonuniformities.

Other than ST-FMR experiments, there are many reported measurements of spin transfer torque, generally falling into two categories: thermally excited ferromagnetic resonance (TE-FMR) and thermally assisted switching. Although with the same underlying dynamic equations as ST-FMR yielding the same formula for resonance linewidth and frequency [42, 92], TE-FMR is an effect

originating from finite temperature and simply does not occur at $T = 0$. Spin torque manifests itself as a secondary effect in modulating the linewidth and frequency (unlike ST-FMR, where we measure the precession amplitude which is a primary effect). Bias dependent heating could induce shifts in resonance frequency and/or linewidth. The spatial uniformity of a given magnetic normal mode could also change as a function of bias due to Oersted field, which makes its frequency and/or linewidth dependent on bias as well. These effects directly add to or compete with the spin torque effects in modulating the frequency and/or linewidth. With practical numbers, since spin torque produces much more significant changes to the linewidth (by in-plane component) than to the frequency (by perpendicular component), the TE-FMR linewidth provides reasonable measurement of in-plane torque just as the ST-FMR linewidth, but the frequency shift is mostly dominated by effects other than spin torque [80]. Even for the in-plane torque measurement based on linewidth, TE-FMR, as a measurement of noise spectrum, typically has lower signal level to achieve good precision. Moreover, TE-FMR cannot to be easily extended to high bias regime because it relies on continuous DC current to bias the MTJ for spectrum measurement.

Thermally assisted switching is another process in which finite temperature plays a significant role. There are several drawbacks with this method for spin torque measurement. Firstly, one has to include the bias-dependent Joule and Peltier heatings, whose quantitative models are still under debate. Secondly, one has to include the recently discovered and largely unexplored bias-dependent magnetic anisotropy which alters the energy barrier [69, 87]. Thirdly, even if one accounts for these effects correctly, this measurement fits a global set of data across the full bias range to determine one or two parameters

about the overall strength of the spin transfer torque, which is far from a point-to-point measurement. In particular, since spin torque-driven magnetic switching is predominantly a high bias effect, the fitting results can hardly include any weight of the property of spin torque in the low bias range.

Furthermore, compared with these two methods, ST-FMR offers differential detection that measures $d\tau/dV$ instead of τ . This may not be important if one only cares about of the absolute value of spin torque at a given bias, but for a bias-dependence study it allows direct measurement of the incremental strength of spin torque for electrons at different energy. For methods that measure τ itself it is difficult to achieve sufficiently small uncertainty to allow numerical differentiation.

ST-FMR also allow one to closely study the angular dependence of the spin transfer torque. However, this is limited in our current device and setup by the low signal at near parallel or anti-parallel state and the fact that we need to tune angles to minimize mode coupling. With limited data, we do not see a meaningful deviation from $\sin \theta$. With a device having an extended fixed layer, the second limitation may be relaxed, and more detailed studies can be enabled. For in-plane torque at near parallel or anti-parallel state, one may consider using TE-FMR for some complementary characterization.

3.4.4 Discussions and Implications

Our measured results for the spin transfer torque in MTJs have important consequences for interpreting many types of spin-torque experiments. Up to now, it has been assumed almost universally in analyzing experimental data

that the bias dependence of the spin torque vector can be described by the simplest possible low-order Taylor series approximations, $\tau_{||}$ and $\tau_{\perp} = a + bV + cV^2$ with a , b , and c constants. This is often done, for example in extrapolating from finite-temperature measurements to determine zero-temperature critical currents and activation energy barriers for switching [36–39], and it is also the underlying assumption in analyzing the statistics of switching to determine the strength of the spin torque vector [40, 41]. Our measurements indicate that these Taylor-series approximations can become seriously inaccurate at high bias, so that extrapolations based on these approximations should not be expected to yield quantitative results. Furthermore, analyses of asymmetric MTJs have generally assumed that the main effect of the asymmetry on the perpendicular torque is to add a linear bias dependence to $\tau_{\perp}(V)$, together with the quadratic dependence present for symmetric junctions [41]. The difference in the saturated values of $d\tau_{\perp}/dV$ for positive and negative V that we observe at high bias suggest that the effects of asymmetry may be significantly larger at high bias than at low bias, and may take functional forms different than can be expressed by a lowest-order Taylor approximation.

The asymmetry we observe for the in-plane spin torque may help to explain the observation that the critical voltage for spin-torque induced switching from the antiparallel (AP) to parallel (P) configuration in MTJs (negative bias in our convention) is often lower than for P-to-AP switching [41, 79, 103–106]. However, we note that in the thermally-assisted switching regime this effect can be somewhat mitigated by contribution from the perpendicular spin torque, which always favors the AP state for our MTJs.

3.5 Applicability on other MTJ devices and Potential Improvements

Our time-domain ST-FMR technique should be applicable to other MTJ devices as long as the signal/background ratio is high enough to resolve the magnetic precession signal out of the background of the residual RF driving pulse. To achieve good signal/background ratio, low resistance, high TMR, and low damping is desired. More specifically, the signal strength is exactly described by the normalized amplitude A_n in our analysis, and from Eq. (3.19) and assuming that the MTJ resistance is generally much higher than 50Ω so that $(R_0 + (50\Omega))(R_0 - (50\Omega)) \approx R_0^2$, we have:

$$A_{n,max} e^{i\Phi_m} \approx \left(\frac{50\Omega}{R_0^2 V_{free}} \right) \frac{\partial V}{\partial \theta} \Big|_I \frac{\gamma}{\sigma} \left[\frac{\partial \tau_{||}}{\partial I} - i \frac{\gamma N_x M_{eff}}{\omega_m} \frac{\partial \tau_{\perp}}{\partial I} \right] \quad (3.35)$$

where the factors $(\partial V / \partial \theta)|_I$ and $(\partial \vec{\tau}) / (\partial I)$ are mostly affected by the TMR of the device, R_0^2 reflects the dependence on resistance of the MTJ device, and σ is mostly controlled by the damping of the magnet. Eq. (3.35) implies that the resistance area product (RA) is the single most critical factor in achieving good signal level in our experiment, because for a given dimension of the free layer (with a fixed V_{free}), the signal/background ratio is inversely proportional to RA -squared. This is because with all else equal, lower RA MTJs not only allow inversely proportional enhancement on precession angle (due to stronger spin transfer torque from larger tunneling current), but also makes inversely proportional improvement on better impedance matching with 50Ω transmission line. Therefore, we did not carry out the same time-domain ST-FMR measurement on the $RA = 12\Omega\mu\text{m}^2$ devices from IBM that we measured with DC-detected ST-FMR as presented in Chapter 2. By our estimate, these devices would produce signal/background ratio about 30 times worse than that

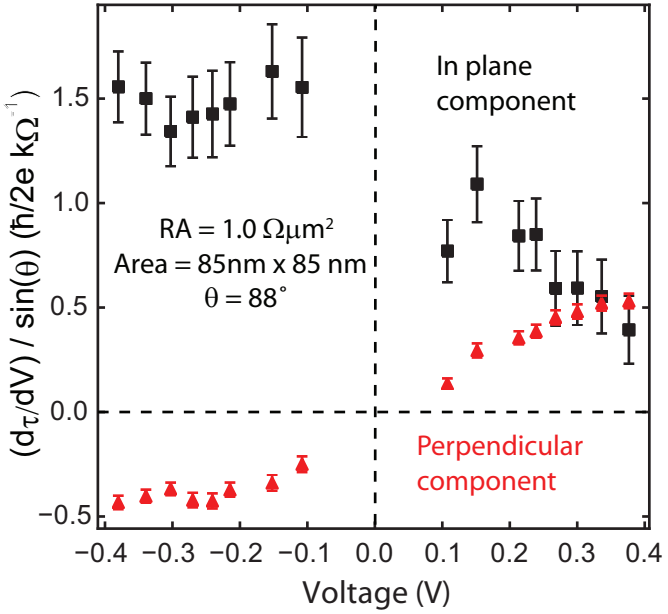


Figure 3.9: Bias dependence of the spin-transfer torkance vector measured by time-domain ST-FMR at an offset angle of $\theta = 88^\circ$ in a circular ($85 \times 85 \text{ nm}^2$) MTJ device with $RA = 1.0 \Omega \mu\text{m}^2$, TMR = 89%.

for the $RA = 1.5 \Omega \mu\text{m}^2$ Hitachi samples. From the data quality of the damped resistance oscillation and the fitting uncertainty of the precession amplitude and phase, my guess is that we can probably apply this technique for high bias spin torque measurements using MTJs with RA up to $5 \Omega \mu\text{m}^2$ with similar TMR ratio.

For lower RA MTJs, of course this technique becomes readily applicable. For a quick check with a different set of MTJ devices, we measured a couple of samples from a newer batch of MTJ devices also from Hitachi with nominal $RA = 1.0 \Omega \mu\text{m}^2$. Fig. 3.9 shows our measured bias-dependence of spin transfer torkance in one of those samples at an offset angle of $\theta = 88^\circ$. This device has a TMR ratio of 89% and a free layer area of $85 \times 85 \text{ nm}^2$. The overall amplitude of the torques in this device is about a factor of 1.5 stronger than in the $RA = 1.5 \Omega \mu\text{m}^2$ devices with approximately the same junction area as reported in the previous section. This is as expected from the difference in the conductance,

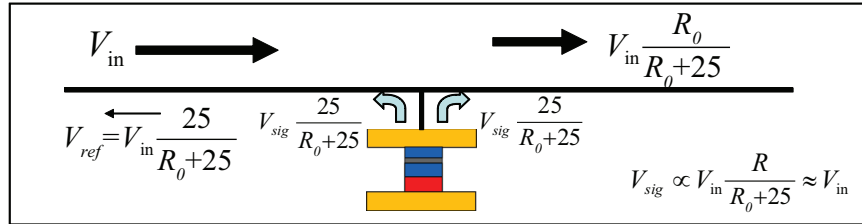
and hence the current density. However, the bias dependence for the two types of samples is very similar.

It should also be noted that for the same RA , the experiment runs better for samples with larger area due to better impedance matching even though the precession angle does not have significant dependence on the sample area at a given RF voltage. In the context of pure spin torque measurement this is probably not particularly useful since larger area may cause more non-uniform magnetic excitations that we try to minimize. However, in some studies if large sample area is not a drawback, increasing the sample area could be a tool to be used in our favor.

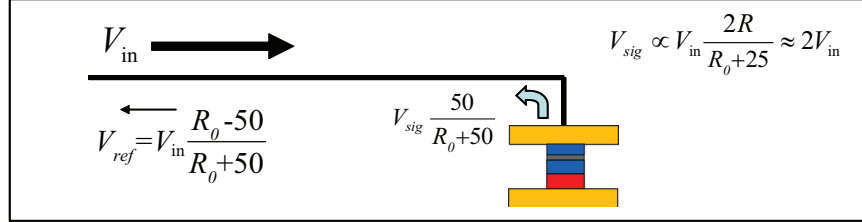
In principle, impedance mismatch is by no means a problem intrinsic to either MTJ devices or our measurement scheme. Imagine that if the transmission line and the oscilloscope are designed to have a higher impedance, all of our measurements will operate in exactly the same way, but with much better signal/background ratio. There are practical ways to potentially improve impedance matching externally for a given MTJ. One can make an LC impedance matching circuit either with lumped elements or with lithographically-defined on-chip elements. With proper choice of capacitor and inductor one can realize near-perfect absorption of incoming microwave voltage by the MTJ device and therefore eliminate the background reflection. This type of “tailored” impedance matching network will only work for one resistance at a time and over a narrow bandwidth (typically tens of MHz), but they can still play an important role for specialized future studies when impedance matching is critical.

Another way to improve impedance matching is to connect a resistor in

(a) Reflection Measurement with an Extra Transmission Path



Pure Reflection Geometry



(b) Frequency Divider

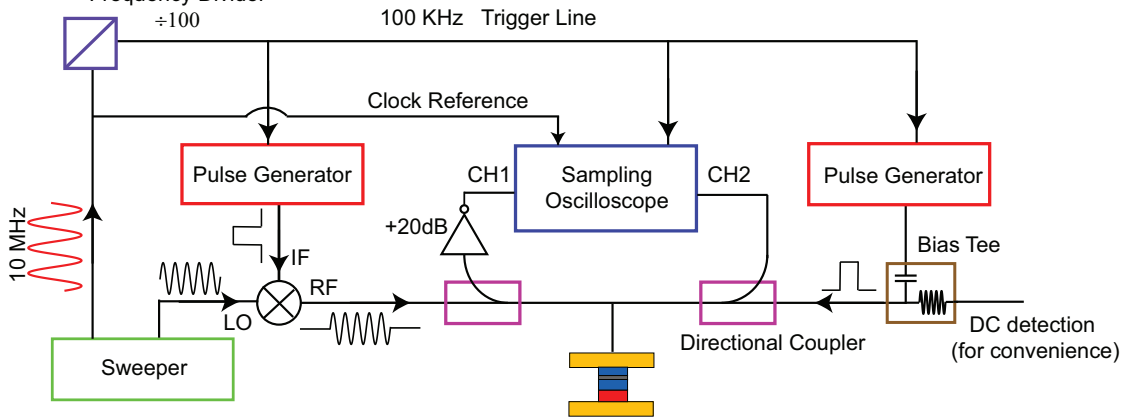


Figure 3.10: An alternative measurement circuit for time domain ST-FMR experiment. (a) Comparison of the precession signal and background reflection before and after an extra transmission line is connected to the MTJ device. (b) Schematic of a two-probe version of measurement circuit for the time domain ST-FMR experiment.

parallel to the MTJ device. For example, a 50Ω parallel resistor will bring the resistance of the total end load to close to 50Ω (assuming the resistance of the MTJ $R_0 \gg 50\Omega$) and strongly reduce the microwave reflection. This method does not make the MTJ absorb more RF driving power or better couple the resistance oscillation to the oscilloscope, but it does suppress the background reflection significantly and can be used to improve signal/background ratio. Moreover,

there is a “cheating” way that one can conveniently place a parallel resistor: just connect an extra RF probe and transmission cable to the contact pads on the MTJ device. This extra transmission cable, with $50\ \Omega$ in impedance, diverts most of the microwave away from reflecting into the original cable that carries the incoming microwave. This is a broadband method and should be directly applicable to our time-domain ST-FMR measurement. A simple quantitative analysis is illustrated in Fig. 3.10(a). When there is an extra transmission path, the reflected microwave has an amplitude a factor of $(25\Omega)/[R_0 + (25\Omega)]$ smaller than the incoming microwave V_{in} , dramatically weaker than the reflection amplitude of $V_{in}[R_0 - (50\Omega)]/[R_0 + (50\Omega)]$ in a pure reflection geometry. At the same time, the magnetic precession signal is reduced by almost a factor of four, with a factor of two coming from the reduction of actual voltage across the MTJ, and another factor of two from loss of the precession signal from the other transmission line. Overall this method still promises an improved signal/background ratio, and therefore we have designed the circuit shown in Fig. 3.10(b) to test this idea.

By having two transmission lines connected to the device, we can now separate the RF pulse and the DC pulse to the two lines, saving the use of a power combiner (as in our original circuit 3.1) which causes loss of power and unwanted reflections. We can also use two directional couplers and source both the transmitted signal and reflected signal into two channels of the oscilloscope so that we can measure simultaneously. The transmitted signal is perfect for measuring the amplitude and phase of the RF driving pulse itself, and the reflected pulse is better suited for measuring the magnetic precession signal with a significantly reduced background. In theory this is a better design than the original version published in ref. [82] and presented in the main content

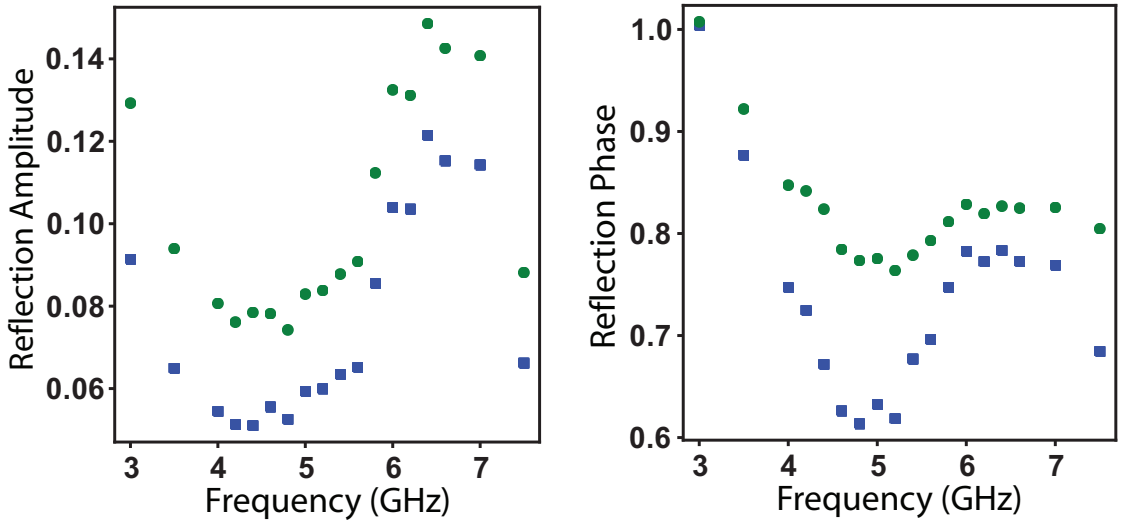


Figure 3.11: An unresolved puzzle of microwave reflection off an MTJ device in the presence of an additional transmission line. (a) The amplitude of the reflected microwave (measured by CH1 in Fig. 3.10) as a function of RF pulse frequency for a high-resistance state and a low-resistance state of an MTJ device, normalized by the amplitude of the same microwave pulse reflected off an infinite impedance (measured with the RF probe lifted/disconnected). (b) The phase of the reflected microwave (also measured by CH1 in Fig. 3.10) as a function of RF pulse frequency, relative to the same microwave pulse reflected off an infinite impedance.

of this chapter (Sections 3.1-3.4). However, there remains a major unsolved puzzle with respect to quantitative modeling of the microwave reflection and its mysterious frequency dependence. Fig. 3.11(a) shows the amplitude of the reflected microwave (measured by CH1 in Fig. 3.10) as a function of RF pulse frequency for a high-resistance state and a low-resistance state of an MTJ device, normalized by the amplitude of the same microwave pulse reflected off an infinite impedance (measured with the RF probe lifted/disconnected). Fig. 3.11(b) shows the phase of the reflected microwave (also measured by CH1 in Fig. 3.10) as a function of RF pulse frequency, relative to the same microwave pulse reflected off an infinite impedance. Without taking account of parasitic capacitances, one expects no frequency dependence on the reflection

amplitude and a constant π phase. The reflection amplitude is indeed reduced dramatically to around 1/10 of a perfect reflection. However, the strong frequency dependences of both amplitude and phase are very bizarre. The non-monotonic frequency dependences suggest some sort of LC resonance effect, but even after adding a few capacitive and inductive elements, so far I have not been able to establish a model that can explain the data. There may be complications related to the coupling between the two RF probes (which are very close and almost in contact with each other) together with the parasitic capacitance of the device. Without a complete understanding of the microwave circuit in this geometry, one cannot quantitatively analyze time-domain ST-FMR using this method yet.

3.6 Other Studies Enabled by Time-domain ST-FMR

Applied more broadly, we expect that our time-resolved measurement technique will also be able to provide new insights about a wide range of other interesting phenomena in MTJs, such as nonlinear magnetic dynamics in response to large spin torques [107], phase locking of magnetic auto-oscillations to microwave inputs [108, 109], and spin torques in very low-RA MTJs for which pinholes may contribute new effects [93, 98].

In particular, our demonstration of time-resolved ST-FMR potentially opens an extra dimension in measuring magnetization dynamics - dynamic response to excitations of different frequencies. Previous studies of the magnetization dynamics in the power emission spectrum [17] or in the time domain [18] allow detection of broadband dynamic response, but only excited by a DC current. On

the other hand, the DC detected ST-FMR allows excitation of the nanomagnet at selected frequencies, but only detected through a DC voltage. Our time-domain technique, with further development, could potentially realize “two-dimensional ST-FMR”, where we tune through a range of frequencies to excite the nanomagnet, and for each excitation frequency the reaction of the system is detected across a broad range of response frequencies. This would provide detailed information about the coupling between different modes. So far since we can only resolve the damped oscillation of MTJ resistance for several (less than 10) precession periods, it is difficult to perform a Fourier transform to track various frequency components. However, we have some preliminary examples that we can use to gain valuable information about the dynamics of a nanomagnet beyond the macrospin model by accessing the time-resolved response to various frequencies.

3.6.1 Selective Excitation of Different Magnetic Normal Modes

A MTJ device is much more complex than a single-mode harmonic oscillator. There are often multiple magnetic normal modes [110] such as shown in Fig. 2.7(b) for our devices from Hitachi. The underlying picture of different magnetic modes in MTJ systems is still an open question. These modes have different resonance frequencies, and we can study them in the time domain by applying RF excitation pulses of selected frequencies. In order to measure the spin transfer torque and its bias dependence, we made efforts to identify the primary resonance corresponding to the most spatially uniform precession mode of the magnetic free layer, and selected such magnetic field conditions that other modes were weak and well-separated from the major resonance. Here to

study multi-mode behavior, we select magnetic field conditions when there is a strong second resonance mode, and sweep the frequency of our RF driving pulse across the whole range covering both resonances.

Figure 3.12(a) shows our measured normalized amplitude, relative phase and frequency of the decaying resistance oscillation after the RF driving pulse as a function of RF driving frequency for a MTJ device (sample 3) nominally identical to sample 1 we presented in section 3.1-3.4. Sample 3 has an area of $90 \times 90 \mu\text{m}^2$, a parallel resistance of 272Ω and a TMR ratio of 85%. Two distinctive modes can be identified with resonance frequencies at $f \approx 5.5 \text{ GHz}$ and $f \approx 7.5 \text{ GHz}$. The frequency of the damped precession follows one of the two intrinsic frequencies that can be excited respectively by either a lower-frequency ($f < 7.2 \text{ GHz}$) or higher-frequency ($f > 7.2 \text{ GHz}$) driving pulse. The oscillation amplitude shows a resonant peak when the driving frequency matches either of the intrinsic frequencies. The two modes show very different oscillation phases Φ_m at resonance, which can provide valuable insights into the nature of the two modes. As we have discussed in Fig. 3.4, a uniform free-layer mode induced by in-plane spin transfer torkance should give $\Phi_m = 0$ (or equivalently 2π) at positive bias and $\Phi_m = \pi$ (or $-\pi$) at negative bias (due to the negative sign from $(\partial V / \partial \theta)|_I$ in Eq. (3.19)). A uniform free-layer mode induced by perpendicular spin transfer torkance should give $\Phi_m = -\pi/2$ (or equivalently $+(3/2)\pi$) at both positive and negative bias (since the sign change of perpendicular torkance cancels the sign change from $(\partial V / \partial \theta)|_I$). The data in Fig. 3.12(a) are measured at a bias voltage of $V = -0.48 \text{ V}$, which should lead to $\Phi_m \approx 4.0 - 4.3$ (between π and $(3/2)\pi$) for pure uniform free layer precession, using our measured bias dependence of the spin transfer torkance (Fig. 3.7). The measured Φ_m for the low frequency resonance [the large peak

in Fig. 3.12(a)] agrees very well with the prediction for a uniform free layer mode, while the high frequency resonance [the small peak in Fig. 3.12(a)] has a precession phase dramatically different (at $\Phi_m \approx 2$). One would guess the high frequency resonance is a fixed layer mode, but we estimate that at $V = -0.48$ V a pure fixed layer mode should display a phase at resonance $\Phi_m \approx 4.8 - 5.1$. The contribution of an in-plane torkance on the fixed layer precession has the same phase as for the free layer, but the effect of precession on TMR is opposite, giving $\Phi_{m,fixed} = 0$ or 2π at negative bias. The perpendicular torkance on the fixed layer is in the opposite direction to that on the free layer, which cancels the sign change from the opposite TMR contribution, giving an unchanged phase $\Phi_{m,fixed} = -\pi/2$ or $+(3/2)\pi$. Therefore the high frequency mode is not a fixed mode either. Our best guess so far is that the high frequency mode describes a coupled precession of both magnetic layers. A more quantitative modeling of the coupled precession mode would allow a comparison with our experimental data.

The high-bias capability allows us to study how these modes evolve with bias. The low-frequency mode in Fig. 3.12(a) dominates at negative bias, but surprisingly it becomes weaker than the high-frequency mode at positive bias [Fig. 3.12(b)]. For comparison, we also plot on the same scale the normalized precession amplitude for sample 1 (which is nominally identical to sample 3) under a similar magnetic field, which only shows one strong resonance in the frequency range we are interested in. The amplitude of this single mode of sample 1 is comparable to the stronger mode of sample 3 for either bias (or, in another way to speculate, the amplitudes combined of the two modes in sample 3)

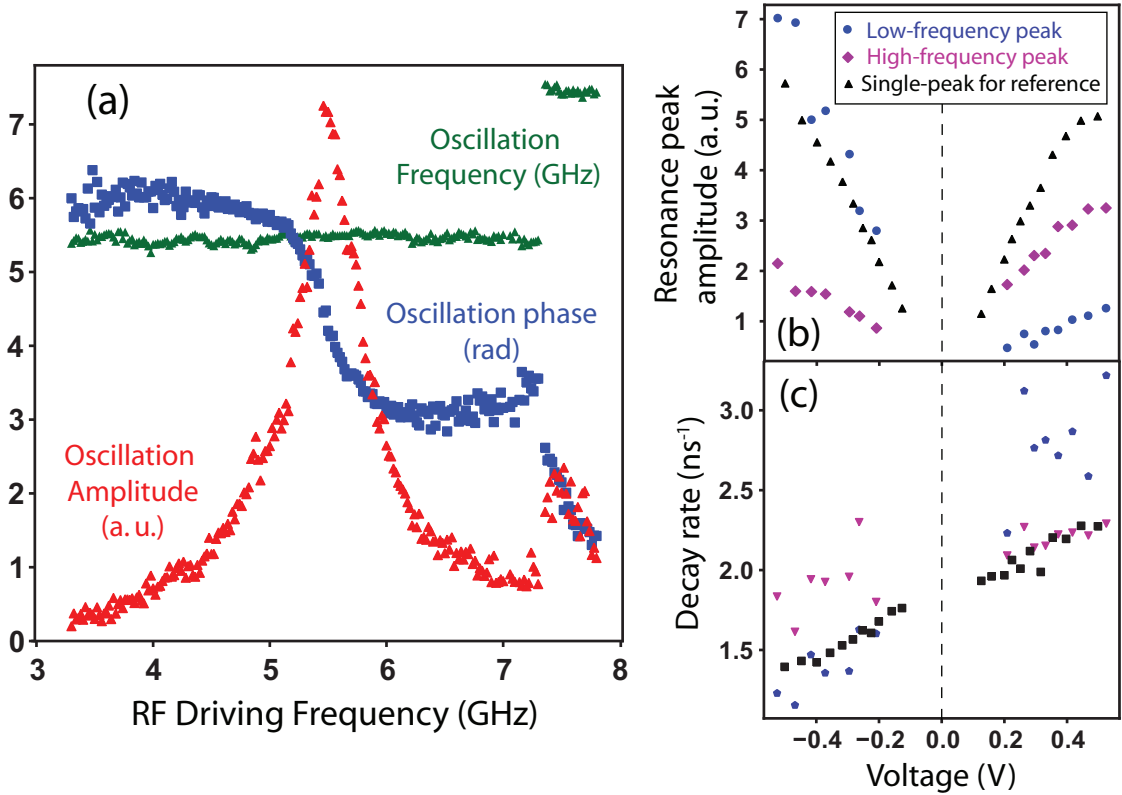


Figure 3.12: Time-domain ST-FMR measurement of two different precession modes. (a) The frequency f , normalized amplitude A_n and relative phase Φ of the damped resistance oscillation of MTJ sample #3 as a function of the frequency of the RF driving pulse under magnetic field $H = 300$ Oe applied from $\varphi = 110^\circ$ (resulting in offset angle $\theta = 105^\circ$) and bias voltage $V = -0.48$ V. (b) and (c) The bias dependence of the peak amplitude and decay rate of the resistance oscillation of the two modes (blue and crimson) of sample #3 under the same magnetic field ($H = 300$ Oe, $\varphi = 110^\circ$) resulting in $\theta = 105^\circ$. Black points denote the peak amplitude and decay rate for sample #2 under a similar offset field ($H = 400$ Oe, $\varphi = 110^\circ$, $\theta = 99^\circ$) where there is only one single strong resonance present.

Measurement of the effective damping as a function of bias for both modes would provide further information to decode the identities of the two modes. Figure 3.12(c) shows that both modes display a positive bias dependence of effective damping as a simple macrospin model of the free layer precession would suggest for the our $\theta = 105^\circ$ geometry (see Section 3.2), but the low-frequency mode shows a much stronger bias-dependence. This suggests that

both modes are free layer modes or coupled modes dominated by free layer.

Even more interestingly, at high positive bias the high frequency mode has a precession phase in good agreement with our calculation for a uniform free layer mode, while the phase of the low frequency mode differs significantly (not shown), in sharp contrast with the situation at high negative bias. I speculate there is significant coupling between the two modes, and there is a hybridization and mode crossing when the bias voltage is tuned. (As side evidence, the frequency of the low frequency mode shows very significant bias dependence, changing by nearly 1.5 GHz across the bias range of ± 0.55 V.) In Fig. 3.12(c), if we compare the effective damping of the stronger mode of sample 3 (crimson at positive bias and blue at negative bias) with the single-mode reference of sample 1 (black), they show very similar bias dependence in good agreement with a free layer macrospin description. Further investigations into these interesting observations are definitely worthwhile.

One could try to identify different magnetic normal modes by using DC detected ST-FMR. But DC detected ST-FMR relies on fitting the resonance line-shape to extract the phase as well as effective damping, which becomes less convincing when one has to fit the spectra with two or three overlapping peaks and lots of parameters. On the other hand, time-domain ST-FMR is a much more direct way to measure the precession, and determines the precession phase and effective damping independently at each frequency. Furthermore our high bias capability is critical in studying the properties of the different modes related to bias dependence, while the bias range of DC detected ST-FMR is very limited (not only by tunnel barrier degradation but also by the artifact voltages related to the change of average resistance).

3.6.2 Fine Dependence of the Precession Mode and Effective Damping on Excitation Frequency

Other than the study of distinctive multiple magnetic modes, the various quantities that we can measure in time-domain ST-FMR allow us to study the detailed dependence on driving frequency of the precession of a nanomagnet including non-harmonic effects. For a perfect externally-driven harmonic oscillator, when the drive stops, it remembers nothing but its instantaneous position and momentum (m_x and m_y in our case). We expect the resistance to always oscillate at its intrinsic frequency after the RF pulse and the decay rate should be independent of the driving frequency. In our measurement, this classical picture is generally true, but we do see signs of deviation. For most samples we measured, the frequency of the post-excitation resistance oscillation shows a small positive slope versus the driving frequency [Fig. 3.13(a)], suggesting there may be mode-locking mechanism in play. The oscillation decay rate, or the effectively damping of the system (consisting of both Gilbert damping and the spin-torque contribution), can depend on the driving frequency as well. Of all the samples under different magnetic field, we find the effective damping is often higher when off-resonance than at resonance [Fig. 3.13(b)], but there are also (but much fewer) cases when the effective damping is lower when off-resonance.

Our tentative explanation is that an off-resonance driving force can alter the mode of the magnetization dynamics (for example, by increasing or decreasing spatial uniformity) and furthermore the ways that energy is dissipated in the system. The data in Fig. 3.13 are far from conclusive, and it needs to be further evaluated in particular how much the residual background reflection

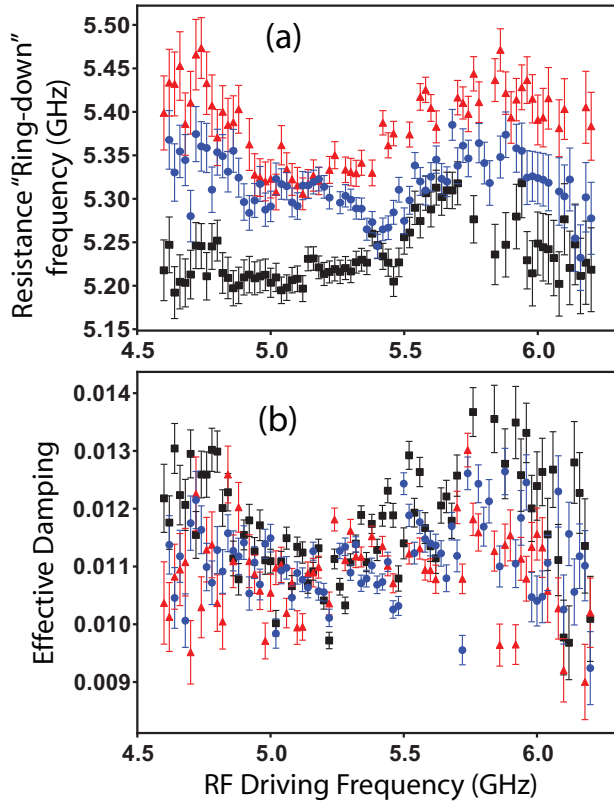


Figure 3.13: (a) The frequency and (b) effective damping measured from the decaying resistance oscillation excited by RF driving pulse of different frequencies for sample #2 under magnetic field $H = 400$ Oe applied from $\varphi = 75^\circ$ (resulting in offset angle $\theta = 69^\circ$) and bias voltage $V = 0.44$ V (black), 0.50 V (red) and 0.60 V (blue).

(even after background subtraction) alters the fitting results. Further study on this frequency-dependent damping (probably after some improvement in our measurement circuit to increase signal/background ratio) would be interesting, and together with the study of dampings of different normal modes, may shed light on the damping mechanisms in these nanoscale magnets.

3.7 Appendices

3.7.1 Effect of Parasitic Capacitance

In Section 3.3.2, we estimated an upper bound for the possible parasitic capacitance associated with our MTJ device $C < 5 \times 10^{-14}$ F. In this appendix, we analyze the effect of such a capacitance on our time domain ST-FMR experiment, and more specifically, our determination of precession phase, which is critical to our measurement of spin transfer torkance vector $d\vec{\tau}/dV$.

Considering the resistance of the MTJ to be connected in parallel with a parasitic capacitance C , the microwave circuit equations for the voltage and *total* current across the MTJ and parasitic capacitance are:

$$\begin{aligned} V(t) &= V + \delta V(t) = V + V_{in}\text{Re}(e^{i\omega t}) + \text{Re}(V_{ref}e^{i\omega t}) \\ I(t) &= I + \delta I(t) = I + V_{in}\text{Re}(e^{i\omega t})/(50\Omega) - \text{Re}(V_{ref}e^{i\omega t})/(50\Omega) \end{aligned} \quad (3.36)$$

The resistance of the device [reflected in $(\partial I/\partial V)$ and $(\partial I/\partial \theta)$] and the capacitance C impose constraint on $V(t)$ and $I(t)$ as

$$I(t) = I + \frac{\partial I}{\partial V}\delta V(t) + \frac{\partial I}{\partial \theta}\delta\theta(t) + C\frac{dV(t)}{dt} \quad (3.37)$$

where $\theta(t) = -\text{Re}(m_{y1}e^{i\omega t})$ as defined in Section 2.3 and Section 3.2. From Equations (3.36) and (3.37), the $e^{i\omega t}$ terms give

$$\begin{aligned} &\text{Re}(V_{in}e^{i\omega t})/(50\Omega) - \text{Re}(V_{ref}e^{i\omega t})/(50\Omega) \\ &= \frac{\partial I}{\partial V}[\text{Re}(V_{in}e^{i\omega t}) - \text{Re}(V_{ref}e^{i\omega t})] \\ &\quad - \frac{\partial I}{\partial \theta}m_{y1}e^{i\omega t} + C [\text{Re}(i\omega V_{in}e^{i\omega t}) + \text{Re}(i\omega V_{ref}e^{i\omega t})] \end{aligned} \quad (3.38)$$

Therefore,

$$V_{ref} = \frac{\left(\frac{1}{(50\Omega)} - \frac{\partial I}{\partial V} - i\omega C\right)V_{in} + \frac{\partial I}{\partial \theta}m_{y1}}{\frac{1}{(50\Omega)} + \frac{\partial I}{\partial V} + i\omega C} \quad (3.39)$$

We define the differential resistance of the MTJ as always $R_0 = \partial V / \partial I$, and noting $(\partial I / \partial \theta)(\partial \theta / \partial V)(\partial V / \partial I) = -1$, we have

$$V_{ref} = \frac{[R_0/(50\Omega) - 1 - i\omega R_0 C]V_{in} - \frac{\partial V}{\partial \theta}m_{y1}}{R_0/(50\Omega) + 1 + i\omega R_0 C} \quad (3.40)$$

So the time dependent voltage on the device is

$$\begin{aligned} V_{RF} &= V_{in} + V_{ref} \\ &= \frac{2R_0}{R_0 + (50\Omega) + i\omega(50\Omega)R_0C}V_{in} - \frac{(50\Omega)}{R_0 + (50\Omega) + i\omega(50\Omega)R_0C}I\frac{\partial V}{\partial \theta}m_{y1} \end{aligned} \quad (3.41)$$

Equation (3.41) is the replacement of Eq. (3.9) and takes into account the feedback effect self-consistently in the presence of parasitic capacitance. It should be noted that the time dependent current on the MTJ device, I_{RF} , is no longer equal to $(V_{in} + V_{ref})/(50\Omega)$. This is because $(V_{in} + V_{ref})/(50\Omega)$ includes the RF current leaked through the capacitance. One can calculate I_{RF} from the expression of V_{RF} [Eq. (3.41)] using on Eq. (3.36), and then substitute it into the 1st order (to I_{RF}) dynamic equations for m_{x1} and m_{y1} [Eq. (3.4)] to solve m_{y1} . Alternatively, it is easier to use the V_{RF} counterpart of the dynamic equations,

$$\begin{aligned} i\omega m_{x1} &= -m_{y1}(\gamma N_y M_{eff} + i\alpha\omega) + \frac{\gamma}{M_s V_{free}} \left[\tau_{||} m_{x1} \cot \theta - \frac{\partial \tau_{\perp}}{\partial V} V_{RF} - \frac{\partial \tau_{\perp}}{\partial \theta} \Big|_V m_{y1} \right] \\ i\omega m_{y1} &= +m_{x1}(\gamma N_y M_{eff} + i\alpha\omega) - \frac{\gamma}{M_s V_{free}} \left[\tau_{\perp} m_{x1} \cot \theta + \frac{\partial \tau_{||}}{\partial V} V_{RF} - \frac{\partial \tau_{||}}{\partial \theta} \Big|_V m_{y1} \right] \end{aligned} \quad (3.42)$$

Equations (3.42) are the counterparts of the dynamic equations Eq. (3.4), with the torkance $\vec{\tau}$ Taylor expanded with respect to V instead of I . This is the group of dynamic equations used in supplementary Note 3 of ref. [82], and would

yield the same result as Eq. (3.12) after the feedback effect is taken into account. Here we substitute the self-consistent condition in the presence of capacitance Eq. (3.41) into Eq. (3.42) and we arrive at

$$\begin{aligned} i\omega m_{x1} &= -m_{y1} (\gamma N_y M_{eff} + i\alpha\omega) - \frac{\gamma}{M_s V_{free}} \left[\frac{2R_0}{R_0 + (50\Omega) + i\omega(50\Omega)R_0C} \frac{\partial\tau_\perp}{\partial V} V_{in} \right. \\ &\quad \left. - \left(\frac{\partial\tau_\perp}{\partial\theta} \Big|_V + \frac{(50\Omega)}{R_0 + (50\Omega) + i\omega(50\Omega)R_0C} \frac{\partial V}{\partial\theta} \Big|_I \frac{\partial\tau_\perp}{\partial V} \Big|_\theta \right) m_{y1} - \tau_{||} m_{x1} \cot\theta \right] \\ i\omega m_{y1} &= -m_{x1} (\gamma N_x M_{eff} + i\alpha\omega) - \frac{\gamma}{M_s V_{free}} \left[\frac{2R_0}{R_0 + (50\Omega) + i\omega(50\Omega)R_0C} \frac{\partial\tau_{||}}{\partial V} V_{in} \right. \\ &\quad \left. - \left(\frac{\partial\tau_{||}}{\partial\theta} \Big|_V + \frac{(50\Omega)}{R_0 + (50\Omega) + i\omega(50\Omega)R_0C} \frac{\partial V}{\partial\theta} \Big|_I \frac{\partial\tau_{||}}{\partial V} \Big|_\theta \right) m_{y1} - \tau_\perp m_{x1} \cot\theta \right] \end{aligned} \quad (3.43)$$

Equations (3.43) are very similar to Eq. (3.12) with only substitutions of

$$\begin{aligned} \frac{2R_0}{R_0 + (50\Omega)} &\Rightarrow \frac{2R_0}{R_0 + (50\Omega) + i\omega(50\Omega)RC} \\ \frac{(50\Omega)}{R_0 + (50\Omega)} &\Rightarrow \frac{(50\Omega)}{R_0 + (50\Omega) + i\omega(50\Omega)RC} \end{aligned} \quad (3.44)$$

It should yield a solution very similar to Eq. (3.13):

$$\begin{aligned} m_{y1} &= \frac{R_0}{R_0 + 50\Omega + i\omega(50\Omega)R_0C} \\ &\times \frac{\gamma V_{in}}{M_s V_{free}} \frac{2\omega}{(\omega^2 - \omega_m^2 - 2i\omega\sigma)} \left[i \frac{\partial\tau_{||}}{\partial V} + \frac{\gamma N_x M_{eff}}{\omega} \frac{\partial\tau_\perp}{\partial V} \right] \end{aligned} \quad (3.45)$$

where

$$\omega_m \approx \gamma M_{eff} \sqrt{N_x \left[N_y - \frac{1}{M_{eff} M_s V_{free}} \left(\frac{\partial\tau_\perp}{\partial\theta} \Big|_V + \frac{(50\Omega)}{R_0 + 50 + i\omega 50 R_0 C} \frac{dV}{d\theta} \frac{\partial\tau_\perp}{\partial V} \right) \right]} \quad (3.46)$$

$$\begin{aligned} \sigma &\approx \frac{\alpha\gamma M_{eff}(N_x + N_y)}{2} \\ &- \frac{\gamma}{2M_s V_{free}} \left[\frac{\partial\tau_{||}}{\partial\theta} \Big|_V + \tau_{||} \cot\theta + \frac{(50\Omega)}{R_0 + (50\Omega) + i\omega(50\Omega)R_0C} \frac{dV}{d\theta} \frac{\partial\tau_\perp}{\partial V} \right] \end{aligned} \quad (3.47)$$

The imaginary part in $R_0 + (50\Omega) + i\omega(50\Omega)R_0C$ causes ω_m^2 and σ not purely real so that rigorously we have to redefine ω_m^2 and σ , but this does not affect the fact

that we can write m_{y1} in the form of

$$m_{y1} = \frac{(R_0/50\Omega)}{[(R_0/50\Omega) + 1 + i\omega R_0 C]} \frac{\gamma V_{in}}{M_s V_{free}} \frac{1}{(\omega - \omega_m - i\sigma)} \left[i \frac{\partial \tau_{||}}{\partial V} + \frac{\gamma N_x M_{eff}}{\omega} \frac{\partial \tau_{\perp}}{\partial V} \right] \quad (3.48)$$

From Eq. (3.40),

$$\frac{V_{ref}}{V_{in}} = \frac{(R_0/50\Omega) - 1 - i\omega R_0 C}{(R_0/50\Omega) + 1 + i\omega R_0 C} - \frac{1}{(R_0/50\Omega) + 1 + i\omega R_0 C} \frac{\partial V}{\partial \theta} \left(\frac{m_{y1}}{V_{in}} \right) \quad (3.49)$$

where (m_{y1}/V_{in}) is given by Eq. (3.48). So the relative phase of the resistance oscillation term [2nd term in Eq. (3.49)] with respect to the background term [1st term in Eq. (3.49)] is

$$\text{Phase} \left\{ -\frac{1}{(R_0/50\Omega) + 1 + i\omega R_0 C} \frac{\partial V}{\partial \theta} \left(\frac{m_{y1}}{V_{in}} \right) \middle/ \frac{(R_0/50\Omega) - 1 - i\omega R_0 C}{(R_0/50\Omega) + 1 + i\omega R_0 C} \right\} = \text{Phase} \left\{ \frac{(R_0/50\Omega)}{[(R_0/50\Omega) + 1 + i\omega R_0 C][(R_0/50\Omega) - 1 - i\omega R_0 C]} \right\} \quad (3.50a)$$

$$- \text{Phase} \left\{ \frac{\gamma V_{in}}{M_s V_{free}} \frac{1}{(\omega - \omega_m - i\sigma)} \left[i \frac{\partial \tau_{||}}{\partial V} + \frac{\gamma N_x M_{eff}}{\omega} \frac{\partial \tau_{\perp}}{\partial V} \right] \right\} \quad (3.50b)$$

The second phase [Eq. (3.50b)] is the actual spin-torque related phase in the absence of parasitic capacitance as we calculated in Section 3.2, and the first phase [Eq. (3.50a)] is the parasitic phase Φ_C arising from the capacitance C . With $C < 5 \times 10^{-14} \text{ F}$, $250\Omega < R_0 < 750\Omega$ and $3 \text{ GHz} < (\omega/2\pi) < 7 \text{ GHz}$, approximately $(50\Omega)\omega C \ll 1$ and $(50\Omega)/R_0 \ll 1$. Therefore,

$$\begin{aligned} \Delta\Phi_C &= \text{Phase} \{ -[(R_0/50\Omega) + 1 + i\omega R_0 C][(R_0/50\Omega) - 1 - i\omega R_0 C] \} \\ &= \frac{-2\omega R_0 C}{(R_0/50)^2 - 1 + (\omega R_0 C)^2} \\ &\approx 2 \left(\frac{50\Omega}{R_0} \right) \left(\frac{50\Omega}{1/\omega C} \right) \end{aligned} \quad (3.51)$$

Therefore,

$$\begin{aligned}
\Delta\Phi_C &= \text{Phase} \left\{ -[(R_0/50\Omega) + 1 + i\omega R_0 C][(R_0/50\Omega) - 1 - i\omega R_0 C] \right\} \\
&= \frac{-2\omega R_0 C}{(R_0/50)^2 - 1 + (\omega R_0 C)^2} \\
&\approx 2 \left(\frac{50\Omega}{R_0} \right) \left(\frac{50\Omega}{1/\omega C} \right) < 0.03 \text{ rad}
\end{aligned} \tag{3.52}$$

In other words, the parasitic phase Φ_C affecting our time-domain ST-FMR is a factor of $(50\Omega)/R_0$ smaller than the extra phase upon probe contact Φ_{ref} we measured in Section 3.3.2, which was 0.15 rad, assuming all of Φ_{ref} is due to parasitic capacitance. Since we did not exclude other effects (notably the extra transmission length introduced by the contact pads of the device), we do not attempt to make numerical correction for this phase introduced by capacitive effect Φ_C , but treat it as a small added experimental uncertainty instead. This uncertainty (< 0.03 rad) is smaller than our fitting uncertainty 0.04 rad for determining the phase of the damped resistance oscillation.

3.7.2 Effect of Finite Fall Time of the RF pulse

During the finite fall time of the RF pulse (~ 180 ps), the magnetization of the precessing layer continue to experience oscillating spin torque, making its dynamics more complicated than the ideal case we considered in Section 3.2, where the precession dynamics switch from ST-FMR to damped oscillation instantly. In this appendix we will show that the finite fall time leads to a fairly small correction in determining the amplitude and phase of ST-FMR so that we treat it as a small added uncertainty in our analysis. This effect is minimized in our experiment by choosing the center of the falling edge as $t = 0$ so that the effect from the extra spin torque at $t > 0$ is mostly canceled by the reduced spin

torque at $t < 0$.

As discussed in Section 3.2, the steady state precession driven by RF pulse $V_{in}(t) = V_{in}\text{Re}(e^{i\omega t})$ can be described by $m_x(t), m_y(t) = \text{Re}(m_{x1}e^{i\omega t}, m_{y1}e^{i\omega t})$, where $(m_{x1}, m_{y1}) = (\chi_x, \chi_y)V_{in}$ with χ_x, χ_y the complex coefficient in Eq. (3.14) and χ_x similarly calculable. The free precession without RF spin torque after any given time $t = t_0$ is

$$[(m_x(t), m_y(t))] = \text{Re} [(m_x, m_y)(t = t_0)e^{(-\Gamma + i\omega_m)(t - t_0)}] \quad (3.53)$$

with $(m_x, m_y)(t = t_0)$ the initial condition at $t = t_0$. In general, due to the linear nature of the equations governing the small angle precession [Equations (3.12) and (3.22)], the magnetization dynamics in response to an input RF voltage with a step drop in amplitude (V_{in1} for $t < t_0$, V_{in2} for $t > t_0$ and $V_{in1} > V_{in2}$) but continuous in phase can be written as (for $t > t_0$)

$$m_x(t), m_y(t) = \text{Re} [(\chi_x, \chi_y)V_{in2}e^{i\omega t}] + \text{Re} [(\chi_x, \chi_y)(V_{in1} - V_{in2})e^{i\omega t_0}e^{(-\Gamma + i\omega_m)(t - t_0)}] \quad (3.54)$$

The first term represents the steady state precession driven by V_{in2} and the second term represents the decay of the precession excited by V_{in1} in excess to the steady precession supported by V_{in2} .

The falling edge of our RF pulse can be generally written as $V_{in} = V_{evp}(t)\text{Re}(e^{i\omega t})$ where $V_{evp}(t)$ is the envelope of the RF pulse and decreases from the value V_{in} to 0 during the pulse fall time. The decaying magnetization precession in the time span we performed fitting in the main paper ($t > 0$) should therefore be integrated over infinitesimal step drops of RF voltages

across the falling edge ($-90 \text{ ns} = t_1 < t < t_2 = 90 \text{ ns}$),

$$m_x(t), m_y(t) = \text{Re} \left[(\chi_x, \chi_y) \int_{t_1}^{t_2} e^{i\omega t_0} e^{(-\Gamma + i\omega_m)(t-t_0)} \left(-\frac{dV_{evp}}{dt_0} \right) dt_0 \right] \quad \text{for } t > t_2 \quad (3.55\text{a})$$

$$m_x(t), m_y(t) = \text{Re} \left\{ (\chi_x, \chi_y) \left[\int_{t_1}^t e^{i\omega t_0} e^{(-\Gamma + i\omega_m)(t-t_0)} \left(-\frac{dV_{evp}}{dt_0} \right) dt_0 + V_{evp}(t) e^{i\omega t} \right] \right\} \quad \text{for } t_1 < t < t_2 \quad (3.55\text{b})$$

or slightly reorganized as,

$$m_x(t), m_y(t) = \text{Re} \left[(\chi_x, \chi_y) e^{(i\omega_m - \Gamma)t} \int_{t_1}^{t_2} e^{i\Delta\omega t_0} e^{-\Gamma t_0} \left(-\frac{dV_{evp}}{dt_0} \right) dt_0 \right] \quad \text{for } t > t_2 \quad (3.56\text{a})$$

$$m_x(t), m_y(t) = \text{Re} \left\{ (\chi_x, \chi_y) e^{(i\omega_m - \Gamma)t} \left[\int_{t_1}^t e^{i\Delta\omega t_0} e^{-\Gamma t_0} \left(-\frac{dV_{evp}}{dt_0} \right) dt_0 + V_{evp}(t) e^{(i\Delta\omega + \Gamma)t} \right] \right\} \quad \text{for } t_1 < t < t_2 \quad (3.56\text{b})$$

where $\Delta\omega = \omega - \omega_m$. Within the frequency range relevant to our torque calculation $|\Delta\omega| < 0.4 \text{ GHz}$ and using realistic decay rate $\Gamma < 2.5 \text{ ns}^{-1}$ so that $|\Delta\omega t_0| < 0.25$, $\Gamma t_0 < 0.25$, we can make Taylor expansion on the exponent,

$$e^{i(\omega - \omega_m)t_0} e^{-\Gamma t_0} = 1 + i(\Delta\omega - \Gamma)t_0 + \frac{1}{2}(\Gamma^2 - \Delta\omega^2 - 2i\Gamma\Delta\omega)t_0^2 + o(t_0^3) \quad (3.57)$$

Therefore,

$$m_x(t), m_y(t) = \operatorname{Re} \left\{ (\chi_x, \chi_y) e^{(i\omega_m - \Gamma)t} \left[V_{in} + (i\Delta\omega - \Gamma) \int_{t_1}^{t_2} \left(-\frac{dV_{evp}}{dt_0} \right) t_0 dt_0 + o(t_2^2) \right] \right\}$$

for $t > t_2$ (3.58a)

$$m_x(t), m_y(t) = \operatorname{Re} \left\{ (\chi_x, \chi_y) e^{(i\omega_m - \Gamma)t} \left[V_{in} + (i\Delta\omega - \Gamma) \int_{t_1}^t \left(-\frac{dV_{evp}}{dt_0} \right) t_0 dt_0 + (i\Delta\omega + \Gamma) t V_{evp}(t) + o(t_2^2) \right] \right\}$$

for $t_1 < t < t_2$ (3.58b)

We find the zeroth order approximation provides the result we derived under the assumption of zero fall time. The first order term in Eq. (3.58a) is also zero since the slope of the falling edge of the envelope is fairly symmetric with respect to $t = 0$ in our experiment. The first order term in Eq. (3.58b) can be evaluated by assuming a reasonable function form for V_{evp} . For example, if we assume $dV_{enp}/dt_0 = -V_{in}/2t_2$ is a constant across the falling edge, Eq. (3.58b) becomes,

$$m_x(t), m_y(t) = \operatorname{Re} \left\{ (\chi_x, \chi_y) e^{(i\omega_m - \Gamma)t} \left[V_{in} + V_{in} \frac{t_2 - t}{4t_2} [i\Delta\omega(3t + t_2) - \Gamma(t_2 - t)] \right] \right\} \quad (3.59)$$

For various t in the range of $0 < t < t_2$, the first order term leads to a correction ranging from 0 up to $|\frac{1}{3}\Delta\omega t_2| < 8\%$ to the imaginary part (or 0.08 radian phase shift) and up to $\frac{1}{4}\Gamma t_2 < 6\%$ correction to the real part. Similarly we can also estimate the second order contribution in Eq. (3.58) (not shown), and the resulting correction exists for both $0 < t < t_2$ and $t > t_2$ but is less than 2% for both the real and the imaginary parts under a constant slope assumption. Contributions from higher orders are even less significant. Given that the slope

of the falling edge of the RF pulse in actual experiments is larger close to $t = t_0$, these estimates should provide an upper limit of possible corrections.

It should be noted that in our main text the amplitude and phase of the damped oscillation are determined from a fit extending from during the pulse fall time to long after the pulse, and only part of the data points within the fall time corresponds to corrections close to the upper limit. Therefore we consider the effect of finite fall time of the RF pulse as an added uncertainty to the oscillation phase of 0.04 radian and oscillation amplitude of 3%, which is reflected in our final results of torkances (Fig. 3.7).

CHAPTER 4

POTENTIAL APPLICATIONS OF SPIN-TRANSFER-DRIVEN FERROMAGNETIC RESONANCE

In the previous two chapters, we studied spin-transfer-driven ferromagnetic resonance (ST-FMR) as a novel resonance phenomenon associated with an individual nanoscale magnet. Our main focus was to use ST-FMR as a tool to measure the spin transfer torque vector in MgO-based magnetic tunnel junctions (MTJs) as a function of bias voltage and offset angle between the two ferromagnetic electrodes. Other than being a tool for the study of the spin transfer effect and nanoscale ferromagnetism, ST-FMR is an effect with quite significant macroscopic magnitude that can see potential applications in its own right. The magnitude of ST-FMR benefits from the microscopic strength of spin transfer torque (on the order of $\hbar/2$ per spin polarized electron), the high tunneling magnetoresistance (TMR) of MTJs (100-200% widely achievable at room temperature) and fabrication of ultra-thin tunnel barrier that enables high tunneling current density at low voltage (resistance-area product of as low as $1 \Omega \mu\text{m}^2$). Recent development in MTJ technology driven mostly by the magnetic storage industry has not only brought STT-MRAM closer to commercialization than was ever before, but also makes ST-FMR effect more interesting for a number of applications. In this chapter, I present a brief evaluation of the potential of MTJs to be used as microwave detectors and microwave amplifiers based on the principle of ST-FMR. The first section discusses microwave detection and is adapted from our work originally published as *J. Appl. Phys.* **106**, 053905 (2009) [111]. The second section discusses microwave amplification and focuses on a microwave voltage/current feedback effect in two-terminal MTJ devices, which is one aspect of our work originally published as *Appl. Phys.*

Lett. **99**, 022505 (2011) [112].

4.1 Microwave Detector

As introduced in Chapter 2, when a microwave signal with frequency close to the natural ferromagnetic resonance frequency of one of the electrodes of a magnetic tunnel junction is incident onto the device, the oscillating tunnel current that it induces can excite magnetic precession via spin transfer. The resistance oscillation that results from this precession mixes with the oscillating current to produce an easily measurable DC voltage component across the tunnel junction. This DC detection of spin-transfer-driven ferromagnetic resonance (ST-FMR), otherwise known as the spin-torque diode effect, can be used as a mechanism to convert incident microwave power into a DC voltage. This effect has been analyzed in great detail to quantitatively measure the spin transfer torque in Chapter 2, and here we perform a similar analysis from a different perspective. We discuss how to maximize the microwave detector sensitivity of a tunnel junction, which we define as $\varepsilon = \langle V_{res} \rangle / P_{inc}$, where $\langle V_{res} \rangle$ is the resonant part of the measured DC voltage (above a non-resonant background) and P_{inc} is the incident microwave power. This sensitivity is of course only one of several parameters important for applications (e.g., background noise, dynamic range, and speed), but achieving a competitive detector sensitivity is a first prerequisite for evaluating whether more detailed studies are warranted.

4.1.1 Analytical Prediction for the Sensitivity of Spin-Torque Diodes for Microwave Detection

We note first that the detector sensitivity can vary as a function of a DC bias applied across the tunnel junction [80]. However, in the devices measured thus far, we find that the maximum detection sensitivity is within 10% of the value at zero bias (see Fig. 4.1). For the purposes of estimating the typical detector sensitivity, we will therefore limit our discussion to the simple case of zero applied bias. The fall-off in sensitivity at large biases can be explained by a reduction in the tunnel magnetoresistance (TMR) as a function of bias, which decreases the size of the resistance oscillations contributing to the mixing signal. The maximum sensitivity is not found exactly at zero bias because there are several other mechanisms by which an applied bias can either enhance or suppress the microwave sensitivity. For example, the strength of the spin torque is bias dependent (see Chapter 2 and 3 or references [80, 82]). An incident microwave signal can also change the time-averaged junction resistance, which in the presence of a non-zero bias gives a contribution $I_{DC}\Delta R$ to the DC voltage on resonance in addition to the mixing contribution noted above (see Chapter 2 or ref. [80]). Furthermore, for the correct sign of bias one can decrease the effective magnetic damping, thereby making the resonant detection more efficient. If future improvements in magnetic-tunnel-junction technology allow for a TMR that does not decrease strongly as a function of bias, it may be possible to take advantage of these other mechanisms by using a non-zero bias to improve the sensitivity substantially beyond the value we estimate for zero bias in this section. The influence of these mechanisms on the detection sensitivity can be calculated using the methods described in Section 2.3 and

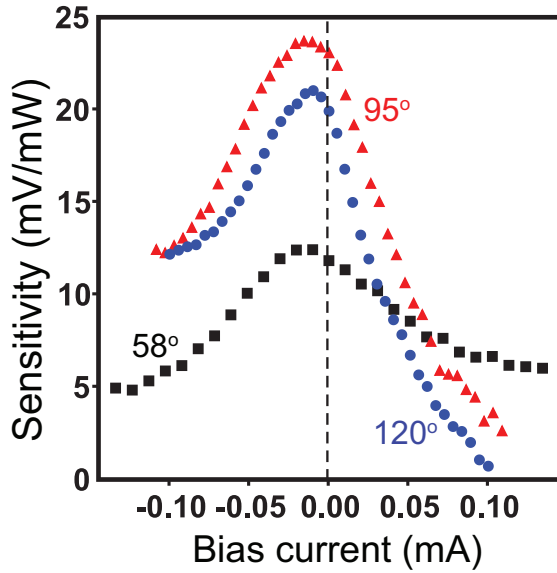


Figure 4.1: Bias dependence of the diode-detector sensitivity for sample #1 measured at room temperature, for three different values of the offset angle, θ , between the free and pinned-layer magnetic moments.

Section 3.2.

If a microwave-frequency current I_{RF} passes through the tunnel junction, following our analysis in Section 2.3, the solution of the LLGS equation [Eq. (2.10)] yields an expression for the resonant DC voltage signal due to the mixing between the spin-torque-driven magnetic precession and I_{RF} (to lowest order in I_{RF}):

$$\langle V_{res} \rangle = \frac{dR_0}{d\theta} \frac{\mu_B}{2\hbar(M_s t A)\sigma} I_{RF}^2 \left[\frac{d\tau_{||}}{dI} S(\omega) - \frac{d\tau_{\perp}}{dI} \frac{\gamma(H_z + 4\pi M_{eff})}{\omega_m} A(\omega) \right] \quad (4.1)$$

where R_0 is the differential resistance of the tunnel junction, H_z is the \hat{z} component of the external magnetic field, $4\pi M_{eff}$ is the effective out-of-plane anisotropy, and $S(\omega) = [1 + (\omega - \omega_m)^2/\sigma^2]^{-1}$ and $A(\omega) = [(\omega - \omega_m)/\sigma] S(\omega)$ are symmetric and antisymmetric components of the resonance line-shape as a function of frequency ω , with ω_m the resonance frequency and σ the linewidth. (We have neglected a small contribution from the within-plane anisotropy.)

Eq. (4.1) is essentially the major mixing voltage term [Eq. (2.19b)] in the full DC signal of ST-FMR [Eq. (2.19)]. Among other terms in Eq. (2.19), since we only focus on the spin-torque diode effect at zero bias in the section, all the high bias terms [Eq. (2.19c)-(2.19g)] are zero. The first term [Eq. (2.19a)] is a non-resonant background and is also relatively small at zero bias.

If the microwave signal is incident onto the tunnel junction from a transmission line with impedance Z_0 ($Z_0 = 50 \Omega$ for our apparatus), after taking into account the impedance mismatch with the junction the incident power can be related to the microwave current in the junction as [97]

$$P_{inc} = \frac{1}{2Z_0} \left(\frac{R_0 + Z_0}{2} \right)^2 I_{RF}^2 \quad (4.2)$$

Therefore the overall sensitivity for the detected signal is

$$\varepsilon \equiv \frac{\langle V_{res} \rangle}{P_{inc}} = \frac{dR_0}{d\theta} \frac{4\mu_B}{\hbar(M_s t A)\sigma} \frac{Z_0}{(R_0 + Z_0)^2} \left[\frac{d\tau_{||}}{dI} S(\omega) - \frac{d\tau_{\perp}}{dI} \frac{\gamma(H_z + 4\pi M_{eff})}{\omega_m} A(\omega) \right] \quad (4.3)$$

This expression can be simplified further. In the case we are considering, for zero applied bias on the tunnel junction, it is predicted theoretically [14, 81] and observed experimentally [76, 79] for a symmetric tunnel junction (with both magnetic electrodes made from the same material) that $d\tau_{\perp}/dI = 0$. Therefore, for this case the second term in the brackets of Eq. (4.3) is zero and the line-shape should be symmetric in frequency, with the maximum detector sensitivity occurring at the resonance frequency, for which $S(\omega_m) = 1$. (The cases of symmetric junctions with non-zero bias or asymmetric junctions may both be more complicated.) The angular dependence of the zero-bias tunnel junction conductance is expected to be purely sinusoidal [113], so that

$$\frac{dR}{d\theta} = \frac{R^2}{2R_P R_{AP}} (R_{AP} - R_P) \sin \theta \quad (4.4)$$

Finally, for a symmetric tunnel junction the in-plane spin torque is predicted to have the magnitude [85] [reprint of Eq. (2.20)],

$$\frac{d\tau_{||}/dV}{\sin \theta} = \frac{\hbar}{4e} \frac{2P}{1+P^2} \left(\frac{dI}{dV} \right)_P \quad (4.5)$$

where the tunneling spin polarization $P^2 = (R_{AP} - R_P)/(R_{AP} + R_P)$. Our ST-FMR measurements [76, 80] have found good quantitative agreement with Eq. (4.5). Incorporating these values into Eq. (4.3), we reach an expression for the maximum detector sensitivity of a symmetric magnetic tunnel junction for zero applied bias:

$$\varepsilon = \frac{R_{AP} - R_P}{R_P} \frac{\mu_B}{2e(M_s t A) \sigma} \frac{R_0 Z_0}{(R_0 + Z_0)^2} \frac{2P}{1+P^2} \frac{R^2}{R_P R_{AP}} \sin^2 \theta \quad (4.6)$$

Equation (4.6) is the main equation used in ref. [111], but here I would like to reorganize it into a further simplified form:

$$\varepsilon = \frac{2P^3 \mu_B}{e(M_s t A) \sigma} \frac{R_0 Z_0}{(R_0 + Z_0)^2} \frac{R_0^2}{R_M^2} \sin^2 \theta \quad (4.7)$$

where R_M is the resistance of the MTJ device when $\theta = 90^\circ$.

4.1.2 Experimental Testing of the Sensitivity of Spin-Torque Diodes

The very same DC-detected ST-FMR experiments described in Chapter 2 can be viewed as an experimental test of the predicted sensitivity based on Eq. (4.7). In Chapter 2, we measure the spin transfer torque from our measured mixing voltage at resonance based on Eq. (4.1) at zero bias, and then compare the measured torque with the prediction of Eq. (4.5). We conclude that for a batch of MTJ devices with extended fixed layer fabricated by IBM, the zero-bias

torkance agrees within experimental uncertainty. However, for a batch of MTJ devices with patterned fixed layer fabricated by Hitachi, the measured zero-bias torkance is about 30-35% smaller than theoretical prediction. Since Eq. (4.7) is derived from Eq. (4.1) and Eq. (4.5), these results are sufficient to conclude that Eq. (4.7) agrees well with experiments on the IBM samples, but overestimates the actual sensitivity by 40-50% for the Hitachi samples. Nevertheless, since we did not focus on the magnitude of mixing voltage (or spin torque) at zero bias in Chapter 2, for completeness we present here additional data on testing Eq. (4.7) from a perspective of microwave detection sensitivity.

Our measurements are performed on the same two batches of MgO-based magnetic tunnel junctions as were measured in Chapter 2). The first batch, with an average resistance-area product for parallel magnetic alignment of $RA = 12 \Omega\mu\text{m}^2$, had the layer structure (in nm) Ta(5)/Cu(20)/Ta(3)/Cu(20)/PtMn(15)/Co₇₀Fe₃₀(2.5)/ Ru(0.85)/ Co₆₀Fe₂₀B₂₀(3)/ MgO(1.25)/ Co₆₀Fe₂₀B₂₀(2.5)/ Ta(5)/Ru(7) deposited on an oxidized silicon wafer. The top ("free") magnetic layer of these samples was etched to be a rounded rectangle, with nominal dimensions either $50 \times 100 \text{ nm}^2$ or $50 \times 150 \text{ nm}^2$, and had a saturation magnetization per unit area measured to be $M_s t = 2.75 \times 10^{-4} \text{ e.m.u./cm}^2$. The milling process used to define the nanopillar was stopped at the tunnel barrier, leaving the bottom magnetic electrode extended. The exchange bias for the bottom electrode was parallel to the magnetic easy axis of the top layer. The second batch of samples, with $RA = 1.5 \Omega\mu\text{m}^2$, had the layer structure (in nm) Ta(3)/CuN(41.8)/Ta(3)/CuN(41.8) / Ta(3) / Ru(3.1) / IrMn(6.1) / CoFe(1.8) / Ru / CoFeB(2) / MgOx/ CoFe(0.5)/CoFeB(3.4)/Ru(6)/Ta(3)/Ru(4). These samples were etched to 90 nm diameter circles, with the etch extending through both the CoFe/CoFeB composite free layer and the IrMn/CoFe/Ru/CoFeB exchange-biased synthetic

antiferromagnetic (SAF) pinned layer. For these free layers, $M_s t = 3.2 \times 10^{-4}$ e.m.u./cm². We measured more than 5 samples from each batch, and found good consistency for each sample type, with microwave detection sensitivities varying within a range of 20%. Here we will report results from 3 samples, whose parameters are listed in Table 4.1.

Table 4.1: Sample parameters for microwave detector characterization

Sample	Nominal cross section (nm ²)	RA value (Ωμm ²)	R_P	R_{AP}	P	$M_s t A$ (emu)
#1	50 × 100	12	3.9 kΩ	10.2 kΩ	0.67	1.1×10^{-14}
#2	50 × 150	12	2.21 kΩ	5.89 kΩ	0.67	1.6×10^{-14}
#3	90 × 90	1.5	279 Ω	537 Ω	0.56	1.8×10^{-14}

The experimental procedure for our room-temperature DC-detected ST-FMR measurement has been described in detail in Chapter 2. Each MTJ sample was contacted to a 50 Ω semi-rigid coaxial cable via a high-frequency probe station. A magnetic field was applied within the sample plane at various directions to control the initial offset angle θ between the magnetic orientations of the two electrodes. We determined θ from the magnetoresistance, measured *in situ* using a lock-in amplifier. To measure the microwave detection sensitivity, we swept the frequency of an incident microwave signal while keeping the power, P_{inc} , constant. The incident microwaves were chopped as a function of time, and the resonant DC detector mixing voltage was measured using a second lock-in amplifier having a large input impedance and connected to the sample via a bias tee. The incident microwave power was calibrated by using a non-resonant background voltage in the mixing signal arising from the nonlinear tunnel junction resistance to determine I_{RF} within the sample, and then using Eq. (4.2) to evaluate P_{inc} . The applied power was kept small enough that the magnetic precession angle was always $< 0.5^\circ$, within the linear-response regime. The dominant uncertainty in comparing the measured and predicted

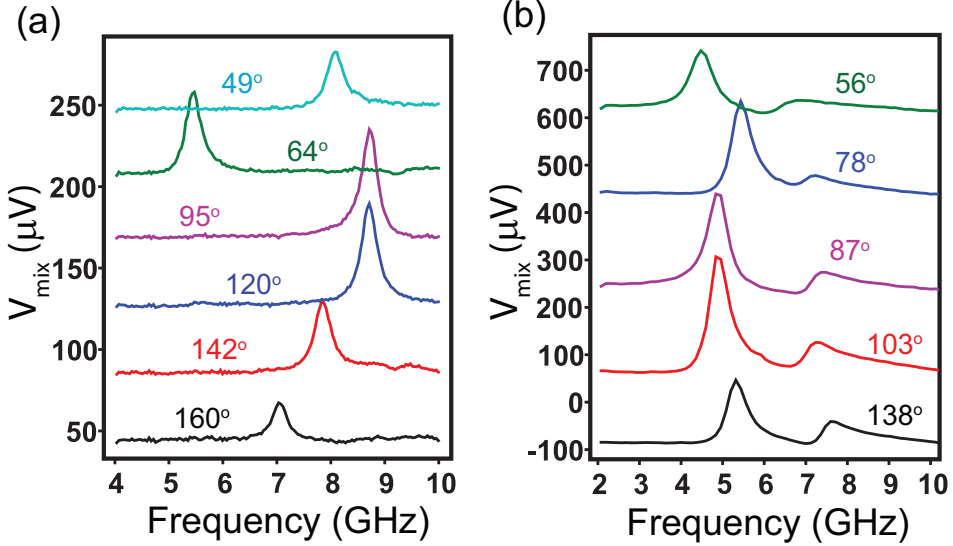


Figure 4.2: Selected ST-FMR resonance spectra, measured at room temperature for selected initial offset angles θ , for (a) sample #1 and (b) sample #3. The data are artificially offset in the vertical direction. The incident power in (a) is $P_{inc} = 2.7 \mu\text{W}$ and in (b) is $P_{inc} = 5.0 \mu\text{W}$. The magnitude and angle (measured relative to the exchange bias direction) of the applied magnetic field corresponding to the various values of θ are (a) $\theta = 49^\circ$: $H = 700 \text{ Oe at } 70^\circ$, $\theta = 64^\circ$: $H = 400 \text{ Oe at } 70^\circ$, $\theta = 95^\circ$: $H = 800 \text{ Oe at } 120^\circ$, $\theta = 120^\circ$: $H = 700 \text{ Oe at } 140^\circ$, $\theta = 142^\circ$: $H = 500 \text{ Oe at } 150^\circ$, and $\theta = 160^\circ$: $H = 300 \text{ Oe at } 160^\circ$, (b) $\theta = 56^\circ$: $H = 200 \text{ Oe at } 62^\circ$, $\theta = 78^\circ$: $H = 200 \text{ Oe at } 88^\circ$, $\theta = 87^\circ$: $H = 200 \text{ Oe at } 92^\circ$, $\theta = 103^\circ$: $H = 200 \text{ Oe at } 118^\circ$, and $\theta = 138^\circ$: $H = 200 \text{ Oe at } 147^\circ$.

values of the detection sensitivity comes from estimating the sample area using scanning electron microscope pictures. The true areas are less than the nominal values listed in Table 1 because the pillars do not have perpendicular sidewalls. We estimate that our values of the true areas (and hence $M_s t A$) are accurate to 15%.

The measured mixing voltage as a function of frequency is shown in Fig. 4.2 for sample #1 for various offset angles, θ . Both the magnitude and angle of the applied magnetic field were varied (as noted in the figure caption) to access a wide range of θ . In each spectrum in Fig. 4.2(a) we observe only a single large resonant peak, with a peak shape that to a good approximation is a symmetric

Lorentzian, as predicted. The measured microwave sensitivities corresponding to the maxima of these resonance curves are listed in Table 2. For sample #1, the measurements show excellent quantitative agreement with the values predicted by Eq. (4.7), within the estimated uncertainty of 15% associated with the determination of the sample area. The detector sensitivity is predicted to be maximal near 90° (to be precise, at $\theta = \arccos [((-1 + \sqrt{1 - P^4})) / P^2]$) in the limit $R_0 \gg Z_0$, or slightly greater than 90°), since this maximizes both the spin torque and the response of the resistance to changes in θ . The angular dependence of the data is in good agreement. Sample #2, with the same RA product but a larger area than sample #1, exhibits very similar maximum detection sensitivities (see Table 2). This is also in agreement with Eq. (4.7). In the limit that the tunnel junction resistance R_0 is much greater than Z_0 (50Ω), the sensitivity is predicted to depend on R_0 and A only through their product RA , which is independent of the area A of the MTJ device patterned from the same magnetic multilayer film stack. Physically, the explanation for the area-independent sensitivity is that the better impedance matching provided by the lower resistance of sample #2 is offset by its larger total magnetic moment. The excellent quantitative agreement between our estimate [Eq. (4.7)] and the sensitivities measured for samples #1 and #2 give us confidence in the reliability of our estimate.

The measured mixing voltage as a function of frequency for a lower-RA sample (sample #3) is shown in Fig. 4.2(b) for various offset angles. Here we observe two peaks in each spectrum, with a significant degree of asymmetry in the peak shapes as a function of frequency, in contrast to the other samples which exhibited only a single large peak symmetric in frequency. We attribute this difference to the fact that the pinned magnetic electrode in samples #1

Table 4.2: Results of the detector diode sensitivity measurements, with a comparison to the sensitivity predicted by Eq. (4.7), calculated using the measured values of σ , R , R_P , and R_{AP} .

Sample	θ (deg)	R (k Ω)	$\sigma/(2\pi)$ (GHz)	Measured ε (mV/mW)	Predicted ε (mV/mW)
#1	49	4.36	0.197	12.3	10
	64	4.71	0.159	18.5	19
	95	5.86	0.174	24.6	27
	120	7.23	0.179	22.8	24
	142	8.65	0.188	15.7	14
	160	9.65	0.150	8.7	6
#2	42	2.41	0.179	7.4	9
	96	3.37	0.188	25.0	28
	153	5.42	0.167	11.0	11
#3	56	0.314	0.327	21.9	33
	87	0.363	0.286	42.6	65
	103	0.403	0.270	54.2	76

and #2 is left as an un-etched extended film, while the pinned electrode in sample #3 is etched. This etching leaves the upper CoFeB layer within the CoFe/Ru/CoFeB SAF in sample #3 free to precess in response to a spin torque, giving a second resonant mode in addition to the free layer. Magnetic coupling between these two modes can induce the asymmetric peak shapes seen in Fig. 4.2(b). We use the larger, lower-frequency resonance peak to determine the resonant detector response $\langle V_{res} \rangle$ (listed in Table 2).

We expect that the sensitivity of sample #3 should be greater than for the other samples, due primarily to its lower RA product, which enables better impedance matching to the 50Ω input waveguide. Indeed, sample #3 exhibits the largest peak sensitivity we have observed to date, 54 mV/mW for θ near 100. However, the measured sensitivities for sample #3 do not agree with Eq. (4.7), in all cases being approximately 30-35% below the predicted values. One potential explanation for this difference could in principle be a weaker

spin torque in these low- RA samples than expected from Eq. (4.5). We suggest that a more likely cause is coupling between the free layer and the top CoFeB layer within the CoFe/Ru/CoFeB SAF “pinned layer”. Coupled motion of these layers would reduce the detector sensitivity because the extra volume of precessing magnetic material would produce an effectively larger value of M_s in Eq. (4.7). To achieve the goal of maximizing the detector sensitivity in spin-torque diodes, we therefore suggest that the pinned layer should be left unetched so that exchange coupling to the extended film can suppress any tendency of the pinned layer to precess, thereby leaving the free layer without undesired coupling to other magnetic modes.

4.1.3 Strategies for Optimization

None of the devices that we have studied thus far were designed with optimization of the detector sensitivity in mind. Equation (4.7) suggests several strategies for significant improvement. For best sensitivity, one should maximize the TMR (or spin polarization P) while minimizing the free layer magnetization M_s and the free-layer thickness. In particular, the free-layer thicknesses can be reduced significantly below the values used for the samples in this paper (2.5 nm and 3.9 nm). For a given free layer volume, Eq. (4.7) predicts that the maximum sensitivity should be achieved by tuning the thickness of the tunnel barrier (or equivalently, the RA product) so as to match the tunnel junction resistance to the impedance of the waveguide (Z_0 , typically $50\ \Omega$) from which the microwaves are incident. However, for a given barrier thickness (*i.e.*, a given RA product) there is no advantage to increasing the tunnel junction area in order to improve the impedance match. We have already noted above in comparing

samples #1 and #2 that for the case $R_0 \gg Z_0$, Eq. (4.7) predicts that the sensitivity should be independent of the junction area for a given value of RA . For the case that R_0 is comparable to Z_0 , for a given barrier thickness the sensitivity should be optimized by always minimizing the junction area, even if this increases the impedance mismatch.

According to Eq. (4.7), the microwave sensitivity is also optimized by minimizing the resonance linewidth, σ . For the usual case that both the applied magnetic field and the initial orientation of the free layer moment are in the sample plane, the solution of the LLGS equation predicts that [76]

$$\sigma_{in\ plane} \approx \alpha\gamma(H_z + 2\pi M_{eff}) \quad (4.8)$$

which is a special case of Eq. (3.16) at zero bias. Here $4\pi M_{eff}$ is the effective demagnetization field perpendicular to the plane, and we have neglected a small contribution from the within-plane anisotropy. The measured linewidths in our samples agree with this expression using the parameters $\alpha = 0.010 \pm 0.002$ and $4\pi M_{eff} = 11 \pm 1$ kOe for samples #1 and #2, and $\alpha = 0.014 \pm 0.002$ and $4\pi M_{eff} = 13 \pm 1$ kOe for sample #3 (as was used in Chapter 2). For the case that H is small relative to $4\pi M_{eff}$, in this in-plane orientation the microwave sensitivity should be relatively insensitive to the applied magnetic field, except through the effect of H on the offset angle θ , and the detection sensitivity should scale inversely with $4\pi M_{eff}$. Consequently, efforts [114] to use interface anisotropy effects to reduce $4\pi M_{eff}$ well below the value $4\pi M_s$ could provide dramatic improvements to the detector sensitivity, as long as the Gilbert damping, α , remains small in the process. The linewidth could also be decreased by designing the tunnel junction so that the free layer magnetization points out of plane, either through the use of materials giving a perpendicular anisotropy [115] or by using a perpendicularly applied magnetic field [78]. In

these limits the form of our estimate for the sensitivity [Eq. (4.7)] is unchanged, but the LLGS prediction for the linewidth is [78]

$$\sigma_{\perp} = \alpha\gamma(H_z \pm 4\pi M_{eff}) \quad (4.9)$$

where the plus sign corresponds to an anisotropy favoring a perpendicular magnetization and the minus sign corresponds to an easy-plane anisotropy.

By extrapolating somewhat the current state of the art in MgO-based tunnel junctions, we estimate that one should be able to achieve the following parameters for a simple tunnel junction with an easy-plane magnetic anisotropy: $t = 1.0$ nm, $RA = 1 \Omega\mu\text{m}^2$, $(R_{AP} - R_P)/R_P = 100\%$ (or $P = 58\%$), $\alpha = 0.01$, $4\pi M_s = 10$ kOe, $4\pi M_{eff} = 1$ kOe [114], and $A = (50 \text{ nm})^2\pi/4$. Using these parameters, Eq. (4.7) predicts an achievable sensitivity for resonant microwave detection of 10,300 mV/mW. In comparison, the zero-bias Schottky diode detectors used commonly for microwave detection at room temperature have sensitivities an order of magnitude less, 500-1000 mV/mW (e.g., Herotek, Inc., San Jose, CA), and are not frequency-tunable. Of course in judging the suitability for applications one should consider the signal-to-noise ratio and other figures of merit, not just the sensitivity. It has been recently shown that the noise limit in diode detectors is governed by Johnson-Nyquist noise for the high-frequency regime and magnetic noise in the low-frequency regime [116].

The detector sensitivity might be improved even more by making devices with two magnetic pinned layers rather than just one (one pinned layer on either side of the free layer). This geometry has been shown to give a factor of 2 or more increase in the strength of the spin torque on the free layer per unit current [37, 117, 118].

4.1.4 Summary

In summary, we have derived an estimate for the sensitivity of resonant microwave detection by magnetic tunnel junctions used as spin-torque diodes. Our estimate is in excellent quantitative agreement with the measured sensitivities for $RA = 12 \Omega\mu\text{m}^2$ MgO-based magnetic tunnel junctions in which the pinned magnetic electrode is left un-etched. The measured sensitivity is decreased below our estimates in $RA = 1.5 \Omega\mu\text{m}^2$ tunnel junctions in which the pinned layer consists of a synthetic antiferromagnet which is etched so that the top magnetic layer of the SAF is able to precess. We suggest that coupled precession of the free layer and this top layer of the SAF may be the cause of the reduced detector sensitivity. The maximum sensitivity that we have observed experimentally to date in our non-optimized tunnel junctions is 54 mV/mW. Our estimate for the detector sensitivity [Eq. (4.7)] suggests that device optimization should be able to improve the sensitivity to greater than 10,000 mV/mW.

4.2 Microwave Amplifier

In Chapter 3 we introduced a time-resolved measurement of the spin-transfer-driven ferromagnetic resonance (ST-FMR), where we use an input microwave signal, V_{in} , to generate resonant magnetic precession via oscillating spin-transfer torque exerted on one electrode of a MTJ, and detect the corresponding resistance oscillation. This resistance oscillation, $\Delta R(t)$, is measured in the form of a RF voltage transmitted out of the MTJ arising from Ohm's law $\Delta V(t) \propto I \Delta R(t)$ when an additional DC bias current I is applied. In other words, at non-zero

bias, when resonance conditions are met, the MTJ not only reflects the incoming microwave signal V_{in} in a trivial way due to impedance mismatch, but also emits an extra microwave signal V_{extra} controllable by DC bias that adds to the normal reflected signal due to impedance mismatch V_{ref0} . While V_{ref0} is always weaker than the V_{in} , there is no fundamental reason that limits V_{extra} to be smaller than V_{in} . If the applied DC bias current is sufficiently large, one expect the total reflected signal V_{ref} can be larger than V_{in} , yielding amplification. Energy is transferred from DC to microwave frequencies to supply the gain. In this section we present the conditions for realizing microwave-frequency amplification by the ST-FMR mechanism. In particular, we discuss how a RF current/voltage feedback mechanism affects the ST-FMR formalism in the high gain regime, and the mathematical and physical arguments why the standard 2-terminal MTJ devices have very limited area in phase space that can realize such an amplification.

4.2.1 Conditions of Microwave Amplification by ST-FMR

We will analyze the simplest case in which the MTJ magnetic layers are in-plane in equilibrium, and the microwave drive excites small-angle, approximately spatially uniform magnetic precession. The high-frequency signal generated by a MTJ in response to a microwave-frequency input can be calculated using microwave circuit equations together with dynamic equations describing magnetic precession in the presence of spin torque (see Section 3.2). Equation (3.17) presents the full solution to the total reflected RF voltage in the presence of magnetization dynamics, which gives the (complex-valued) voltage gain

defined as ratio between the reflected RF voltage and the input RF voltage:

$$S_{11} \equiv \frac{V_{ref}}{V_{in}} = \frac{R_0 - (50\Omega)}{R_0 + (50\Omega)} - \frac{R_0(50\Omega)}{[R_0 + (50\Omega)]^2} \frac{\partial V}{\partial \theta} \Big|_I \frac{\gamma}{M_s V_{free}} \frac{1}{(\omega - \omega_m - i\sigma)} \left[i \frac{\partial \tau_{||}}{\partial V} + \frac{\gamma N_x M_{eff}}{\omega_m} \frac{\partial \tau_{\perp}}{\partial V} \right] \quad (4.10)$$

where $R_0 = \partial V / \partial I$ is the differential resistance of the MTJ, which is a function of bias current I and offset angle θ between the two magnetic electrode, $M_s V_{free}$ is the total magnetic moment of the precessing layer of the MTJ, γ is the absolute value of the gyromagnetic ratio, and $\partial \vec{\tau} / \partial V$ is the voltage derivative of the spin transfer torque, or spin transfer “torkance”. $N_x M_{eff} = 4\pi M_{eff} + H_z$ with $4\pi M_{eff}$ the easy-plane anisotropy of the free layer, and H_z the applied external magnetic field along the equilibrium direction of the free layer. ω_m is given by Eq. (3.15) and σ is the linewidth of the resonance response [from Eq. (3.16) and considering $\partial \tau_{||} / \partial \theta|_V = \tau_{||} \cot \theta$]

$$\sigma \approx \frac{\alpha \gamma M_{eff} (N_x + N_y)}{2} - \frac{\gamma}{2 M_s V_{free}} \left[2 \frac{\partial \tau_{||}}{\partial \theta} \Big|_V + \frac{(50\Omega)}{R_0 + (50\Omega)} \frac{\partial V}{\partial \theta} \Big|_I \frac{\partial \tau_{||}}{\partial V} \right] \quad (4.11)$$

Equation (4.10) contains all the information needed to determine the conditions to realize amplification. The first term in Eq. (4.10) is a result of impedance mismatch between the 50Ω transmission cable and the MTJ device which typically has a resistance larger than 50Ω . The second term describes the microwave signal generated by the MTJ resulting from the magnetic precession driven by the RF spin torque. One can directly measure this gain factor S_{11} by a single-port reflection measurement with a network analyzer [112, 119]. Our measured gain (shown in Fig. 4.3) for a MTJ device (similar to the one used for Fig. 3.9) agrees well with the prediction by Eq. (4.10). (More details of the measurements are expected to be described in L. Xue’s dissertation next year.)

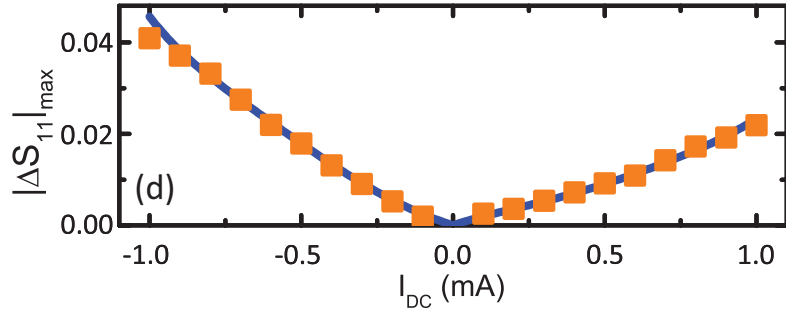


Figure 4.3: Points: Measured gain factor for microwave reflection from a MTJ device as a function of bias current. Line: prediction of Eq. (4.10) with parameters for the spin torque vector: $\partial\tau_{||}/\partial V|_\theta = 1.8(\hbar/2e)\text{k}\Omega^{-1} - 930I(\hbar/2e)\text{kV}^{-1}$ and $\partial\tau_{\perp}/\partial V|_\theta = -0.06(\hbar/2e)\text{k}\Omega^{-1} + 520I(\hbar/2e)\text{kV}^{-1}$

It turns out that the contribution to the gain factor S_{11} from the resonance effect [second term in (4.10)] is small for a typical unoptimized MTJ device, up to 4% with a bias current of 1.0 mA for the device presented in Fig. 4.3. However, there is a lot of room for improvement. Firstly, one can increase the area of the MTJ device by a few times, which improves impedance matching. Secondly, one can further reduce the thickness of the free layer by a factor of two to three so as to minimize V_{free} . Thirdly, one can reduce of the linewidth σ by reducing the easy-plane anisotropy of the free layer by using interface perpendicular anisotropy, which has shown an improvement of a factor of 10 [114]. As always, higher TMR ratio and lower RA product also helps to increase the gain factor.

We can estimate what is the maximum possible voltage gain from a optimized MTJ by evaluating Eq. (4.10) using the following optimistic but reasonable sample parameters: resistance for parallel electrode magnetizations $R_P = 50\Omega$; tunneling magnetoresistance TMR = 150%; $M_s V_{free} = 5.8 \times 10^{-15}$ emu; $\alpha = 0.01$; $H = 100$ Oe; $4\pi M_{eff} = 1.1$ kOe; $\tau_{\perp}(V, \theta) \approx 3.8V^2 \sin \theta (\hbar/2e)\text{k}\Omega^{-1}\text{V}^{-1}$, and $\tau_{||}(V, \theta) \approx 6.9V \sin \theta (\hbar/2e)\text{k}\Omega^{-1}$. These spin-torque values are determined by scaling the results in Fig 3.7(b) inversely by the ratio of the samples' zero-bias

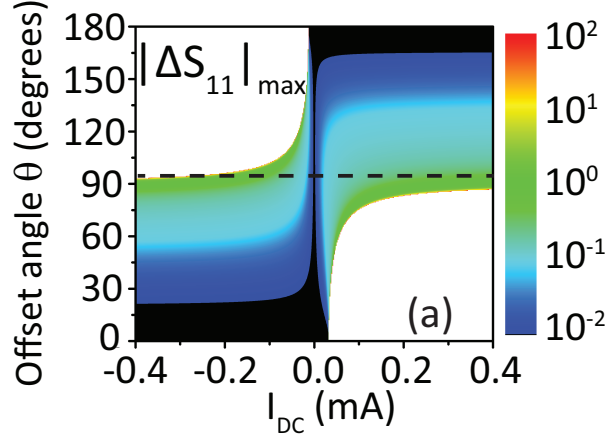


Figure 4.4: Log-scale color plot of the calculated maximum value of $|\Delta S_{11}|$ for an optimized MTJ device, as a function of I_{DC} and the offset angle θ between the magnetization directions of the two electrodes. The white regions at the upper left and lower right represent parts of the phase diagram where the DC current generates auto-oscillations with no applied oscillatory current.

parallel resistances and assuming for simplicity that $\tau_{\perp} \propto V^2$ and $\tau_{||} \propto V$. In Fig. 4.4, we plot the magnitude of the maximum change in S_{11} near resonance. We find that voltage gains greater than one are possible, but they require fine-tuning the offset angle θ and I_{DC} very precisely to bias the sample near the critical current where the bias-dependent linewidth σ goes to zero, the threshold for exciting DC-driven auto-oscillations.

4.2.2 Mathematical Analysis of Amplification and the Feedback Effect

In Section 3.2, we briefly introduced a feedback effect present in ST-FMR experiment when a non-zero bias is applied. The applied RF current I_{RF} induces magnetization precession $\delta\theta$, which in turn produces an extra RF signal that alters the applied RF current. This is exactly the same mechanism we investigate

to realize microwave amplification in this section, and Eq. (4.10) has already taken this feedback effect into account self-consistently. The gain factor from resonance effect [the second term in Eq. (4.10)] can be viewed an order parameter that describes the significance of the feedback effect. As shown in Fig. 4.3, in typical experimental conditional that is not optimized for amplification, the gain factor is relatively small. Equivalently speaking, the feedback is small, which is the reason that we did not pay close attention to this effect in analyzing the early experiments of ST-FMR [76, 80]. However, it becomes significant by definition if one aims to achieve microwave amplification. Here I would like to discuss in more detail how this feedback mechanism in the high gain regime changes the ST-FMR formalism from our early analysis presented in Section 2.3 and in references [76, 80].

When an external RF current I_{RF} is applied to the MTJ device, in Section 2.3 we assumed that I_{RF} is not affected by the resonance, and solved the complex-valued (\hat{y} -component of) magnetic precession amplitude [Eq. (2.15)]:

$$m_{y1} = \frac{\gamma I_{RF}}{2M_s V_{free}} \frac{1}{(\omega - \omega_{Irf} - i\sigma_{Irf})} \left[i \frac{\partial \tau_{||}}{\partial I} + \frac{\gamma N_x M_{eff}}{\omega_{Irf}} \frac{\partial \tau_{\perp}}{\partial I} \right] \quad (4.12)$$

Alternatively, it can be viewed that an external RF voltage V_{RF} is applied to the MTJ device and drive resonant precession, which leads to:

$$m_{y1} = \frac{\gamma V_{RF}}{2M_s V_{free}} \frac{1}{(\omega - \omega_{Vrf} - i\sigma_{Vrf})} \left[i \frac{\partial \tau_{||}}{\partial V} + \frac{\gamma N_x M_{eff}}{\omega_{Vrf}} \frac{\partial \tau_{\perp}}{\partial V} \right] \quad (4.13)$$

These two solutions to m_{y1} are extremely similar since $\partial \vec{\tau} / \partial I = (\partial \vec{\tau} / \partial V) R_0$ and $V_{RF} \approx I_{RF} R_0$. However, there is a difference embedded in the expression of linewidth, σ_{Irf} versus σ_{Vrf} , that becomes critical in the high gain regime. (The resonance frequencies, ω_{Irf} and ω_{Vrf} , are also different, but this effect is less

important than the linewidth, so we will only focus on the linewidth.)

$$\begin{aligned}\sigma_{Irf} &= \frac{\alpha\gamma M_{eff}(N_x + N_y)}{2} - \frac{\gamma}{2M_s V_{free}} \left[\frac{\partial \tau_{||}}{\partial \theta} \Big|_I + \tau_{||} \cot \theta \right] \\ \sigma_{Vrf} &= \frac{\alpha\gamma M_{eff}(N_x + N_y)}{2} - \frac{\gamma}{2M_s V_{free}} \left[\frac{\partial \tau_{||}}{\partial \theta} \Big|_V + \tau_{||} \cot \theta \right]\end{aligned}\quad (4.14)$$

These two expressions are nearly identical other than whether the partial derivatives $\partial \vec{\tau} / \partial \theta$ are taken with respect to I or V . This originates from how the Taylor expansion on the spin torque is taken (with respect to I and θ for I_{RF} -based analysis, and with respect to V and θ for V_{RF} -based analysis). Noting that $(\partial \tau_{||} / \partial \theta)|_I = (\partial \tau_{||} / \partial \theta)|_V + (\partial \tau_{||} / \partial V)|_\theta (\partial V / \partial \theta)|_I$, and $\partial \tau_{||} / \partial \theta|_V = \tau_{||} \cot \theta$, Eq. (4.14) can be written as:

$$\sigma_{Irf} = \frac{\alpha\gamma M_{eff}(N_x + N_y)}{2} - \frac{\gamma}{2M_s V_{free}} \left[2 \frac{\partial \tau_{||}}{\partial \theta} \Big|_V + \frac{\partial \tau_{||}}{\partial V} \Big|_\theta \frac{\partial V}{\partial \theta} \Big|_I \right]\quad (4.15)$$

$$\sigma_{Vrf} = \frac{\alpha\gamma M_{eff}(N_x + N_y)}{2} - \frac{\gamma}{2M_s V_{free}} \left[2 \frac{\partial \tau_{||}}{\partial \theta} \Big|_V \right]\quad (4.16)$$

In the presence of the feedback effect, neither I_{RF} and V_{RF} can be modeled as constants as a function of frequency in the analysis, and the exact solution shown in Eq. (4.11) is between the two solutions shown in Eq. (4.16). There is a natural reason that the feedback effect comes into play in the denominator as a correction to the linewidth. Imagine that the initial applied RF voltage V_{RF0} produces a resonant precession that feed back into the RF voltage as $\Delta_1 V_{RF}$, and $\Delta_1 V_{RF} = \lambda V_{RF0}$ with λ a feedback factor, then the second order feedback effect will be $\Delta_2 V_{RF} = \lambda^2 V_{RF}$. The extra RF voltage produced by the resonance effect after feedback is taken into full consideration should be a sum of all the feedback terms:

$$\begin{aligned}V_{RF} &= V_{RF0}(\lambda + \lambda^2 + \lambda^3 + \dots) \\ &= V_{RF0} \left(\frac{\lambda}{1 - \lambda} \right)\end{aligned}\quad (4.17)$$

This translates into a resonance gain factor $\Delta S_{11} = \lambda/(1 - \lambda)$ subject to a pre-factor of the order of unity. For simplicity if we neglect the perpendicular component of the spin torque and consider the amplification at $\theta = 90^\circ$ at resonance frequency, the feedback factor is

$$\lambda = \left[-\frac{(50\Omega)}{R_0 + (50\Omega)} \frac{\gamma}{M_s V_{free}} \frac{\partial \tau_{||}}{\partial V} \Big|_\theta \frac{\partial V}{\partial \theta} \Big|_I \right] \Big/ [\alpha \gamma M_{eff} (N_x + N_y)] \quad (4.18)$$

and the gain factor S_{11} [Eq. (4.10)] becomes:

$$S_{11} \equiv \frac{V_{ref}}{V_{in}} = \frac{R_0 - (50\Omega)}{R_0 + (50\Omega)} + \frac{2R_0}{[R_0 + (50\Omega)]} \frac{\lambda}{1 - \lambda} \quad (4.19)$$

For the optimistic parameters we used for Fig. 4.4, the pre-factor $2R_0/[R_0 + (50\Omega)]$ is 1. In order to achieve amplification ($\Delta S_{11} > 1$), a feedback factor of $\lambda > 1/2$ is required. On the other hand, when $\lambda > 1$, the feedback voltage becomes stronger by each order. This means that an infinitesimal microwave perturbation at the resonance frequency would be amplified out of the linear-response range. Practically this means that only a DC current without RF drive can produce microwave emission, a well-known phenomenon studied since 2003 [17]. The form of $\lambda/(1 - \lambda)$ is a direct consequence of the feedback mechanism, and as a result one has to bias the MTJ device very close to the onset of instability to achieve a useful gain. For example, for a gain of 10, one has to approach the critical current within 10%. With better optimized MTJ devices, the potential of a practical amplifier based on ST-FMR is actually not limited by the ability to make large λ (which can easily exceed 10 with the optimistic parameter set used for Fig. 4.4), but limited by the difficulty to utilize any λ greater than 1. While λ is more related to the intuitive “strength” of the MTJ to amplify RF signal and can be improved with higher TMR, better impedance matching, higher tolerance (to current) of the tunnel barrier, the fact that $\lambda > 1$ causes instability is a more fundamental obstacle to overcome.

With $\theta \neq 90^\circ$, the linewidth acquires another term in bias dependence, $(\gamma/M_s V_{free})(\partial\tau_{||}/\partial\theta)|_V$. This is known as the major damping/anti-damping effect of spin transfer torque [42, 78], which scales as $\cos\theta$. In most previous experiments, since $R_0 \gg 50\Omega$, this is the only term considered in the bias dependence of linewidth, and the feedback term [the last term in Eq. (4.11)] is neglected. With low RA tunnel junctions with R_0 approaching 50Ω , both terms need to be considered. In the simplest approximation, both term scale linearly with bias current. One can change the relative sign and relative magnitude of the two terms by varying the offset angle θ since the feedback term scales with $\sin\theta$ while the damping/anti-damping term scales with $\cos\theta$.

$$S_{11} \equiv \frac{V_{ref}}{V_{in}} = \frac{R_0 - (50\Omega)}{R_0 + (50\Omega)} + \frac{2R_0}{[R_0 + (50\Omega)]} \frac{\lambda}{1 - \lambda - \epsilon\lambda \cot\theta} \quad (4.20)$$

This presents a hope for a practical amplifier, because one can use the damping/anti-damping term to work against the feedback term to mitigate the divergence problem and allow higher λ to kick in. Unfortunately, ϵ is at least 10 even for very optimistic parameters and has little room for further reduction (limited by $\partial V/\partial\theta < V/2$, $\partial\tau_{||}/\partial\theta \approx (\partial\tau_{||}/\partial V)V \cos\theta$), leading to a range of only 6° ($90^\circ < \theta < 96^\circ$) that the divergence problem is improved from Eq. (4.19) (while not making $1 - \lambda - \epsilon\lambda \cot\theta > 1$). For $\theta < 90^\circ$, the divergence problem becomes worse, while for $\theta > 96^\circ$, $1 - \lambda - \epsilon\lambda \cot\theta > 1$, and maximum possible gain is dramatically reduced because of effective damping increasing with increasing bias. Of the 6° range, there is an even smaller window that the stability (to bias current) is significantly improved for practical purpose. This ultra-sensitivity to offset angle also likely prohibits the application potential.

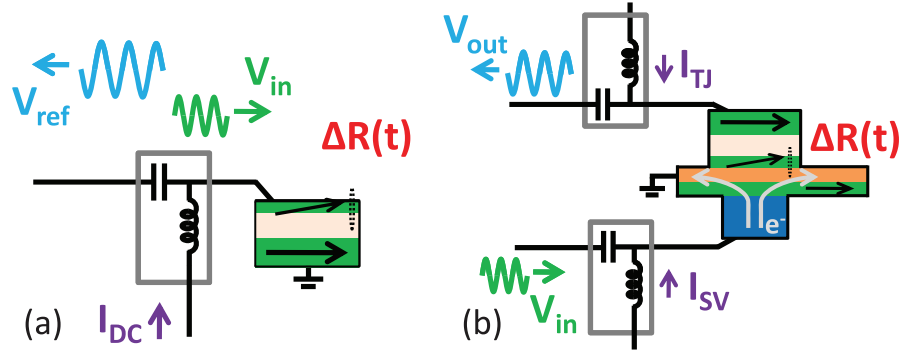


Figure 4.5: Schematic illustration of microwave amplification with (a) a conventional 2-terminal MTJ and (b) a proposed 3-terminal MTJ device.

4.2.3 Summary

Owing to the nature of the feedback mechanism and the strong angular dependence of the damping/anti-damping effect from spin torque, there is only a very small area left on the (θ, I) phase space (Fig. 4.4) that one can utilize to realize microwave amplification for a conventional 2-terminal MTJ device based on ST-FMR, which likely prohibits the use of these MTJs for microwave amplifier applications [Fig. 4.5(a)]. In ref. [112], we further investigated a type of 3-terminal devices [Fig. 4.5(b)] that somewhat tackles the limitation presented here in a 2-terminal MTJ device. While it does not fundamentally solve the problem of ultra-sensitivity of gain factor on I or θ , it introduces an extra knob (in the DC current through spin valve) that one can tune the effective damping to compensate for this deficiency of parametric sensitivity. I will not go into further details to discuss ST-FMR in a 3-terminal device, which is covered by ref. [61, 112] and L. Xue's dissertation expected in 2013.

CHAPTER 5

SPIN DEPENDENT TUNNELING AND SPIN TRANSFER TORQUE IN FERROMAGNETIC NANOPARTICLES

So far most previous experiments in the field of spin transfer torque, such as I discussed in Chapter 2-4, have studied the effects of spin torque on lithographically-defined ferromagnets with sizes on the order of 100 nm x 100 nm x 3 nm, large enough to be treated as macroscopic objects in the context of electronic band structure and magnetization dynamics. As mentioned in the introductory chapter, there have been predictions that in very small magnetic nanoparticles, only a couple of nanometers in size, spin transfer torque might display resonance enhancement due to quantized electronic states, and/or drive magnetic switching with very low current due to reduced magnetic damping. In this chapter, I discuss our ongoing experiment aiming to study spin-polarized tunneling and the effects of spin transfer torque in magnetic nanoparticles.

In this experiment, we fabricate MgO-based magnetic tunnel junction devices with CoFeB or Co magnetic nanoparticles 1-3 nm in diameter embedded in the MgO tunnel barrier (Fig. 5.1). By making nano-pillar devices (less than 50 nm in lateral dimension) containing less than 100 nanoparticles and taking advantage of the Coulomb blockade effect, we are able to resolve the magnetoresistance associated with the magnetic switching of single nanoparticles. We present the first experimental evidence of spin transfer torque (from tunneling current) in single magnetic nanoparticles by observing an asymmetry in the single-particle switching phase diagram. We also detect a DC mixing voltage likely arising from spin-transfer-driven ferromagnetic resonance (ST-FMR) associated with the nanoparticles.

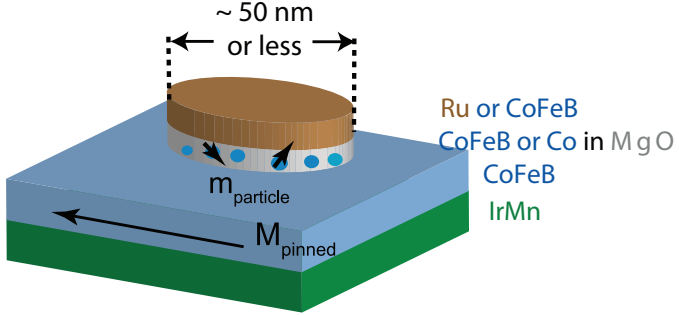


Figure 5.1: Schematic geometry of a nanopillar MTJ device with embedded magnetic nanoparticles.

5.1 Device Fabrication

Our magnetic nanoparticles are fabricated by deposition of a very thin layer (4-8 Å) of CoFeB or Co on MgO. Since CoFeB (or Co) atoms are more attracted to other CoFeB (or Co) atoms than the MgO surface, the deposited CoFeB (or Co) automatically forms a layer of nanoparticles 1-3 nm in size instead of a continuous film. Deposition of another MgO layer on top of the nanoparticles isolates them from metals subsequently deposited so that tunnel barriers are formed on both sides of the nanoparticle ensembles. Such a self-assembly mechanism has been well known and there have been a few previous studies where magnetic nanoparticles are embedded in MgO tunnel barriers in such a way [120–123]. These experiments have generated interesting results related to the tunneling magnetoresistance in the Coulomb blockade regime. Similar experiments have also been done with nanoparticles in an AlO_x tunnel barrier [124, 125]. Compared with these experiments designed for tunneling transport studies of nanoparticle ensembles at low current densities, our fabrication requires significant improvements on two fronts. Firstly, we have to make the MgO tunnel barrier as thin as possible (so that the resistance-area product, RA , is sufficiently low) to allow high tunneling current density

to produce measurable effects from spin transfer torque. Secondly, we would like to have as few nanoparticles as possible in our devices so that we can study both spin transport and spin torque in single nanoparticles and approach the single-electron-tunneling regime.

Our fabrication processes are adapted from the recipe developed by H.-W. Tseng and Y. Li for making MgO-based nano-pillar MTJ devices at Cornell, with additional testing and optimization on the growth of ferromagnetic nanoparticles and double MgO tunnel barriers. Fabrication of two full 4-inch wafers of devices, on good days, can be finished in less than a week. The whole process can be divided into three major steps: deposition of the full film stack, definition of the nanopillar devices, and making contact leads.

The complete film stack is deposited onto an oxidized Si wafer in the AJA sputtering chamber in D-12 of Clark Hall, with the typical layered structure and growth parameters shown in Table 5.1. The MgO layers are grown by RF magnetron sputtering at 100 W, and all other materials use DC magnetron sputtering. By using the AJA magnetic stage to mount the wafer, the magnetic field (of about 200 Oe at the center of the wafer) induces an exchange bias on the IrMn/CoFeB interface so that the bottom CoFeB electrode has a favored magnetization direction. In order to produce low-RA MgO tunnel barriers on both side of the nanoparticles, we grow both layers of MgO with small wedges. This is done by first growing MgO for 3-4 minutes with the stage rotating (as during the deposition of other materials), and then growing MgO for about 1 minute with the stage not rotating (nr). The MgO target is placed in Gun #2 as always in AJA chamber, and naturally the gun is at an angle to the stage so that the near side of the stage could see growth rate perhaps several times

higher than the far side. The orientation of the wafer relative to the MgO gun during the growth of the wedge is checked visually by eye using a flashlight, and we make sure that the two layers of MgO have wedges in approximately orthogonal directions to each other. In Table 5.1, the waiting time stands for the approximate time between lighting up the gun and opening the shutter. Although not critical, it is believed that before starting deposition of some metallic layers one needs to get rid of potential oxidized surface of the target induced by sputtering of MgO.

Table 5.1: Layer structures and growth parameters for magnetic nanoparticle tunnel junctions

Gun#	Target	Power (W)	Pressure (mTorr)	rate (Å/s)	Waiting time	Depos. time	Thickness (nm)
1	Ta	100	2	~0.65	10"	2'00"	8
6	Ru	100	2	~0.40	10"	10'00"	24
1	Ta	100	2	~0.65	10"	2'00"	8
3	IrMn	100	2	~0.55	2'00"	5'00"	17
4	CoFeB	75	2	~0.29	1'00"	2'10"	3.5
2	MgO	100(RF)	2	N/A	15"	3'05"	
						+55"nr	1
4	CoFeB	75	2	~0.29	1'00"	20"	0.6
2	MgO	100(RF)	2	N/A	15"	3'40"	
						+1'10"nr	1
6	Ru	100	2	~0.40	1'00"	1'40"	4
1	Ta	100	2	~0.65	10"	2'20"	9
6	Ru	100	2	~0.40	10"	3'30"	8.5

By growing the layer structure shown in Table. 5.1, we have a double-barrier tunnel junction system of IrMn-pinned CoFeB electrode/ MgO/ CoFeB nanoparticles/ MgO/ Ru (normal metal) electrode. This is the main structure on which we will present experimental data. We have also made a number of other similar structures, including IrMn/ CoFeB/ MgO/ CoFeB nanoparticles/ MgO/ CoFeB, where there are three different ferromagnetic layers in the structure, similar to what was used in studying the cotunneling enhancement

of TMR [120–123]. We have also fabricated Co nanoparticles in a layer structure of CoFeB/ MgO/ Co nanoparticles/ MgO/ Ru, which shows some striking differences in electrical and magnetic properties compared with CoFeB nanoparticles.

We use a HSQ-based recipe of electron beam lithography to pattern the nanopillar devices. The processes are listed as the following:

1. Spin omnicoat at 1500 rpm for 40 sec, bake at 180 °C for 1 min. Repeat this step to increase the thickness of omnicoat.
2. Spin 495k PMMA (4%) at 4000rpm (2000rpm² acceleration) for 30 sec (~150nm) and bake at 170 °C for 1 min.
3. Spin 6% HSQ at 4000rpm (2000rpm² acceleration) (~80nm) for 30 sec and bake at 170 °C for 1 min.
4. Expose in the JEOL 6300 (4th lens) or the JEOL 9300 at 1 nA current. To make small devices, one can design dimensions ranging from 5 nm × 5 nm to 40 nm × 40 nm in L-edit files, and the doses used for exposure range from 5000-25000 μ C/cm².
5. Develop in 726 MIF for 2 min 05 sec, rinse with DI water, and blow dry with nitrogen.
6. Oxygen plasma etching in the Oxford 80#1 RIE, 100 W, 50 mTorr, 20 sccm for 1 min 30 sec.
7. Check under optical microscope and SEM.
8. Ion mill etching with the new IBD system in E-7 Clark Hall at 150 V and 35 mA at an angle of 3° (very close to normal). 30 sec / 30 sec duty cycle is required to reduce heating. Use the end-point elemental detector to

monitor the etching and stop in the middle of MgO or IrMn depending on whether we want the bottom electrode extended. This etching step typically takes ~20-25 duty cycles.

9. Continue ion mill etching at 150 V and 35 mA at an angle of 65° to clean the side-wall of nanopillars for 2 min.
10. Evaporate 36 nm of SiO₂ at ~1 Å/sec with the SC4500 even-hour evaporator at CNF.
11. For lift-off, soak the wafer in Remover PG on a hot plate set to 65 °C for 30 min, and then sonicate for 15 min. Transfer the wafer into IPA and sonicate for 15 min. The lift-off steps can be extended in time or repeated multiple times if necessary for increasing the chances of successful lift-off.
12. Check with optical microscope and AFM. Repeat the lift-off process if the lift-off yield is low.

Up to this point we have nanopillar devices with SiO₂ protected side-walls and open Ru tops. The next step is to make contact leads and pads for both the top and bottom electrodes with photolithography. The processes are briefly listed as the following:

1. Photolith #1 to define bottom lead and isolate devices. Spin P-20 primer at 3000 rpm for 30 sec, and Shipley S1827 at 2000 rpm for 30 sec, bake at 115 °C for 120 sec, and expose with 5× Stepper with 1.7 sec exposure time.
2. Ion milling with the new IBD system (E-7 Clark Hall) at 150 V, 35 mA, 20° all the way into the SiO₂ substrate (no duty cycle required, usually takes ~35 min) followed by 65° side wall cleaning for 2 min. Strip photoresists by acetone and IPA.

3. Photolith #2 to open bottom contact pad. Spin P-20 primer at 3000 rpm for 30 sec, and Shipley S1827 at 2000 rpm for 30 sec, bake at 115 °C for 120 sec, and expose with 5× Stepper with 1.5 sec exposure time.
4. CF4/H4 oxide etch with Oxford 80#1 RIE. CF4 30 sccm, H₂ 10 sccm, 40mT, 120W for 2 min 45 sec. (Etching rate ~20 nm / min). Strip photoresists by acetone and IPA.
5. Photolith #3 to protect short (on the sidewalls produced by Photolith #1 etching). Spin P-20 primer at 3000 rpm for 30 sec, and Shipley S1827 at 2000 rpm for 30 sec, bake at 115 °C for 120 sec, and expose with 5× Stepper with 1.5 sec exposure time.
6. Evaporate 150 nm of SiO₂ with the SC4500 even hour evaporator at CNF at 1-2 Å/sec. Lift-off (strip photoresists) by acetone and IPA.
7. Photolith #4 to make top leads. Spin P-20 primer at 3000 rpm for 30 sec, and Shipley S1827 at 2000 rpm for 30 sec, bake at 115 °C for 120 sec, and expose with 5× Stepper with 1.7 sec exposure time.
8. O₂ plasma clean with the Oxford 80#1 RIE for 1 min at 150 W to remove both photoresists residues and PMMA/omnicoat residues.
9. Deposit top leads by sputtering with the AJA sputtering system in D-12 Clark Hall. Ta 100 W for 26 min, and Ru 100 W for 16 min. Lift-off (strip photoresists) by acetone and IPA.

For most of the devices we will discuss in this chapter, we do not perform high-temperature annealing at any stage of the fabrication. We attempted annealing in the early stage of the project, but we do not understand the complex changes of electrical and magnetic properties of the devices after

annealing. We will discuss the effect of annealing briefly in an appendix section of this chapter.

5.2 Device and Film Characterization for CoFeB nanoparticles

5.2.1 Magnetometry Characterization of CoFeB Nanoparticle Assembles

Even before we proceed to pattern the nano-pillar devices, we look for evidence to confirm that nanoparticles are formed during our deposition of the ultra-thin layer of CoFeB or Co. Magnetometry of un-patterned film stack turns out to be a very useful tool not only for early-stage debug of our fabrication, but also for basic characterization of the nanoparticles for comparison to our later electrical measurements.

At room temperature a nanoparticle behaves superparamagnetically [126] with its magnetization fluctuating wildly because the thermal excitation energy $k_B T$ usually far exceeds the energy scale associated with the magnetic anisotropy of the nanoparticle. For an ensemble of nanoparticles, the macroscopic magnetization M is zero in the absence of external magnetic field. When an external magnetic field \vec{H} is applied, the magnetization of a particle has higher probability to be near parallel to \vec{H} than near anti-parallel to \vec{H} as described by the Boltzmann distribution [Fig. 5.2(c)]. The possible orientations of nanoparticle magnetization can be described by a unit sphere, and the probability density for the single-particle magnetization to be at a given angle θ

relative to \vec{H} is

$$P \propto e^{N\mu_B H \cos(\theta)/k_B T} \sin \theta \quad (5.1)$$

where k_B is the Boltzmann constant, μ_B is the Bohr magneton, and N is the number of net single electron spins this nanoparticle contains. (Since the size of the nanoparticles are very small, we consider the magnitude of the single-particle magnetization fixed at $N\mu_B$.) Such a probability distribution of single-particle magnetization increasingly favors parallel to \vec{H} with increasing amplitude of \vec{H} . Therefore the macroscopic magnetization for a particle ensemble M is aligned and gradually increased with the external magnetic field, with the saturation field scale determined by the competition between the thermal excitation $k_B T$ and the in-field magnetostatic energy of the nanoparticle $N\mu_B H$. More quantitatively, the statistical averaged magnetization for a nanoparticle with N spins is

$$M_H = N\mu_B \frac{e^{2A}(1 - 1/A) + (1 + 1/A)}{e^{2A} - 1} \quad (5.2)$$

where $A = N\mu_B H/k_B T$. Therefore by measuring the magnetic field-dependence of the nanoparticle magnetization, we can estimate the number of spins contained in the nanoparticle. On the other hand, for a continuous film the thermal energy is insignificant, so one expects the external field to compete only with magnetic anisotropies instead, and abrupt switching should happen when field is applied in certain directions.

We attempted to measure the magnetization of the nanoparticle ensembles embedded in a magnetic tunnel junction film stack such as in Table. 5.1. However, the bottom ferromagnetic electrode has a magnetization that is about 10 times larger than the nanoparticles, which makes it very difficult to separate the magnetization behavior of nanoparticles alone. Therefore, we made a film

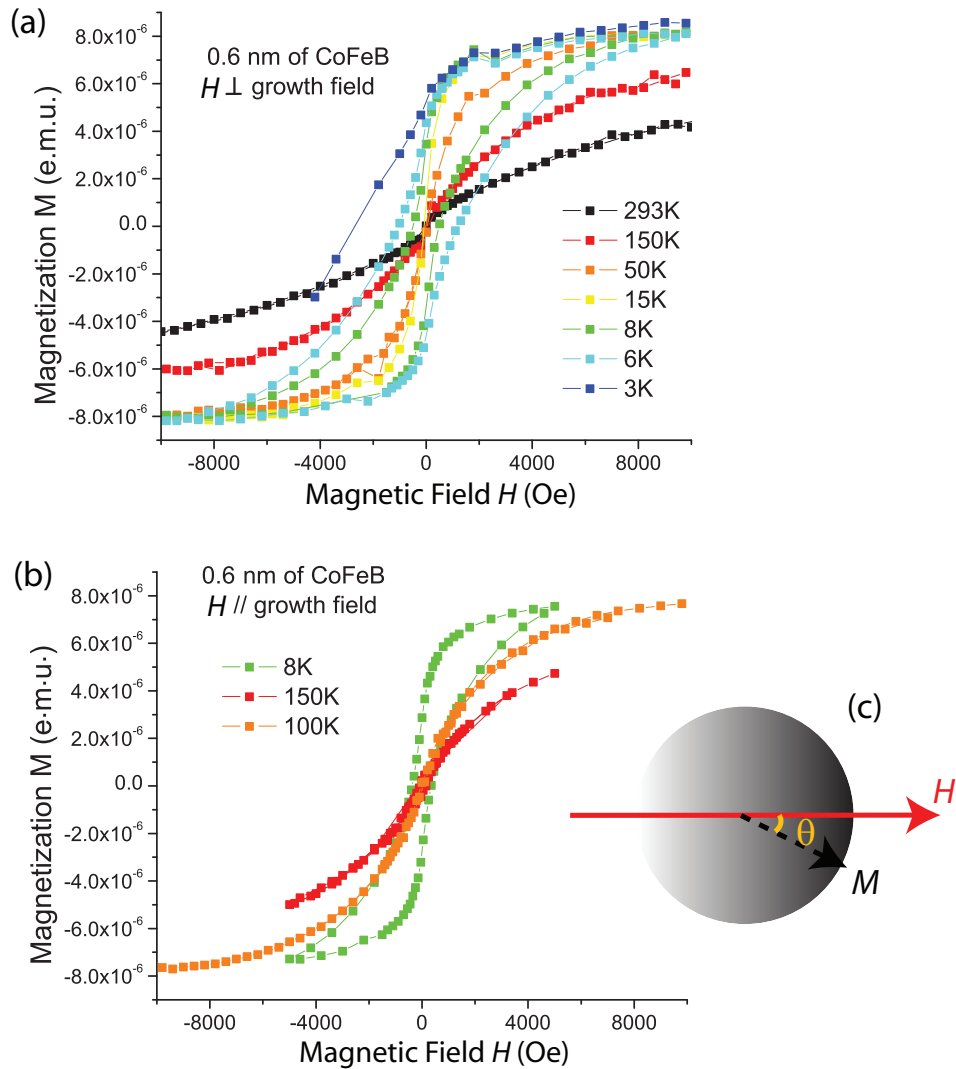


Figure 5.2: Characterization of CoFeB nanoparticles by SQUID magnetometry. (a) Magnetization M as a function of external magnetic field H applied in-plane and perpendicular to the growth field for a thin layer of CoFeB nanoparticles (nominal thickness 6 Å) at various temperatures. (b) M vs. H applied parallel to the growth field for the same CoFeB nanoparticles at various temperatures. (c) Schematic of the effect of an external field on the magnetization distribution of a nanoparticle ensemble at finite temperature.

stack very similar to Table. 5.1 but with the bottom CoFeB electrode replaced with 3.5 nm of Ru, and magnetometry characterizations of such a film stack is shown in Fig. 5.2. Figures 5.2(a) and (b) show the magnetization M of a 5.5 mm \times 5.5 mm chip of such a CoFeB nanoparticle sample as a function of magnetic field H applied perpendicular and parallel to the growth field, respectively, measured by SQUID magnetometer under various temperatures. It should be noted that these curves are not directly comparable to Eq. (5.2) since the nanoparticles do not have uniform sizes. However, it shows the qualitative trend that we expect from a competition between thermal energy and magnetostatic energy. At room temperature, the magnetization of the nanoparticle ensemble is far from saturated at 1 T, but at lower and lower temperature, the saturation becomes more evident at lower field, and the $M - H$ slope at low field becomes steeper.

Equation (5.2) predicts $M \approx M_{max}/3$ when $N\mu_B H = k_B T$ and $M \approx M_{max}/2$ when $N\mu_B H = 2k_B T$, which can be used as a rough estimate of the mean (or average) number of spins per particle in our nanoparticle ensemble. In both Fig. 5.2(a) and (b) M reaches half maximum at about $H = 4000$ Oe at $T = 150$ K (and scales inversely with temperature pretty well), suggesting $N \approx 1000$. From the unit-volume saturation magnetization of CoFeB of ~ 1100 Oe, we can estimate that the volume of a 1000-spin nanoparticle is about 8 nm³, corresponding to a diameter of 2.5 nm if we imagine the nanoparticle as a sphere. Intuitively, this number is also consistent with the number of atoms expected for the nanoparticle, considering ~ 1.5 spins per atom (with dilution from boron) and lattice spacing ~ 2.5 Å. Moreover, we can also estimate the total number of nanoparticles in our 5.5 mm \times 5.5 mm chip from the saturated value of magnetization M in Fig. 5.2, which gives the area density of the CoFeB

nanoparticles, about 3 per $10\text{ nm} \times 10\text{ nm}$ area.

More interesting magnetic behavior occurs below ~ 12 K for the CoFeB nanoparticles, when hysteresis starts to emerge on M vs. H measurements shown in Fig. 5.2(a) and (b). Such hysteresis reflects the magnetic anisotropy of the nanoparticles along the direction of the field applied during SQUID measurement. Magnetic anisotropy induces well-defined energy minima and maxima for each nanoparticle, but at higher temperature thermal excitation allows the nanoparticles to hop over the energy barrier so that no hysteresis is observed. The transition temperature (blocking temperature) [126],

$$T_B = N\mu BH_{anis}/25k_B \quad (5.3)$$

which is 12 K measured here, allows us to estimate the maximum anisotropy field of the nanoparticle $H_{anis} = 4000$ Oe. However, this estimation corresponds to maximum detectable anisotropy energy scale for all the nanoparticles. The average anisotropy of the particle ensemble is much smaller, evidenced by significant widening of hysteresis with lower temperature. Moreover, the largest anisotropy energy found among these nanoparticles is likely associated with particles somewhat larger than average in size instead of $N = 1000$. This should also lead to much lower H_{anis} than our estimate here. Another important observation is that there is no significant difference in M vs. H between Fig. 5.2(a), where field is applied perpendicular to growth field and Fig. 5.2(b) where field is applied parallel to growth field. It suggests that anisotropies of the nanoparticles are randomly oriented (at least for in-plane directions), and the grow field (~ 200 Oe) is insignificant in inducing the anisotropy.

5.2.2 STEM images of the Embedded Nanoparticles

A sample chip from the tunnel junction film stack containing nanoparticles as deposited (Table 5.1, wafer #ADTJ-1) was imaged by scanning transmission electron microscopy by Qing-Yun Mao and Pinshane Y. Huang in D. A. Muller's group at Cornell. Figure 5.3 shows cross section images of the film stack taken at the Nion UltraSTEM with aberration correction in 150 Duffield Hall. The full layer-by-layer structure can be resolved [Fig. 5.3(a)] and there appear to be some unexpected interface roughness starting from as low as the 25 nm-thick bottom Ru layer. Close-up view of the layers near MgO tunnel barrier demonstrates the existence of nanoparticles, and electron energy loss spectroscopy (EELS) elemental mapping further confirms the chemical composition of the nanoparticles [Fig. 5.3(b)]. The yellow color in the RGB(Fe/Co/Ru) mapping shows that the nanoparticle contains Fe and Co. The green color (instead of yellow) of the particles in RGB(O/Co/Ru) mapping shows that particles are relatively intact from oxidation from the surrounding O atoms.

The sizes of the nanoparticles estimated from the images are 2-2.5 nm in diameter. The density of the nanoparticles can also be estimated in a STEM experiment after the lateral dimension of the polished sample (the "depth" of the cross section images in Fig. 5.3) is estimated from the overall absorption level of electron beam in Si substrate, which is ≤ 10 nm for the images shown in Fig. 5.3(b). Such an estimate yields about 2.5 per $10\text{ nm} \times 10\text{ nm}$ for the area density of the nanoparticles, with a factor of 2 uncertainty. Both the size and the density inferred from the STEM images are astoundingly close to the estimates we arrived from the magnetometry measurements, given how rough both methods are expected to be.

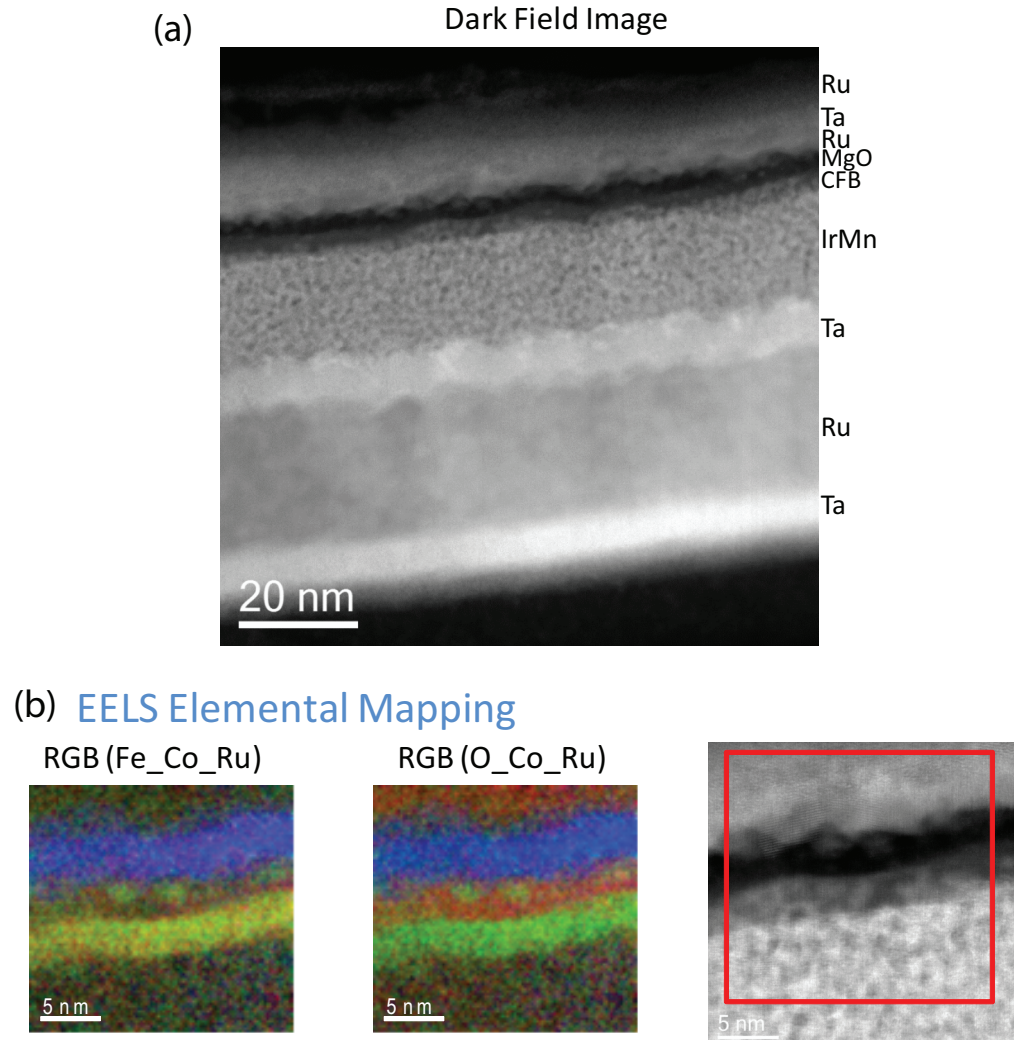


Figure 5.3: (a) Scanning transmission electron microscopy (STEM) image of a complete sputtered layer stack (wafer #ADTJ-1) of MgO-based ferromagnetic nanoparticle tunnel junction. (b) Electron energy loss spectroscopy (EELS) elemental mapping of a few nanoparticles embedded in the MgO tunnel barrier. Courtesy of Qing-Yun Mao and Pinshane Y. Huang in Muller Group at Cornell.

5.2.3 Full Wafer Electrical Characterization

After the nano-pillar devices are fabricated, we electrically test a large number of devices on a room temperature probe station (such as the projected field magnet probe station in D-10 Clark Hall). Such a test provides a brief idea of how well our wedged MgO produces devices of various *RA*, and how much magnetoresistance response these devices show.

We make 13×13 dies of devices across the 4-inch wafers, and each die contains 16 devices with different designed dimensions and doses for e-beam exposure. Most of them are made as small as possible and some of them are designed larger. The largest device in each die ($500 \text{ nm} \times 500 \text{ nm}$) has the highest yield and the most consistent size that is presumably closest to the designed size, which we can use as a reference point to characterize the *RA* of the double-barrier tunnel junction in different areas across the wafer. Table 5.2 lists the resistances of some of these $500 \text{ nm} \times 500 \text{ nm}$ devices across the wafer which demonstrates the double wedges of MgO that we have grown. The devices on the left side of the wafer (and left side of Table 5.2) have thicker MgO layer below the nanoparticles, and the devices on the bottom side have thicker MgO layer above the nanoparticles. The distribution of the resistances confirms that both MgO wedges are effective in creating a gradient in the *RA* of devices across the wafer.

The electrical transport characteristics of the devices involving nanoparticles are demonstrated in Fig. 5.4. The bias dependence of the resistance of a typical magnetic nanoparticle tunnel junction device [red curve in Fig. 5.4(a)] shows a sharp zero-bias resistance peak, in striking contrast to the weak bias dependence of the resistance of a conventional MTJ (without nanoparticles) in the parallel

Table 5.2: The resistances (in $k\Omega$) of $500 \text{ nm} \times 500 \text{ nm}$ magnetic nanoparticles tunnel junction devices across 13×13 dies at different locations of a 4-inch wafer

1	2	3	4	5	6	7	8	9	10	11	12	13
					0.35	0.31						
					0.34	0.26						
	1.2	1.02	0.75	0.57	0.34	0.29					0.14	
	1.2	0.82	0.61	0.50	0.28	0.23						
1.9	1.4	1.00	0.62	0.46	0.31	0.26				0.22	0.23	
				0.69	0.51	0.31	0.23					
											0.25	0.25
			1.03	0.79	0.58							
2.0	1.93			1.16	0.94	0.83	0.72	0.61	0.60	0.41	0.36	0.28
2.4	1.86					1.14	0.93	0.85	0.84	0.44	0.42	
	2.89					3.95	2.00	2.63	1.46	1.33		
	5.78					7.60	6.40					

state [black in Fig. 5.4(a)]. We have also briefly measured devices in the continuous helium-flow probe station in D-10 of Clark Hall, and the resistances of all the nanoparticle MTJ devices show a strong increase with decreasing temperature similar to Fig. 5.4(b). Since the thermal response time of the low-T probe station appears to be very slow, for quantitative purposes Fig. 5.4(b) presents the temperature dependence data of a typical device measured by the PPMS.

We attribute both the zero-bias resistance peak and the strong temperature dependence of resistance to the Coulomb blockade effect. From a simple back-of-envelope calculation, the capacitance of a single nanoparticle $\sim 2 \text{ nm}$ in size embedded in MgO tunnel barrier has a capacitance of $\sim 10^{-18} \text{ F}$, resulting in single electron charging energy more than 100 meV, which is higher than the thermal excitation energy scale even at room temperature. Therefore a significant portion of the nanoparticles do not contribute to low-bias electrical

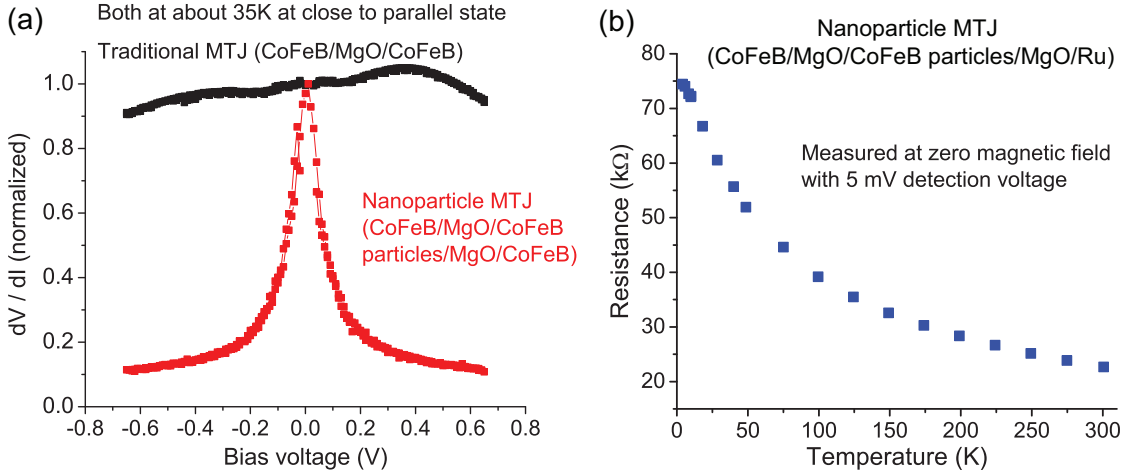


Figure 5.4: (a) Bias dependence of the resistance of a typical magnetic nanoparticle tunnel junction device (red). The sharp zero-bias resistance peak is in striking contrast with the weak bias dependence of the resistance of a conventional MgO-based MTJ without nanoparticles (black). (b) Temperature dependence of the resistance of a typical magnetic nanoparticle tunnel junction device.

conductance when the bias voltage does not provide sufficient energy to add one single electron onto a nanoparticle. Only some of the nanoparticles whose single-electron energy level (including charging energy) happen to align with the Fermi level within $k_B T$ participate in the zero-bias transport effectively. With the decrease of temperature the number of nanoparticles that can conduct current therefore decreases, resulting in increase of resistance. Similarly, the high-bias fall-off of the resistance reflects the increased number of conducting nanoparticles when the bias voltage exceeds the charging energy of more and more nanoparticles. The size distribution of the nanoparticles also comes into play in determining the shape of the bias and temperature dependence of the resistance. These signatures of Coulomb blockade effect provide strong evidence that our tunneling conductance is dominated by transport through small nanoparticles isolated from the electrodes.

5.3 Measurement Apparatus–PPMS and Vector Magnet Cryostat

Most of our low temperature measurements are performed on either the Physical Property Measurement System (PPMS) (with its resistivity option) in D-20 Clark Hall or the vector magnet cryostat in H-8 Clark Hall. We have not made any custom improvement on either setup yet, and as is there are pros and cons for each of the two. The PPMS with a sample rotator allows either in-plane or out-of-plane physical rotation (but not simultaneously) of the sample with a magnetic field up to 9 Tesla. With the vector magnet cryostat, the sample can be mounted in any fixed direction, and magnetic field can be applied up to 7 Tesla in the vertical direction, or up to 1 Tesla in arbitrary directions, but not simultaneously. Therefore, if the desired field is less than 1 T, the vector magnet cryostat offers more versatility, but if the desired field is more than 1 T, the tunability of field direction is severely limited on the vector magnet cryostat. Temperature control on the PPMS is amazingly easy and fast, variable between 1.9 K to 400 K, making it the best choice for a temperature dependence study. On the contrary, temperature control on the dipstick I used on the vector magnet cryostat so far has been problematic, and most measurements on the vector magnet cryostat so far have been at 4.2 K. The PPMS, however, is mostly limited to DC resistance measurement, while with the vector magnet cryostat we can apply microwave currents to the devices. The PPMS with its built-in options also has serious problems in electrostatic protection of the devices.

The PPMS can measure the resistance of samples in general with either its built-in AC transport option or its built-in DC resistivity option. However, the

AC transport option is limited to samples with resistances lower than $10\text{ k}\Omega$, and is therefore not directly usable for our nanopillar devices. As a result, we use the DC resistivity option for all our measurements done on the PPMS. The rotating stage of the PPMS makes out-of-plane rotation of the mounted devices by its design, but we wire-bond our devices to the vertical plane of a T-shaped sample holder (“puck”) to realize in-plane rotation of our device. Such an in-plane rotation is desired because for most of our measurements we need the magnetic field to be aligned with the exchange bias acting on the bottom CoFeB electrode, which is an in-plane direction that varies from device to device (due to the nonuniform growth field in AJA sputtering system). Extra care on electrostatic protection (grounding everything) is needed for every step from wire bonding to loading the sample rod into the PPMS. The cables for the PPMS resistivity option run from the power supply rack to a LEMO connector on the cryostat which connects to the sample puck from inside the cryostat near the bottom of the dewar. The power rack outputs / cables are found to be floating in idle state, which presents a risk when the device is plugged into the connectors inside the dewar and brought into electrical contact with these cables. Our temporary solution so far is to disconnect the cable and briefly discharge the pins with a multimeter right before connecting to the device. So far the successful rate of loading a device into the PPMS staying alive has been about 50%, but none of the devices stay alive after removal from the PPMS. Other PPMS users measuring sensitive devices have also found similar problem. A better long-term solution would be to use a break-out box with better grounding design, which will also enable custom setups to perform lock-in measurements of differential resistance as a function of bias voltage. As of this writing such break-out boxes have been subsequently built for this

PPMS for a few different projects, but we have not tried measurements on our nanoparticle MTJ devices with a PPMS break-out box yet.

The vector magnetic cryostat is brought into action mainly for the purpose of microwave measurements. At the same time it allows the direction of the magnetic field (at $H < 1$ T) to be tuned to adapt to the exchange bias and anisotropies of the device. The procedures for operating the vector magnetic cryostat have been described in detail in K. V. Thadani's thesis [127]. The cryostat consumes helium at a rather fast rate, making it more expensive than what CCMR charges for using the close-looped PPMS. It typically takes about 15-20 L of helium to cool down the cryostat from 77 K to 4 K, and then takes about 80 L of helium to nearly completely fill the inner dewar (considering the volume of the dewar 65 L and a transfer loss of $\sim 20\%$). Without warming up, a transfer of a full 68-liter dewar of liquid helium typically lasts between 2.5 to 3 days. This corresponds to a helium run rate of about 20 L/day (after $\sim 20\%$ transfer loss is taking into account), which compares with the designed number of 12 L/day shown on the manu of the cryostat. The helium level meter is functional (as opposed to described in ref. [127]), but it should be noted that it by design measures the height of the helium level instead of volume. Due to the shape of the dewar, most helium is stored at the vertical height between 40% to 75%. Meter reading below 30% indicates a dangerously low helium level, and filling helium to above 80% is not recommended because of inefficient helium consumption.

The same dipstick as shown in ref. [127] is used in our measurements on the vector magnet cryostat, which contains a coaxial SMA cable for microwave transmission. We use our traditional custom high frequency sample carrier

(used in Ralph/Buhrman group for spin torque nanopillar devices for nearly a decade, described in N. C. Emley's thesis [128]) to mount our devices, and an additional temperature sensor is mounted to the body of the sample carrier in good thermal contact for better readout of the temperature of the device. (The original sensor mounted to the heater stage is at a very different temperature with the device when the heater is in operation.) The sample carrier is mounted to the end of the coaxial cable at the bottom of the dipstick, and a vacuum can is attached to the bottom of the dipstick to form a compartment containing the sample carrier which is then pumped into vacuum using a turbo pumping station.

Our measurement electronics are connected to the device from the top of the dipstick via coaxial cables. A bias-tee is used for combining the low frequency components which perform measurements at DC and kHz lock-in frequency and the high frequency components which apply GHz radio-frequency (RF) currents by a sweeping signal generator (Agilent E8257C) or apply nanosecond pulses by fast pulse generators (Picosecond Pulse Labs 10070A and 10300A). One point to note for measuring devices in the \sim 100 k Ω range is that all the BNC cables have capacitances, and triaxial cables have particularly large capacitances. When many of these cables are used in the low-frequency circuit, the cumulative capacitance can be as large as a couple of nF, providing a significant current leakage path at kHz lock-in frequency. By removing unnecessary cables, reducing cable lengths, avoiding triaxial cables when possible and selecting lower lock-in frequency, one can better manage this capacitive effect and improve measurement efficiency.

5.4 Electrical Measurements on CoFeB/ MgO/ CoFeB (Nanoparticles)/ MgO/ Ru Devices

In this section, I will discuss our measurements on spin dependent tunneling and spin transfer torque on CoFeB nanoparticles embedded in a tunnel junction with one ferromagnetic (FM) electrode (CoFeB) and one normal electrode (Ru). The complete layer structure and growth parameters are exactly the same as listed in Table 5.1, and most of the devices that we report data from have lateral dimensions between $45\text{ nm} \times 45\text{ nm}$ to $50\text{ nm} \times 50\text{ nm}$. Such a lateral size is estimated by comparing the resistance of a given device at room temperature with a $500\text{ nm} \times 500\text{ nm}$ device within the same die on the wafer. We assume that the two devices have the same RA since they are located close to each other, and that the dimension of the large device ($500\text{ nm} \times 500\text{ nm}$) is reliable since it is less affected by the variations induced by the etching / lift-off processes.

Since there are only two ferromagnetic components in this device structure, any TMR is from between the bottom FM electrode and the nanoparticles, and any potential spin torque effect acting on the nanoparticles can only be associated with the spin polarization of one electrode. This is a significant simplification from the case where both electrodes are ferromagnetic as in references [121–125]. It should be noted that two distinctive tunneling mechanisms – sequential tunneling and coherent tunneling – still both contribute to the transport as studied in these references, but the complexity related to spin transport is significantly reduced.

5.4.1 Temperature Dependence of the Tunneling Magnetoresistance

Figure 5.5(a) shows the DC resistance, R , of a $50\text{ nm} \times 50\text{ nm}$ CoFeB/ MgO/ CoFeB nanoparticle/ MgO/ Ru device as a function of magnetic field H at various temperatures measured by the PPMS. The magnetic field is applied in-plane and along the same axis as the exchange bias of the bottom CoFeB electrode and is swept in both ways. The resistance is measured with a small bias voltage of 1 mV. There is one large sharp switching at a negative field at each of the three temperatures, which corresponds to one side of the hysteretic switching of the bottom CoFeB electrode that is pinned by exchange bias. The other side of the electrode switching occurs at close to zero field (as a result of a combination of exchange bias and coercivity), which can be still seen for $T = 50\text{ K}$ and to a less degree for $T = 150\text{ K}$. Other features of the R vs. H result from the change of magnetic orientation of the nanoparticles as a function of magnetic field. At high field for all temperatures the resistance saturates to a low value (R_P), because the nanoparticles are gradually aligned with the bottom electrode with increasing magnetic field. The field scale required for such a saturation decreases with decreasing temperature as indicated by the 50 K curve and 150 K curve, which are in good agreement with the magnetometry measurements (Fig. 5.2). At lower field, the resistance of the devices increases due to the random orientation of the nanoparticles. The highest resistance is achieved for the field range where the magnetic field is antiparallel with the bottom electrode so that the majority of the nanoparticles are antiparallel to the electrode.

To make a better visual comparison with the magnetic properties of the

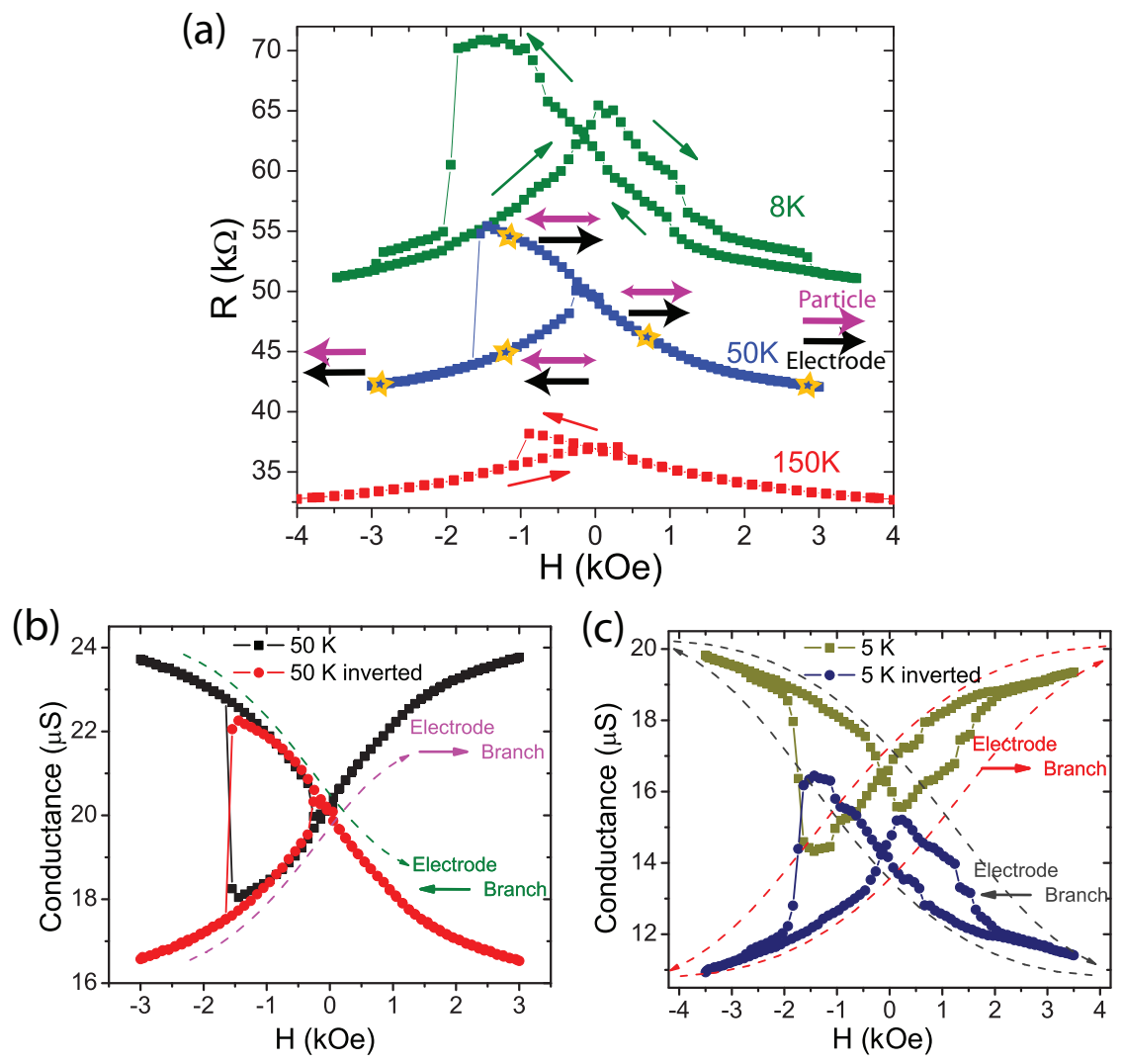


Figure 5.5: (a) DC resistance R of a 50 nm \times 50 nm CoFeB / MgO / CoFeB nanoparticle / MgO / Ru device (ADTJ-1 #8-10-44) as a function of magnetic field H parallel to the exchange bias of the bottom CoFeB electrode, sweeping field in both ways at various temperatures. (b) and (c) Measured DC conductance G and hypothetical DC conductance G' if the magnetization of the bottom CoFeB electrode is reversed for the device as a function of magnetic field at (b) 50 K and (c) 5 K. G' is estimated by inverting (flipping up-side-down) the measured G vs. H curve and vertically offsetting to be consistent with G . G and G' together form two branches of conductances versus H , each of which corresponds to one fixed configuration of the bottom CoFeB electrode and can be directly compared to the magnetometry measurement of the nanoparticles (Fig. 5.2).

nanoparticles as determined from the magnetometry measurements (Fig. 5.2), we plot the same R vs. H data in the form of conductance G as a function of H . For each G vs. H curve, we further plot the corresponding hypothetical conductance G' if the magnetization of the bottom electrode is reversed to the opposite direction [Fig. 5.5(b) and (c)]. Such G' vs. H plots are obtained by inverting (flipping up-side-down) the measured G vs. H curve and vertically offsetting to be consistent (smoothly connected and overlapping in hysteretic regime) with G . This is because for any state of the nanoparticle ensemble, its tunneling conductance G with the bottom electrode in one orientation and its tunneling conductance G' with the bottom electrode in the opposite orientation should add up to a constant. This can be seen by considering the tunneling conductance contribution of a single nanoparticle (with its magnetization at an angle θ to the bottom electrode)

$$G_n = \frac{G_{n,P} + G_{n,AP}}{2} + \frac{G_{n,P} - G_{n,AP}}{2} \cos \theta \quad (5.4)$$

and the corresponding single-particle hypothetical conductance

$$G'_n = \frac{G_{n,P} + G_{n,AP}}{2} + \frac{G_{n,P} - G_{n,AP}}{2} \cos(\pi - \theta) \quad (5.5)$$

Therefore,

$$G_n + G'_n = G_{n,P} + G_{n,AP} \quad (5.6)$$

and the total conductance of the device consisting of many nanoparticle conduction paths in parallel is

$$G + G' = \sum_n (G_{n,P} + G_{n,AP}) = G_P + G_{AP} \quad (5.7)$$

regardless of the magnetization distribution of the nanoparticle ensemble. The G vs. H and G' vs. H curves together form two branches of conductances

versus H , each of which corresponds to one fixed configuration (\rightarrow or \leftarrow) of the bottom CoFeB electrode. A transition between the two branches occurs when the magnetic field sweeps to the point that switches the magnetization of the bottom electrode. The change of conductance in the \rightarrow branch [Fig. 5.5(b) and (c)] shows very similar shape compared with the M vs. H data from SQUID magnetometry (Fig. 5.2) (and so does the \leftarrow branch after a horizontal inversion) because both measure the collective orientation of the nanoparticle ensemble. Magnetometry measures the total magnetization of the nanoparticles ensemble along a fixed axis (the positive field direction)

$$M = \sum_n M_n \cos \theta \quad (5.8)$$

and the \rightarrow branch of conductance measures the total magnetoconductance of the nanoparticles relative to a fixed reference magnet

$$G_{\rightarrow} = \frac{G_P + G_{AP}}{2} + \sum_n \frac{G_{n,P} - G_{n,AP}}{2} \cos \theta \quad (5.9)$$

Both quantities measures some ensemble average of $\cos \theta$, with the former weighted by the magnetic moments of individual nanoparticles, and the later weighted by the magnetoconductance of individual nanoparticles. With different weighted averaging we do not expect the two measurable quantities to be quantitatively proportional, but qualitatively larger nanoparticles contribute more to both quantities in a comparable fashion. The magnetization of nanoparticles scale to its volume, while the magnetoconductance scales to its lateral area and is perhaps more sensitive to the vertical height through effective tunnel barrier thickness. Nevertheless, the strong similarity between G vs. H and M vs. H curves confirms our characterization for the magnetic properties of the nanoparticles, and indicates that our measured magnetoresistance originates from tunneling transport through the magnetic nanoparticles.

Similar to the magnetometry data (Fig. 5.2), the magnetoresistance measurements also confirm a transition at about 12 K where hysteresis of the nanoparticles start to emerge. When $T > 12$ K, all of the hysteresis in the R vs. H measurement is due to the bottom electrode. When we plot the G vs. H curves in two branches, each branch has no hysteresis [Fig. 5.5(b)]. When $T < 12$ K, hysteresis emerges for a fixed direction of the bottom electrode [see Fig. 5.5(c) and the 8 K data in Fig. 5.5(a)] because the magnetic anisotropy of particles exceeds the energy scale of thermal excitation. In this low temperature regime, the R vs. H or G vs. H data show distinctive small steps that are not associated with the switching of electrodes. Compared with the low temperature data in Fig. 5.2(a) and (b) where the magnetization of nanoparticles shows a smooth hysteresis loop, the hysteresis loop in either branch in Fig. 5.5(c) is composed of a mixture of smooth changes and discrete steps. We attribute these discrete steps to the magnetic switching of single nanoparticles. It is exciting progress to be able to identify single nanoparticles electrically given the large number of nanoparticles we started with, but such a single particle resolution in our measurement can be reasonably justified. Unlike the extended film sample for SQUID measurement which contains $\sim 10^{12}$ nanoparticles, based on our estimate of nanoparticle density the $50 \text{ nm} \times 50 \text{ nm}$ nanopillar device contains ~ 75 nanoparticles. Due to the Coulomb blockade effect the nanoparticles participating in low bias transport at low temperature should be significantly fewer. It is not unconceivable that some nanoparticles may each contribute 10% or more of the total conductance of the device, and if such a nanoparticle happens to have its magnetic anisotropy axis close to the direction of the applied magnetic field, hysteretic switching of this nanoparticle should register as a clear jump in $R \sim H$ when the magnetic field is swept in either

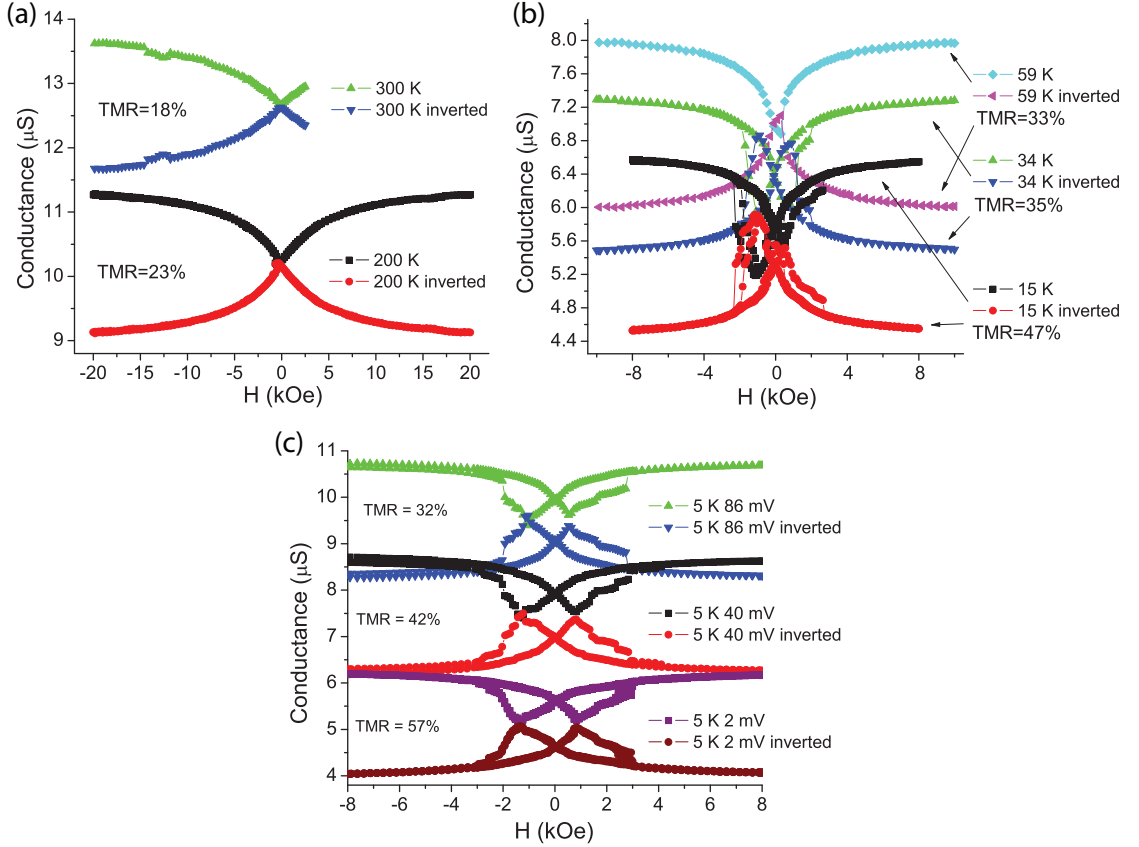


Figure 5.6: Tunneling magnetoresistance of CoFeB nanoparticle MTJs at various temperatures and bias voltages. (a) and (b) DC conductance G and hypothetical DC conductance G' (see main text) of a $50 \text{ nm} \times 50 \text{ nm}$ CoFeB/ MgO/ CoFeB nanoparticles/ MgO/ Ru device (ADTJ-1 #5-4-44) as a function of magnetic field at various temperatures. The bias voltage ranges from 2 mV for 15 K to 8 mV for 300 K. (c), DC conductance G and hypothetical DC conductance G' of the same device as a function of magnetic field measured at 5 K at various bias voltages. The TMR ratio for each temperature or bias is extracted and listed.

direction, similar to the larger jumps seen in either of the conductance branches in Fig. 5.5(c). The gradual changes in $R \sim H$ coexisting with the discrete steps can come from nanoparticles either with small conductance, or behaving superparamagnetically (with lower blocking temperature), or with magnetic anisotropy axis closer to perpendicular to the applied magnetic field. We will further discuss the single particle behavior in the next subsection concerning our search for effects due to the spin transfer torque.

The tunneling magnetoresistance ratio (TMR), defined as $(R_{AP} - R_P)/R_P$ as usual, can be determined from the R vs. H measurements. Since a complete antiparallel state between the nanoparticles and bottom electrode can not be reached in our experiment, we extract R_{AP} from our plot of hypothetical conductance G' . The TMR ratios for a typical 50 nm \times 50 nm CoFeB/ MgO/ CoFeB nanoparticles/ MgO/ Ru device at a few selected temperatures are extracted from Fig. 5.6(a) and (b) and listed in the same figures. The TMR ratio increases dramatically from about 18% at 300 K to 57% at 5 K [shown in Fig. 5.6(c)]. The bias voltage ranges from 2 mV for 5 K to 8 mV for 300 K, which is chosen to be not larger than the thermal energy scale and therefore approximately detects zero-bias tunneling. The magnetoresistance measurements are also carried out at a few different bias voltages at 5 K [in Fig. 5.6(c)], which shows a decrease of the both R_P and R_{AP} with increasing bias voltage as expected from the mechanism of the Coulomb blockade. A substantial decrease of TMR is seen at higher bias voltage.

Previous experiments studied TMR in ferromagnetic nanoparticle MTJ devices with both electrodes ferromagnetic (with a layer structure of FM/I/FM particle/I/FM) and showed a strong increase of TMR ratio with decreasing temperature. The TMR ratio at around 4 K typically grows to several times of its room temperature value [121, 122, 124], a stronger temperature dependence than in a single-barrier conventional MTJ without nanoparticles. This effect has been explained by a transition from a sequential-tunneling regime to a coherent-tunneling (co-tunneling) regime where the TMRs across both tunnel barriers stack together in a multiplied fashion to create a higher total TMR. In our experiment, the argument that co-tunneling becomes more significant at low temperature is still valid, but the mechanism of coherent enhancement of

TMR from two spin-dependent tunneling processes is absent since one of the electrodes is non-magnetic in our device. Nevertheless, we observe a strong temperature dependence of TMR similar to reported in ref. [121, 122, 124], and the absolute magnitude of TMR at both high temperature and low temperature are also similar to those studies using MgO tunnel barrier [121, 122].

The temperature dependence of the TMR seen in our devices has yet to be understood completely, but there are a few points to note. Firstly, a transition from a sequential tunneling regime to a co-tunneling regime does enhance the TMR ratio for our devices, albeit for a reason different from the case with two ferromagnetic electrodes. Assuming the tunneling resistance between a nanoparticle and the normal electrode is R_N , and the tunneling resistance between the nanoparticle and the ferromagnetic electrode R_F is between R_P and R_{AP} [following $\cos \theta$ angular dependence described by Eq. (5.4)]. Then the total tunneling resistance through this nanoparticle by sequential tunneling is simply $R_N + R_F$. Electrons can also tunnel through the nanoparticle by co-tunneling, which is a second-order process where an electron tunnels from one electrode to the other electrode via a virtual state at the nanoparticle. The resistance of such a co-tunneling process can be described by $R_N R_F / R_q$, where $R_q = \hbar / 2e^2 \approx 12.4 \text{ k}\Omega$ is the resistance quantum. Therefore the co-tunneling resistance has a TMR ratio that is equal to the TMR associated with R_F , or $(R_{AP} - R_P) / R_P$, while the sequential tunneling resistance has a TMR ratio of $(R_{AP} - R_P) / (R_P + R_N)$, which is reduced due to the contribution from the spin-independent tunneling associated with the normal electrode. For a nanoparticle that does not experience Coulomb blockade, sequential tunneling is always dominant because $R_N, R_F \gg R_q$. However, all particles participate in co-tunneling, but the number of particles allowing sequential tunneling (not

Coulomb-blockaded) decreases with decreasing temperature. Therefore, with a transition from sequential tunneling dominance at room temperature to co-tunneling dominance at low temperature, TMR is expected to increase by a factor of $(R_P + R_N)/R_P$, subject to weighted averaging over all nanoparticles. Of course this is a very simplified analysis. The symmetry-filtering effect has proven important to MgO-based tunnel junctions, and for the co-tunneling process it needs to be evaluated on the normal electrode side as well.

Secondly, another conductance channel to consider is the direct tunneling between the two electrodes. Since the tunnel barrier is probably not uniform, it is possible that it is thin enough in some area without nanoparticles to allow direct tunneling from CoFeB electrode to Ru electrode. Another possibility is that some CoFeB nanoparticles might be in metallic contact with one of the electrodes, so that such nanoparticles effectively become part of the electrode and can conduct current without seeing the Coulomb blockade effect. Both scenarios should allow additional tunneling current that is relatively insensitive to temperature (since no Coulomb blockade is present) and should become more significant at low temperature when sequential tunneling through isolated nanoparticles are blocked to a larger extent. The first scenario with direct CoFeB/MgO/Ru tunneling should have no tunneling magnetoresistance associated and would therefore reduce TMR ratio at low temperature, which contradicts with our observation. For the second scenario, the STEM images (Fig. 5.3) seem to indicate that the nanoparticles are relatively well-separated from the bottom electrode but are nearly in contact with the top (Ru) electrode. (But it is important to note that the STEM sample is from an area on the wafer that has thinner-than-average top MgO layer.) If this is true, such a geometry allows direct CoFeB/MgO/CoFeB tunneling similar to a conventional

MTJ without nanoparticles. This conductance channel can potentially provide higher TMR than the isolated nanoparticles in the sequential regime, and therefore can contribute to our measured higher TMR ratio at low temperature.

Furthermore, a very interesting observation from Fig. 5.6(a) and (b) is that the absolute difference of tunneling conductance between parallel state G_P and anti-parallel state G_{AP} is roughly a constant ($\sim 2.2 \mu\text{S}$ for the given device) for all temperatures. This observation makes one wonder whether low temperature simply “freezes out” some contributions in the tunneling conductance that is independent of magnetic field. This speculation, however, is incompatible with our explanation above based on sequential vs. coherent vs. direct tunneling, since taking out sequential tunneling contribution by reducing temperature should surely reduce $G_P - G_{AP}$. Of course this observation could just be a coincidence when some intrinsic increase of $G_P - G_{AP}$ in other channels compensates for the loss of sequential tunneling at low temperature. (Since G_{AP} generally decreases somewhat at low temperature even for a conventional MTJ without nanoparticles, it is reasonable to think there is some intrinsic increase of $G_P - G_{AP}$.) More experiments and analyses are certainly desired for understanding the mechanism of TMR enhancement at low temperature.

5.4.2 Pulsed Switching Measurements

Below the blocking temperature of the nanoparticles, we see distinctive steps in the magnetoresistance measurement [Fig. 5.5(a) and (c)], which we attribute to the hysteretic switching of magnetic nanoparticles. This can be further demonstrated by minor-loop magnetic field sweeps that identify the pair of

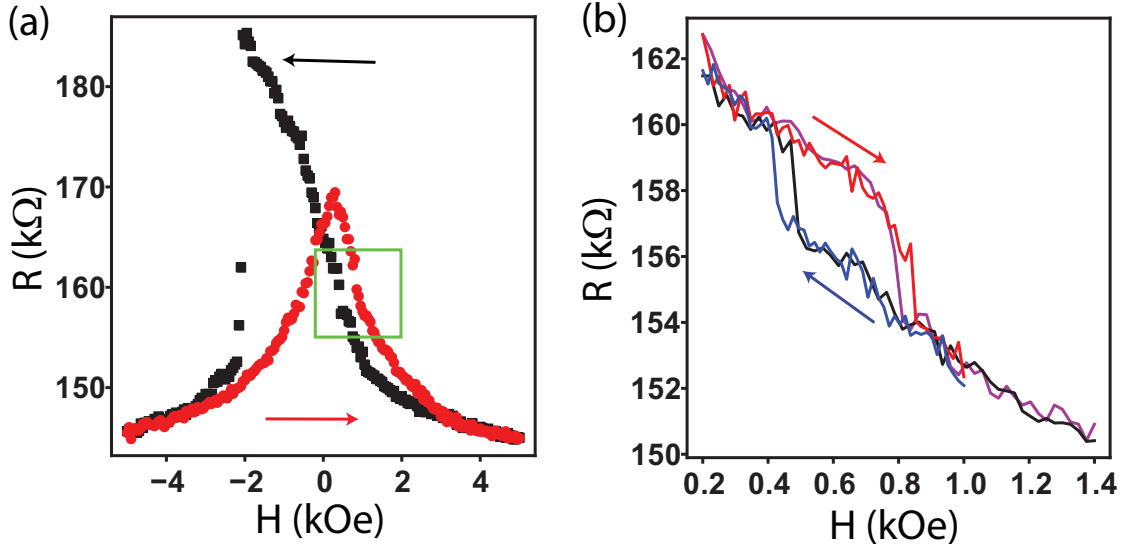


Figure 5.7: Hysteretic magnetoresistance of a single nanoparticle. (a) Differential resistance R of a CoFeB nanoparticle MTJ device (ADTJ-1 #4-5-44) (~ 45 nm \times 45 nm) as a function of magnetic field H applied parallel to the exchange bias of the bottom CoFeB electrode at 4.2 K. A discrete step can be seen inside the green box for both directions of magnetic field sweep. (b) Minor loop magnetic field sweep corresponding to the field range of the green box in (a).

switching events for the same nanoparticle. Figure 5.7(b) shows such a minor-loop sweep focusing on the distinctive resistance jumps in the field range marked by the green box in Fig. 5.7(a), which shows the differential resistance R of a CoFeB nanoparticle MTJ device (~ 45 nm \times 45 nm) measured at 4.2 K at the vector magnet cryostat. Repeated measurements confirm the existence of a pair of sharp switching transitions at about 450 Oe and 800 Oe in Fig. 5.7(b) that form a hysteretic loop typical to a magnetic object with uniaxial anisotropy.

To provide further evidence that this type of hysteretic switching is from single CoFeB nanoparticles, we study the temperature dependence of the critical switching fields [Fig. 5.8(a)]. For a typical nanoparticle, the hysteretic range, *i.e.* the field range that the resistance of the device shows bi-stability, becomes smaller with higher temperature. For a nanoparticle embedded in a

CoFeB/MgO/CoFeB nanoparticles/MgO/Ru nanopillar device, figure 5.8(a) shows the upper switching field decreases and the lower switching field increases with higher temperature as expected. Both switching fields show similar slopes in absolute values in their temperature dependence, and the average (absolute) slope of 250 Oe/K indicates that this ferromagnetic object has a total magnetic moment of about $1500 \mu_B$ based on the Brown's thermal fluctuation model of a single-domain nanomagnet [129].

A schematic illustration of the thermal effect on the hysteresis of a nanoparticle is presented in Fig. 5.8(b). The energy profile of a nanoparticle with uniaxial anisotropy can be modeled as a double-well system, with each well representing one orientation of the magnetization. The energy barrier E_b between the two wells at zero field corresponds to the strength of the uniaxial anisotropy, while an external field along the anisotropy direction tilts the two wells, reducing the energy barrier for one well while increasing the other. Magnetic switching occurs when the external field reduces the energy barrier for one well to be comparable to the thermal excitation energy $\Delta k_B T$, where Δ is a coefficient related to the time scale τ allowed for such a switching to occur.

$$\tau \approx f_0^{-1} e^\Delta \quad (5.10)$$

where $f_0 \sim 1$ ns, is the thermal agitation frequency. For a nanomagnet to be considered thermally stable at one out of two bi-stable states for information storage application purposes, $\Delta > 40$ is required, corresponding to a time scale of 10 years. In our lab-scale measurement such as a field sweep for magnetoresistance measurement, the appropriate time scale is a few seconds to a few minutes, or $\Delta \sim 25$. Since magnetic field H modifies the energy barrier by $\sim N\mu_B H$, with $N\mu_B$ the magnetic moment of the nanoparticle, the critical

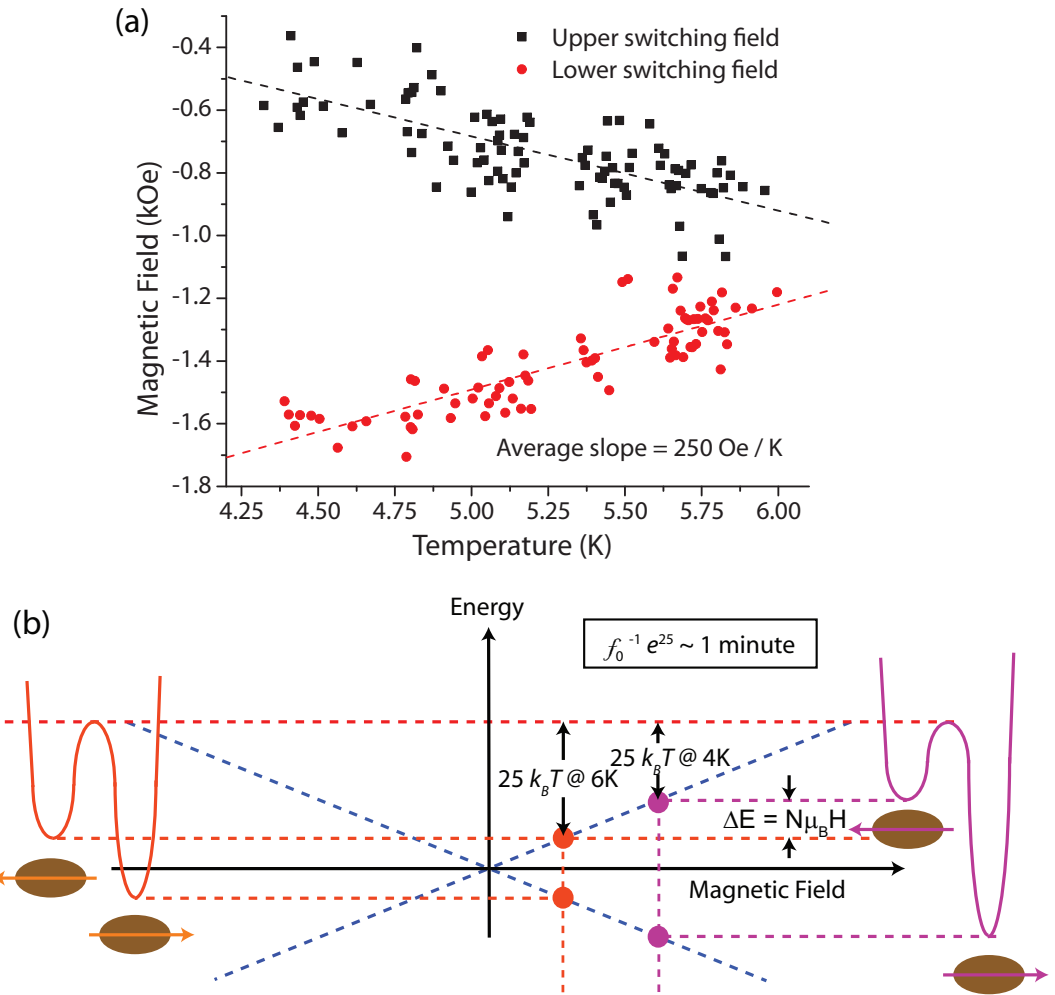


Figure 5.8: Temperature dependence of the nanoparticle hysteresis. (a) Critical switching fields of a single nanoparticle embedded in a MTJ device (ADTJ-1 #5-10-44) ($\sim 45 \text{ nm} \times 45 \text{ nm}$) determined from the magnetoresistance of the device. (b) Schematic illustration of the thermal effect on the critical switching field of a nanoparticle.

switching field H_c is related to the temperature T by

$$N\mu_B H_c + 25k_B T = E_b \quad (5.11)$$

Such a linear relation between H_c and T is manifested in Fig. 5.8(a), which not only confirms the nanoparticle origin of the hysteresis but also gives an estimate of the total moment of this particular particle, $1500 \mu_B$, which is fairly close to the average moment, $1000 \mu_B$, of the particle ensemble we

characterized by magnetometry and STEM. It should be noted that since the magnetic field acting on the nanoparticle can include dipole coupling from other particles and potential exchange bias pinning from its surrounding oxides, most nanoparticles do not have hysteretic loops centered around zero field, so all the critical switching fields H_c described by Eq. (5.11) and equations thereafter are subject to a constant offset when compared with experimental data.

So far these magnetoresistance measurements allow us to determine the magnetic stability of the nanoparticles at low temperature under essentially no effect from electrical transport. (Only a very small current is needed for resistance measurement.) For the next step we study the magnetic stability of the nanoparticles under the influence of a spin polarized current. The spin transfer torque, if present, should stabilize one of the magnetic orientations (one of the two energy wells) while destabilizing the other. As we have discussed in previous chapters, such an effect is reflected in modification of effective damping for the two magnetic orientations, which in turn can be equivalently expressed in the form of modified effective temperature T^* [36]. Under the influence of spin transfer torque, one of the energy well experiences a cooling effect so that the critical switching field is shifted in the direction that expands the hysteresis. The other energy well experiences a heating effect so that the critical switching field is shifted in the direction that shrinks the hysteresis. Current of reversed polarity should produce the opposite effect. Such an asymmetric change of switching field would be a signature of the spin transfer torque. On the other hand, a bias current induces very significant heating in our highly resistive devices at low base temperature. We estimate that a small bias current at 30 mV could easily heat the device to 15-30 K, far above the blocking temperature which is typically 6-10 K for most single nanoparticles we identi-

fied electrically (and at most 12 K as indicated by our early characterizations). To extend the accessible bias range to maximize the effect of spin transfer torque, we apply (spin-polarized) current in nanosecond pulses instead of continuous DC current. Since the heating effect only lasts during the nanosecond pulses in this case, the blocking temperature is effectively raised by about a factor of 10 ($\Delta \approx 2.5$ for $\tau = 10$ ns compared with $\Delta \approx 25$ for $\tau = 1$ min).

We apply such nanosecond electric pulses of a fixed voltage, V , at a slow repetition rate of 5 Hz while sweeping the magnetic field H (on the time scale of seconds to minutes), and detect by magnetoresistance measurement whether a particular magnetic nanoparticle switches its magnetization. By repeating this measurement for various pulse voltages, a switching phase boundary of H vs. V can be mapped out and shown in Fig. 5.9(a) for 4 ns pulses and Fig. 5.9(b) for 30 ns pulses at 4.2 K. We see the magnetic field range for which the nanoparticle has bi-stable states (the difference between the upper switching field and lower switching field) is dramatically reduced and eventually diminishes at high bias, due to the heating effect from the voltage pulse. At the same time, we note that the phase boundary is not symmetric for positive and negative bias, with the center field of the bi-stable range higher for negative bias than for positive bias. This asymmetry of switching phase diagram is evidence for the existence of the spin transfer torque effect in magnetic nanoparticles.

There have been very few studies of spin transfer torque in ferromagnetic nanoparticles. Chen *et al.* [56] obtained spin torque in a granular system, which consists of a large number of Co particles embedded in a copper matrix. Wang *et al.* [115] reported spin torque switching of a small number (5-50) of Co particles contained by Cu and Ag in a point contact device. In these studies the

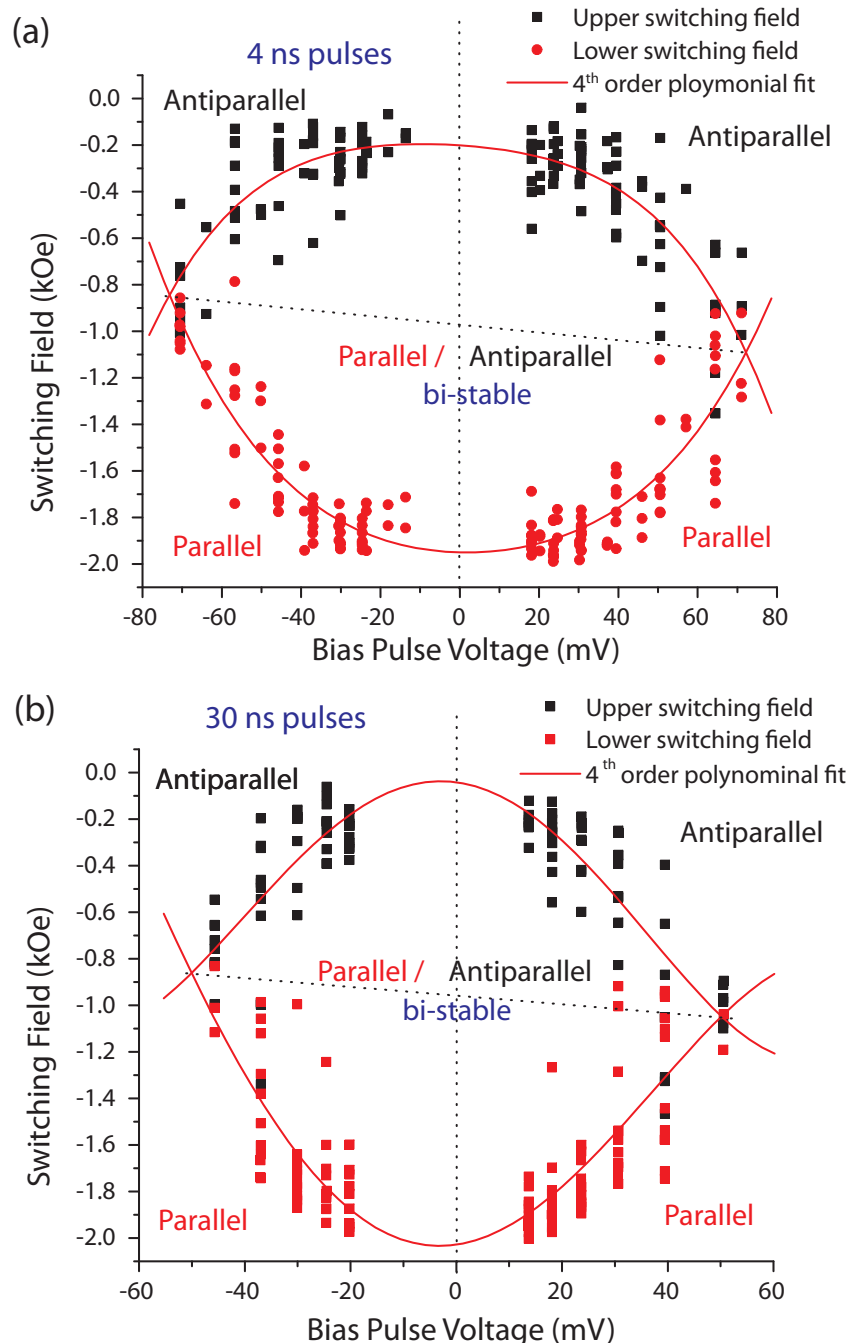


Figure 5.9: Switching phase diagram (H vs. V) of a CoFeB nanoparticle embedded in a MTJ device (ADTJ-1 #5-10-44) ($\sim 45 \text{ nm} \times 45 \text{ nm}$) with (a) 4 ns voltage pulses and (b) 30 ns voltage pulses.

spin transport is metallic with the ferromagnetic nanoparticles surrounded by other metals, and therefore these nanomagnets are not the electron-confining nanoparticles in electrical sense. Krause *et al.* [55] used spin polarized scanning tunneling microscope to inject a spin current into a superparamagnetic Fe nanoparticle and observed asymmetric lifetimes of two magnetic states, which are attributed to spin transfer torque. This is a spin-dependent tunneling measurement between a Fe particle and a spin-polarized STM tip, but again the Fe particle is in contact with a conducting substrate and not insulated from the electron reservoir. Our experiment shares the common spirit with ref. [55] in probing the effect of spin torque on the thermal stability of the bi-stable magnetic states of a nanoparticle, but in a very different experimental system (MgO-based MTJ device vs. *in situ* STM). More importantly, our experiment provides the first evidence of spin transfer torque in individual electrically-isolated ferromagnetic nanoparticles.

The in-plane component of the spin transfer torque modifies the magnetic damping in a linear fashion so that the effective damping at bias V is $\alpha^*(V) = \alpha[1 - \tau_{||}(V)/\tau_c]$, or $\alpha^*(V) = \alpha(1 - V/V_c)$ if we assume a linear voltage dependence for the in-plane component of spin torque. Here τ_c and V_c is the zero-temperature critical torque and critical voltage respectively for spin-transfer-driven magnetization reversal [14]. In the thermally-assisted switching regime ($V < V_c$) the modification of effective damping is equivalent to modification of effective temperature $T^*(V) = T(|V|)/(1 - V/V_c)$ [36], where $T(|V|)$ is a function describing the effect of Joule heating on the temperature of the device, which depends on the details of the heating model but should be an even function in V . Note that such an increased effective temperature is only applicable during the pulse, while on lab time scale the device is still at its base temperature ($T_0 =$

4.2 K for most of our measurements), and Eq. (5.11) can be modified including both the background thermal agitation and added thermal agitation during the pulse

$$f_0\tau_0 e^{-(E_b - N\mu_B H_c)/k_B T} + f_0\tau e^{-(E_b - N\mu_B H_c)/k_B T^*(V)} = 1 \quad (5.12)$$

where $\tau_0 \sim 1$ minute is the lab time scale, and τ is the length of the voltage pulse. Therefore,

$$e^{25 - (E_b - N\mu_B H_c)/k_B T} + e^{\Delta - (E_b - N\mu_B H_c)(1 - V/V_c)/k_B T(|V|)} = 1 \quad (5.13)$$

where $\Delta = \ln f_0\tau \approx 1.5\text{-}4.5$ for pulses between 4-100 ns. To be quantitative, an appropriate heating model $T = T(|V|)$ needs to be adapted to fit our measured switching phase boundary based on Eq. (5.13), and the statistical method of bootstrapping [130] can be applied to estimate the uncertainty of the fitting parameters, especially the strength of the spin torque, due to the wide distribution of the switching fields. As a work in progress with limited data, we temporarily use polynomial fits (to the 4th order) of the upper switching fields and the lower switching fields as a function of pulse voltage to illustrate the degree of asymmetry of the switching phase diagram (the red curves in Fig. 5.9). Such a fit captures the major properties of both theoretical expectations and the experimental data of switching phase boundary. Due to the exponential form of the thermal agitation, usually one of the two terms in Eq. (5.13) is dominant and the other term can be neglected. At low pulse voltages (when $T < \sim 40$ K), the 4.2 K background agitation is dominant and H_c is approximately independent of V , and at high pulse voltages, considering only the second term in Eq. (5.13),

$$H_c = \frac{1}{N\mu_B} \left[E_b - \frac{\Delta k_B T(|V|)}{1 - V/V_c} \right] \approx \frac{E_b}{N\mu_B} - \frac{\Delta k_B T(|V|)}{N\mu_B} \left(1 + \frac{V}{V_c} \right) \quad (5.14)$$

which can be reasonably described by a polynomial function in V .

Compared with Eq. (5.14) which describes one side of the switching phase boundary (at high bias), its counterpart for the other side can be written similarly as

$$H'_c = \frac{1}{N\mu_B} \left[-E_b + \frac{\Delta k_B T(|V|)}{1 + V/V_c} \right] \approx -\frac{E_b}{N\mu_B} + \frac{\Delta k_B T(|V|)}{N\mu_B} \left(1 - \frac{V}{V_c} \right) \quad (5.15)$$

The hysteresis diminishes when $H_c = H'_c$, or $E_b = \Delta k_B T(|V|)$, not affected by the spin transfer torque. This is not surprising since the effect of hysteresis expansion for one side of the switching boundary is canceled by the shrinking on the other side. Furthermore, Eq. (5.14) and (5.15) allow us to evaluate the magnitude of the spin torque from the asymmetry of $H_c(H'_c) \sim V$. At the two points $V = \pm V_H$ where $H_c = H'_c$, the switching fields at both $V = V_H$ and $V = -V_H$ are described by $H_c = (E_b/N\mu_B)(V/V_c)$ and therefore differ from each other by

$$\delta H_c = 2 \frac{E_b}{N\mu_B} \frac{V_H}{V_c} \quad (5.16)$$

$E_b/N\mu_B$ is the anisotropy field of the nanoparticle, which can be obtained by extrapolating the upper and lower switching field of the nanoparticle [Fig. 5.8(a)] to zero temperature, which is about 1700 Oe for the nanoparticle shown in Fig. 5.8(a) and Fig. 5.9. Using $\delta H_c \approx 250$ Oe from Fig. 5.9(a), Eq. (5.16) yields $V_H/V_c \approx 7\%$ at $V_H \approx 70$ mV, or $V_c \approx 1$ V. The switching phase diagrams measured with 30 ns pulses [Fig. 5.9(b)], 4 ns pulses (not shown), and 100 ns pulses (not shown) all show similar slopes in $\delta H_c/V_H$ within $\sim 25\%$ and would result in similar estimates of V_c .

We can very roughly calculate the critical voltage V_c for spin torque induced magnetization reversal based on the measured and estimated parameters of the

nanoparticle and the formalism developed for conventional spin torque devices

$$I_c = \frac{2e}{\hbar} \frac{\alpha}{P} N \mu_B \left(H + \frac{H_{xz} + H_{yz}}{2} \right) \quad (5.17)$$

where I_c is the critical spin-torque switching current, α is the Gilbert damping coefficient, P is the tunneling spin polarization, $N \mu_B$ is the magnetic moment of the nanoparticle, H is the applied magnetic field, H_{xz} and H_{yz} are the magnetic anisotropy field of the other two axes relative to the easy axis. For the nanoparticle measured in Fig. 5.9, assuming that its TMR is equal to the TMR of the whole device $\sim 50\%$, the corresponding spin polarization is 45%. N is 1500 based on Fig. 5.8. H is about 1000 Oe at the center of the hysteresis loop as shown in Fig. 5.9. It is difficult to determine H_{xz} and H_{yz} quantitatively, but they have an upper bound that $H_{xz} + H_{yz} \leq 4\pi M_s \approx 14000$ Oe for CoFeB, which is unlikely to be approached for a realistic shape of the nanoparticle. At the same time, both H_{xz} and H_{yz} have to be equal or larger than the extrapolated zero-temperature coercive field 1700 Oe. A reasonable speculation is that the nanoparticle has somewhat larger lateral dimension than its height, so that the in-plane anisotropy H_{yz} is close to 1700 Oe, while the out-of-plane anisotropy is somewhat larger, say, 3000-5000 Oe. Therefore, we estimate $\left(H + \frac{H_{xz} + H_{yz}}{2} \right) = 3500 \pm 1000$ Oe. The Gilbert damping α of a ferromagnet nanoparticle is an interesting open question we intend to study, and we tentatively use a value $\alpha = 0.012$ similar to CoFeB bulk (see our measured α in Chapter 2 and Chapter 3). These numbers lead to the value of critical current $I_c = 0.4 \mu\text{A}$. Since we measure a conductance change of $\Delta G = 0.4 \mu\text{S}$ at zero-bias associated with the magnetic switching of the nanoparticle, we estimate the tunneling resistance through this single nanoparticle to be $\sim 1 \text{ M}\Omega$ ($0.85 \text{ M}\Omega$ at P state, and $1.25 \text{ M}\Omega$ at AP state), assuming 50% TMR ratio. Such a resistance translates the critical current I_c to critical voltage of $V_c = 0.4 \text{ V}$.

The critical voltage inferred from the switching phase diagram (1 V) is larger than the value expected from the simplest model for a conventional spin torque device (0.4 V). This could mean that either the spin transfer torque is moderately weaker in nanoparticles for a given spin-polarized current, or the magnetic damping in nanoparticles are moderately stronger than in the bulk as opposed to weaker as indicated in some early reports [45, 46]. Nevertheless, considering the various uncertainties associated with both calculations, the fact that the two numbers fall within a factor of 2.5 should be considered a fairly good agreement. Therefore our first experimental evidence of spin torque in nanoparticles does not reveal any result substantially different from in a bulk ferromagnet. However, we note that the strong heating inherent to our high power pulse measurement most likely destroys any quantum effect only present at low temperature. In order to truly probe spin transfer effect associated with single-electron tunneling, the measurement has to be performed at low bias. So our next step is to perform spin-transfer-driven ferromagnetic resonance (ST-FMR) measurements on these magnetic nanoparticle devices.

5.4.3 Spin-Transfer-Driven Ferromagnetic Resonance

We performed DC-detected spin-transfer-driven ferromagnetic resonance (ST-FMR) measurements on the nanoparticle MTJ devices. In ST-FMR, a radio-frequency (RF) current is applied to the device, and the oscillating spin transfer torque excites resonant magnetization precession of a magnetic component of the device which would be one or several magnetic nanoparticles in this case. We measure the DC voltage arising from the mixing of the applied oscillating (RF) current and the resultant oscillating resistance as a function of RF driving

frequency.

The measurement circuit and details for DC-detected ST-FMR have been described in Section 2.2. One disadvantage related to the nanoparticle nanopillar MTJ devices is their high resistance. The illustrated loss factors in Fig. 2.6 become significant in high resistance case, and it is preferable to use lower lock-in frequencies and high DC-source impedances in the circuit to minimize any lost mixing voltage signal. Our measured mixing voltage signal always decays very strongly with RF frequency, by a factor of 100-500 between 1 GHz to 10 GHz, much more significant than the frequency dependence of cable transmission loss. This is likely due to the RF absorption by the Si substrate. (I happened to have used degenerately doped Si wafers for recent rounds of device fabrications without foreseeing the problem.) Such a high-frequency decay has been handled by aggressive flatness correction (increasing the RF input power drastically at higher frequencies), but it is not entirely clear whether this is free of side effects.

Our preliminary measurements have found resonance peaks in the ST-FMR spectra under some biasing field conditions. So far all ST-FMR measurements are done under zero bias voltage. Figure 5.10 shows the ST-FMR spectra measured for a CoFeB/MgO/CoFeB nanoparticles/MgO/Ru device (~ 45 nm \times 45 nm) under magnetic fields with different amplitudes applied along the in-plane hard axis (perpendicular to the exchange bias) of the bottom CoFeB electrode. The RF voltage is estimated to be between 5-10 mV. In the high-field regime ($H > 1000$ Oe), the resonance peaks shift to higher frequencies with higher field, as one would expect from a magnetic resonance response. In the low-field regime ($H < 1000$ Oe), it appears that the resonance frequency

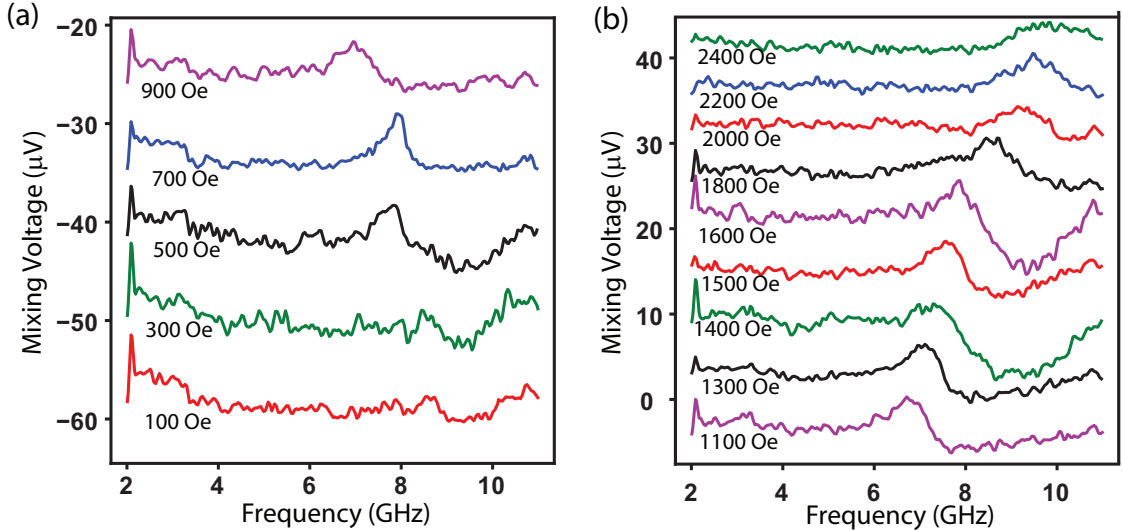


Figure 5.10: ST-FMR spectra associated with CoFeB ferromagnetic nanoparticles embedded in a MTJ device (ADTJ-1 #5-10-44) ($\sim 45 \text{ nm} \times 45 \text{ nm}$) with magnetic field of (a) 100-900 Oe and (b) 1100-2400 Oe applied along the in-plane hard axis (perpendicular to the exchange bias) of the bottom CoFeB electrode. The RF voltage is estimated to be between 5-10 mV.

decreases with higher field. This could be explained by some other effective fields such as the dipole field or shape anisotropies that become dominant in a weaker external field. It should be noted that so far the measured ST-FMR signal is generally weak, and we have not been able to resolved clear resonance peaks out of the background (which could include artifacts from non-perfect flatness corrections) consistently for arbitrary biasing field conditions. For example, for the same field direction as in Fig. 5.10 when $H < -400 \text{ Oe}$, we no longer see any resonance peaks. It could also be a result of resonance frequencies higher than our detected range.

Since the resonance peaks shift in frequency under different applied magnetic field, it rules out the possibility of any circuit artifacts such as LC resonance causing this effect and confirms the ferromagnetic resonance (FMR) origin of the measured voltages. Because there are only two ferromagnet components

(the bottom CoFeB electrode and the CoFeB nanoparticles) in our device, any voltage signal arising from FMR has to be related to the TMR between the bottom electrode and the ferromagnetic nanoparticles. Other than driven by spin transfer torque, another possibility of FMR is driven by RF magnetic field (as was done conventionally on magnetic films close to a co-planar waveguide) and detected by the mixing voltage via TMR. A nanoparticle experiences oscillating magnetic field produced by tunneling current through neighboring nanoparticles, which could induce ferromagnetic resonance, but such a field torque should be perpendicular to film plane of the device (since the magnetic field is in-plane) and leads to anti-symmetric Lorentzian line-shape in mixing voltage spectra, similar to the effect of perpendicular (“field-like”) spin torque discussed in Chapter 2. Our measured ST-FMR spectra in Fig. 5.10, on the other hand, show mostly symmetric peaks. Strong leakage current flowing in-plane in metallic leads or substrates could potentially produce in-plane field torques on the nanoparticles driving FMR matching the symmetric peak shape. However, simple order of magnitude estimates indicate that this is probably not a significant factor unless the leakage current all flows very close (within \sim 100 nm) to the nanoparticles. Ruling out field-driven FMR, we then attribute the measured mixing voltage spectra to spin-transfer-driven ferromagnetic resonance (ST-FMR). Furthermore, the positive sign of the resonance peaks (as oppose to dips) indicates that the precession magnet is the upper magnetic layer [78] – the CoFeB nanoparticles in our devices.

Since there are \sim 75 nanoparticles in our MTJ devices, presumably many nanoparticles experience spin transfer torque and precess under the influence of RF spin transfer torque, each of our measured ST-FMR spectra should reflect the behavior of the whole ensemble of particles, or a superposition of the ST-FMR

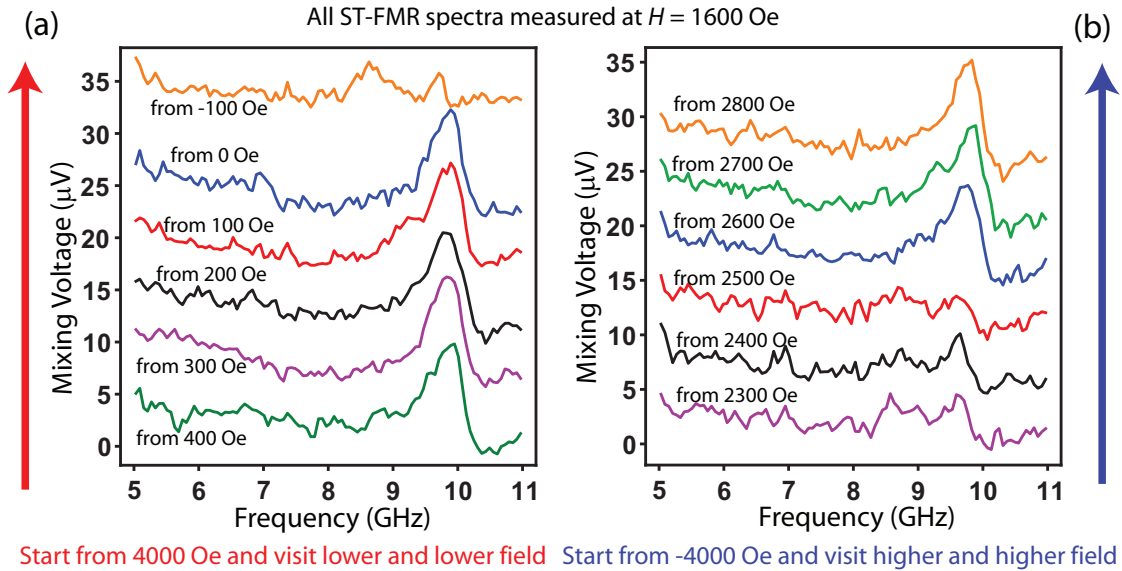


Figure 5.11: ST-FMR spectra associated with CoFeB ferromagnetic nanoparticles embedded in a MTJ device (ADTJ-1 #5-10-44) ($\sim 45 \text{ nm} \times 45 \text{ nm}$) under the same magnetic field of 1600 Oe applied along the in-plane hard axis of the bottom CoFeB electrode but with different history. (a) The device is first positively saturated by a magnetic field of 4000 Oe, and then taken to lower and lower field before each of the ST-FMR spectra is measured at 1600 Oe. (b) The device is first negatively saturated by a magnetic field of -4000 Oe, and then taken to higher and higher field before each of the ST-FMR spectra is measured at 1600 Oe. The RF voltage is estimated to be between 5-10 mV.

spectra of all the individual nanoparticles. Due to the Coulomb blockade effect, the actual number of particles showing up in each ST-FMR spectrum could be much smaller, but it is difficult to tell whether a resonance peak we measure is from a single nanoparticle or a result of multi-particle superposition. One very interesting observation in our experiment could potentially open the door for resolving single-particle behavior in ST-FMR. All of the curves in Fig. 5.11 are ST-FMR spectra (DC Mixing voltage V_{mix} versus RF driving frequency f) measured for the same nanoparticle MTJ device ($\sim 45 \text{ nm} \times 45 \text{ nm}$) under the same magnetic field of $H = 1600$ Oe applied along the in-plane hard axis of the bottom CoFeB electrode. However, out of the 12 spectra shown Fig. 5.11(a) and (b), there are two distinctively different shapes of spectra depending on the

history of how external magnetic field has been applied. (All fields are applied along the in-plane hard axis of the bottom electrode.) When the magnetic field is swept down from 4000 Oe and set to $H = 1600$ Oe, the device shows one large peak at about 9.8 GHz in ST-FMR spectrum. When the magnetic field is swept up from -4000 Oe and set to $H = 1600$ Oe, the device shows two small peaks at about 8.6 GHz and 9.6 GHz in ST-FMR spectrum. In Fig. 5.11(a), we execute a sequence of setting magnetic field and performing ST-FMR measurement as 4000 Oe → 400 Oe → 1600 Oe → measure → 300 Oe → 1600 Oe → measure → 200 Oe → 1600 Oe → measure → 100 Oe → 1600 Oe → measure → 0 Oe → 1600 Oe → measure → -100 Oe → 1600 Oe → measure. The ST-FMR spectrum remains the same single large peak structure until the magnetic field has visited $H = -100$ Oe, when the ST-FMR spectrum suddenly changes to the shape with double small peaks. Similarly in Fig. 5.11(b), the device is first saturated at low field $H = -4000$ Oe, and gradually visits higher and higher field from 2300 Oe to 2800 Oe before one ST-FMR spectrum is measured at 1600 Oe for each of the steps. The ST-FMR spectrum remains the same double small peak structure until the magnetic field has visited $H = 2600$ Oe, when the ST-FMR spectrum suddenly changes back to the shape with a single large peak.

This pair of measurement sequences demonstrates that there is a pair of hysteretic transitions between the two distinctive states of the device that happen at -100 Oe and 2600 Oe. If such a hysteretic transition corresponds to the magnetization switching of a nanoparticle, a subtraction of the two ST-FMR spectra before and after the switching would yield the ST-FMR spectrum of a single nanoparticle. To confirm that such a transition is a magnetic switching of a nanoparticle, we look for signatures of the switching in the magnetoresistance measurement. However, so far no definitive correlations have been

made between resistance jumps in magnetoresistance measurement and the transitions seen in the ST-FMR spectra. Other possibilities of the transitions seen in ST-FMR spectra include magnetic switchings of the bottom electrode. We applied magnetic field along the in-plane hard axis of the electrode in order to deliberately avoid hysteresis of the electrode. However, we cannot completely rule out such a possibility due to complicated magnetic anisotropy of the bottom electrode from possible irregularity in the shape of the nanopillar device as well as micromagnetic behaviors (spatial non-uniformity). Our further study of the ST-FMR transition seems to show relatively weak temperature dependence of the transition field, which suggests that this transition is probably not from a nanoparticle. On the other hand, a magnetic switching of the bottom electrode is expected to show an even more pronounced magnetoresistance signature, which has not been seen either. The dramatic transitions seen in the ST-FMR spectra have remained a puzzling question, and further investigations on more devices would be definitely interesting.

5.5 Summary and Outlook

In summary, we have fabricated magnetic tunnel junction nanopillar devices (~ 50 nm in lateral dimension) with ferromagnetic nanoparticles embedded in the MgO tunnel barrier, and demonstrated tunneling transport through very thin tunnel barrier via isolated nanoparticles. We focused on a type of CoFeB/MgO/CoFeB nanoparticles/MgO/Ru device, measured strong temperature dependences of the tunneling resistance and TMR ratio, and resolved the magnetoresistance changes associated with the magnetic switchings of single nanoparticles, partially owing to the Coulomb blockade effect.

We measured the switching phase diagram (the switching field as a function bias pulse voltage) of a single nanoparticle and provided the first evidence of the effect of spin transfer torque in a single (electrically-isolated) magnetic nanoparticle from the asymmetry of the switching phase diagram. Studies of the thermal stability of the nanoparticles allow estimation of the size of a single nanoparticle, and combined with a thermally-assisted spin torque switching model we arrived at a semi-quantitative agreement between the observed magnitude of spin transfer torque and the simplest theoretical prediction used for a conventional \sim 100 nm nanomagnet. Therefore, at least for a relatively high-bias regime with strong heating, our measurement of spin torque in ferromagnetic nanoparticles did not reveal any result substantially different from in a bulk ferromagnet.

To minimize heating in order to truly probe spin transfer torque at low temperature with quantum effects, we went on to study low-bias spin-transfer-driven ferromagnetic resonance (ST-FMR) of ferromagnetic nanoparticles, and have detected DC mixing voltage likely arising from ST-FMR of multiple nanoparticles. More interestingly, we have observed hysteretic transitions in the ST-FMR spectra, which have yet to be identified but are more likely to be related to magnetic behavior of the bottom electrode.

Our hope and our next goal is to resolve the ST-FMR spectrum of a single particle by a subtraction method after identifying the transitions in the ST-FMR spectrum associated with the magnetic switching of the single nanoparticle. To achieve this goal and to achieve better ST-FMR measurement in general, several improvements can be made on the device side, including using an insulating substrate to reduce microwave loss, fully patterning through the bottom CoFeB

electrode to reduce magnetic spatial non-uniformity, and perhaps reducing further the tunnel barrier RA and the nanoparticle densities. Compared with ST-FMR experiment in a conventional MTJ (without nanoparticles) where extended fixed layer (bottom electrode) is desired to reduce precession of the fixed layer, for our purpose on nanoparticle ST-FMR, it is probably beneficial or even critical to pattern the bottom electrode into sub-50 nm pillars so that it has a much better chance to behave as a single-domain magnet. The precession of the bottom electrode should be less of a concern because its volume is much larger than all of the nanoparticles combined.

Once single-particle ST-FMR can be measured, the next step would be to reduce the RF voltage from 5-10 mV currently used to \sim 1 mV, comparable to the discrete energy level spacing of some nanoparticles and the thermal energy scale at 4.2 K. This would result in a reduction of ST-FMR signal level of a factor of \sim 50, and requires some improvement on the signal/noise ratio. On a good day our current noise level is about $0.2 \mu\text{V}/\sqrt{\text{Hz}}$, and each spectrum in Fig. 5.11 takes about 3 minutes to measure. Given that we can afford to average somewhat longer and resolve a resonance peak from a somewhat noisier spectrum than Fig. 5.11, some modest improvement in signal/noise ratio should make measurement at 1 mV practical. If good signal/noise ratio can be achieved at 1 mV, moving to a ^3He fridge, or even dilution fridge, can be considered, allowing for better energy resolution.

The envisioned ultimate goal of this project is to study the spin transfer torque in the single-electron tunneling regime. We have come a long way towards this goal by detecting ST-FMR spectrum of a few(or at most 10's)-nanoparticle system with sub-10 mV RF drive, and observing hysteretic transi-

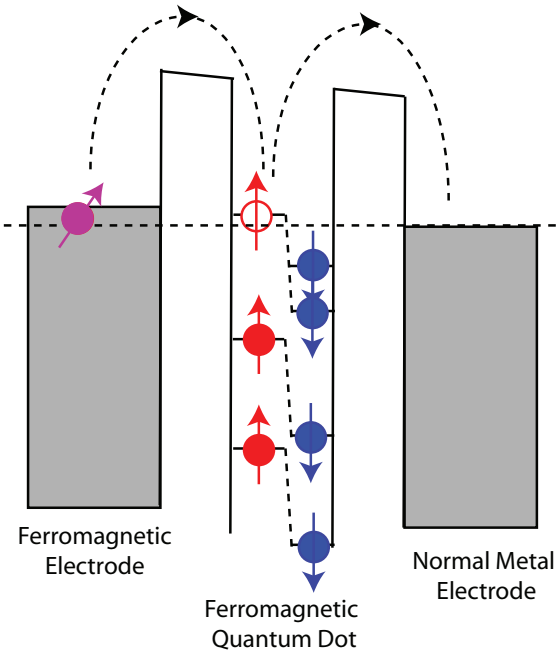


Figure 5.12: A naive picture of a ferromagnetic quantum dot for considering spin transfer torque in the single-electron tunneling regime.

tions that would be the key to the separation of single-particle ST-FMR spectrum down the road. With a little further progress I am cautiously optimistic that spin transfer torque in the single-electron tunneling regime can be probed.

If we think about a ferromagnetic nanoparticle as a quantum dot where the spin-up band and spin-down band are quantized respectively (Fig. 5.12), it becomes a perfect spin filter when one of the single-spin quantum state aligns with the Fermi level. However, if the quantum dot really acts as a spin filter from this single-electron state at the Fermi energy, with no other states operative, no transverse angular momentum can be absorbed by the dot, and no spin transfer torque would be present. If spin torque were to act on the dot, it has to be mediated by an electron-electron interaction that passes the spin of the quantized state at the Fermi level to other electrons on the dot. Of course an independent-electron picture of ferromagnetic nanoparticle is perhaps overly

naive, but the dichotomy of electronic transport governed by a single state while resulting spin torque (likely) linked to many other states appears to be a physically intriguing problem. An experiment testing the existence and the magnitude of spin transfer torque on the single-electron level would shed light on how spin torque really works from the most basic perspective. Early works on energy quantization in ferromagnetic nanoparticles [45] suggest a complicated energy profile associated with collective spin excitations of the nanoparticle. Measurement of the individual-state dependence of spin transfer torque, if possible, would add an extra dimension of information to transport studies to fully unravel the spin states of the electronic spectra of ferromagnetic nanoparticles.

5.6 Appendices

In the process of searching for spin transfer torque in ferromagnetic nanoparticles, we have made other variations of the devices for our study, such as CoFeB nanoparticle MTJs with both electrodes ferromagnetic, MTJs with Co nanoparticles, and also devices with post-fabrication annealing. Here I would like to briefly list some measurement results in a few of these different devices.

5.6.1 Electrical Measurements on CoFeB/ MgO/ CoFeB (Nanoparticles)/ MgO/ CoFeB Devices

CoFeB nanoparticle MTJs with both electrodes ferromagnetic are the first type of devices we attempted to make in the initial stage of the project, which have

been the type of devices used for studying cotunneling enhancement of TMR in ref. [121, 122, 124, 125]. Figure 5.13(a) shows measured room-temperature resistance R of a CoFeB/MgO/CoFeB nanoparticles/MgO/CoFeB device as a function of magnetic field H , which can be compared with room-temperature R vs. H of a conventional CoFeB/MgO/CoFeB MTJ device [Fig. 5.13(b)]. Both devices show switching of the electrodes at around $H = 0$ (for the free top electrode) and $H = 200$ Oe (for the exchange bias pinned bottom electrode). With the knowledge of the superparamagnetic behavior of nanoparticles characterized in previous sections, we identify the long tails in R vs. H in Fig. 5.13(a) as the contribution from the gradual alignment of nanoparticles to the external field. The magnetoresistance (R vs. H) measurements at various temperatures show that the magnetic field required to saturate the resistance (to make the long tail in R vs. H flat) decreases at lower temperature [Fig. 5.13(c)], in agreement with our previous characterization of CoFeB nanoparticles.

Although we have a well-explained correspondence between the magnetoresistance data and the expected magnetization orientations of all three magnetic layers in the system, the relative magnitude of TMR ratio related to the electrodes and the nanoparticles remains somewhat puzzling. In sequential tunneling regime, the total resistance of a FM1/I/FM2/I/FM3 device is the sum of the two MTJs (FM1/I/FM2) and (FM2/I/FM3). Therefore when FM2 is in a superparamagnetic state with nearly no preferable orientation as the nanoparticles are expected to behave at low field ($H < \sim 200$ Oe), switching of either FM1 or FM3 [such as from point A to point B in Fig. 5.13(c)] should not change the total resistance significantly, compared with the change of resistance due to a high magnetic field aligning the nanoparticles [such as from point B to point C in Fig. 5.13(c)]. However, in experimental data we often see more

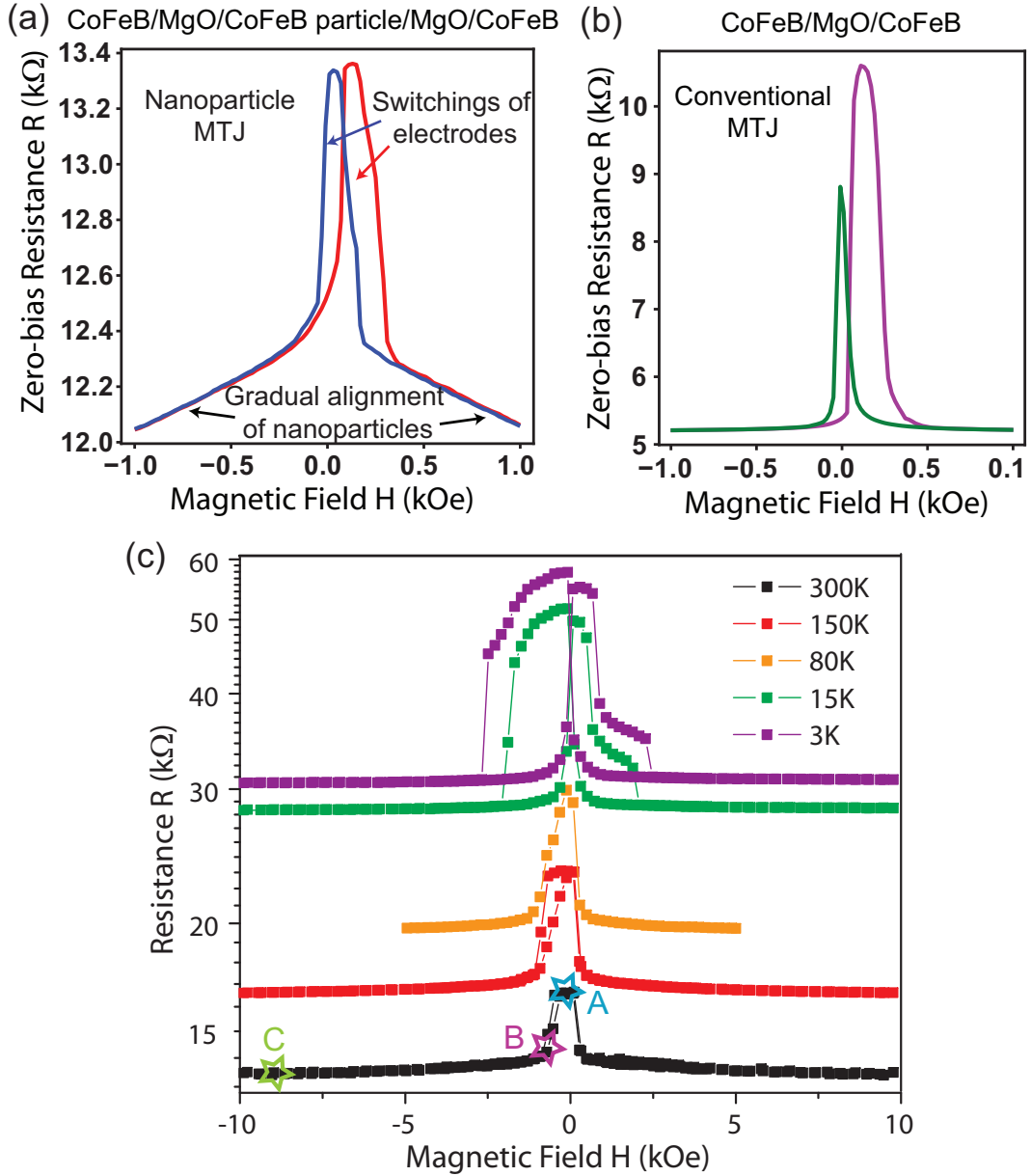


Figure 5.13: Magnetoresistance measurement of magnetic nanoparticle tunneling devices with double magnetic electrodes. (a) Room-temperature resistance R of a CoFeB/MgO/CoFeB nanoparticles/MgO/CoFeB device as a function of magnetic field H , compared with (b) room-temperature R vs. H of a conventional CoFeB/MgO/CoFeB MTJ device. Both devices show switching of the electrodes at around $H = 0$ (for the free top electrode) and $H = 200$ Oe (for the exchange bias pinned bottom electrode). The contribution of the nanoparticles to the resistance is seen as the long tails in R vs. H in (a). (c) R vs. H for a different CoFeB/MgO/CoFeB nanoparticle device (~ 80 nm \times 250 nm) at various temperatures.

significant resistance change between point A and point B than between point B and point C. In other words, the resistance of the device appears to be more sensitive to the relative orientation of the electrodes than the orientation of the nanoparticles. One natural explanation one can think of is the contribution of direct tunneling between the two electrodes, but we have not made further investigation to test such a possibility. The relative weight of nanoparticles in the total TMR varies for different devices, and depends on whether we anneal the devices (as will be discussed in another Appendix section). The device shown in Fig. 5.13(a) probably has a larger contribution from nanoparticles if we extrapolate (and gradually flatten out) the resistance tails towards $H = 10$ kOe, but we did not make higher field measurement on that device.

Due to the complexity arising from having three ferromagnetic components in the device, it would be more difficult to interpret the magnetoresistance data and furthermore the spin torque effects. Therefore, we shifted away from this type of device with double ferromagnetic electrodes for the spin torque studies presented in the main content of this chapter.

5.6.2 CoFeB/ MgO/ Co (Nanoparticles)/ MgO/ Ru Devices

Other than CoFeB nanoparticles, we have also investigated Co nanoparticles embedded in MgO tunnel barrier of nanopillar devices. The full layer structure is seeding layers/ CoFeB/ MgO/ Co particles/ MgO/ Ru/ capping layer. For the devices we measured and discussed below, there is no IrMn layer that provides exchange bias pinning to the bottom CoFeB electrode (not intentional, just due to sputtering target availability), so presumably the bottom CoFeB

electrode switches its moment near $H = 0$ under a sweeping external magnetic field H .

The original rationale for trying Co nanoparticles in replacement of CoFeB is that the Co material probably has stronger surface tension in favor of larger and fewer nanoparticles in a nanopillar device with a given size. However, it turns out that for similar nominal thickness the size of Co nanoparticles formed by our fabrication procedures are generally smaller than the CoFeB nanoparticles, at least in the sense of the number N of single electron spins in each nanoparticle on average. At the same time, the density of the nanoparticles is probably also slightly lower than the CoFeB nanoparticles. This means a lot of “lost” magnetic moment in the deposited Co material. The measured total magnetization of a nominally 5 Å-thick layer of Co nanoparticles are only about 10% of the value expected from its bulk volume, compared with roughly 40% in the case of CoFeB. Losing a few Å worth of magnetic moment is well-known in magnetic thin film growth when continuous films are formed and called “magnetic dead layer”, which, however, has not been well-understood. Here we attribute the lost of momoent in the case of CoFeB to such a dead layer effect, but losing 90% of magnetic moment in the case of Co seems too much and we suspect heavy oxidation may be a factor. It should be noted that for the growth of the Co nanoparticles, we mostly sputtered at a power of 25 W compared with 75 W for CoFeB, which might be partially responsible for resulting in smaller size and lower total moment for the nanoparticles. Later on we have briefly tested the growth of CoFeB nanoparticles at different sputtering power with SQUID magnetometry, and lower sputtering power does appears to result in lower total moment as well as smaller particles. Therefore, it is not entirely clear at this point how much the material difference play a role in tuning the size of the

nanoparticles.

Nevertheless, both the lower density and the smaller size of our fabricated Co nanoparticles are beneficial for approaching the single-electron-tunneling regime, making Co nanoparticles a worthy system for additional experiments. Indeed, Co nanoparticle devices offer much better single particle resolution than CoFeB nanoparticle devices. Moreover, our fabricated Co nanoparticles show an astounding property in extremely high magnetic anisotropy, in excess of 2 Tesla. On the flip side, the TMR ratio for the CoFeB/MgO/Co nanoparticle tunneling system is small, at most 10-15% at 4.2 K for the devices we have measured. In addition, the resistance-area product, RA , of the devices are nearly 1 order of magnitude higher compared with the CoFeB devices. All these observations contribute to our speculation that the Co nanoparticles may be heavily oxidized, leaving only small metallic Co cores surrounded by a shell of CoO_x .

Fig. 5.14(a) shows the resistance R of a $\sim 50 \text{ nm} \times 50 \text{ nm}$ CoFeB/MgO/Co nanoparticles/MgO/Ru device as a function of magnetic field H in an plane direction swept both ways at various temperatures. The sharp switching transitions seen close to $H = 0$ can be identified as due to magnetic switching of the bottom CoFeB electrode (with no exchange bias pinning). A pair of hysteretic switching events are present far away from $H = 0$ for each of the three lower temperatures. Since the magnetic behavior of a $\sim 50 \text{ nm} \times 50 \text{ nm}$ free CoFeB electrode is highly unlikely to undergo any sudden change of magnetic orientation for an in-plane field higher than 1 kOe, the high-field switching has to be attributed to a Co nanoparticle. The linear relationship between the critical switching field H_{sw} measured from the R vs. H curve and the temperature T

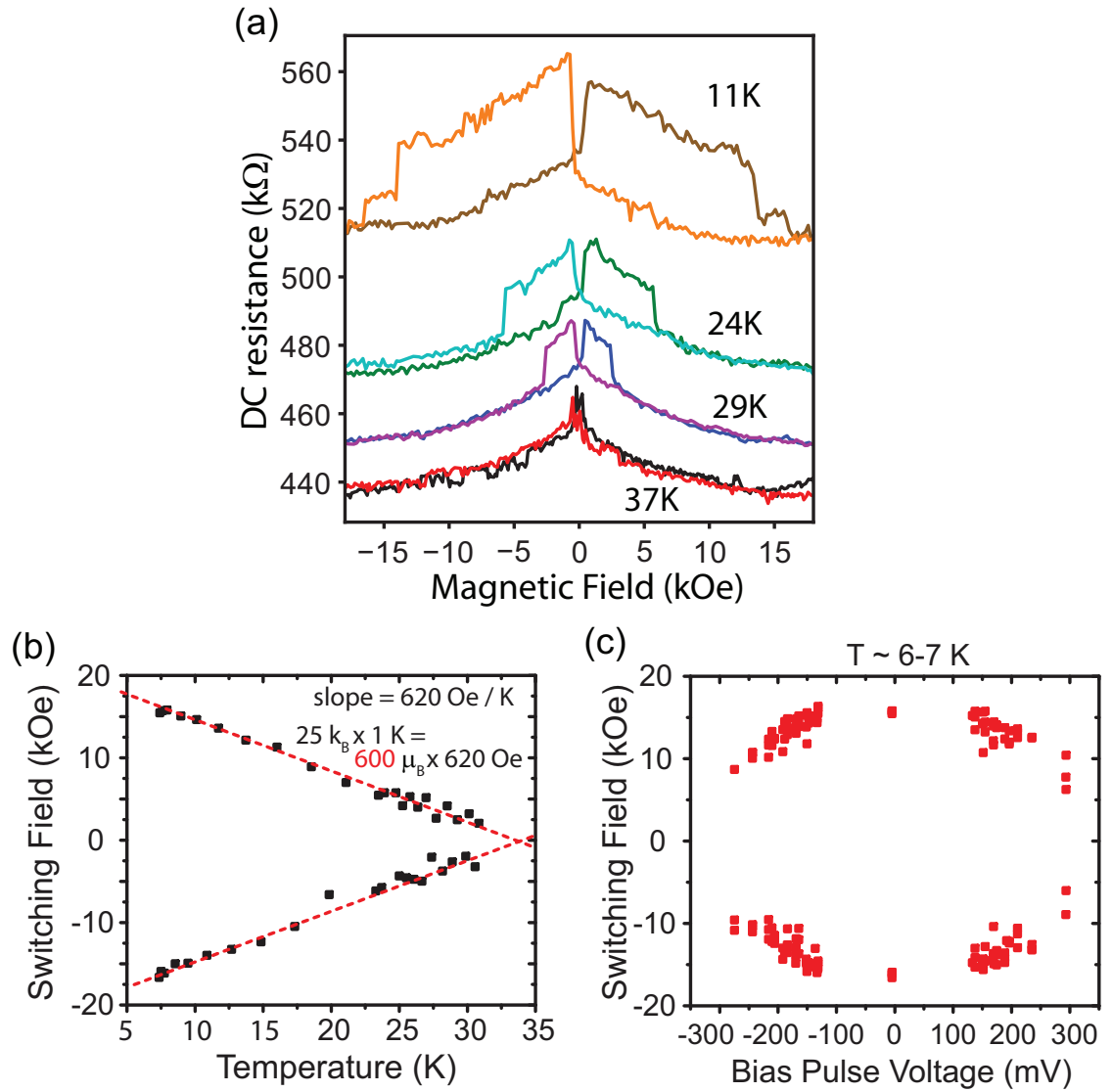


Figure 5.14: Electrical measurements on a $\sim 50 \text{ nm} \times 50 \text{ nm}$ CoFeB/MgO/Co nanoparticles/MgO/Ru device (ADTJ2 #6-11-43). (a) Resistance R as a function of magnetic field H in an plane direction swept both ways at various temperatures. A pair of hysteretic switchings of a single nanoparticle are shown far away from $H = 0$. (b) The critical switching field of the Co nanoparticle as a function of temperature. (c) Switching phase diagram (H vs. V) of the Co nanoparticle with 10 ns voltage pulses.

[Fig. 5.14(b)] allows us to determine the magnetic moment of the nanoparticle from the Brown model [129], which yields $600 \mu_B$. Similar to the measurement in CoFeB nanoparticle device, we apply 10 ns voltage pulses repeatedly to the Co nanoparticle device, measure the switching field of the nanoparticle as a function of pulse voltage, and the resulting switching phase diagram is shown in Fig. 5.14(c). Due to the strong anisotropy, this device can tolerate much higher heating than the CoFeB device, and we can apply several hundred mV of voltage pulses without destroying the magnetic hysteresis. Up to 300 mV, no visible asymmetry is seen in the switching phase diagram. Higher voltages have not been attempted for safety purposes. Due to the low conductance, low spin polarization (inferred from low TMR) and strong magnetic anisotropy, the critical voltage of spin torque switching based on Eq. (5.17) is expected to be more than an order of magnitude higher than the case of CoFeB nanoparticle. Therefore, unless spin torque is enhanced or damping is reduced at nanoscale, it is not surprising to see no significant spin torque effect in Fig. 5.14(c).

In summary, the Co nanoparticles samples offer a great advantage in showing well-resolved single-particle magnetoresistance, but so far the weak spin polarization and high resistance makes it hard for spin torque to make any significant impact. If the *RA* of the device can be improved towards its CoFeB counterpart, this tunneling system would have very good potential for spin torque studies. The unexpected huge magnetic anisotropy, $H_{an} \approx 21$ kOe (determined by extrapolation of H_{sw} vs. H to zero temperature), of the Co nanoparticles is by itself a very interesting phenomenon yet to be explained as well.

5.6.3 Effects of Annealing on Nanoparticle MTJ devices

In standard recipes to fabricate conventional MgO-based MTJ devices (without nanoparticles), the MTJs are annealed at 350 °C either before or after being etched into nanopillar devices. This annealing process allows the critical layers for spin-dependent tunneling – CoFeB/MgO/CoFeB – to crystallize which increases the room temperature TMR from ~20% before annealing to ~100% or higher after annealing. Naturally we started out assuming annealing is a necessary step for our device fabrication. For convenience, we performed annealing on our nanoparticle MTJ devices after all the lithography processes are completed. Some of the devices are annealed in vacuum at 350 °C for 1-2 hours, and some of the devices are annealed in air at 350 °C for 10-15 minutes. Both annealing processes had proved similarly effective in improving the TMR of conventional MTJ devices without changing their parallel state resistance significantly.

Table 5.3: The resistances (in kΩ) of 500 nm × 500 nm magnetic nanoparticles tunnel junction devices across 13 × 13 dies on a 4-inch wafer after annealing at 350 °C

1	2	3	4	5	6	7	8	9	10	11	12	13
							22.0					
			38.0	39.0	24.0		25.0	24.0	23.0			
							20.0	25.0	23.0	12.5		
							6.50	6.60	6.90			
							8.00	8.00	7.70	13.0	16.0	
							3.40	3.30	3.40	6.30	7.20	7.6
26.2	17.7	11.0	14.0	9.10	7.00	3.5	3.30	3.50	3.80	4.10	5.30	5.9
14.0	14.0	9.40			5.90	3.0	3.00	2.70	2.60			
17.2	13.2	9.40				3.9	3.80	3.60	3.50	4.00	4.30	
							7.90	8.00	7.00			
							17.0	18.0	17.0			
							35.0	33.0	34.0			

It turns out that the annealing processes, both air-anneal and vacuum-anneal, have drastic and unexpected effects on the nanoparticle MTJ devices. Firstly, the resistance, or RA product, of the devices are increased by one order of magnitude on average. Secondly, the resistances of the annealed devices at different locations across a wafer not always follow the original gradient from designed MgO wedges. Table 5.3 displays the distribution of resistances for 500 nm \times 500 nm nanoparticle MTJ devices across 13×13 dies on the same 4-inch wafer shown in Table 5.2 after annealing. Thirdly, the TMR ratios of the devices, by rough estimates, stay in a similar range of 10-20% at room temperature for most devices, and sometimes decrease slightly. Lastly, the temperature dependence and bias dependence of the resistance become stronger, indicating a more significant Coulomb blockade effect. So far what the annealing process actually does to nanoparticle devices remains a mystery. Since annealing does not help with TMR as hoped but on the other hand increases the RA of the tunneling system, we consider un-annealed samples as more advantageous for spin torque studies.

CHAPTER 6

MAKING SPIN VALVE DEVICES WITH MULTIFERROIC HETEROSTRUCTURES

As was introduced in Chapter 1, there are ways one can attempt to control magnetic moments with pure electric voltages, dramatically different from spin transfer torque which uses a spin transport effect to manipulate magnetic moments. Among the actively pursued avenues, building multiferroic heterostructures that combine inter-coupled ferromagnetic property and ferroelectric property is one promising research direction. BiFeO_3 is the only known multiferroic material showing strong ferroelectric and antiferromagnetic order at room temperature. Because the two order parameters are intrinsically coupled to each other, an applied electric field that switches the electric polarization of a BiFeO_3 domain can simultaneously switch the antiferromagnetic order parameter as well [74]. It has also been observed that BiFeO_3 can produce an exchange bias pinning field on an adjacent magnetic film, and this exchange bias field can be switched together with the antiferromagnetic order parameter [67]. This presents a possibility that one can make a magnetic storage device controlled entirely by an applied electric field, with negligible energy dissipation from Joule heat during for the writing process. In the chapter, I describe our experiments aiming at such a goal by fabricating spin valve devices with current-in-plane (CIP) geometry exchange biased by multiferroic BiFeO_3 .

This project is a collaboration between Ralph group at Cornell and R. Ramesh's group at Univ. of California at Berkeley. The Ramesh group has been the pioneer in studying various properties (including magnetoelectric properties) of BiFeO_3 , and provides BiFeO_3 film samples grown on SrTiO_3 or

DyScO₃ substrates by pulsed laser deposition (PLD). We in Ralph group mostly focus on exploring the potential of permalloy(Py), or Ni₈₁Fe₁₉, as the material coupled to BiFeO₃ in a GMR device. We observe exchange bias coupling at the BiFeO₃/Py interface for some of the film samples, and fabricated “micro-strip” (2 μm × 50 μm) or “nano-strip” (80 nm × 5 μm) GMR devices with multilayer structures of BiFeO₃/Py/Cu/Py/Pt. Our GMR devices allow quantitative study of the exchange bias locally at the device scale as opposed to a full film, and allow us to observe spatial variations of exchange bias at the length scale close to the multiferroic domain of BiFeO₃. With electric field pulses applied to BiFeO₃, we found degradation and very occasionally partially-recoverable change of exchange bias, but so far we haven’t been able to reverse the sign of exchange bias by electric field.

6.1 Introduction to BiFeO₃

6.1.1 Multiferroicity and Magnetoelectric Coupling in BiFeO₃

BiFeO₃ in bulk crystals has a Perovskite structure [Fig. 6.1(a)], which has a cubic unit cell with one Fe³⁺ cation at the body center, one Bi³⁺ cation at the (eight) cubic corners, and three O²⁻ anions at the (six) face centers. Below ~820 °C (Curie temperature T_C), a structural instability reduces the cubic symmetry to rhombohedral, and the Fe³⁺ cations and Bi³⁺ cations are collectively shifted with respect to the O²⁻ anions along one of the eight [111] axes, which produces an electrical polarization \vec{P} . Simultaneously there is also a collective rotation of the O²⁻ anions along the [111] polarization direction which alternates in sign for neighboring cubic cells along the [111] polarization direction [Fig. 6.1(a)].

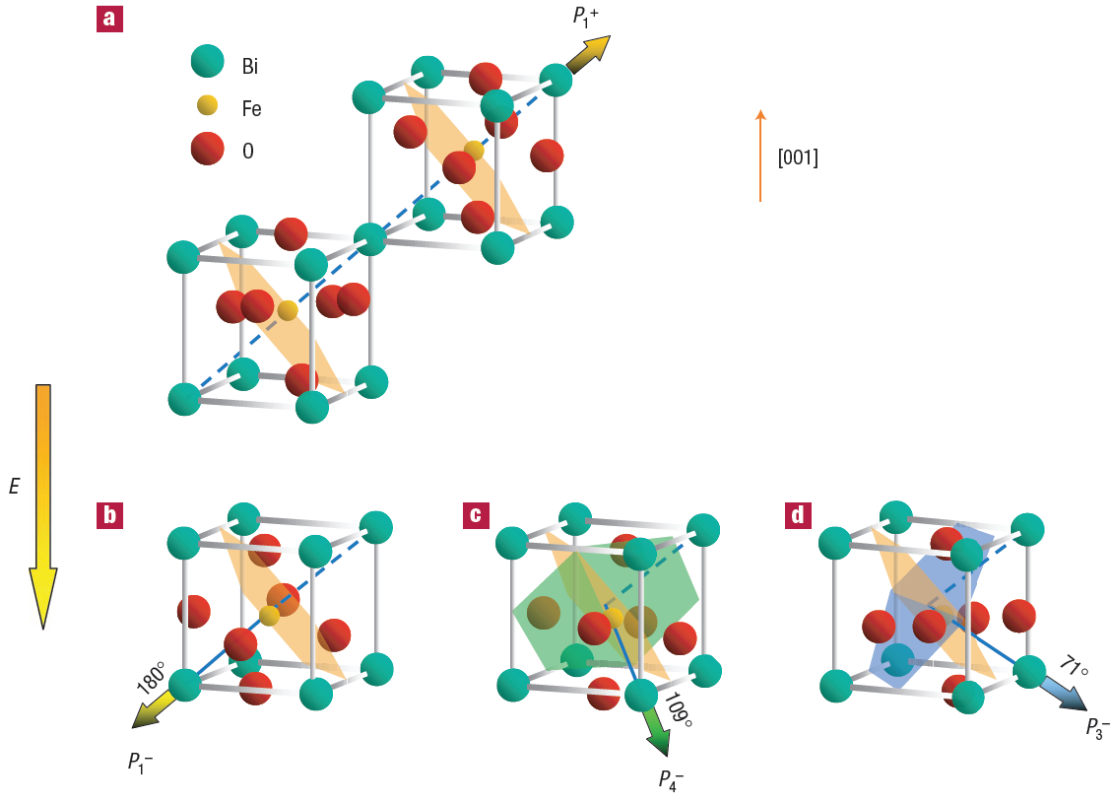


Figure 6.1: Schematic diagram of (001)-oriented BiFeO_3 crystal structure and the ferroelectric polarization (bold arrows) and antiferromagnetic plane (shaded planes). (a) Polarization with an up out-of-plane component before electrical poling. (b) 180° polarization switching mechanism with the out-of-plane component switched down by an external electrical field. The antiferromagnetic plane does not change with the 180° ferroelectric polarization switching. (c) and (d) 109° and 71° polarization switching mechanisms, with the out-of-plane component switched down by an external electrical field. The antiferromagnetic plane changes from the orange plane to the green and blue planes during 109° and 71° polarization switching respectively. Adapted from ref. [74].

BiFeO_3 has also long been known in its bulk form to be an antiferromagnet with Neel temperature $T_N \sim 643$ K. The antiferromagnetic ordering is G-type; that is nearest neighbor Fe moments are aligned antiparallel to each other in all three Cartesian directions.

These bulk properties of BiFeO_3 did not attract much attention until 2003 when it was reported [72] that epitaxially grown BiFeO_3 thin film samples

display nearly an order of magnitude stronger electric polarization P than was reported in bulk samples as well as an unexpected ferromagnetism. Intensive studies followed, and nowadays many initial confusions were clarified, including the strength of electrical polarization P converging to $\sim 90 \mu\text{C cm}^{-2}$ for both bulk and thin film samples (much stronger than was measured decades ago [131]), and the existence of a weak ferromagnetism in thin film samples due to the Dzyaloshinskii-Moriya (D-M) interaction [132, 133] (which is suppressed by a spiral spin structure in a bulk crystal [134, 135]). However, this ferromagnetism from the D-M type of canted moment turned out to be much weaker than was first reported [72], and has yet to be demonstrated useful for practical purposes. So far the rhombohedral structure [Fig. 6.1(a)] has still been the starting point to consider the ferroelectricity and antiferromagnetism and their changes under manipulation, but it is well-known that in strained thin films the structure of BiFeO_3 acquires a tetragonal distortion as well, with the lattice spacing c in the thin film normal direction up to a few tens of percent different from the in-plane lattice spacing a .

The direction of the antiferromagnetic order parameter, \vec{L} , is calculated to be perpendicular to the rhombohedral [111] axis, *i.e.*, perpendicular to the electric polarization \vec{P} [136]. There is a six fold degeneracy within the (111) “easy-magnetic plane” that the antiferromagnetic order can take its direction. It is likely that this degeneracy will be broken if one considers the asymmetry induced by tetragonal distortion in strained thin films, which however has not been systematically studied. Because \vec{L} and \vec{P} are locked to be perpendicular by this intrinsic coupling, an electric-field induced ferroelectric switching of \vec{P} also produces reorientation of \vec{L} , as demonstrated by Zhao *et al.* in R. Ramesh’s group in U. C. Berkeley in 2006 [74]. More specifically, as shown

in Fig. 6.1(b)-(d), there are three types of ferroelectric switching between the eight possible orientations of \vec{P} for a given perovskite lattice. For the case that \vec{P} is completely reversed (by 180°), the easy magnetic plane does not change, and therefore the antiferromagnetism is likely not re-ordered. For the other two types of switching where the electric polarization \vec{P} rotates by 71° or 109° , the easy magnetic plane is changed, and (unless the original \vec{L} happens to be the common line of the easy magnetic plane before and after switching) the antiferromagnetism will be reorganized to find a new ordering direction \vec{L} .

6.1.2 Early Experiments on Exchange Bias at the BiFeO₃/Ferromagnet Interface

This type of magnetoelectric coupling allows one to manipulate the spin structure inside BiFeO₃ by an electric field, but a change of antiferromagnetic ordering is very difficult to detect and it is so far impractical to use antiferromagnetism to serve as information storage media. It would be beneficial to transfer the antiferromagnetic ordering of the BiFeO₃ to a ferromagnetic material, and interface exchange bias, such as what is routinely used between antiferromagnetic IrMn (or FeMn) and ferromagnetic CoFe in MTJs, seems one of the most natural ways to achieve that.

When an antiferromagnetic (AFM) material is intimately coupled with a ferromagnet (FM) at the interface, there are two types of coupling effects that alter the magnetic property of the FM. First effect is coercive enhancement where the coercive field of the FM is increased by the coupling as if the magnetic moment acquires extra viscosity [see the red curve compared with

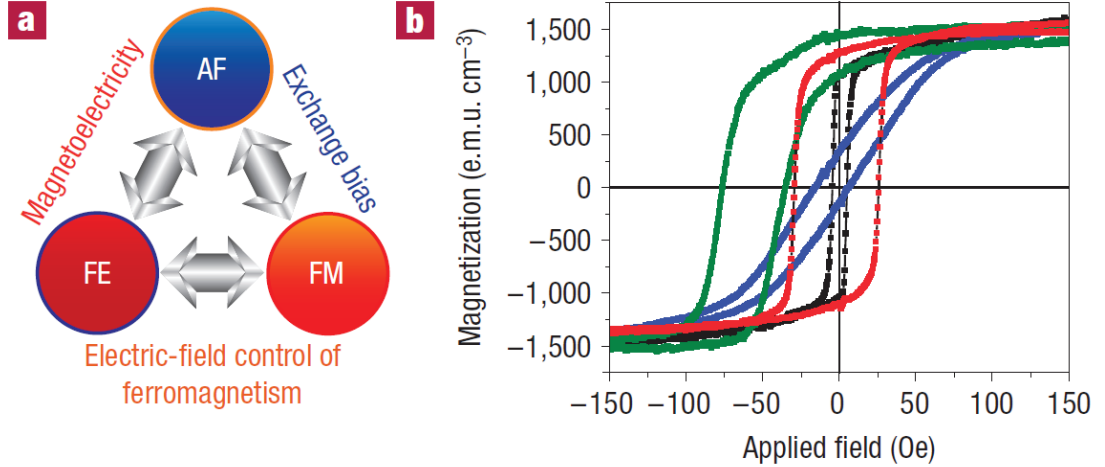


Figure 6.2: (a) Schematic diagram showing the approach we take in this chapter towards electrical control of magnetism. The connection between ferroelectricity, antiferromagnetism and ferromagnetism is shown. (b) Exchange interactions between CoFe and BFO result in either an enhanced coercive field (red and blue data for hysteresis loops measured parallel and perpendicular to growth field, respectively) or an exchange-biased hysteresis loop (green data measured parallel to growth field) for the CoFe layer compared with CoFe grown directly on STO(001) (black data). Adapted from ref. [67].

black curve in Fig. 6.2(b)]. In other words, the FM acquires an increased uniaxial anisotropy. The second effect is exchange bias where the magnetic hysteresis of the FM is shifted towards one certain magnetic field direction [see the green curve compared with red curve in Fig. 6.2(b)]. In other words, the FM acquires a unidirectional anisotropy. Both effects have been reported in the case of $\text{BiFeO}_3/\text{CoFe}$, dependent on the growth conditions of the BiFeO_3 film [137]. The exchange bias effect is of particular interest, because if one can control the direction of the exchange bias acting on the FM via controlling the AFM structure of BiFeO_3 (which can be done by electric field), one achieves electric-field control of ferromagnetism [Fig. 6.2(a)]. Such an experiment was first reported in 2008 by Chu *et al.* in Ramesh group [67], where the magnetic moment of a $2 \mu\text{m} \times 6 \mu\text{m}$ CoFe dot was shown to be reversed after an electric

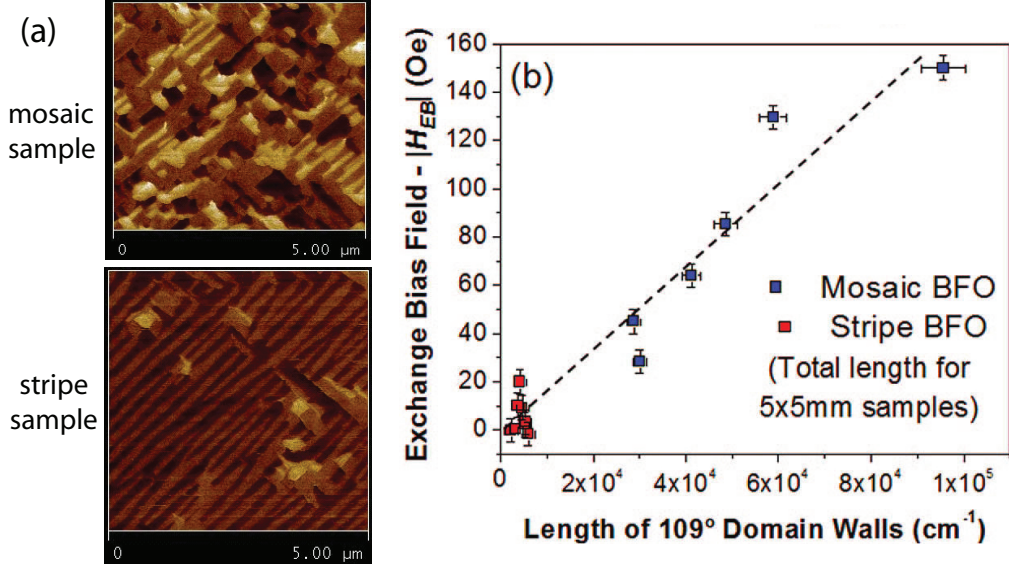


Figure 6.3: The exchange bias between CoFe and BiFeO₃ (BFO) of mosaic or striped domain patterns. (a) Comparison of in-plane piezoresponse force microscopy (PFM) images of a typical mosaic BFO sample and a typical striped BFO sample. (b) The magnitude of exchange bias between various BFO samples and CoFe as a function of the density of 109° domain walls in the BFO samples. Adapted from ref. [137].

field was applied to the area of BiFeO₃ that is underneath the CoFe dot. The direction of the magnetic moment was measured by X-ray magnetic circular dichroism (XMCD) – photoemission electron microscopy (PEEM).

Our experimental efforts to be described in this chapter started based upon the successful demonstration in ref. [67]. The experiment of ref. [67] has been explained as a 90° in-plane switching of the exchange bias between BiFeO₃ and CoFe, and we would like to verify and quantify the strength of this exchange bias exactly before and after switching. More importantly, we aim at building the first prototypical GMR device that one can read out the magnetic moment electrically, and test if one can truly use only electric fields to toggle between high resistance and low resistance states.

However, the possibility of the making a reliable GMR device is not as

optimistic as the breakthrough in ref. [67] would imply. There are many groups that have studied the exchange coupling between BiFeO₃ and a traditional ferromagnetic material grown on top of it, and the results have been mixed. The exchange bias at BiFeO₃/CoFe interface is reported to be critically dependent on the domain structure of the BiFeO₃ [137]. In one type of BiFeO₃ samples with highly disordered domain structures (which are called “mosaic samples”) the exchange bias is relatively large, up to about 100 Oe for a 2-3 nm CoFe ferromagnet. In another type of BiFeO₃ samples with well-ordered domain stripes (which are called “striped samples”) the exchange bias is far weaker, only about ~ 10 Oe, much smaller than the typical coercive field of the CoFe film [Fig. 6.3(a)]. It is then hypothesized that it is the 109° domain walls present in the mosaic samples (but not in striped samples) where the exchange bias is originated [Fig. 6.3(b)]. As a metastable phase, the domain structures of mosaic samples can be dramatically changed under repeated electric field pulses, which would quickly eliminate the exchange bias. Even the striped samples undergo complete reorientation of domain walls under electric fields, and the exact domain structures are never fully recoverable. We later learned that the results reported in ref. [67] came from a one-in-thirty or one-in-fifty hero device at that time, and one could not switch the magnetic moment of the CoFe dot by more than a couple of cycles.

6.2 Statistical Study of Exchange Bias at the BiFeO₃/Permalloy Interface

Most previous studies of exchange bias at the interface between BiFeO₃ (BFO) and a ferromagnet used CoFe (Co_{0.9}Fe_{0.1} or Co_{0.5}Fe_{0.5}) as the ferromagnetic material. Although BFO/CoFe produces good exchange bias (up to 100 Oe) for mosaic BiFeO₃ samples, these samples are not in a stable phase to allow repetitive manipulation as a device. On the other hand, the more stable stripe BFO samples exhibit only small exchange bias (at most 10-20 Oe), much smaller than the typical 30-50 Oe coercive field of a CoFe film deposited on BFO coming from the crystalline anisotropy of CoFe. In order to make GMR devices, we test the potential of another common ferromagnetic material, Ni₈₁Fe₁₉, or permalloy (Py), as the ferromagnet to receive pinning from BFO. In order to make a ferromagnet whose moment can be switched by controlling the exchange bias, the exchange bias H_{EB} (or the change of exchange bias) must be stronger than the coercive field H_C . Otherwise the magnetic moment will not be switched. For this reason, Py is our material of choice because its very small crystalline-anisotropy induced coercive field ($H_C \sim 1$ Oe) can potentially make even a fairly small H_{EB} of ~ 20 Oe usable.

In order to study the exchange bias at the interface of BFO/Py, we deposit Py films of various thicknesses onto the BFO film samples (50-100 nm) grown by pulsed laser deposition (PLD) on 5 mm \times 5 mm or 5 mm \times 10 mm SrTiO₃ or DyScO₃ substrates. Immediately before the deposition of Py, our standard pre-cleaning procedure is soaking the BFO samples in first acetone and then IPA for sonication of 1 minute respectively. The sonication time and

power (by using different sonication tools) have been varied, but no statistically significant difference in results has been noticed. The deposition is either by DC magnetron sputtering in the AJA sputtering tool in D-12 of Clark Hall, or by electron-beam evaporation in the Sharon evaporator in D-18 of Clark Hall. At the AJA sputtering tool the magnetic stage (sample holder) is used, which provides about 200 Oe of magnetic field parallel to the sample surface during the sputtering process. At the Sharon evaporator, the “Alex LN₂” sample stage is used, and a pair of permanent magnets are mounted to the stage by the sides of the BFO sample, providing an in-plane magnetic field of about 700 Oe during the evaporation. A thin capping layer of Pt (for AJA) or Au (for Sharon) is used to protect the deposited Py film from oxidation in air, so the full layer stack is (from top to bottom): Pt (2-3 nm) / Py (2.5-10 nm) / BiFeO₃ (50-100 nm) / SrTiO₃ or DyScO₃ (substrate). No post-deposition annealing has been performed because we were told BFO will start to lose oxygen to Py and to ambient environment at around 200 °C.

The exchange bias at the BFO/Py interface is characterized by magnetometry measurements performed with the vibrating sample magnetometer (VSM) in Van Dover’s group in Bard Hall or the Quantum Design Superconducting Quantum Interference Device (SQUID) in the CCMR shared facilities. We measured the total magnetic moment M as a function of magnetic field H applied parallel (in-plane) to the direction of the growth field. The Bard Hall VSM tends to produce a background slope in M vs. H as well as an offset that is larger than the small magnetic moment ($10^{-4} - 10^{-5}$ emu) we look to measure. This artifact with unknown source is dependent on the exact position of the sample relative to the pick-up coil. Due to this artifact one can not simply try to maximize the VSM voltage signal to center the sample when initializing the

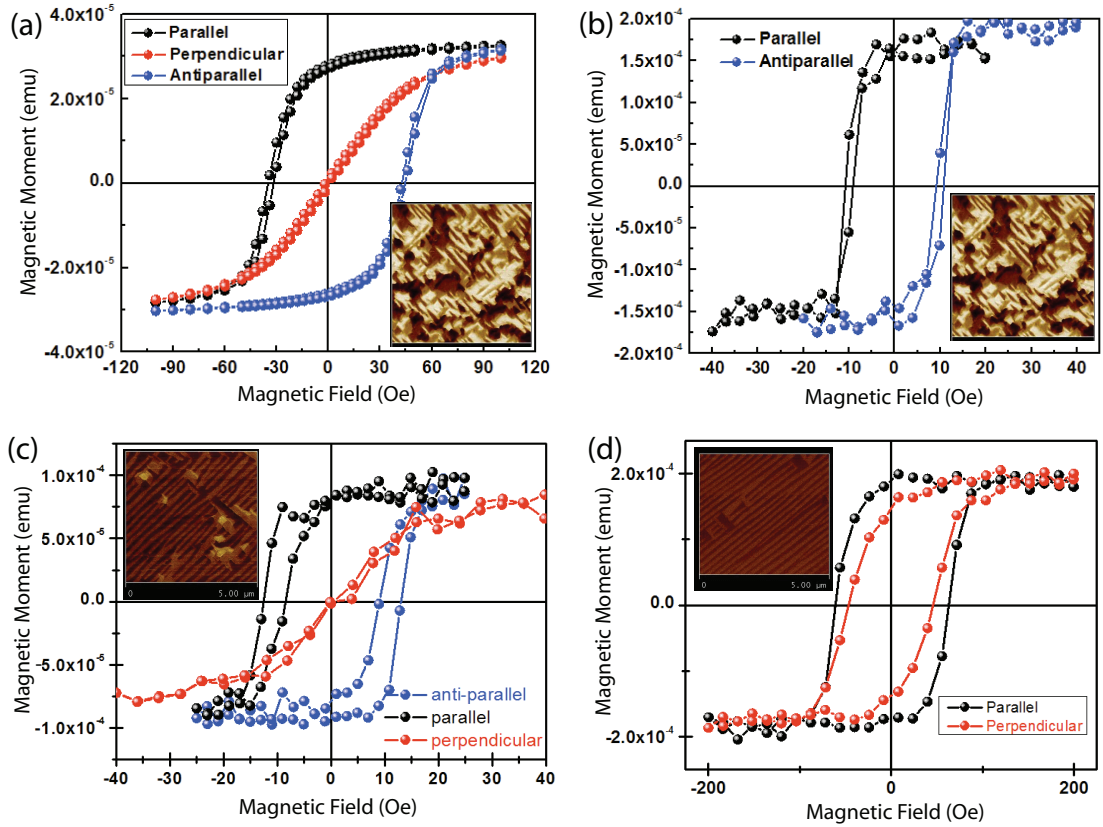


Figure 6.4: Magnetometry measurements (magnetic moment as a function of applied magnetic field) of BiFeO_3/Py samples for characterization of exchange bias. (a) and (b) Demonstration of exchange bias for the same BFO sample (nominally-striped, but with $\sim 25\%$ of domain walls in the 109° type) with (a) 2.5 nm of Py (measured by SQUID) and (b) 10 nm of Py (measured by VSM). (c) Demonstration of ~ 12 Oe exchange bias, much larger than coercive field, for 5 nm of Py on a stripe BFO sample. (d) Absence of exchange bias compared with coercive field for 5 nm of $\text{Co}_{0.5}\text{Fe}_{0.5}$ on a stripe BFO sample.

measurement. My experience is to manually ramp the field back and forth by a few hundred Oe, and look for the position that will minimize the $M \sim H$ response (which is an artifact), which typically corresponds to a well-centered position for the sample. With good centering and sufficient averaging (30 second per point), the VSM is capable of a resolution of 1×10^{-5} emu.

The initial results on BFO/Py exchange bias were promising, such as shown in Fig. 6.4. The exchange bias was present in most samples, and showed

consistency with respect to the thicknesses of the deposited Py layer. Fig. 6.4(a) and (b) demonstrate the exchange bias for the same nominally-striped BFO sample (which is cut in halves for deposition of Py of different thicknesses) with 2.5 nm of Py and 10 nm of Py respectively. The thicker the Py is, the smaller the exchange bias is because the same pinning strength acts on a larger total magnetic moment. The exchange bias of about 40 Oe shown in Fig. 6.4(a) is about 4 times larger than the exchange bias of about 10 Oe shown in Fig. 6.4(b), agreeing very well with their thickness ratio. More interestingly, Py appeared to show better exchange bias with stripe BFO samples compared with CoFe, not only in relative terms (compared with its coercive field) but also in absolute terms. For 2.5 nm of Py, we found an exchange bias as large as 50 Oe in stripe BFO samples with partial mosaic structure [such as the sample in Fig. 6.4(a)], and as large as 25 Oe in relatively well-ordered stripe BFO samples [such as the sample in Fig. 6.4(c)]. We found no significant enhancement of the coercive field for Py when it is coupled to BFO, allowing the exchange bias of 10-20 Oe for a stripe BFO sample to stand out [Fig. 6.4(c)]. By comparison, CoFe on a similar BFO sample displays even smaller exchange bias and a much larger coercive field.

However, as time went on and more BFO samples were grown with the BFO/Py exchange bias measured, we found that the exchange bias varied from sample to sample dramatically and unpredictably (see Fig. 6.5). Moreover, it seems that with gradually improved quality of the BFO samples (with better ordered stripe domain structures) the chance of measuring a sizable exchange bias became smaller. On our Cornell side, some parameters have been deliberately tuned including the growth rate of Py, the direction of the growth field with respect to the domain stripes, the time of sonication, but none

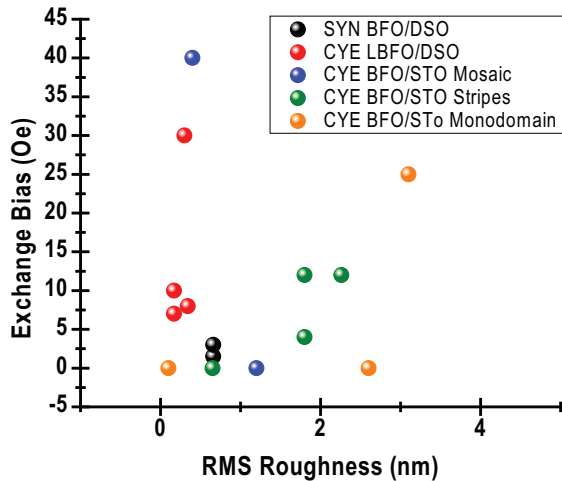


Figure 6.5: Brief statistics of the exchange bias observed for various BFO samples with Py, plotted as a function of surface roughness. Courtesy of John Heron in Ramesh Group at UC-Berkeley.

of these factors appear to be correlated well with the amount of exchange bias shown for the sample. In a few tries, we have also baked the BFO sample *in situ* up to 100 °C before depositing Py, in an attempt to remove the water molecules at the BFO surface that could be detrimental to a good interface. In the AJA sputtering tool, heating was done by the internal heating lamp, set to a nominal temperature of 250 °C for about 30 minutes while the sample stage was inside the main chamber, with the real temperature pre-calibrated. In Sharon Evaporator, heating was done by the heater on the “Alex LN₂” stage, and the temperature could be monitored by a thermocouple. Whether the sample was baked or not did not show any correlation with the resultant exchange bias either. We believe that the variation of exchange bias is more likely related to the details of the growth process of the BFO film rather than the cleaning step leading up to the Py deposition or the Py deposition itself.

The BFO films were grown in Berkeley and shipped to Cornell via FedEx overnight, and they were also typically idled for various periods of time

between the growth of BFO and the deposition of Py on both locations. We suspect that the BFO films degrade over time, and there is a (still elusive) statistical trend that the BFO films that are fresher at the point of Py deposition are more likely to show larger exchange bias. Scanning transmission electron microscopy (STEM) images of the BFO/Py interface taken by Muller group at Cornell found that there exists one or two atomic layers of Fe/Ni-oxide layer between BFO and Py (Fig. 6.6), indicating that we do have some deterioration at the interface. However, what role this oxide layer plays in affecting the exchange bias remains unclear. We took STEM images on two BFO/Py samples in total, one [labeled mtBFO67nD, Fig. 6.6(a)] with nearly no exchange bias ($H_{EB} < 2$ Oe) and one [labeled mtBFO67nD, Fig. 6.6(b)] with pretty good exchange bias ($H_{EB} \approx 25 - 30$ Oe), and both samples showed a similar oxide layer. It is not clear whether this layer is already present before the deposition of Py, or forms during or after the deposition of Py. Electron energy loss spectroscopy (EELS) (Fig. 6.7) mapping in STEM reveals that the chemical state of Fe is mostly 3+ (the same as in BFO), and the ratio of Fe/Ni in the oxide layer is higher than in Py, so it's possible that the Fe and O atoms in BFO play a significant role in forming this oxide layer.

Ideally we would like to get rid of this oxide layer, and other than baking we also made a few tries to perform a back-sputtering *in situ* before the deposition of Py. Back-sputtering is essentially an etching process on the sample surface, which we hope removes any degraded/oxidized layer that is present before the deposition. We did not try STEM on such samples, but magnetometry measurements showed no significant improvement in getting exchange for the two or three samples on which we tried back-sputtering. Note that etching may not only remove existing surface layers, but also induce dislocations or

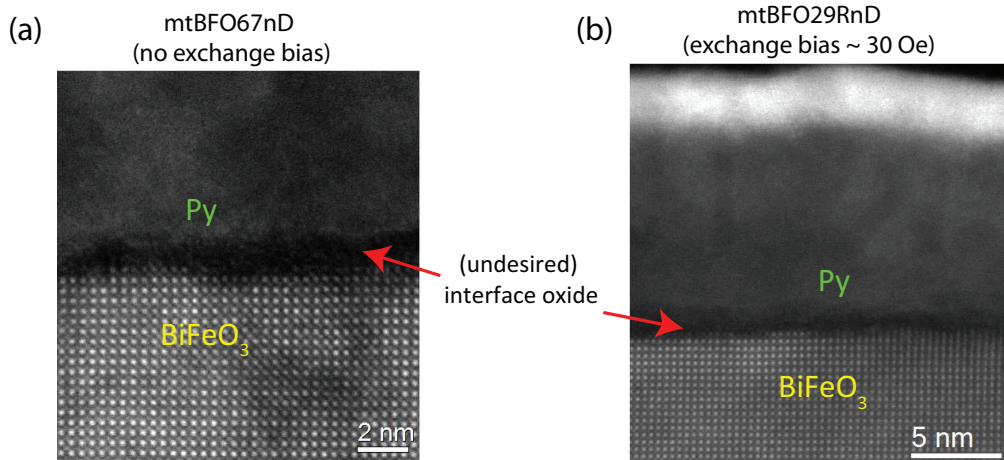


Figure 6.6: STEM images of the BFO/Py interfaces for two samples, showing (a) no exchange bias and (b) 30 Oe exchange bias, respectively. No apparent differences at the interfaces are found between the two samples. Courtesy of Ye Zhu in Muller Group at Cornell.

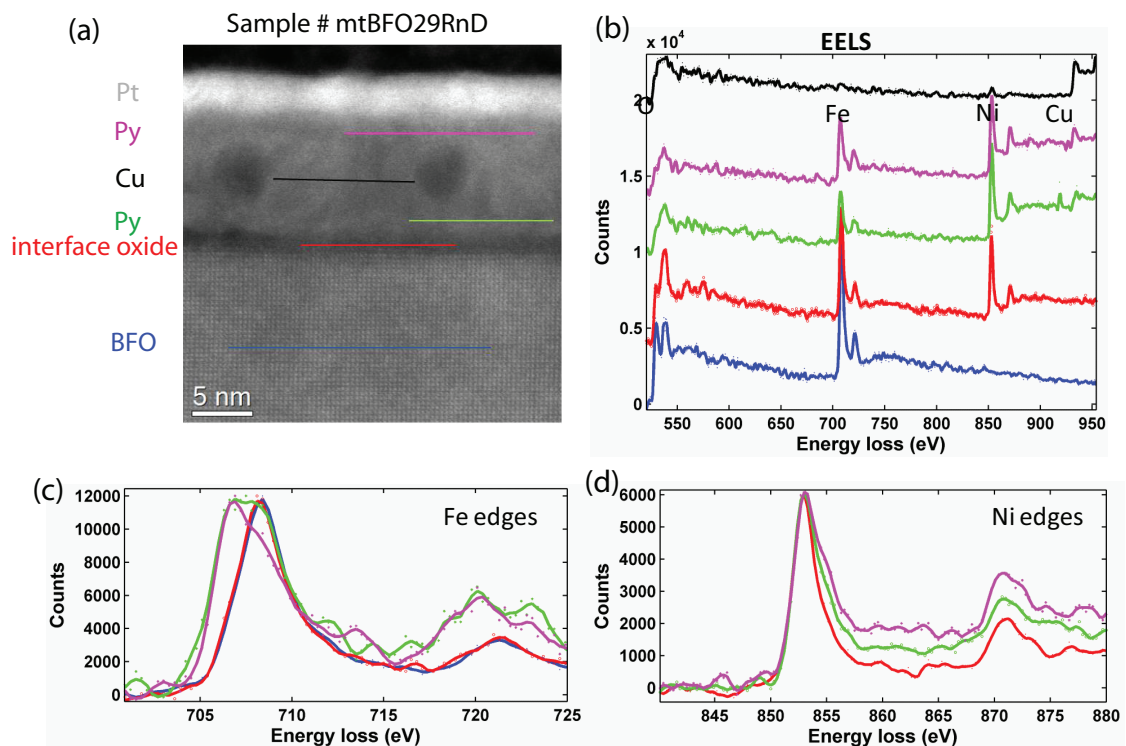


Figure 6.7: EELS spectra of different atomic layers in a BFO/Py/Cu/Py spin valve film stack. (a) STEM image of a BFO/Py/Cu/Py spin valve film stack. (b) EELS spectra of the different atomic layers marked with colored lines in (a). (c) and (d) Close-up views of the (c) Fe and (d) Ni edges for different layers. Courtesy of Ye Zhu in Muller Group at Cornell.

even chemical changes to the newly uncovered surface as well. So etching is generally not recommended for producing an interface that is critical to device functionality. Noting that the STEM images in ref. [67] show great interface with no oxidation at the interface between BFO and CoFe, which involves the same pre-cleaning process (only solvent clean and sonication) between the growth of BFO and CoFe, we suspect shorter wait time between the growth of BFO and the magnetic layer is likely critical to achieve good interfaces.

6.3 Spin Valve Devices Exchange-Biased by BiFeO₃

Although we did not find a way to achieve consistent exchange bias. For the samples that do display $H_{EB} \approx 15 - 30$ Oe exchange bias, it should be sufficiently large compared with the small coercive field (typically $H_C \approx 1 - 5$ Oe) of Py to allow control of the magnetic moment direction of Py, assuming that the direction of the exchange bias can be controlled electrically as we discussed in the introduction section. Therefore we made spin valve devices with these selected samples that showed sizable exchange bias.

6.3.1 Device Structure and Fabrication

To make the GMR devices, we perform the same surface cleaning procedure on BiFeO₃ films as described above and deposit a metallic multi-layer stack (from bottom to top) of Py(2.5 nm)/ Cu(4-8 nm)/ Py(2.5 nm)/ Pt(2.5 nm) onto the sample. The AJA sputtering tool is mostly used for this study since the evaporated spin valve structure (in limited number of tries) showed relatively

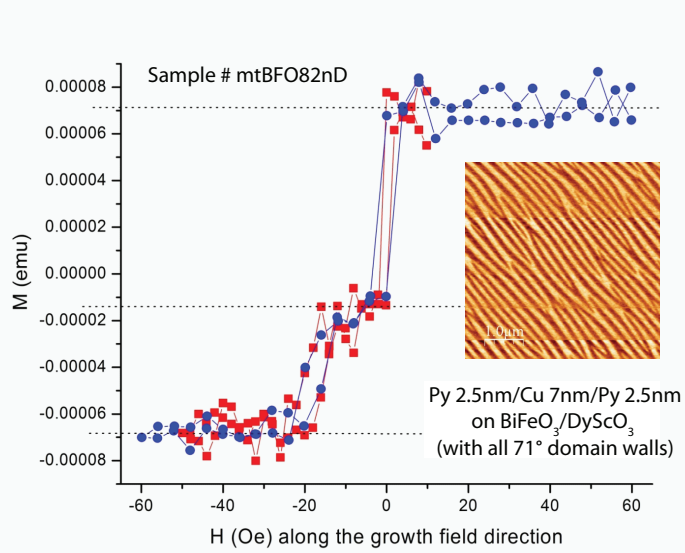


Figure 6.8: Magnetometry measurement (M-H) for a spin valve layer stack of BFO/Py/Cu/Py/Pt.

large inter-layer coupling, likely due to greater film roughness. The magnetic stage in AJA is used to mount the sample, which provides a 200 Oe in-plane magnetic field during sputtering. We then perform a VSM or SQUID magnetometry scan to characterize the exchange bias acting on the bottom Py layer. A desired film stack should show two distinctive magnetic switching loops both with small hysteresis, such as shown in Fig. 6.8. One magnetic switching loop should be centered around zero field corresponding to the top Py layer that receives no pinning, and the other magnetic switching loop should be horizontally shifted by H_{EB} .

For samples showing an exchange bias of more than 10 Oe, we further pattern the extended film stacks into giant magnetoresistance (GMR) devices with current-in-plane (CIP) geometry. A schematic of the device is shown in Fig. 6.9(a). The devices can be conveniently fabricated in two steps. In the first step, we use (optical) photolithography and ion milling to define the “micro-

strip” devices with the size of $50 \mu\text{m} \times 2 \mu\text{m}$. Then in the second step, we do a second stage of photolithography and deposit 200-250 nm copper (Cu) to the sides of the micro-strip, forming a $4.5 - 6 \mu\text{m}$ non-contact gap over where the device is located [as shown in Fig. 6.9(a)], and also at the ends of the device strips to make electrical contacts [that are not shown in Fig. 6.9(a) but can be seen in Fig. 6.9(b)]. An optical microscope image of the fabricated device is shown in Fig. 6.9(b). The side electrodes are used to apply an electric field to the area of BFO underneath the device strip, while the contacts made to the device are used for a four-point electrical measurement of the resistance of the device. The direction of the micro-strip is designed at a 45° angle to the direction of the exchange bias. If the hypothesis in ref. [67] is correct, the direction of the exchange bias should be switched in-plane by 90 degree after an electric field switches the ferroelectric polarization \vec{P} of the BFO [as shown in Fig. 6.9(b)].

For both photolithography steps, standard Shipley S1813 is used as the photoresist, and the $5\times$ stepper is used for exposure. The small size of the substrate ($5 \text{ mm} \times 5 \text{ mm}$) makes resist spinning relatively difficult, but in CNF photolith room there is a tiny-sized chip holder that holds our small samples well. P-20 primer is spun at 3000 rpm (and 2000 rpm^2 acceleration) for 30 s, followed by spinning S1813 at 4000 rpm (and 2000 rpm^2 acceleration) for 30 s, and baking at 115°C for 70 s. Since the STO or DSO substrate is semi-transparent, at the $5\times$ stepper one can use the “transparent” setting, which seems to help with focusing. A ring-shaped metallic shield available to the stepper is used to cover the vacuum groove so that the small sample can be held tight. Stepper exposure time is usually set between 0.35 to 0.45 s. One has to align the patterns carefully in order to have the side electrodes well-spaced from the device strip. After exposure, the chip is soaked in 300MIF or 726MIF

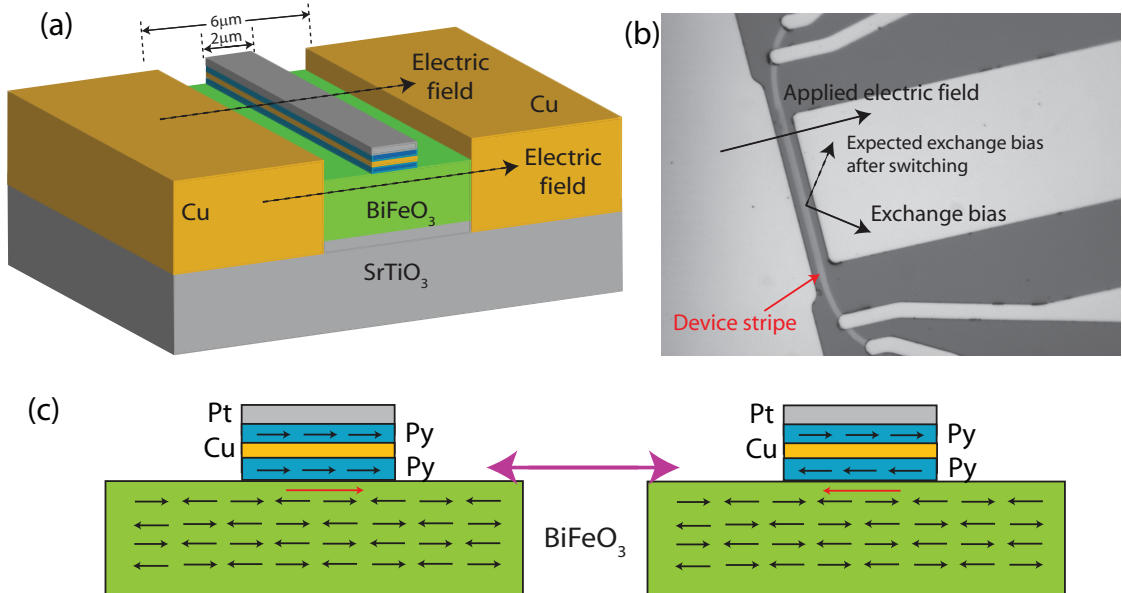


Figure 6.9: (a) Schematic of our GMR device based on BFO and Py. (b) Optical microscope image of the GMR device. (c) Schematic of the operation of the GMR device, where the bottom Py moment is controlled by the exchange bias from BFO.

for 70 s for development, followed by an oxygen plasma descum in Oxford 80#1 at 75 W for 20 sec.

The new IBD system in E-7 Clark Hall with end-point detection works well for the etching task. It takes about 2 to 2.25 minutes to etch through the metallic layers at 150 V / 35 mA, and even with sample size as small as it is, one can still clearly see the Bi signal arising on the element-resolved end-point detector. We typically stop etching about 20 s after seeing the Bi signal, corresponding to about 1-2 nm of over-etching into the BFO as allowance of non-uniformity. The deposition of Cu is done using the old IBD system in D-12. As generally recommended, we perform a slight etching of about 5-10 s as a pre-cleaning, and then deposit Cu at 500 V / 100 mA for 18-22 minutes. Lift-off is done by sonication in acetone for a few minutes.

In the initial trials of the fabrication, between the two steps, we did an

additional etching to remove the BFO $2 \mu\text{m}$ away from the sides of the device to make room for the Cu side electrodes as illustrated by Fig. 6.9(a). This step, however, was unnecessary since the electric field can be applied to the BFO by the side electrodes regardless of whether these electrodes are over the BFO surface or embedded into the BFO. Furthermore, there is evidence from Ramesh group that excessive ion milling of BFO produces oxygen vacancies all over the BFO film (even in areas that are not directly exposed to ion mill), which damages the insulating property of the BFO sample. Therefore, we did not perform the extra etching step for most of the devices.

6.3.2 Electrical Measurements of GMR and Exchange Bias

Figure 6.10 shows the resistance of our device as a function of external magnetic field applied parallel to the device strip. Due to the shape anisotropy from the large aspect ratio of the device strip, the magnetic moment of both Py layers are relaxed parallel to the strip. (Note that for a micro-strip, both magnetic layers are unlikely to be single domains, but on average the total magnetic moment has an easy axis along the device strip.) Therefore there are two distinctive states for the spin valve device, parallel (P) state with low resistance and anti-parallel (AP) state with high resistance (Fig. 6.10). There are a pair of switching events centered at around zero magnetic field, which can be identified as the switching of the top unpinned Py magnetic moment. Another pair of switching events occur around a positive magnetic field, which can be identified as the switching of the bottom Py magnetic moment pinned by the exchange bias from BFO. We can determine the magnitude of the exchange bias (projected to the direction of the strip) from the hysteretic center of the bottom Py layer in GMR

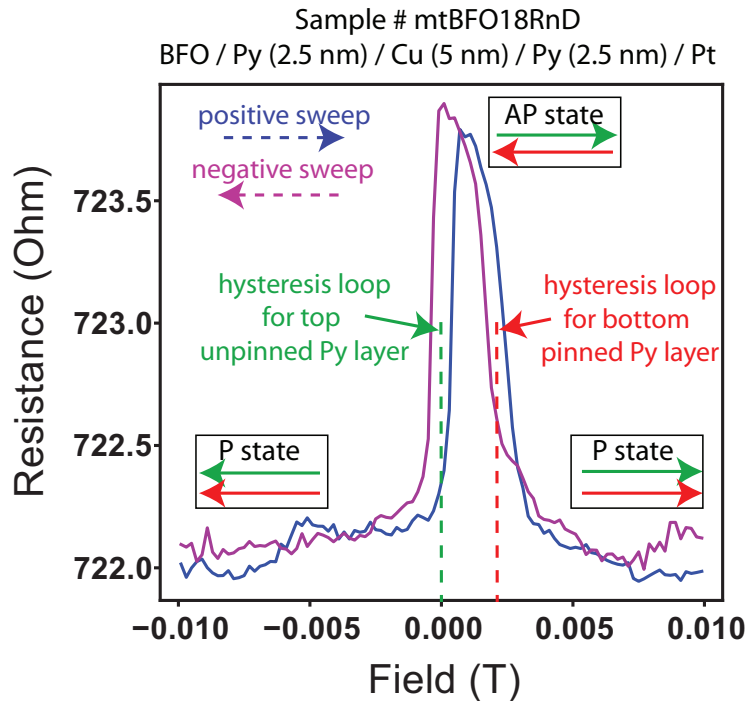


Figure 6.10: Giant magnetoresistance of a Py/Cu/Py spin valve device pinned by BiFeO_3 .

measurements, which is about 20 Oe for the sample shown in Fig. 6.10. The magnetic moment of both Py layers remain soft, showing small coercive field, which is very good news.

Since the micro-strips are at a 45° angle relative to the exchange bias by design, the horizontal shift in hysteresis loop observed from the GMR signal corresponds to the exchange bias projected to the axis of the device strip. Therefore the exchange bias measured from the GMR devices is usually about 30% smaller than measured from magnetometry of the continuous film stacks. Our data in most cases agree well with this prediction. Furthermore for micro-strip devices, the measured exchange bias are usually fairly consistent among different devices (with the same nominal size and orientation) [See Fig. 6.12(a) for instance].

6.3.3 Effect of Electric Field Pulses on Exchange bias

The successful observation of clear magnetic switching with sizable exchange bias H_{EB} relative to the coercive field H_C encourages us to test the possibility of electric-field driven magnetic switching. In our designed geometry, ferroelectric switching should induce a 90° rotation of the in-plane projection of \vec{P} . If the exchange bias is closely coupled with ferroelectricity via the antiferromagnetic ordering [67], such a switching will likely induce a 90° in-plane rotation of exchange bias \vec{H}_{EB} as shown in Fig. 6.9(b) so that its projection along the device strip is reversed. Since the coercive field of the magnetic layer is smaller than the magnitude of exchange bias (as shown in Fig. 6.10), such a switching of exchange bias can in principle drive switching of the pinned layer magnetization direction near zero applied magnetic field.

As a first step towards this goal, we study the effect of electric field on the magnitude of exchange bias by measuring the GMR switching signal (resistance versus field) after various electric field pulses are applied. The electric field must be strong enough to switch the electric polarization \vec{P} of BFO. The ferroelectric coercivity of BFO depends on the underlying substrate on which the BFO is grown, ranging from 150-300 kV/cm on SrTiO₃ substrate to 100-200 kV/cm on DyScO₃ substrates. Over a 4-6 μm distance, an electric voltage of about 75-200 V is needed to switch the ferroelectric polarization. BFO is in principle an insulator, which in realistic samples, however, sometimes conducts electric current due to defects or impurities, oxygen vacancies in particular. Those leakage current under such high voltages could generate huge amount of heat and destroy the device. To somewhat mitigate this effect so that the device can withstand higher voltage, we typically apply 10 or 20 ms voltage pulses, and

gradually step-ramp the voltage from 30 V up to 250 V when necessary. The voltage pulse is generated by a Physik Instrumente E-507 piezoelectric amplifier driven by a HP pulse generator. The pulse generator produces pulses on the order of \sim 1 V, while the E-507 piezoelectric amplifier provides $100 \times$ amplification. The high voltage pulses are applied across the pair of side electrodes, with one electrode at ground voltage and the other at high positive or negative voltage. Noting that the device strip is expected at a medium voltage (which is typically several tens of volts) during the pulse, we electrically float the device potential by disconnecting it from the measurement setup (while shorting the both ends of the device with each other for additional protection). For the same reason, I don't think GMR can be measured simultaneously with the pulse, and the cable connection/disconnection for pulsing/measurement sequence so far has to be manually executed¹.

Unfortunately, we have not been able to observe any reversible and reproducible change of exchange bias induced by the voltage pulse. In the majority of samples, no change of exchange bias was observed at all up to ± 200 V of pulses. Applying pulses larger than ± 200 V runs significantly higher risk for a complete burn-out of the device due to leakage current [such as shown in Fig. 6.11(a) and (b)]. For the BFO samples on STO substrates, it is likely that 200 V may not be enough to induce ferroelectric switching, but at the later stage of this project we have shifted mostly to DSO substrate with less ferroelectric coercivity, so the voltage we applied should be generally sufficient. We verified that at least the BFO ferroelectric domains not covered by the device strip and within the gap of the side electrodes have been switched by the voltage pulses [Fig. 6.11(c) and (d)], but the GMR measurement still does not show any

¹I'm sure there are ways to improve automation if the physical results prove worth it.

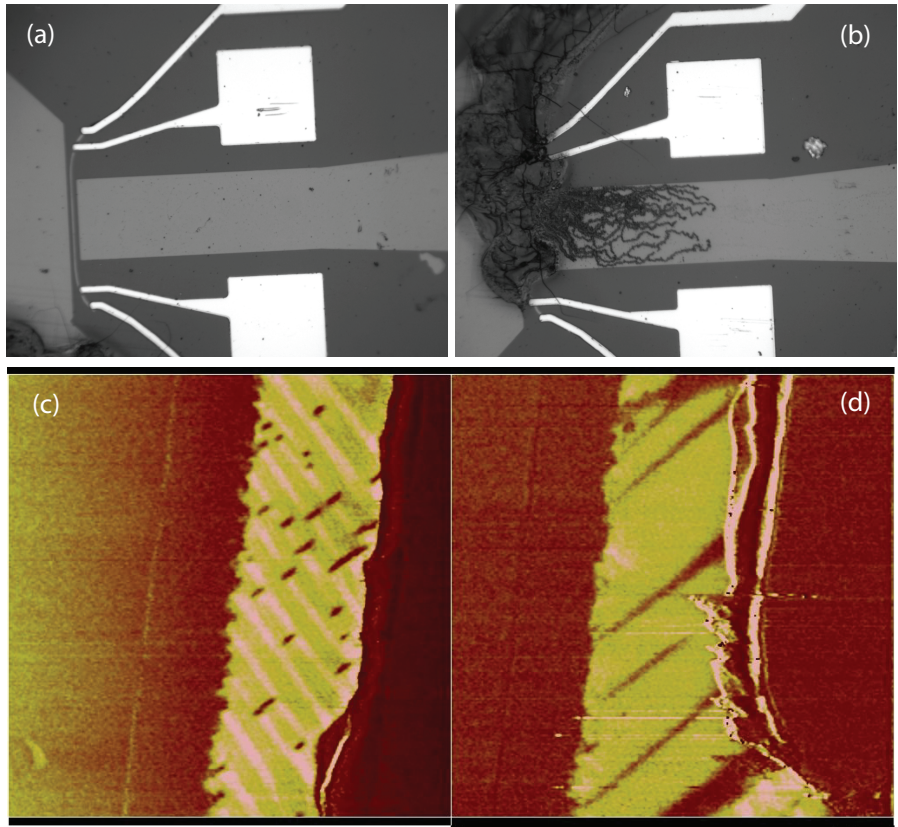


Figure 6.11: Images of the spin valve devices under electric-field induced ferroelectric switching. (a) and (b) A remarkable failure mode: a pristine device (a) is completely burned (b) after an electric field of about 300 kV/cm is applied across the side electrodes. (c) and (d) Comparison of the ferroelectric domain structure of the area of BFO inside the $6 \mu\text{m}$ electrode gap (but not covered by the device strip) before and after successful ferroelectric switching.

change before and after the ferroelectric switching. One possibility is that the BFO directly underneath the device strip is decoupled from the exposed areas and not switched under the voltage pulse because the electric field underneath the device strip can be mostly shunted by the device (which is metallic) itself. However, experiments in Ramesh group [67, 138] have shown that it is possible to switch the electric polarization of BFO directly under the metallic device by application of electric field from side electrodes in a very similar geometry. Furthermore, we expect that this shunting effect will be significantly mitigated if the device strip is made sub-100 nm wide, comparable to the thickness of

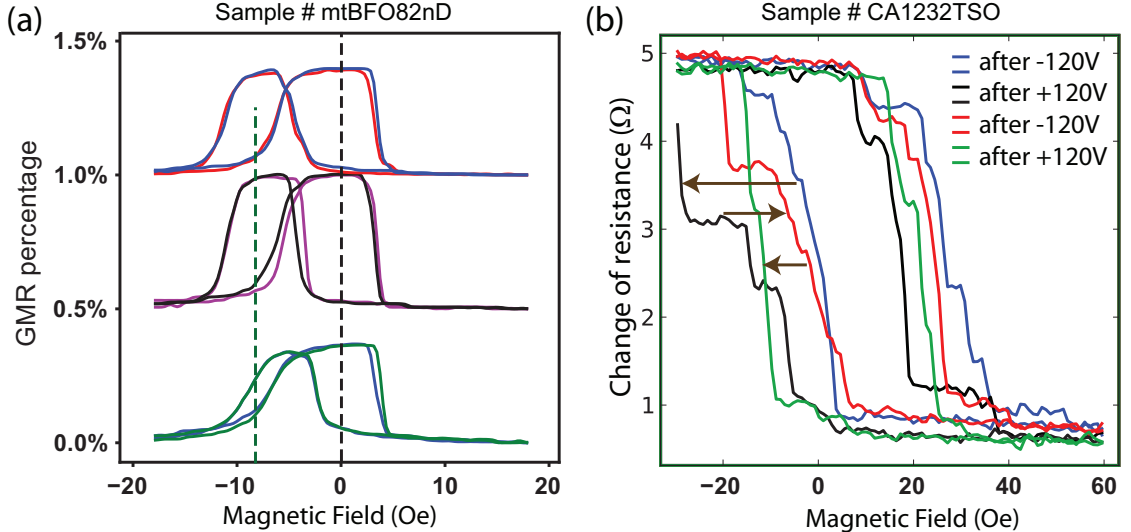


Figure 6.12: (a) The GMR loops (resistance versus magnetic field applied along the device strip) for three DSO/BFO/Py/Cu/Py devices on sample # mtBFO82nD, after voltage pulses of +180 V and -180 V are applied. For all device, no changes in the GMR loop are observed after different polarities of voltage pulses. (b) The minor loop GMR scan for the bottom Py layer of a TSO/BFO/Py/Cu/Py hero device on sample # CA1232TSO, where negative pulses appears to reduce the exchange bias while positive pulses partially restore the exchange bias.

the BFO film. 100 nm is also the length scale of the domain size of the BFO film so that the electric polarization under a sub-100 nm device is unlikely to be decoupled from the exposed areas. Therefore we also fabricated nano-strip devices with the dimension of 80 nm (or 160 nm, 240 nm, 320 nm) \times 5 μm by electron-beam lithography (with the same recipe as will be discussed in the next section), replacing the micro-strip devices in between the side electrodes. Again we observe exchange bias consistent among devices and consistent with the magnetometry characterization for extended film stacks although the coercive field for nano-strip devices appear to be slightly increased compared with micro-strip devices. However, in most devices the GMR measurements show strictly no change after whatever electric field is applied [Fig. 6.12(a)].

Of the 8-10 BFO samples that we have patterned into micro-strip or nano-strip spin valves devices and attempted voltage-induced switching, only devices made on 2 samples showed some decrease of exchange bias. For these devices, the exchange bias decreased gradually and saturated to a small value after several large voltage pulses. There was one single sample where we observed a change of exchange bias by electric field in a partially reversible fashion. Electric field in one direction could reduce the exchange bias, while a reversed electric field could produce a partial restoration [Fig. 6.12(b)], but after repeated electric poling the exchange bias eventually decreased and saturated to a small value. It should be noted that this BFO film is from the only batch of samples that we acquired from Schlom group at Cornell instead of Ramesh group at Berkeley. It was grown by molecular beam epitaxy (MBE) on TbScO_3 substrate instead of SrTiO_3 or DyScO_3 . MBE growth of BFO, with further optimization, will probably provide better quality of BFO films than PLD in the end. However, at this stage unlike the samples from Berkeley that are optimized and tested to eliminate 109° domain walls and show well-ordered striped domains, the samples from Schlom group did not have control over the domain structure. I suspect there is significant amount of 109° domain walls in the sample shown in Fig. 6.12(b), so that this hero sample does not represent a stable state of the BFO/Py interface.

6.4 Study of Nanoscale Variations of Exchange Bias at the BiFeO₃/ Permalloy Interface

Our inability to alter the exchange bias with electric field, together with the wildly inconsistent exchange biases across different samples, casts some doubt on the coupling between the antiferromagnetic ordering \vec{L} of BFO and the exchange bias \vec{H}_{EB} at BFO/Py interface. Although there is little doubt that antiferromagnetism is an essential prerequisite for any possible exchange bias, the exact origin of exchange bias in an AFM/FM system in general has remained an open question. In a G-type antiferromagnet such as BFO where the surface (with alternating spins) should be macroscopically spin-neutral, one cannot explain any exchange bias without resorting to surface roughness, disorder, or more complex reorganization at the interface. Malozemoff's random field model [139] argues that exchange bias originates from the alignment of the small number of interface odd spins in each AFM domains by the growth or annealing field. Other studies have phenomenologically established the existence of interface uncompensated spins [140, 141] which are usually believed to reside in the AFM domain walls.

Studies in mono-domain BiFeO₃ single crystals have found no exchange bias [142] at either the BFO/Py or the BFO/CoFe interface, which is compatible with the hypothesis that 109° domain walls are responsible for the large exchange bias seen in BFO/CoFe samples. Another important observation is that the exchange bias in our BFO/Py system nearly always appears aligned with the growth field regardless of the direction of antiferromagnetic order parameter \vec{L} of the underlying BFO. From these pieces of evidence, my view is

that there is no intrinsic linkage between the AFM order parameter \vec{L} of a given BiFeO_3 domain and the exchange bias pinning field \vec{H}_{EB} that domain would possibly act on the adjacent FM. Instead exchange bias has a closer correlation with some interface spins that can be decoupled from \vec{L} and whose spatial distribution depends on the domain structure.

In Fig 6.11(c) and (d), the piezoresponse force microscopy (PFM) images showed that the ferroelectric switching mechanism in such striped multi-domain BFO films is not a simple reorientation of \vec{P} in each of the domains, but a spatial redistribution of ferroelectric (and therefore antiferromagnetic) domains. Typically after an electric field is applied, the orientation of the striped domain walls is rotated in-plane by 90° [Fig. 6.11(c) and (d)]. This is consistent with the domain structure changes in previous studies [67, 74] and with the expected 90° switch of the net in-plane polarization. However, we also note that after back-and-forth electric-field poling the domain size becomes much larger and more spatially-varied than in its pristine state, indicating some irreversibility of the complex multi-domain ferroelectric ordering. Therefore we think it is important to probe whether the exchange bias has a nano-scale spatial distribution associated with the domain structure, and to understand whether the exchange bias is a property associated with the order parameter of the internal regions of the domains, or a property associated with the domain walls.

Our GMR measurement described in previous sections allows us to measure the exchange bias locally acting on a patterned spin valve device as opposed to averaging over the full extended film by magnetometry measurements. By reducing the size of the BFO/Py/Cu/Py spin valve devices from “micro-

strip” ($\sim 2 \mu\text{m}$ wide) to “nano-wire” (40-80 nm wide), we can measure the local exchange bias coupling at the length scale comparable to the ferroelectric domain size of BFO. In this section, we report some preliminary results of measured nanoscale spatial variations of the exchange bias.

6.4.1 Fabrication

To fabricate nano-wire devices for study of local exchange bias, we follow the same procedure to deposit a film stack of Py(2.5 nm)/ Cu(4-8 nm)/ Py(2.5 nm)/ Pt(2.5 nm) onto $\text{DyScO}_3/\text{SrRuO}_3/\text{BiFeO}_3$. Most of the samples we used for this study have a SRO layer in between BFO and DSO substrate, which is due to some considerations on the PLD growth of BFO in Berkeley. These samples are not suitable for applying in-plane electric fields because SRO is a conductor and shunts any electric field one attempts to apply laterally across BFO. Therefore these samples mostly ended up in this study of nanoscale exchange bias, where we did not attempt ferroelectric switching. Again we look for film samples showing sizable exchange bias ($H_{EB} > 15 \text{ Oe}$) for further fabrication of devices.

We use electron-beam lithography and ion milling to etch the metallic layers into wires 40-80 nm in width and $25 \mu\text{m}$ in length. Electron-beam lithography was performed at the JEOL 6300 e-beam system at CNF using a HSQ-based fabrication recipe listed as the following:

1. Sonicate the sample in acetone for 1 min, and then clean with IPA. Blow dry, and bake at 115°C for 60 sec. This helps with resist spinning quality.
2. Spin PMMA 495k (4%) at 4000 rpm (2000 rpm² acceleration) for 60 sec, and bake at 115°C for 60 sec.

3. Spin HSQ (6%) at 3000 rpm (3000 rpm² acceleration) for 60 sec, and bake at 115 °C for 60 sec.
4. Use the chip holder with 5 mm slot at JEOL 6300 to mount the sample for e-beam exposure. Due to a dent at the center of the sample holder, the sample needs to be mounted off-center by a few millimeters. Roughly estimate (with a ruler) and remember the position of the sample on the holder.
5. After running the standard calibration procedures on JEOL 6300, run the program “Heightmap” multiple times with different position offset parameters to determine the boundary of the sample in JEOL coordinate system so that the exposure is centered on the sample. (When the coordinates are outside the sample area, the Heightmap should report error.) If one cannot find the sample from Heightmap at all, vent and re-load the sample since it is likely tilted out of plane.
6. Use the 4th lens of JEOL 6300 at 1 nA of current for exposure. The doses are 1000 $\mu\text{C}/\text{cm}^2$ for alignment mark, and 1600-2800 $\mu\text{C}/\text{cm}^2$ for nano-strip devices 40-80 nm wide.
7. Develop the pattern in 726MIF for 130 sec.
8. Etch the PMMA layer with oxygen plasma in Oxford 80#1 at 90 W for 3 min.
9. Check under microscope to verify the position of the alignment marks, and check under SEM to verify the dimension of the devices.
10. Etch through all the metallic layers by ion milling with the new IBD system in E-7. It takes about 2 min to 2.25 min to see the Bi signal rising from the end-point detector, and after that we etch for about 30 sec to be safe.

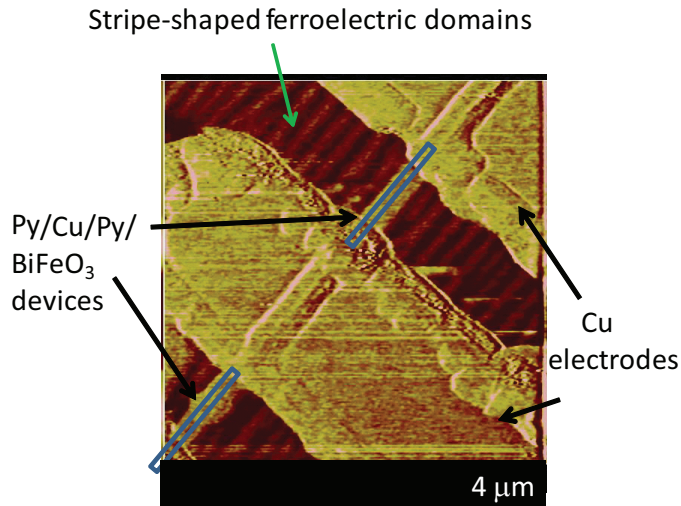


Figure 6.13: PFM image of nano-wire spin valve devices for study of local exchange bias at the BFO/Py interface. The blue rectangles mark the Py/Cu/Py spin valve devices exchange bias pinned by BFO, whose stripe-shaped domain structure can be seen in areas on two sides of the devices. Micron-scale Cu electrodes are in contact with the devices for current-in-plane GMR measurements.

11. To remove the developed PMMA/HSQ bilayer, soak the device in acetone overnight, and then sonicate for 2 minutes. Sonicate another 1 minute in IPA.

This process is not optimized in terms of choice of chemicals for resists and removers. One can probably make cleaner removal of HSQ residuals with the recipe described in Chapter 5 for fabrication of nanoparticle MTJ devices, where an additional omnicoat is used as sticking layer and Remover PG is used to strip the resists.

The next step is to make metallic contacts to small segments of the nanowire for CIP GMR measurements. For convenience, we use photolithography (with the same recipe as described in the previous section) to make 9 contacts to each 24 μm long nano-wire, resulting in 8 different 1μm long nano-wire devices. Fig. 6.13 shows two of such devices together with the Cu contact leads and

the stripe-shaped ferroelectric domains of BFO imaged by piezoresponse force microscopy (PFM). It should be noted the actual width of the devices (as measured by SEM) is slightly wider than the nominal value (typically 40 nm or 60 nm) due to shading effects in etching, but narrower than shown in PFM images such as Fig. 6.13 (~ 100 nm), possibly because the screening effect from the metals can interfere with PFM imaging tip at a non-zero distance. Each contact lead is spaced equally, and about 1.5-2 μm wide at the contact with the nano-wire, limited by the photolithography resolution. Therefore we have multiple devices only a couple of microns apart. One can certainly use electron-beam lithography to make denser contacts to make multiple devices closer to each other. The contact leads are made of ~ 200 nm Cu by ion beam deposition with the old IBD system in D-12 of Clark Hall. Again, lift-off is done by sonication in acetone for a few minutes. One point to note here is that the fabrication of our CIP spin valve device is less critical in requiring the metal strip to be uncovered from the top because the sidewalls of the device strip are exposed and can make contact with the deposited Cu. Therefore I did not test how well the developed PMMA/HSQ bilayer is removed. For some samples, nearly all devices show resistances one order of magnitude larger than expected, and the GMR ratio is dramatically lower, which is possibly related to poor contacts between the nano-wire and the contact pads. For the latest samples, yields have been $\sim 90\%$ for 60 nm nano-wire devices and $\sim 60\%$ for 40 nm nano-wire devices.

6.4.2 Nanoscale Variations of Exchange Bias Illustrated by GMR Measurements

We will report some results from three different samples (Sample # mtBFO33RnD, mtBFO48RnD and mtBFO66RnD). All samples have the same film stacks of DSO/SRO/BFO/Py/Cu/Py/Pt with the metallic layers deposited by DC magnetron sputtering in the AJA. For sample # mtBFO66RnD, the growth field is applied parallel to the domain stripes, and SQUID shows about 12 Oe exchange bias on the bottom Py layer for the un-patterned film stack [Fig. 6.14(a)]. After the film stack is patterned into $60\text{ nm} \times 1\text{ }\mu\text{m}$ nano-wire devices, Fig. 6.14(b) and (c) show the GMR measurements (resistance versus magnetic field applied parallel to the wires) for 16 such devices, with each panel presenting all 8 devices separated by the contact leads from one single nano-wire.

From the GMR signals of each of the devices, as described in previous sections, we can identify one switching loop centered close to zero field corresponding to the top unpinned Py layer, and one switching loop horizontally shifted corresponding to the bottom Py layer pinned by the exchange bias. If the exchange bias field (12 Oe) is uniform on the whole sample surface, we should see all the devices (on the same film sample) show the same switching field for the bottom Py layer. However, we found that the local exchange bias measured from GMR signal varies from device to device dramatically between -20 Oe to 20 Oe [Fig. 6.14(b) and (c)] and can even change sign for two neighboring devices just $2\text{ }\mu\text{m}$ apart. A sign change means that the direction of the local exchange bias acting within some $60\text{ nm} \times 1\text{ }\mu\text{m}$ areas can actually be opposite to the applied field during the growth of the film stack.

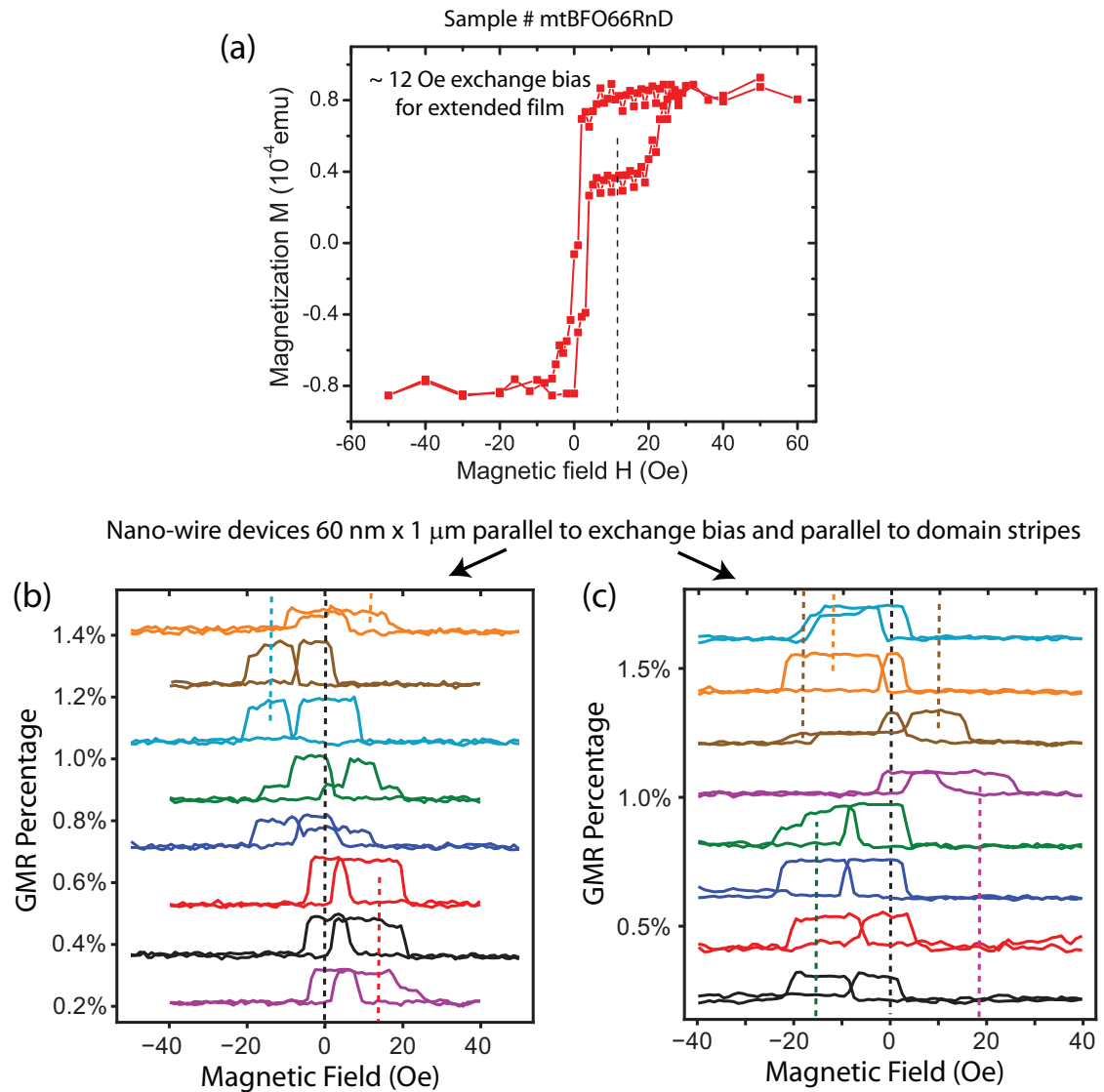


Figure 6.14: Large variations of exchange bias for nano-wire devices patterned parallel to the domain stripes of BFO. (a) SQUID magnetometry characterization of the BFO/Py/Cu/Py spin valve film stack, showing an exchange bias of about 12 Oe. (b) and (c) GMR data (resistance versus magnetic field) of 16 spin-valves devices from two nano-wires patterned parallel to the domain stripes of BFO.

Because the width of a domain stripe is about 120-150 nm (Fig. 6.13), we expect some of the nominally 60 nm (actual \sim 80 nm) \times 1 μm devices (parallel to domain stripes) to be on top of single domains, and some of the devices will involve two (or possibly more) domains and contain domain walls. If exchange bias is induced by surface uncompensated spins residing in the domain walls, no exchange bias should be observed for the devices covering a single domain. In all 16 devices we presented (from two nano-wires without data selection) we see exchange bias comparable to the absolute bulk value (12 Oe), and no device shows close to zero exchange bias. In fact samples with smaller exchange bias tend to show multiple switching steps [such as the blue curve in Fig. 6.14(b)] indicating different parts of the nano-wire devices experience different exchange bias. Therefore our measurements suggest that the exchange bias originates from spins spreading all over the interface instead of limited to the domain walls.

For sample # mtBFO48RnD we applied growth field and patterned the nano-wires both orthogonal to the stripe-shaped domains. We measured about 30 Oe exchange bias by VSM for the full film [Fig. 6.15(a)], and nearly all of the nano-wire devices showed exchange bias within a small range of 17 - 25 Oe [Fig. 6.15(b) and (c)]. In our previous experiments where we measured GMR effect from micro-strip devices (2 μm \times 50 μm), we never saw variations of exchange bias of more than 10% for different devices on the same film sample.

These results suggest a correlation between the local exchange bias between BFO/Py and the ferroelectric/antiferromagnetic domains of BFO. Our hypothesis is that each domain produces its own exchange bias, and neighboring domains can have very different exchange bias. Since all of the orthogonal

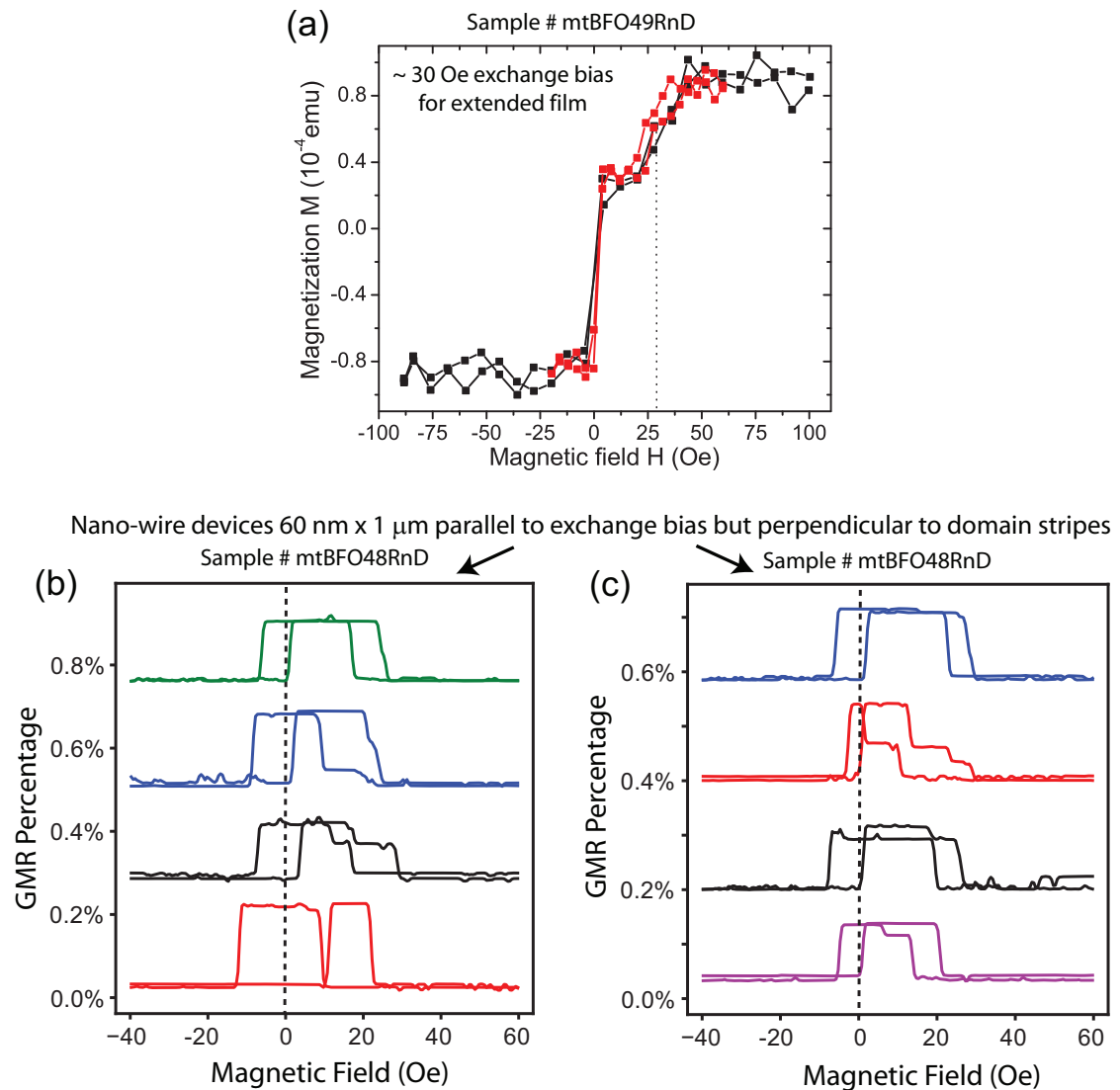


Figure 6.15: Relatively small variations of exchange bias for nano-wire devices patterned orthogonal to the domain stripes of BFO. (a) SQUID magnetometry characterization of the BFO/Py/Cu/Py spin valve film stack, showing an exchange bias of about 30 Oe. (b) and (c) GMR data (resistance versus magnetic field) of 8 spin-valves devices from two nano-wires patterned orthogonal to the domain stripes of BFO.

devices have to involve more than ten domains, the nanoscale variations of local exchange bias for different domains are averaged out. For micro-strip devices, the spatial variations are further suppressed by more averaging.

We have measured another different sample (Sample # mtBFO33RnD) that shows some interesting results. On this sample we did some back-sputtering treatment *in situ* before the deposition of metallic layers in an attempt to get rid of the interface oxide. As we have mentioned in section 6.2, compared with similar samples acquired in that period of time, we did not observe significant improvement in the full-film exchange bias [Fig. 6.16(a)] by back-sputtering treatment, instead the coercive field of the bottom Py film is larger than usual (~ 40 Oe). This sample has been patterned into nano-wire devices of a few different widths and $7 \mu\text{m}$ long. For $80 \text{ nm} \times 7 \mu\text{m}$ devices parallel to the domain strips (and parallel to exchange bias) we see the largest variations in exchange bias [Fig. 6.16(b)]. $80 \text{ nm} \times 7 \mu\text{m}$ devices patterned at a 22° angle show slightly smaller variations [Fig. 6.16(c)]. At the same time we see that the measured exchange bias values are overall significantly higher than the full-film value, exceeding 100 Oe for some devices. This enhancement in exchange bias in nano-devices, together with its device-to-device variations, are reduced when the width of the devices are increased to 240 nm [Fig. 6.16(d)]. Since we did not study samples with back-sputtering treatment systematically, we do not attempt to draw conclusions from this measurement. My speculation is that back-sputtering may have induced spatial non-uniformity in exchange bias on the length scale of the millimeters in addition to the nanoscale variations so that devices in certain area of the sample surface may display an overall larger exchange bias.

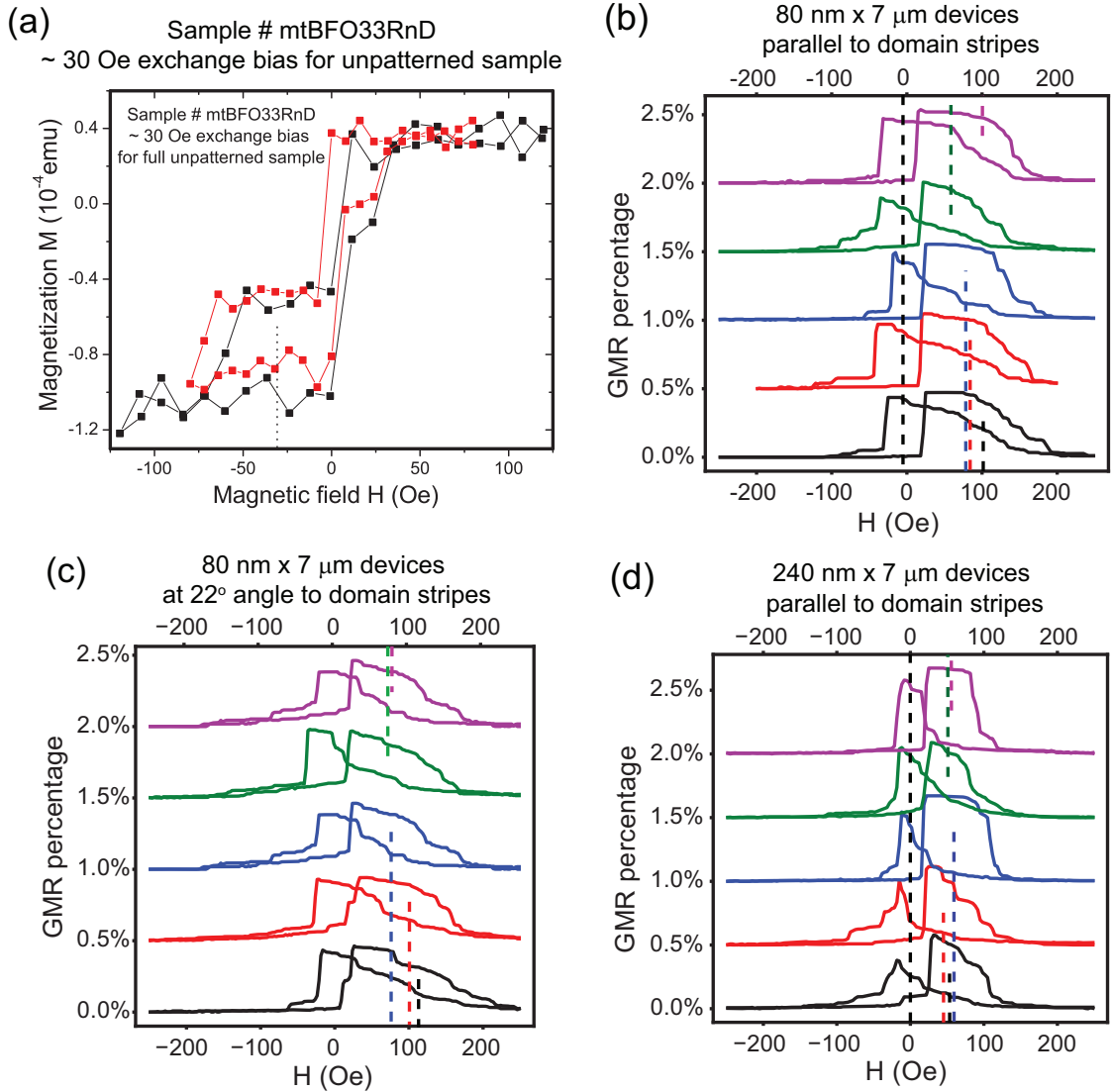


Figure 6.16: Nanoscale variations and enhancements of exchange bias for a BFO sample with back-sputtering treatment. (a) VSM magnetometry characterization of the BFO/Py/Cu/Py spin valve film stack, showing an exchange bias of about 30 Oe, and a larger-than-usual coercive field of about 40 Oe. (b) GMR data (resistance versus magnetic field) of a few 80 nm \times 7 μ m spin-valves devices patterned parallel to the domain stripes of BFO. (c) GMR data of a few 80 nm \times 7 μ m spin-valves devices patterned at a 22° angle to the domain stripes of BFO. (d) GMR data of a few 240 nm \times 7 μ m spin-valves devices patterned parallel to the domain stripes of BFO.

6.4.3 Piezoresponse Force Microscopy Imaging and Correlation with Exchange bias

We can further correlate the measured GMR data for a particular device with its surrounding domain positions from piezoresponse force microscopy (PFM) imaging. Our study so far is limited by our PFM capabilities, but with better PFM imaging such a study should reveal the detailed spatial distribution of exchange bias relative to domains and domain walls. Our PFM imaging is performed at the Dimension 3100 AFM tool of CCMR at D-12 Clark Hall. By replacing the normal AFM tip with a conductive tip (we used MikroMasch #NSC19 Ti/Pt tips), we can measure the out-of-plane ferroelectric response of the BFO film. Since the striped BFO with supposedly all 71° domain walls should in principle only show in-plane contrast of electric polarization \vec{P} but not out-of-plane contrast, the signal level we achieved in PFM imaging is very small. In our initial efforts, we did not find a way to image in-plane polarizations. In addition neither the spatial resolution nor the out-of-plane signal resolution were optimized to the full potential of the equipment. As a starting point, here we present images of all 8 devices from a same nano-wire [B1-B8 in Fig. 6.17(b)] on sample # mtBFO65RnD, together with a few devices [only T8 is shown in Fig. 6.17(c)] at a nearby nano-wire (less than $10 \mu\text{m}$ from B1-B8). Also we show the GMR data of these devices.

This sample has a full-film exchange bias of about 12 Oe induced along the direction of the domains stripes during Py deposition. The fabrication of nano-wire spin valve devices on this sample turns out not as successful as for sample # mtBFO66RnD, reflected in lower device yield. Several devices (B3-B6) appear damaged [Fig. 6.17(b)] to different degrees, and indeed devices B4 and B5 are

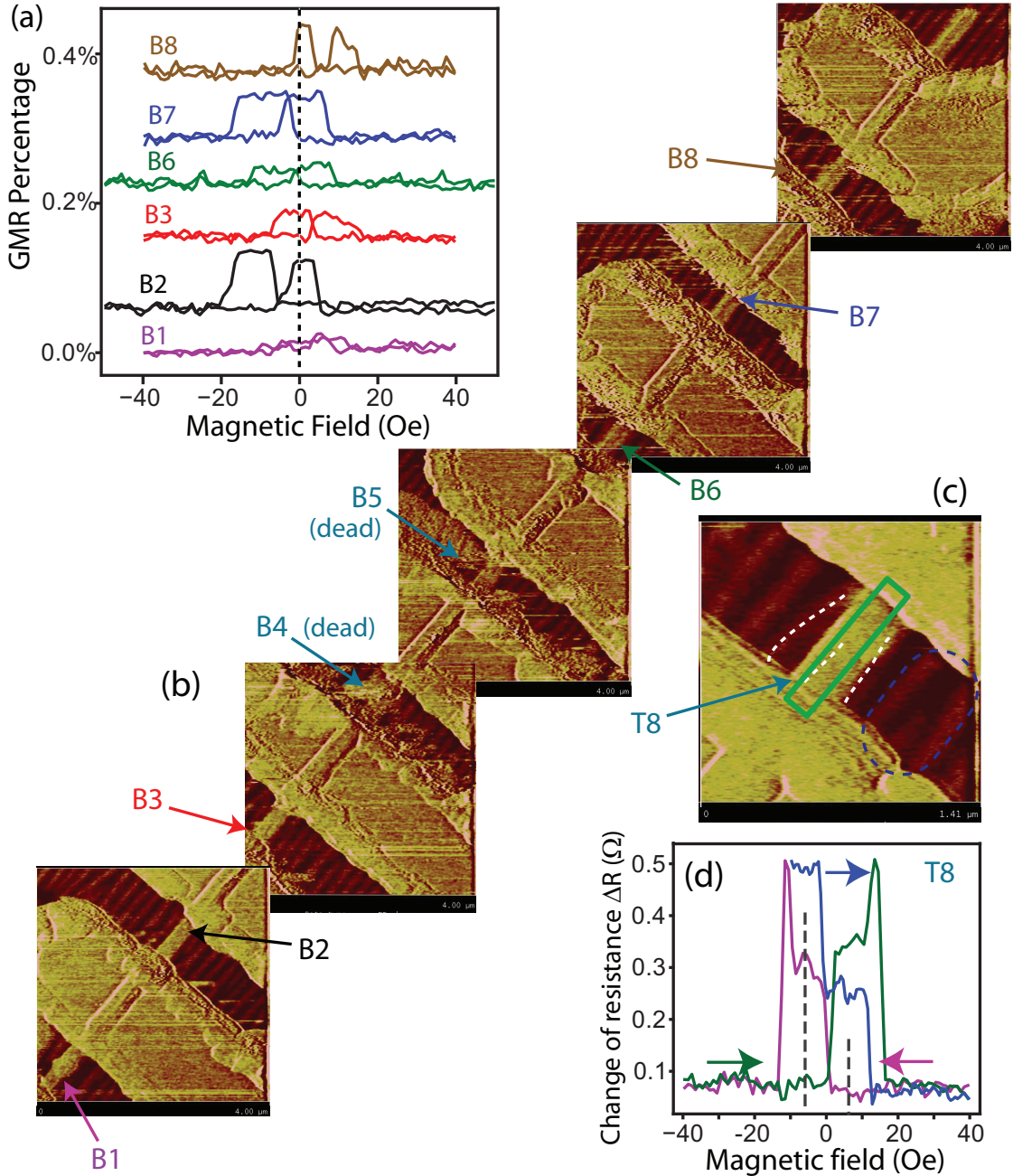


Figure 6.17: Correlation of exchange bias with location of nano-wire spin valve devices. (a) GMR data of several spin-valves devices from one nano-wire patterned parallel to the domain stripes of BFO. (b) Out-of-plane PFM images of all 8 devices along the same nano-wire, including the 6 devices in (a), and 2 dead devices. (c) PFM image of another device, whose surrounding BFO domain structure (marked by the white dashed lines) suggests that it is likely located above two distinctive BFO domains, with a structure similar to the area marked with a blue dashed-line oval. (d) GMR data of the device shown in (c), showing distinctive 2-step switching of the bottom Py layer.

dead (open circuit) in electrical measurements, and B3 and B6 show very weak GMR signal. B2, B7, B8 are the best devices both from the PFM image and the GMR data [Fig. 6.17(a)]. Of course our goal is to correlate the GMR data with the location of the device relative to BFO domains (not with the failure modes of nanofabrication). Although one can not directly image the ferroelectric domains underneath the metallic devices, one can “extrapolate” the domain walls from the PFM images of the surrounding area to the area underneath the devices. For example, in Fig. 6.17(c) one can identify two bright-contrast domains on the sides of the device T8. These two domains are significantly tilted relative to each other, with wider spacing on the lower-left side and narrower spacing on the upper-right side. Based on this observation, one can imagine another bright-contrast domain would be located underneath the lower-left part of device T8, but the upper-right part of the device is likely in contact with a dark-contrast domain. (For visual help, see the blue dashed-line oval near the lower-right corner of Fig. 6.17(c) to get a sense of how the BFO domain probably looks underneath the device.) This type of underlying domain structure separates the device T8 into two parts in the longitudinal direction, and the magnetic switching of its bottom Py layer is separated into two steps. In Fig. 6.17(d), the outer switching edges corresponds to the top unpinned layer (which shows somewhat larger coercivity than usual), and the minor switching loops formed by the pink and blue curves demonstrates the two-step switching of the bottom Py layer. The exchange biases acting on the two segments of the bottom Py layer are +6 Oe and -6 Oe respectively, likely indicating the two domains produce different exchange biases on the Py layer. So far our data allowing such a comparison between GMR measurements and the location of the devices relative to the BFO domains are very limited. Improvement on

the resolution and stability of our PFM should allow easier imaging in larger quantities, and make more convincing correlation between exchange bias and individual domains of BFO.

6.5 Summary

In this chapter, we studied the exchange bias at the interface between BiFeO_3 (with striped domains) and Py ($\text{Ni}_{81}\text{Fe}_{19}$) by both magnetometry measurements on continuous films and GMR measurements on patterned BFO/Py/Cu/Py spin valve devices. The exchange bias at the BFO/Py interface varies from sample to sample and so far we have not been able to produce consistent exchange bias across different BFO samples. We made efforts to modulate the exchange bias acting on spin valve devices by an electric field but had little success. Our experiments suggest that the exchange bias is likely extrinsic to the systematic antiferromagnetic ordering of BFO. We demonstrated that the local exchange bias acting on nano-scale spin valve devices varies dramatically from device to device, and this variation is correlated with the number of domains each device covers on average. A detailed study of the correlation between the local exchange bias and the position of the device relative to domains and domain walls should identify the area that produces positive or negative exchange bias and shed light on the underlying mechanism of the exchange bias pinning. Since the domain structures are often significantly reorganized under electric field, we believe understanding exchange bias at the single domain level together with a way to control the domain structure under electric field are critical for realizing robust switching of exchange bias.

BIBLIOGRAPHY

- [1] M. N. Baibich, J. M. Broto, A. Fert, F. N. Van Dau, F. Petroff, P. Etienne, G. Creuzet, A. Friederich, and J. Chazelas, "Giant magnetoresistance of (001)Fe/(001)Cr magnetic superlattices," *Phys. Rev. Lett.* **61**, 2472 (1988).
- [2] G. Binasch, P. Grünberg, F. Saurenbach, and W. Zinn, "Enhanced magnetoresistance in layered magnetic structures with antiferromagnetic interlayer exchange," *Phys. Rev. B* **39**, 4828 (1989).
- [3] N. F. Mott, "The electrical conductivity of transition metals," *Proc. Roy. Soc. A* **153**, 699 (1936).
- [4] A. Fert and I. A. Campbell, "Two current conduction in nickel," *Phys. Rev. Lett.* **21**, 1190 (1968).
- [5] A. Fert and I. A. Campbell, "Transport properties of ferromagnetic transition metals," *J. Phys.* **32**, C1 (1971).
- [6] B. Loegel and F. Gautier, "Origine de la resistivite dans le cobalt et ses alliages dilues," *J. Phys. Chem. Sol.* **32**, 2723 (1971).
- [7] E. Y. Tsymbal, "Physics of spin dependent tunneling," *APS March Meeting Tutorial* (2012).
- [8] M. Johnson and R. H. Silsbee, "Interfacial charge-spin coupling: Injection and detection of spin magnetization in metals," *Phys. Rev. Lett.* **55**, 1790 (1985).
- [9] J. Slonczewski, "Current-driven excitation of magnetic multilayers," *J. Magn. Magn. Mater.* **159**, L1 (1996).

- [10] L. Berger, "Emission of spin waves by a magnetic multilayer traversed by a current," *Phys. Rev. B* **54**, 9353 (1996).
- [11] M. Tsoi, A. G. M. Jansen, J. Bass, W.-C. Chiang, M. Seck, V. Tsoi, and P. Wyder, "Excitation of a magnetic multilayer by an electric current," *Phys. Rev. Lett.* **80**, 42814284 (1998).
- [12] E. B. Myers, "Current-Induced switching of domains in magnetic multi-layer devices," *Science* **285**, 867 (1999).
- [13] J. A. Katine, R. A. Buhrman, E. B. Myers, and D. C. Ralph, "Current-driven magnetization reversal and spin-wave excitations in Co/Cu/Co pillars," *Phys. Rev. Lett.* **84**, 3149 (2000).
- [14] D. Ralph and M. Stiles, "Spin transfer torques," *J. Magn. Magn. Mater.* **320**, 1190 (2008).
- [15] J. C. Slonczewski, "Currents and torques in metallic magnetic multilayers," *J. Magn. Magn. Mater.* **247**, 324 (2002).
- [16] Y.-T. Cui, *Characterization of magnetic dynamics excited by spin transfer torque in a nanomagnet*, Ph.D. Dissertation, Cornell University (2011).
- [17] S. I. Kiselev, J. C. Sankey, I. N. Krivorotov, N. C. Emley, R. J. Schoelkopf, R. A. Buhrman, and D. C. Ralph, "Microwave oscillations of a nanomagnet driven by a spin-polarized current," *Nature* **425**, 380 (2003).
- [18] I. N. Krivorotov, N. C. Emley, J. C. Sankey, S. I. Kiselev, D. C. Ralph, and R. A. Buhrman, "Time-domain measurements of nanomagnet dynamics driven by spin-transfer torques," *Science* **307**, 228 (2005).

- [19] I. Giaever, "Energy gap in superconductors measured by electron tunneling," *Phys. Rev. Lett.* **5**, 147 (1960).
- [20] P. M. Tedrow and R. Meservey, "Spin-dependent tunneling into ferromagnetic nickel," *Phys. Rev. Lett.* **26**, 192 (1971).
- [21] J. S. Moodera, G. Miao, and T. S. Santos, "Frontiers in spin-polarized tunneling," *Phys. Today* **63**, 46 (2010).
- [22] M. Jullière, "Tunneling between ferromagnetic films," *Phys. Lett. A* **54**, 225 (1975).
- [23] S. Maekawa and U. Gäfvert, "Electron tunneling between ferromagnetic films," *IEEE Trans. Magn. MAG* **18**, 707 (1982).
- [24] J. S. Moodera, L. R. Kinder, T. M. Wong, and R. Meservey, "Large magnetoresistance at room temperature in ferromagnetic thin film tunnel junctions," *Phys. Rev. Lett.* **74**, 3273 (1995).
- [25] T. Miyazaki and N. Tezuka, "Giant magnetic tunneling effect in Fe/Al₂O₃/Fe junction," *J. Magn. Magn. Mater.* **139**, L231 (1995).
- [26] W. Eib and S. F. Alvarado, "Spin-polarized photoelectrons from nickel single crystals," *Phys. Rev. Lett.* **37**, 444 (1976).
- [27] M. B. Stearns, "Simple explanation of tunneling spin-polarization of Fe, Co, Ni and its alloys," *J. Magn. Magn. Mater.* **5**, 167 (1977).
- [28] W. Butler, X. Zhang, T. Schulthess, and J. MacLaren, "Spin-dependent tunneling conductance of Fe/MgO/Fe sandwiches," *Phys. Rev. B* **63**, 054416 (2001).

- [29] J. Mathon and A. Umerski, "Theory of tunneling magnetoresistance of an epitaxial Fe/MgO/Fe(001) junction," *Phys. Rev. B* **63**, 220403 (2001).
- [30] S. Yuasa, T. Nagahama, A. Fukushima, Y. Suzuki, and K. Ando, "Giant room-temperature magnetoresistance in single-crystal Fe/MgO/Fe magnetic tunnel junctions," *Nature Mater.* **3**, 868 (2004).
- [31] S. S. P. Parkin, C. Kaiser, A. Panchula, P. M. Rice, B. Hughes, M. Samant, and S. Yang, "Giant tunnelling magnetoresistance at room temperature with MgO (100) tunnel barriers," *Nature Mater.* **3**, 862 (2004).
- [32] X.-G. Zhang and W. H. Butler, "Large magnetoresistance in bcc Co/MgO/Co and FeCo/MgO/FeCo tunnel junctions," *Phys. Rev. B* **70**, 172407 (2004).
- [33] J. J. Cha, J. C. Read, W. F. Egelhoff, P. Y. Huang, H. W. Tseng, Y. Li, R. A. Buhrman, and D. A. Muller, "Atomic-scale spectroscopic imaging of CoFeB/MgBO/CoFeB magnetic tunnel junctions," *Appl. Phys. Lett.* **95**, 032506 (2009).
- [34] H. L. Meyerheim, R. Popescu, J. Kirschner, N. Jedrecy, M. Sauvage-Simkin, B. Heinrich, and R. Pinchaux, "Geometrical and compositional structure at Metal-oxide interfaces: MgO on Fe(001)," *Phys. Rev. Lett.* **87**, 076102 (2001).
- [35] E. Y. Tsymbal, A. Sokolov, I. F. Sabirianov, and B. Doudin, "Resonant inversion of tunneling magnetoresistance," *Phys. Rev. Lett.* **90**, 186602 (2003).
- [36] Z. Li and S. Zhang, "Thermally assisted magnetization reversal in the presence of a spin-transfer torque," *Phys. Rev. B* **69**, 134416 (2004).

- [37] G. D. Fuchs, I. N. Krivorotov, P. M. Braganca, N. C. Emley, A. G. F. Garcia, D. C. Ralph, and R. A. Buhrman, "Adjustable spin torque in magnetic tunnel junctions with two fixed layers," *Appl. Phys. Lett.* **86**, 152509 (2005).
- [38] Z. Diao, D. Apalkov, M. Pakala, Y. Ding, A. Panchula, and Y. Huai, "Spin transfer switching and spin polarization in magnetic tunnel junctions with MgO and AlOx barriers," *Appl. Phys. Lett.* **87**, 232502 (2005).
- [39] S. Ikeda, J. Hayakawa, Y. M. Lee, F. Matsukura, Y. Ohno, T. Hanyu, and H. Ohno, "Magnetic tunnel junctions for spintronic memories and beyond," *IEEE Trans. Electron Devices* **54**, 991 (2007).
- [40] Z. Li, S. Zhang, Z. Diao, Y. Ding, X. Tang, D. M. Apalkov, Z. Yang, K. Kawabata, and Y. Huai, "Perpendicular spin torques in magnetic tunnel junctions," *Phys. Rev. Lett.* **100**, 246602 (2008).
- [41] S. Oh, S. Park, A. Manchon, M. Chshiev, J.-H. Han, H. Lee, J.-E. Lee, K.-T. Nam, Y. Jo, Y.-C. Kong, B. Dieny, and K.-J. Lee, "Bias-voltage dependence of perpendicular spin-transfer torque in asymmetric MgO-based magnetic tunnel junctions," *Nature Phys.* **5**, 898 (2009).
- [42] S. Petit, C. Baraduc, C. Thirion, U. Ebels, Y. Liu, M. Li, P. Wang, and B. Dieny, "Spin-Torque influence on the High-Frequency magnetization fluctuations in magnetic tunnel junctions," *Phys. Rev. Lett.* **98**, 077203 (2007).
- [43] H. Mu, G. Su, and Q. Zheng, "Spin current and current-induced spin transfer torque in ferromagnetquantum dotferromagnet coupled systems," *Phys. Rev. B* **73**, 054414 (2006).

- [44] I. Theodonis, A. Kalitsov, and N. Kioussis, "Enhancing spin-transfer torque through the proximity of quantum well states," *Phys. Rev. B* **76**, 224406 (2007).
- [45] M. M. Deshmukh, S. Kleff, S. Guèron, E. Bonet, A. N. Pasupathy, J. von Delft, and D. C. Ralph, "Magnetic anisotropy variations and nonequilibrium tunneling in a cobalt nanoparticle," *Phys. Rev. Lett.* **87**, 226801 (2001).
- [46] K. Yakushiji, F. Ernult, H. Imamura, K. Yamane, S. Mitani, K. Takanashi, S. Takahashi, S. Maekawa, and H. Fujimori, "Enhanced spin accumulation and novel magnetotransport in nanoparticles," *Nature Mater.* **4**, 57 (2005).
- [47] V. Kambersk, "On ferromagnetic resonance damping in metals," *Czech. J. Phys.* **26**, 1366 (1976).
- [48] K. Gilmore, Y. U. Idzerda, and M. D. Stiles, "Identification of the dominant Precession-damping mechanism in fe, co, and ni by First-Principles calculations," *Phys. Rev. Lett.* **99** (2007), 10.1103/PhysRevLett.99.027204.
- [49] X. Waintal and O. Parcollet, "Current-induced spin torque in a nanomagnet," *Phys. Rev. Lett.* **94**, 247206 (2005).
- [50] M. Jalil and S. Tan, "Spin transfer and current-induced switching in a ferromagnetic single-electron transistor," *Phys. Rev. B* **72**, 214417 (2005).
- [51] J.-i. Inoue and A. Brataas, "Magnetization reversal induced by spin accumulation in ferromagnetic transition-metal dots," *Phys. Rev. B* **70**, 140406 (2004).
- [52] S. Guèron, M. M. Deshmukh, E. B. Myers, and D. C. Ralph, "Tunneling

- via individual electronic states in ferromagnetic nanoparticles," *Phys. Rev. Lett.* **83**, 4148 (1999).
- [53] W. Jiang, F. T. Birk, and D. Davidovic, "Microwave coupled electron tunneling measurement of co nanoparticles," *Appl. Phys. Lett.* **99**, 032510 (2011).
- [54] K. I. Bolotin, F. Kuemmeth, A. N. Pasupathy, and D. C. Ralph, "Metal-nanoparticle single-electron transistors fabricated using electromigration," *Appl. Phys. Lett.* **84**, 3154 (2004).
- [55] S. Krause, L. Berbil-Bautista, G. Herzog, M. Bode, and R. Wiesendanger, "Current-induced magnetization switching with a spin-polarized scanning tunneling microscope," *Science* **317**, 1537 (2007).
- [56] T. Y. Chen, S. X. Huang, C. L. Chien, and M. D. Stiles, "Enhanced magnetoresistance induced by spin transfer torque in granular films with a magnetic field," *Phys. Rev. Lett.* **96**, 207203 (2006).
- [57] X. J. Wang, H. Zou, and Y. Ji, "Spin transfer torque switching of cobalt nanoparticles," *Appl. Phys. Lett.* **93**, 162501 (2008).
- [58] T. Kimura, Y. Otani, and J. Hamrle, "Switching magnetization of a nanoscale ferromagnetic particle using nonlocal spin injection," *Phys. Rev. Lett.* **96**, 037201 (2006).
- [59] T. Yang, T. Kimura, and Y. Otani, "Giant spin-accumulation signal and pure spin-current-induced reversible magnetization switching," *Nature Phys.* **4**, 851 (2008).
- [60] J. Z. Sun, M. C. Gaidis, E. J. OSullivan, E. A. Joseph, G. Hu, D. W. Abraham, J. J. Nowak, P. L. Trouilloud, Y. Lu, S. L. Brown, D. C.

Worledge, and W. J. Gallagher, "A three-terminal spin-torque-driven magnetic switch," *Appl. Phys. Lett.* **95**, 083506 (2009).

- [61] L. Xue, C. Wang, Y.-T. Cui, L. Liu, A. Swander, J. Sun, R. Buhrman, and D. Ralph, "Resonance measurement of nonlocal spin torque in a three-terminal magnetic device," *Phys. Rev. Lett.* **108**, 147201 (2012).
- [62] L. Liu, C.-F. Pai, Y. Li, H. W. Tseng, D. C. Ralph, and R. A. Buhrman, "Spin-Torque switching with the giant spin Hall effect of tantalum," *Science* **336**, 555 (2012).
- [63] S. O. Valenzuela and M. Tinkham, "Direct electronic measurement of the spin Hall effect," *Nature* **442**, 176 (2006).
- [64] L. Liu, T. Moriyama, D. C. Ralph, and R. A. Buhrman, "Spin-torque ferromagnetic resonance induced by the spin Hall effect," *Phys. Rev. Lett.* **106**, 036601 (2011).
- [65] M. Weisheit, S. Fahler, A. Marty, Y. Souche, C. Poinsignon, and D. Givord, "Electric field-induced modification of magnetism in thin-film ferromagnets," *Science* **315**, 349 (2007).
- [66] H. Ohno, D. Chiba, F. Matsukura, T. Omiya, E. Abe, T. Dietl, Y. Ohno, and K. Ohtani, "Electric-field control of ferromagnetism," *Nature* **408**, 944 (2000).
- [67] Y.-H. Chu, L. W. Martin, M. B. Holcomb, M. Gajek, S.-J. Han, Q. He, N. Balke, C.-H. Yang, D. Lee, W. Hu, Q. Zhan, P.-L. Yang, A. Fraile-Rodrguez, A. Scholl, S. X. Wang, and R. Ramesh, "Electric-field control of local ferromagnetism using a magnetoelectric multiferroic," *Nature Mater.* **7**, 478 (2008).

- [68] V. Novosad, Y. Otani, A. Ohsawa, S. G. Kim, K. Fukamichi, J. Koike, K. Maruyama, O. Kitakami, and Y. Shimada, "Novel magnetostrictive memory device," *J. Appl. Phys.* **87**, 6400 (2000).
- [69] T. Maruyama, Y. Shiota, T. Nozaki, K. Ohta, N. Toda, M. Mizuguchi, A. A. Tulapurkar, T. Shinjo, M. Shiraishi, S. Mizukami, Y. Ando, and Y. Suzuki, "Large voltage-induced magnetic anisotropy change in a few atomic layers of iron," *Nature Nanotech.* **4**, 158 (2009).
- [70] Y. Shiota, T. Nozaki, F. Bonell, S. Murakami, T. Shinjo, and Y. Suzuki, "Induction of coherent magnetization switching in a few atomic layers of FeCo using voltage pulses," *Nature Mater.* **11**, 39 (2012).
- [71] W.-G. Wang, M. Li, S. Hageman, and C. L. Chien, "Electric-field-assisted switching in magnetic tunnel junctions," *Nature Mater.* **11**, 64 (2012).
- [72] J. Wang, J. B. Neaton, H. Zheng, V. Nagarajan, S. B. Ogale, B. Liu, D. Viehland, V. Vaithyanathan, D. G. Schlom, U. V. Waghmare, N. A. Spaldin, K. M. Rabe, M. Wuttig, and R. Ramesh, "Epitaxial BiFeO₃ multiferroic thin film heterostructures," *Science* **299**, 1719 (2003).
- [73] R. Ramesh and N. A. Spaldin, "Multiferroics: progress and prospects in thin films," *Nature Mater.* **6**, 21 (2007).
- [74] T. Zhao, A. Scholl, F. Zavaliche, K. Lee, M. Barry, A. Doran, M. P. Cruz, Y. H. Chu, C. Ederer, N. A. Spaldin, R. R. Das, D. M. Kim, S. H. Baek, C. B. Eom, and R. Ramesh, "Electrical control of antiferromagnetic domains in multiferroic BiFeO₃ films at room temperature," *Nature Mater.* **5**, 823 (2006).

- [75] J. C. Sankey, *Microwave-frequency characterization of spin transfer and individual nanomagnets*, Ph.D. Dissertation, Cornell University (2007).
- [76] J. C. Sankey, Y.-T. Cui, J. Z. Sun, J. C. Slonczewski, R. A. Buhrman, and D. C. Ralph, “Measurement of the spin-transfer-torque vector in magnetic tunnel junctions,” *Nature Phys.* **4**, 67 (2008).
- [77] A. A. Tulapurkar, Y. Suzuki, A. Fukushima, H. Kubota, H. Maehara, K. Tsunekawa, D. D. Djayaprawira, N. Watanabe, and S. Yuasa, “Spin-torque diode effect in magnetic tunnel junctions,” *Nature* **438**, 339 (2005).
- [78] J. C. Sankey, P. M. Braganca, A. G. F. Garcia, I. N. Krivorotov, R. A. Buhrman, and D. C. Ralph, “Spin-transfer-driven ferromagnetic resonance of individual nanomagnets,” *Phys. Rev. Lett.* **96**, 227601 (2006).
- [79] H. Kubota, A. Fukushima, K. Yakushiji, T. Nagahama, S. Yuasa, K. Ando, H. Maehara, Y. Nagamine, K. Tsunekawa, D. D. Djayaprawira, N. Watanabe, and Y. Suzuki, “Quantitative measurement of voltage dependence of spin-transfer torque in MgO-based magnetic tunnel junctions,” *Nature Phys.* **4**, 37 (2008).
- [80] C. Wang, Y.-T. Cui, J. Z. Sun, J. A. Katine, R. A. Buhrman, and D. C. Ralph, “Bias and angular dependence of spin-transfer torque in magnetic tunnel junctions,” *Phys. Rev. B* **79**, 224416 (2009).
- [81] I. Theodonis, N. Kioussis, A. Kalitsov, M. Chshiev, and W. Butler, “Anomalous bias dependence of spin torque in magnetic tunnel junctions,” *Phys. Rev. Lett.* **97**, 237205 (2006).
- [82] C. Wang, Y.-T. Cui, J. A. Katine, R. A. Buhrman, and D. C. Ralph, “Time-

- resolved measurement of spin-transfer-driven ferromagnetic resonance and spin torque in magnetic tunnel junctions," *Nature Phys.* **7**, 496 (2011).
- [83] J. Xiao, G. E. W. Bauer, and A. Brataas, "Spin-transfer torque in magnetic tunnel junctions: Scattering theory," *Phys. Rev. B* **77**, 224419 (2008).
- [84] C. Heiliger and M. D. Stiles, "Ab initio studies of the spin-transfer torque in magnetic tunnel junctions," *Phys. Rev. Lett.* **100**, 186805 (2008).
- [85] J. Slonczewski and J. Sun, "Theory of voltage-driven current and torque in magnetic tunnel junctions," *J. Magn. Magn. Mater.* **310**, 169 (2007).
- [86] J. Bass and W. Pratt Jr., "Current-perpendicular (CPP) magnetoresistance in magnetic metallic multilayers," *J. Magn. Magn. Mater.* **200**, 274 (1999).
- [87] J. Z. Sun, M. C. Gaidis, G. Hu, E. J. OSullivan, S. L. Brown, J. J. Nowak, P. L. Trouilloud, and D. C. Worledge, "High-bias backhopping in nanosecond time-domain spin-torque switches of MgO-based magnetic tunnel junctions," *J. Appl. Phys.* **105**, 07D109 (2009).
- [88] C. Bilzer, T. Devolder, J. Kim, G. Counil, C. Chappert, S. Cardoso, and P. P. Freitas, "Study of the dynamic magnetic properties of soft CoFeB films," *J. Appl. Phys.* **100**, 053903 (2006).
- [89] G. D. Fuchs, J. C. Sankey, V. S. Pribiag, L. Qian, P. M. Braganca, A. G. F. Garcia, E. M. Ryan, Z. Li, O. Ozatay, D. C. Ralph, and R. A. Buhrman, "Spin-torque ferromagnetic resonance measurements of damping in nanomagnets," *Appl. Phys. Lett.* **91**, 062507 (2007).
- [90] M. L. Polianski and P. W. Brouwer, "Current-induced transverse spin-wave instability in a thin nanomagnet," *Phys. Rev. Lett.* **92**, 026602 (2004).

- [91] M. D. Stiles, J. Xiao, and A. Zangwill, "Phenomenological theory of current-induced magnetization precession," *Phys. Rev. B* **69**, 054408 (2004).
- [92] A. M. Deac, A. Fukushima, H. Kubota, H. Maehara, Y. Suzuki, S. Yuasa, Y. Nagamine, K. Tsunekawa, D. D. Djayaprawira, and N. Watanabe, "Bias-driven high-power microwave emission from MgO-based tunnel magnetoresistance devices," *Nature Phys.* **4**, 803 (2008).
- [93] T. Devolder, J. Kim, C. Chappert, J. Hayakawa, K. Ito, H. Takahashi, S. Ikeda, and H. Ohno, "Direct measurement of current-induced fieldlike torque in magnetic tunnel junctions," *J. Appl. Phys.* **105**, 113924 (2009).
- [94] S. Petit, N. de Mestier, C. Baraduc, C. Thirion, Y. Liu, M. Li, P. Wang, and B. Dieny, "Influence of spin-transfer torque on thermally activated ferromagnetic resonance excitations in magnetic tunnel junctions," *Phys. Rev. B* **78**, 184420 (2008).
- [95] M. H. Jung, S. Park, C. You, and S. Yuasa, "Bias dependences of in-plane and out-of-plane spin-transfer torques in symmetric MgO-based magnetic tunnel junctions," *Phys. Rev. B* **81**, 134419 (2010).
- [96] O. G. Heinonen, S. W. Stokes, and J. Y. Yi, "Perpendicular spin torque in magnetic tunnel junctions," *Phys. Rev. Lett.* **105**, 066602 (2010).
- [97] D. M. Pozar, *Microwave Engineering*, 3rd ed. (John Wiley & Sons, Inc., Hoboken, New Jersey, 2005).
- [98] D. Houssameddine, S. H. Florez, J. A. Katine, J. Michel, U. Ebels, D. Mauri, O. Ozatay, B. Delaet, B. Viala, L. Folks, B. D. Terris, and M. Cyrille, "Spin transfer induced coherent microwave emission with large power from nanoscale MgO tunnel junctions," *Appl. Phys. Lett.* **93**, 022505 (2008).

- [99] J. C. Slonczewski, "Currents, torques, and polarization factors in magnetic tunnel junctions," *Phys. Rev. B* **71**, 024411 (2005).
- [100] M. Wilczyński, J. Barnaś, and R. Świrkowicz, "Free-electron model of current-induced spin-transfer torque in magnetic tunnel junctions," *Phys. Rev. B* **77**, 054434 (2008).
- [101] A. Manchon, S. Zhang, and K. Lee, "Signatures of asymmetric and inelastic tunneling on the spin torque bias dependence," *Phys. Rev. B* **82**, 174420 (2010).
- [102] O. Ozatay, P. G. Gowtham, K. W. Tan, J. C. Read, K. A. Mkhoyan, M. G. Thomas, G. D. Fuchs, P. M. Braganca, E. M. Ryan, K. V. Thadani, J. Silcox, D. C. Ralph, and R. A. Buhrman, "Sidewall oxide effects on spin-torque- and magnetic-field-induced reversal characteristics of thin-film nanomagnets," *Nature Mater.* **7**, 567 (2008).
- [103] M. Yoshikawa, T. Ueda, H. Aikawa, N. Shimomura, E. Kitagawa, M. Nakayama, T. Kai, K. Nishiyama, T. Nagase, T. Kishi, S. Ikegawa, and H. Yoda, "Estimation of spin transfer torque effect and thermal activation effect on magnetization reversal in CoFeB/MgO/CoFeB magnetoresistive tunneling junctions," *J. Appl. Phys.* **101**, 09A511 (2007).
- [104] T. Devolder, J. Hayakawa, K. Ito, H. Takahashi, S. Ikeda, P. Crozat, N. Zerounian, J.-V. Kim, C. Chappert, and H. Ohno, "Single-shot time-resolved measurements of nanosecond-scale spin-transfer induced switching: Stochastic versus deterministic aspects," *Phys. Rev. Lett.* **100**, 057206 (2008).
- [105] K. Lee and S. H. Kang, "Design consideration of magnetic tunnel junctions

- for reliable High-Temperature operation of STT-MRAM," *IEEE Trans. Magn.* **46**, 1537 (2010).
- [106] E. Chen, D. Apalkov, Z. Diao, A. Driskill-Smith, D. Druist, D. Lottis, V. Nikitin, X. Tang, S. Watts, S. Wang, S. A. Wolf, A. W. Ghosh, J. W. Lu, S. J. Poon, M. Stan, W. H. Butler, S. Gupta, C. K. A. Mewes, T. Mewes, and P. B. Visscher, "Advances and future prospects of Spin-Transfer torque random access memory," *IEEE Trans. Magn.* **46**, 1873 (2010).
- [107] W. Chen, G. de Loubens, J. L. Beaujour, J. Z. Sun, and A. D. Kent, "Spin-torque driven ferromagnetic resonance in a nonlinear regime," *Appl. Phys. Lett.* **95**, 172513 (2009).
- [108] W. H. Rippard, M. R. Pufall, S. Kaka, T. J. Silva, S. E. Russek, and J. A. Katine, "Injection locking and phase control of spin transfer nano-oscillators," *Phys. Rev. Lett.* **95**, 067203 (2005).
- [109] J. Grollier, V. Cros, and A. Fert, "Synchronization of spin-transfer oscillators driven by stimulated microwave currents," *Phys. Rev. B* **73**, 060409 (2006).
- [110] R. D. McMichael and M. D. Stiles, "Magnetic normal modes of nanoelements," *J. Appl. Phys.* **97**, 10J901 (2005).
- [111] C. Wang, Y.-T. Cui, J. Z. Sun, J. A. Katine, R. A. Buhrman, and D. C. Ralph, "Sensitivity of spin-torque diodes for frequency-tunable resonant microwave detection," *J. Appl. Phys.* **106**, 053905 (2009).
- [112] L. Xue, C. Wang, Y.-T. Cui, J. A. Katine, R. A. Buhrman, and D. C. Ralph, "Conditions for microwave amplification due to spin-torque dynamics in magnetic tunnel junctions," *Appl. Phys. Lett.* **99**, 022505 (2011).

- [113] J. Slonczewski, "Conductance and exchange coupling of two ferromagnets separated by a tunneling barrier," *Phys. Rev. B* **39**, 6995 (1989).
- [114] L. Liu, T. Moriyama, D. C. Ralph, and R. A. Buhrman, "Reduction of the spin-torque critical current by partially canceling the free layer demagnetization field," *Appl. Phys. Lett.* **94**, 122508 (2009).
- [115] W. Chen, J.-M. L. Beaujour, G. de Loubens, A. D. Kent, and J. Z. Sun, "Spin-torque driven ferromagnetic resonance of Co/Ni synthetic layers in spin valves," *Appl. Phys. Lett.* **92**, 012507 (2008).
- [116] O. Prokopenko, G. Melkov, E. Bankowski, T. Meitzler, V. Tiberkevich, and A. Slavin, "Noise properties of a resonance-type spin-torque microwave detector," *Appl. Phys. Lett.* **99**, 032507 (2011).
- [117] L. Berger, "Multilayer configuration for experiments of spin precession induced by a dc current," *J. Appl. Phys.* **93**, 7693 (2003).
- [118] Y. Huai, M. Pakala, Z. Diao, and Y. Ding, "Spin transfer switching current reduction in magnetic tunnel junction based dual spin filter structures," *Appl. Phys. Lett.* **87**, 222510 (2005).
- [119] L. Xue, C. Wang, Y.-T. Cui, J. A. Katine, R. A. Buhrman, and D. C. Ralph, "Network analyzer measurements of spin transfer torques in magnetic tunnel junctions," *Appl. Phys. Lett.* **101**, 022417 (2012).
- [120] F. Ernult, K. Yamane, S. Mitani, K. Yakushiji, K. Takanashi, Y. K. Takahashi, and K. Hono, "Spin-dependent single-electron-tunneling effects in epitaxial fe nanoparticles," *Appl. Phys. Lett.* **84**, 3106 (2004).
- [121] G. Feng, S. van Dijken, and J. M. D. Coey, "MgO-based double barrier

- magnetic tunnel junctions with thin free layers," *J. Appl. Phys.* **105**, 07C926 (2009).
- [122] H. Yang, S.-H. Yang, and S. S. P. Parkin, "Crossover from Kondo-assisted suppression to Co-tunneling enhancement of tunneling magnetoresistance via ferromagnetic nanodots in MgO tunnel barriers," *Nano Lett.* **8**, 340 (2008).
- [123] H. Yang, S.-H. Yang, G. Ilnicki, J. Martinek, and S. Parkin, "Coexistence of the kondo effect and a ferromagnetic phase in magnetic tunnel junctions," *Phys. Rev. B* **83**, 174437 (2011).
- [124] H. Sukegawa, S. Nakamura, A. Hirohata, N. Tezuka, and K. Inomata, "Significant magnetoresistance enhancement due to a cotunneling process in a double tunnel junction with single discontinuous ferromagnetic layer insertion," *Phys. Rev. Lett.* **94**, 068304 (2005).
- [125] K. J. Dempsey, A. T. Hindmarch, H.-X. Wei, Q.-H. Qin, Z.-C. Wen, W.-X. Wang, G. Vallejo-Fernandez, D. A. Arena, X.-F. Han, and C. H. Marrows, "Cotunneling enhancement of magnetoresistance in double magnetic tunnel junctions with embedded superparamagnetic NiFe nanoparticles," *Phys. Rev. B* **82**, 214415 (2010).
- [126] J. I. Gittleman, B. Abeles, and S. Bozowski, "Superparamagnetism and relaxation effects in granular Ni-SiO₂ and Ni-Al₂O₃ films," *Phys. Rev. B* **9**, 3891 (1974).
- [127] K. V. Thadani, *Spin-torque-driven microwave frequency dynamics in magnetic nanopillar devices*, Ph.D. Dissertation, Cornell University (2009).

- [128] N. C. Emley, *Magnetic multilayer nanopillars for the study of current-induced reversal of a thin magnetic layer*, Ph.D. Dissertation, Cornell University (2005).
- [129] W. F. Brown, "Thermal fluctuations of a single-domain particle," *Phys. Rev.* **130**, 1677 (1963).
- [130] B. Efron and R. Tibshirani, *An introduction to the bootstrap* (Chapman & Hall, New York, 1994).
- [131] J. R. Teague, R. Gerson, and W. James, "Dielectric hysteresis in single crystal BiFeO₃," *Solid State Commun.* **8**, 1073 (1970).
- [132] I. E. Dzyaloshinskii, "Thermodynamic theory of "weak ferromagnetism in antiferromagnetic substances," *Sov. Phys. JETP* **5**, 12591272 (1957).
- [133] T. Moriya, "Anisotropic superexchange interaction and weak ferromagnetism," *Phys. Rev.* **120**, 91 (1960).
- [134] I. Sosnowska, T. P. Neumaier, and E. Steichele, "Spiral magnetic ordering in bismuth ferrite," *J. Phys. C* **15**, 4835 (1982).
- [135] D. Lebeugle, D. Colson, A. Forget, M. Viret, A. M. Bataille, and A. Gukasov, "Electric-field-induced spin flop in BiFeO₃ single crystals at room temperature," *Phys. Rev. Lett.* **100**, 227602 (2008).
- [136] C. Ederer and N. A. Spaldin, "Weak ferromagnetism and magnetoelectric coupling in bismuth ferrite," *Phys. Rev. B* **71**, 060401 (2005).
- [137] L. W. Martin, Y.-H. Chu, M. B. Holcomb, M. Huijben, P. Yu, S.-J. Han, D. Lee, S. X. Wang, and R. Ramesh, "Nanoscale control of exchange bias with BiFeO₃ thin films," *Nano Lett.* **8**, 2050 (2008).

- [138] J. T. Heron, M. Trassin, K. Ashraf, M. Gajek, Q. He, S. Y. Yang, D. E. Nikonov, Y. Chu, S. Salahuddin, and R. Ramesh, "Electric-field-induced magnetization reversal in a ferromagnet-multiferroic heterostructure," *Phys. Rev. Lett.* **107**, 217202 (2011).
- [139] A. P. Malozemoff, "Random-field model of exchange anisotropy at rough ferromagnetic-antiferromagnetic interfaces," *Phys. Rev. B* **35**, 3679 (1987).
- [140] K. Takano, R. H. Kodama, A. E. Berkowitz, W. Cao, and G. Thomas, "Interfacial uncompensated antiferromagnetic spins: Role in unidirectional anisotropy in polycrystalline Ni₈₁Fe₁₉/CoO bilayers," *Phys. Rev. Lett.* **79**, 1130 (1997).
- [141] H. Ohldag, A. Scholl, F. Nolting, E. Arenholz, S. Maat, A. Young, M. Carey, and J. Sthr, "Correlation between exchange bias and pinned interfacial spins," *Phys. Rev. Lett.* **91**, 017203 (2003).
- [142] D. Lebeugle, A. Mougin, M. Viret, D. Colson, and L. Ranno, "Electric field switching of the magnetic anisotropy of a ferromagnetic layer exchange coupled to the multiferroic compound BiFeO₃," *Phys. Rev. Lett.* **103**, 257601 (2009).